Characterization, Analysis and Modeling of Complex Flow Networks in Mammalian Organs.

DISSERTATION

Zur Erlangung des akademischen Grades

Doctor rerum naturalium (Dr. rer. nat.)

vorgelegt

dem Bereich Mathematik und Naturwissenschaften der Technischen Universität Dresden

von

Felix Kramer

Geboren 04.10.1990, Berlin

Gutachter:

Stephan Grill

Eleni Katifori

Verteidigt am 01.06.2022
Die Dissertation wurde vom 04.09.2017 bis 04.03.2021
am Center for Systems Biology Dresden (CSBD) angefertigt.

Zusammenfassung

Das Studium von Transportmechanismen in komplexen Organismen stellt eine zentrale Herausforderung dar, nicht nur in medizinischen und biologischen Disziplinen, sondern auch zunehmend in der Physik und Netzwerktheorie. Insbesondere sind bionisch inspirierte Designprinzipien zunehmend relevant, da sie zuverlässige Lösungsansätze zu verschiedenen theoretischen und technischen Problemen bieten. Herausstechend sind dabei vaskuläre Netzwerke in Säugetieren, deren Entwicklung auffällig stark auf Selbstorganisation beruhen und die korrekte Verteilung von Sauerstoff, Wasser, Blut oder Ähnlichem erlaubt. Dies wird erreicht durch ein komplexes biochemisches Signalsystem, welches an makroskopische Stimulationen, wie z. B. Reibung und Stress, gekoppelt ist. Die Morphogenese solcher Flussnetzwerke ist allerdings noch anderen Restriktionen unterworfen, da diese räumlich eingebettete Objekte darstellen. Sie sind als solche signifikant beschränkter in ihrer Skalierbarkeitund Dynamik.
Diese Dissertation addressiert daher relevante Fragestellungen zur Charakterisierung von Netzwerken und der Morphogenesesimulationen von drei-dimensional eingebetteten Netzwerken Die Schlüsselmechanismen auf die wir uns hier konzentrieren sind Flussfluktuationen, Interaktionen zwischen Paarstrukturen und die Aufnahme von Nährstoffen. Zu Beginn zeigen wir, wie sich konventionelle Ansätze zu Flussfluktuationen als allgemeine Einparametermodelle darstellen lassen. Wir demonstrieren damit den kontinuierlichen Übergang zu zunehmend vernetzten Strukturen und indizieren Topologieabhängigkeiten der Plexus in Anbetracht dieses Übergangs. Darauf aufbauend formulieren wir ein neues Adaptationsmodell für ineinander verwobene Gefäßnetzwerke wie sie auch in der Leber, Bauchspeicheldrüse oder Niere vorkommen. Wir diskutieren anhand dieser Strukturen lokale Wechselwirkungen von dreidimensionalen Netzwerken. Dadurch können wir zeigen, dass repulsiv gekoppelte Netzwerke fluktuationsinduzierte Vernetzungen auflösen und attraktive Kopplungen einen neuen Mechanismus zur Erzeugung eben jener darstellen. Als nächstes verallgemeinern wir die Murray Regel für solch komplexe Wechselwirkungen und Fluktuationen. Die daraus abgeleiteten Relationen nutzen wir zur Regression der Modellparameter und testen diese an den Gefäßnetzwerken der Leber.
Weiterhin verallgemeinern wir konventionelle Transportmodelle für die Nährstoffaufnahme in beliebigem Gewebe und testen diese in Morphogenesemodellen gegen die bekannten Ansätze zur Dissipationsminimierung. Hier zeigen sich komplexe Übergänge zwischen vernetzten Strukturen und unkonvetionelles Phasenverhalten. Allerdings indizieren die Ergebnisse Widersprüche zu echten Kapillargefäßen und wir vermuten Adaptationsmethoden ohne Gefäßgrößenänderung als wahrscheinlicheren Mechanismus. Im Ausblick schlagen wir auf unseren Ergebnissen aufbauende Folgemodelle vor, welche die Modellierung komplexer Transportprozesse zwischen verschränkten Gefäßnetzwerken zum Ziel haben.

Abstract

Understanding the transport of fluid in complex organisms has proven to be a key challenge not only in the medical and biological sciences, but in physics and network theory as well. This is even more so as biologically-inspired design principles have been increasing in popularity, reliably generating solutions to common theoretical and technical problems. On that note, vascular networks in mammalian organs display a magnificent level of self-organization, allowing them to develop and mature, yet miraculously orchestrate the correct transport of oxygen, water, blood etc. This is achieved by a dedicated biochemical feedback system, which is coupled to macroscopic stimuli, such as mechanical stresses. Another important constraint for the morphogenesis of flow networks is their environment, as these networks are spatially embedded. They are therefore exposed to significant constraints with regards to their scalability and dynamical behavior, which are not yet well understood.

This thesis addresses the current challenges of network characterization and morphogenesis modeling for three-dimensional embedded networks. In order to derive proper maturation mechanisms, we propose a set of toy models for the creation of non-planar, entangled and reticulated networks. The key mechanisms we focus on in this thesis are flow fluctuation, coupling of pairing structures and metabolite uptake. We show that in accordance with previous theoretical approaches, fluctuation induced nullity can be formulated as a single parameter problem. We demonstrate that the reticulation transition follows a logarithmic law and find plexi with certain topologies to have limited nullity transitions, rendering such plexi intrinsically wasteful in terms of fluctuation generated reticulation. Moreover, we formulate a new coupling model for entangled adapting networks as an approach for vasculature found in the liver lobules, pancreas, kidneys etc. We discuss a model based on local, distance-dependent interactions between pairs of three-dimensional network skeletons. In doing so we find unprecedented delay and breakdown of the fluctuation induced nullity transition for repulsive interactions. In addition we find a new nullity transition emerging for attractive coupling. Next, we study how flow fluctuations and complex metabolic costs can be incorporated into Murray's Law. Utilizing this law for interpolation, we are able to derive order of magnitude estimation for the parameters in liver networks, suggesting fluctuation driven adaptation to be the dominant factor. We also conclude that attractive coupling is a reasonable mechanism to account for the maintenance of entangled structures. We test optimal metabolite uptake in Kirchhoff networks by evaluating the impact of solute uptake driven dynamics relative to wall-shear stress driven adaptation. Here, we find that a nullity transition emerges in case of a dominant metabolite uptake machinery. In addition to that, we find re-entrant behavior in case of high absorption rates and discover a complex interaction between shear-stress generation and feedback. Nevertheless, we conclude that metabolite uptake optimization is not likely to occur due to radial adaptation alone. We suggest areas for further studies, which should consider absorption rate variation in order to account for realistic uptake profiles. In our outlook, we suggest a complex morphogenesis model for intertwined networks based on the results of this thesis.

Acknowledgements

Special thanks goes to my supervisor, Carl D. Modes, who took me in as his very first doctoral student and provided me with this research opportunity. Together, we lived through the beginnings of the CSBD, up to these early days of March. Carl is a wonderful supervisor, with an unmatched open door policy and incredible scientific wit, as he, seemingly with ease, was able to immediately grasp the nature of any problem I presented and discussed with him. Thanks to him I could grow as a part of the group, whose members, previous and current, made the academic life in Dresden so much more enjoyable. On this note I would like to thank my doctoral siblings, Abhijeet Krishna and Mohammad Bahadorian, who traveled to the midst of India with me in search for biophysical knowledge and who taught me that even broken ostrich eggs can be a source of inspiration. My thanks go to Stephan Daetwyler, Szabolcs Horvat and Allyson Ryan being the wise postdoctoral entities of the lab and surprisingly, big animal lovers.

I would like to thank my TAC members Stephan Grill and Marino Zerial for their constructive feedback and insightful suggestions which have guided me through the depths of systems biology. Further, my thanks go to Fabian Segovia-Miranda and Hernan Morales-Navarrete for their experimental work and subsequent analysis, providing me with the data sets on the liver lobule, which has formed a central part of my study. I would like to thank Julien Delpierre, Yannis Kalaidzidis and Marino Zerial for their guidance and advice as well as for their patience. Thanks are in order to Oleksandr Ostrenko, Quentin Vagne, Felix Meigel, Benjamin Friedrich and all members of the Zechner Lab & Norden Lab for helpful discussions and useful feedback throughout the process of creating this work.

I would like to thank the CSBD and MPI-CBG staff for their administrative support and technical advice, particularly Oscar Gonzalez, Peter Steinbach, Susanne Gierth and Anja Glenk without whom everyday work would not even have been possible. My thanks go to Brian van Ruden and Birgit Knepper-Nicolai for their guidance on avoiding the pitfalls of predoc-life in Dresden. I gratefully acknowledge support from the German Federal Ministry of Education and Research (BMBF), Grant No. 031L0044 (SYSBIO II). On the same note I would like to thank the IMPRS program for chaperoning my academic career and enabling me to wok on this project. Finally, I want to thank all my friends, the old ones as well as the new ones found along the way during my time here in Dresden, those part of the DIPP program and otherwise. As a tradition which is to be kept till the end of times, I thank my dear friends Belle, Daniel and Timo. Without all of them, it would not have been the pleasant episode in my life it has been up to this point.

It fills me with sadness though, that in these days, four years after my initial interview with Carl, inside a new and empty CSBD, one finds the building similarly deserted as when it was opened, due to the circumstances of a pandemic. Full-heartedly I hope for better days and I want to thank the entire CSBD and MPI-CBG family for having me in their midst and letting me write this thesis.

Which I hope you as the reader, will enjoy very much.

Contents

Für Denita

Chapter 1

Introduction

1.1 Complex networks in biology

The world that we live in is defined by its numerous constituting components and the manifold possible interactions among them. Modern mathematicians and physicists have coined this very specifically: a complex system [11]. The approach to study, understand and engineer such systems has ever been a bit schizophrenic though [78]. Roughly four hundred years ago, influential polymaths such as Descartes and Newton advanced the idea of the universe as a clockwork, being nothing more than the sum of its parts. This reductionist approach prevailed for a long time, permeating the fundamental philosophy of the natural sciences, arguing that any elaborate system is to be broken down into simpler and simpler isolated sub-components in order to make sense of it. There has been criticism though on the effectiveness of this approach in modern scientific disciplines, e.g. molecular biology [71], in terms of the overwhelming macroscopic output of incremental discoveries. In parallel, many scientists have advocated alternative approaches, such as positing the emergence of complex behavior on the grounds of non-trivial interactions of the systems sub-components [8]. In particular, it has been proposed that non-linearity of these interactions is a prerequisite of emergence as well as a separation of scales [33, 48]. This further encapsulate the notion that such systems can be characterized by hierarchical levels of organization, which each are governed by the emergent rule sets of its respective subordinate levels, who are in turn not governed by the same laws. It would indeed be unfair to assume that these considerations have not already begun to bear fruit in the biological sciences [28, 78], where they even have given rise to interdisciplinary fields such as systems biology [63, 142].
In this interdisciplinary context, network theory has been utilized extensively in order to study a multitude of complex biological problems in metabolism, genetics, neurology, ecology, transport etc [95]. Though particular focus has been directed toward networks which abstract the complex interactions of their agents, its is clear to see that another discipline is increasingly gaining in popularity: Spatially embedded networks.
As these networks are physically embedded in their environment, with respect to their junctions and links, there underlie significant constraints regarding their scalability and dynamical behavior. In this thesis, the subclass of biological networks considered, are the fluid transport systems of individual organisms. Such networks, e.g arteries, veins and capillaries, are usually referred to as flow networks and are spatially embedded objects, which imposes significant constraints regarding their topology and connection characteristics. As laid out, for example by Barthelemy et al [12], one may

argue that such embedded networks do not tend to display scale-free behavior, show primarily short-range connections between branchings or hubs, and display limits of effectiveness in their economic costs and transport capacities etc. Moreover, studying and understanding the morphogenesis of such networks has become a sub-field of its own. Strikingly, many such vessel systems are constantly developing and maturing throughout an organisms lifespan, yet miraculously orchestrate the correct transport of oxygen, water and blood etc, rerouting flow in case of vessel failure and seemingly doing so without the guidance of a central plan or intelligence.
An extensive number of experimental studies have shown that this development is only achieved by a dedicated biochemical feedback system controlling the dynamic process for each specific vessel type [115, 74]. Further, it has been shown that in certain stages of morphogenesis the relevant biochemical signaling pathways are triggered by macroscopic mechanical stresses [96]. This concept of mechanotransduction was observed more than a hundred years ago for vasculature [134] and has become a widely popular idea in biophysics [5]. Naturally the field has expanded to address network theoretical questions, i.e. formulating dynamic models, simulating the development of vessel systems and analyzing the impact of different hydrodynamic approaches, the underlying graph topologies and pathological deformations. In the process, it was repeatedly demonstrated that the emergence of complex network structures can be accounted for by a simple fluid-driven morphogenesis machinery. Although there is a consensus that this phenomenon occurs in a self-organized matter for small vessel systems, one has to recognize the seeming efficiency of these flow networks in terms of robustness and resource management [121]. Even more so as modern analysis of genomes and fossils suggest a tunability of the underlying machinery on an evolutionary scale [46, 18]. Subsequently a growing focus has been directed toward the development of new metrics, allowing for characterization and comparison of real flow networks with the output of their model counterpart.
These design principles and derivative metrics are further increasing in popularity, as they reliably generate solutions to common network theory problems. For example, one may formulate morphogenesis problems to find the shortest paths through a maze [132], optimize traffic [140] or generate Steiner trees [73]. Eventually it was demonstrated that some metrics developed for vasculature are more generally suited to identify topological markers in complex spatial networks, e.g. cycle hierarchies [60, 85, 86].
In this thesis, we extend the theoretical framework of network morphogenesis as well as its subsequent characterization. In the following sections we briefly lay out the development and maturation processes found in vessel systems (sections 1.1.1 & 1.1.2), and the state of the art of the modeling framework (section 1.2). This thesis will be particularly focused on the morphogenesis of flow networks found in mammals, with particular regard toward the vessel systems found in the liver lobule. We will accordingly discuss the interaction of such systems and their respective environment, as well as the importance of considering three dimensionally embedded networks. And finally, in section 1.3 we shall present our problem statement, featuring the fundamental questions this thesis addresses

1.1.1 Flow networks in mammals

Flow networks found in mammals have to fulfill a variety of tasks, quickly rising in complexity the closer one dares to look, and being even more dangerous for researchers to be lost in their seemingly bottomless magnificence. For example, the circulatory system transport blood from the heart through a branching system of aortas, arteries, arterioles, etc. toward the capillary beds where exchange of oxygen and other metabolites can occur in the local tissue of the organs [139]. Then blood is recollected from the capillary beds by the venous system and redirected towards the heart by a converging tree structure. One finds the physiology of this system to greatly change from large compliant arteries, built from multiple layers of endothelial cells, pericytes, muscles etc toward endothelial monolayers of fenestrated capillaries which are densely meshed. One also finds completely different hydrodynamic scenarios varying from highly dynamic pulse wave propagation in aortas to nearly stationary flow on the capillary level [24]. And though this layering of complexity has been enough to keep researchers occupied for centuries, it has become apparent that this system works seemingly in concert with all the completely different organs along the way. Nearly every organ by itself has its own secondary vessel system, e.g. for supplying and redistributing nutrients, hormones and immuno cells or providing waste removal and water management [22].

As it would fill several textbooks to list all these organs and their vessels in detail, taking precious space and time to display our own studies, we shall focus here on one exemplary system: The liver.
The intention here is not to marginalize the work of other researchers, the significance of the rest of organs, nor to limit the applicability of this thesis' results. Nevertheless it is hard not to see the liver as the metabolic workhorse of the mammalian body, while simultaneously displaying some of the most interesting developmental and regenerative characteristics found so far [22, 84]. In this thesis we particularly focus on the microscopic vessel systems existent in the liver, rather than its macroscopic organ anatomy, which changes significantly for each animal. Yet what seems preserved across species are the essential tissue building blocks which are called liver lobules. We would like to illuminate its histology here in detail: The liver lobule contains two highly reticulated vessel systems, the sinusoids and the bile canaliculi, see Figure 1.1a. The sinusoids are fenestrated capillaries distributing blood rich in oxygen and nutrient among the hepatocytes. These hepatocytes are cells, which are the main building block of the parenchyma (bulk of tissue). The hepatocytes' membrane sections facing the sinusoids are also referred to as 'basal'. The liver metabolism is performed primarily by the hepatocytes, wherein they secrete waste products and bile salts together with water into the bile canaliculi. The canaliculi are channels formed by fused membrane pieces of neighboring hepatocytes, referred to as 'apical'. The secretions are collected in these channels and transported towards the bile ducts at the portal triad. The portal triad is a vessel cluster, consisting of a hepatic artery, a portal vein and the duct. While bile is extracted from the liver tissue at this point (guided towards the bile bladder) we also have blood entering the lobule at this section. The blood flows converges toward the central vein, which is generally surrounded by six portal triads.
Though we have focused on the liver system here, note that other organs, such as the kidneys [126, 125], pancreas [75, 137, 10], brain [14], or the body spanning lymphatic system [105], have similarly elaborated interactions and vessel organizations. Moreover,

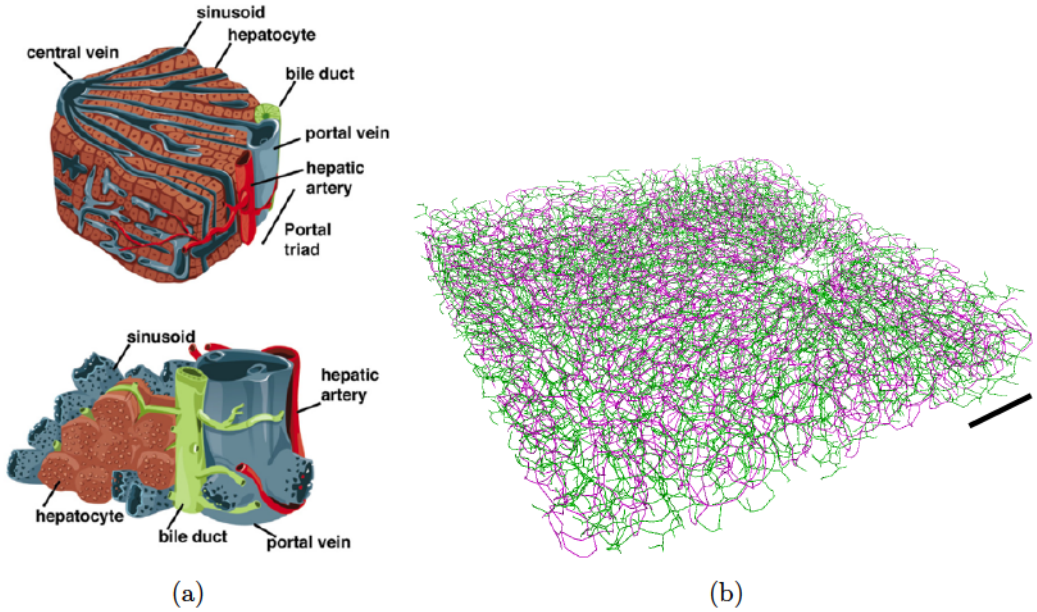

(a) (b)

Figure 1.1: The liver lobule and its vessel systems: (a) Schematic representation of the liver lobule accroding to [128] (b) Segment of bile canaliculi (green) and sinusoids (magenta) in the mouse's liver acinus (presented as network skeletons, see also [88]), scale bar is 200 μm.

while all these organs' vessel systems display significant differences in their respective organization and cellular make-up, they do display common design principles in accordance to the liver.
First, these networks are physically embedded and non-planar in a graph-theoretic sense (they can't simply be laid out in a plane without crossing elements). In fact, they need to be non-planar to ensure the existence of intertwined structures without which none of the function described above could be performed. Note that we refer to a graph abstraction of vasculature where branching points are seen as nodes or vertices and the vessels in between as links or edges. Further interrogating such graphs one finds degree distributions of $d \approx 3$ (number of edges per node), short-ranged connections between branching points yet largely varying levels of reticulation.
Second, these flow networks are entangled and interacting in one way or another with the circulatory system. This form of spatial compartmentalization, where educts and products of the organism's metabolism are not in their entirety transported by the same network, is crucial in preventing pathogens to be spread across the entire organism and keeping the relevant metabolic functions running. The exchange of material between the circulatory system and the client organ networks is generally facilitated by mediating tissue elements, adding another layer of complexity to the system as they can act as simple filters or active pumps. These networks rarely have merging points where the two networks are physically connected to exchange any material. The fact that these complex systems are actually functioning in concert and provide the essential tools for an organism to survive become most painfully clear when they are not doing so anymore. This may be of a pathological nature a living being may encounter in its life eventually, but could also occur due to failures of the initial morphogenesis of these structures at its very beginning.

Morphogenesis of intertwined biological networks is still insufficiently understood during embryogenesis and wound healing, when these flow networks are created or recreated in their rudimentary form. Likewise, it is important to understand the complexity of these design principles when dealing with pathological complications, such as tumor growth [108] or poly-cystic diseases [145]. It is known that vessel networks do not directly grow fully developed and matured in their final and functional form, but seem to self-organize bit by bit in the context of its surrounding tissue, perfusion and other stimuli over a long time span (in comparison to the hydrodynamic time scales) [32]. And they have to do so again when general changes in the organism's metabolism occur, every time based on a complex biochemical signaling cascade [116]. In the next section we will elaborate on the nature of this organization process and current efforts to illuminate its dynamics, experimentally and theoretically.

1.1.2 Network morphogenesis

Biological flow networks are dynamic throughout development and thereafter. To demonstrate this let us walk through the creation of a new network during embryogenesis. In mammalian tissue this is usually performed in two separate steps: First, rudimentary lumen are created from progenitor cells specific to the network type. Subsequently the individual lumen merge and a network of high redundancy with little care for sizing, overall volume or effectiveness of any kind is formed [135, 58]. Such a prototype network is called a plexus in developmental biology and generally describes the status of a network which is not yet perfused, though the lumen are kept open and extend by internal fluid pressure. We will use the term 'plexus' for the rest of the thesis for such pre-built, non-perfused networks.
These plexi are then refined, given tissue specific stimuli, which lead to vessel expansion or degeneration. If vessels grow large enough they will trigger secondary tissue elements for support, e.g. forming additional muscle layer or connective tissue around the vessel [135]. Degenerating vessels eventually collapse and are retracted, thereby performing a process called 'pruning', removing the link completely. Furthermore this process is accompanied by sprouting events and intersucception, i.e. new vessel tips emerge from pre-exisiting lumen and single vessels split in two. In the same manner one observe the inverse operations, having vessel retract to their root or merge into one [72]. The topology of the plexus will therefore change dramatically, from its initial formation to a seemingly stable point which ensures perfusion of the tissue. Note that it was argued that neither random pruning [31], nor morphogen-gradient models [42, 43], to properly account for the structures observed.
The onset of refinement rather seems to be correlated with mechanical stresses (such as shear flow) as has been explicitly shown in a variety of model vertebrae organisms, e.g. in chicken [96], zebrafish [72] or mouse [31]. This remodeling procedure is present in the endothelium and epithelium alike, see Figure 1.2. It should be noted that this principle of plexus build-up and flow driven remodeling seems universally present in the biosphere, as it has also been observed in non-vertebrae, like plants [123] and slime mold [132]. Whether this homology is actually based on a common building plan is unclear, even though there seem to be indications for the existence of similar blueprints inside certain groups [87, 104] Particular focus has been directed to the long-term re-

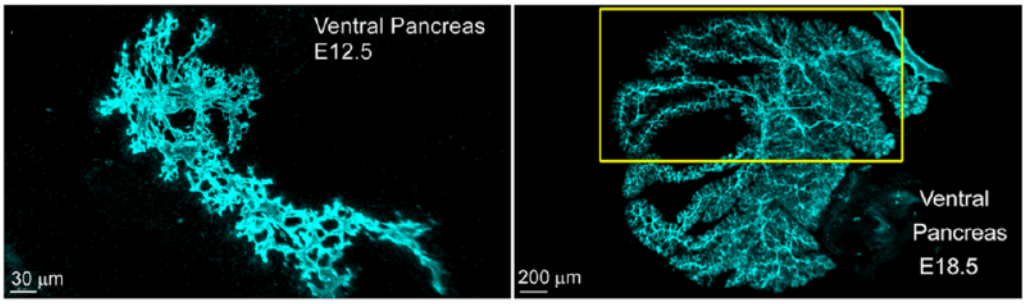

(a)

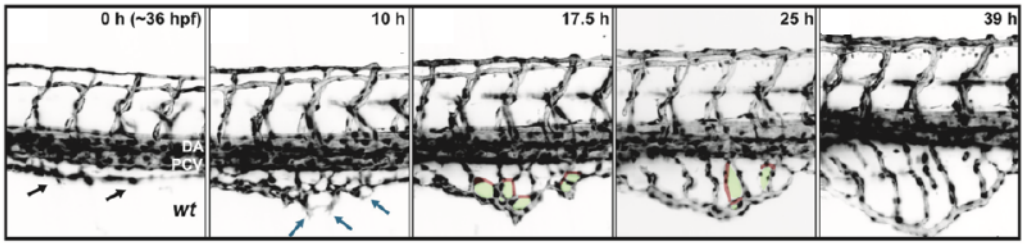

(b)

Figure 1.2: Perfusion based morphology changes during embryogenesis: (a) Mouse, pruning of the pancreatic duct shown for a time difference of six days, reprinted from [31]. (b) Zebrafish, development and pruning of the sub-intestinal-vein (SIV) over the course of 40 hours, reprinted from [72].

modeling of the capillary plexus and other rudimentary transport systems in the early developmental stages of organisms, i.e. by studying complex signaling cascades involving growth factors like VEGF in vascular systems of mammals [115]. Recently it was argued that initial plexus design is crucial in order to provide the network with the chance to actually adapt, according to the principle: It is easier to tune and refine an existing redundant structure than add pieces to an underdeveloped set [119]. This brings us to the next important point: Adaptation and optimal network design.
As matured vessel networks do not display features of random networks, one might follow the narrative that adaptation is based on the obvious macroscopic stimuli present in either network type; perfusion and metabolite transport (or mechanical stability for plants). In particular it has been argued over a century ago by Murray [92, 93] that the design of arteries and veins is based on constrained minimization of the overall hydrodynamic resistance. The principle of optimal flow networks has been the primary angle for theoreticians ever since and particularly for the last two decades, as we will illuminate in the next section. In particular these optimality principles aim at reproducing perfusion based pruning behavior and geometric relations of vascular branchings as well as generating network topologies comparing to the redundancy and degree sequence of real vessel systems. In the next section, we will give a brief review of the current approaches for remodeling simulations and their metrics, which the general approach of this thesis is based on.
It should be noted at this point again that understanding the principle design rules of flow networks will enable us to understand the initial network morphogenesis , but even more so its pathology: it has been shown that tumors and cystic diseases either actively hijack the bio-mechanical machinery behind vessel remodeling, or display its

complete disruption. Tumor cells can proliferate the endothelium by facilitating the growth of vasculature, thereby enhancing the local supply with nutrients in order to sustain further growth [108]. A cause of cystic diseases can be that epithelial ducts locally loose the ability to sense mechanical stresses correctly, e.g. by hampering with given surface cilia, see Figure [145]. Understanding the dynamics of vessel remodeling in healthy as well as in compromised tissue shall give us essential knowledge on the treatment of such diseases and the general field of developmental biology.

1.2 State of the art

In this section we give a brief overview of the state of the art in theory and simulation of plexus remodeling. Particular focus will be directed here towards radial adaptation schemes, based on incremental changes of the circumferential size of vessels, while reevaluating the driving stimuli. We will give a more detailed introduction to the mathematical background of these techniques in chapter 2.

1.2.1 Modelling flow network adaptation

Early theoretical approaches by Murray [92, 93] posited that diameter adaptation would minimize the overall power dissipation of the system, while constrained by the overall volume. Following this ansatz of network optimization, many recent models used optimization schemes on expanded vessel networks taking into account variations of link conductivity via changes of the geometric parameters of vessels. We would like to direct our focus to such studies dealing with capillary networks approximated as linear networks [38, 39, 141]: the plexi is seen as a Kirchhoff network, with defined volume flow rate f_e and conductance C_e on its links. Generally one node is defined as a root from which fluid is injected into the plexus while all other vertices are consumers, acting as sinks to the current injected. Hence one may write for each node

$$\sum_{e \in inc(v)} f_e = s_v \tag{1.1}$$

where $inc(v)$ indicates the set of incident edges for vertex v, i.e. the set of edges connected to it. The term s_v is the balance of incident flows, called a sink or source depending on whether flow is extracted or injected here. Generally, in these previous works [20, 61, 30], this was then dealt with as a Lagrangian problem where the Lagrange function is constructed for the flow networks at hand:

$$\mathcal{L} = \sum_e \left\{ \frac{f_e^2}{C_e} + a C_e^\gamma \right\} + \sum_v \left\{ s_v - \sum_{e \in inc(v)} f_e \right\} \tag{1.2}$$

Here the first term, from the left, is the power dissipation and the second a metabolic cost term including the conductance C_e^γ explicitly, with proportionality factor a. This second term encapsulates the notion that a biological organism is constrained by the metabolic costs to deploy and sustain a vessel of a certain conductance. In detail this assumes that in order to build larger vessels with increased volume or surface area the tissue needs more cells which have to be supplied with oxygen and nutrients. The exponent $\gamma > 0$ represents a degree of freedom to vary the relative importance of vessels of low or high conductance.
The minimization of the function (1.2) is performed numerically by finding the set of conductances C_e which minimizes (1.2) for the given boundary conditions (1.1). In order to simulate the long term refinement of real biological systems, such iterative minimization of (1.2) is accompanied by the removal of edges with C_e below a given threshold.

It has been shown that for systems with $s_{root} > 0$ (all other vertices $s_v < 0$) one only acquires spanning trees for $\gamma < 1$ [20] from plexus refinement, see Figure 1.3a. These trees connect the predefined sinks and sources by direct pathways, while cutting down any weakly perfused links, never leaving any loops intact; a dramatic reduction of the previous complexity and redundancy. This topological transition is seemingly independent of the underlying plexus topology, but depends only on the chosen boundary conditions. Reticulation may be restored in this framework by considering $\gamma > 1$ [20], which will restore the initial plexus. Further, the introduction of noisy flow patterns by breaking links or varying the spatial correlations of sinks and sources has been proposed [121, 61]. With this ansatz one considers an effective separation of time scales, assuming that developing vessels integrate stimuli multiple times before adapting. Hence one has to compute the average dissipation instead, over the many instantaneous realizations between two adaptation steps,

$$\frac{f_e^2}{C_e} \to \left\langle \frac{f_e^2}{C_e} \right\rangle \tag{1.3}$$

which may also restore reticulation, see Figure 1.3b,1.3c.

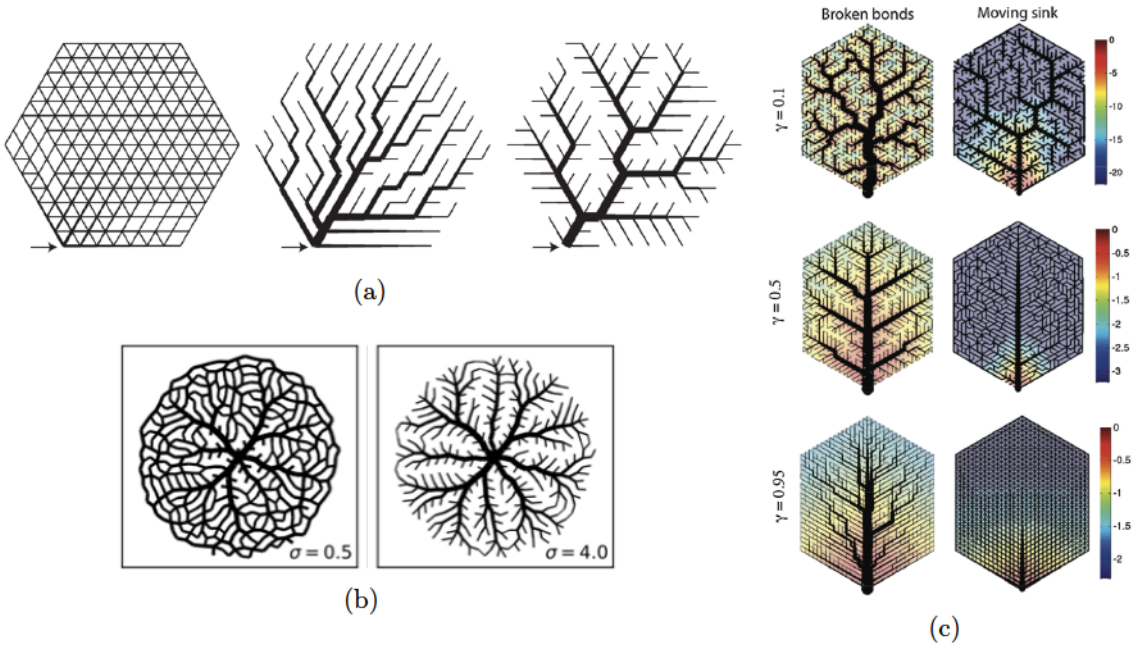

Figure 1.3: Topological transition in linear flow networks, from trees to meshes: (a) Increasing cost scaling exponent from $\gamma \geq 1$(left) to $\gamma = 0.5$(right) leads to emerging reticulated structures, reprinted from[20] (c) Broken links and randomized sink-source closure will lead to a topological transition. The colormap indicates the pressure gradient, reprinted from [61]. (b) Local adaptation model with spatially correlated sinks-sources. A single source is created in the center together with a single random sink. Inside a radius σ around the sink, any vertex is also becoming a sink, the wider the spatial correlation becomes the more the network becomes a tree, reprinted from [121]

Though appealing at first one may recognize that this optimization process typically assumes a global actor driving the organism into a desired state. On the other hand a

variety of different schemes have been proposed to model self-organized adaptation of single vessels inside a network. For example, in heuristic approaches proposed by Pries et al [107], a set of local stimuli S_e leads to individual radial changes as

$$\partial_t r_e(t) = S_e(t)\, r_e(t) \tag{1.4}$$

In these studies stimuli S_e would incorporate macroscopic hydrodynamic variables such as wall shear stress (friction of the fluid layer on the inner vessel wall), transmural pressure (pressure difference between lumen and surrounding tissue) and also hypoxia. Note that wall-shear stress stimuli lead to shunting, i.e. the pruning of the plexi down to single connecting channels. Yet saturation stimuli, incorporating the saturation of blood with oxygen, may maintain redundancy. Further studies incorporating complex stimuli such as wall shear stress or hemodynamical complications [27], or simple heuristic uptake rules ensuring vessel pruning reproduce this topological transition behavior [133, 51, 120, 122, 57, 27]. It has further been shown that the outcomes of locally adapting networks are robust against variations of the initial topological structure [51] and that simultaneous plexus growth and correlated flow fluctuations can provide elaborate hierarchies [120, 122], see Figure 1.3b.
It has been shown that there is a bridge between these two schools though: Following the ansatz in [56] one may derive local temporal adaptation rules via the gradient descent method directly from (1.2). The dynamical system constructed this way usually takes the form

$$\partial_t C_e = a_0 \left(\frac{f_e^2}{C_e^{\gamma+1}} - a_1 \right) C_e \tag{1.5}$$

and has been studied in greater detail in combination with growth, flow fluctuations and exponent variations by Ronellenfitsch et al[120, 122]. Particularly interesting is the fact that (1.5) corresponds to an adaptation of the vessel to the wall-shear stress. Following this dynamical system one adapts the conductivity of any single vessel to a local level of shear stress and simultaneously minimizes the global dissipation-conductance of the system. An optimal network design via self-organization. This ansatz has further been extended to continuous models as well, i.e. in porous media [52, 53]. Deriving local dynamics from gradient descent based methods has become rather popular, as it enables the construction of arbitrary self-organizing flow networks based on desired design features[26]. The majority of self-organized adaptation models presented here is conceived for perfusion based remodeling, intending to generate reticulated, space-filling structures. But capillaries are not just passive actors, i.e. being the mere medium of fluid transport between arterioles and venules. It is general consensus that any major exchange of metabolites between vasculature and tissue, such as oxygen, salts, glucose, proteins etc., is performed on the capillary level. Needless to say, theoreticians and experimentalist have created a plethora of elaborate models on metabolite transport in capillaries over the last century. In the process there have been suggestions for heuristic metabolic stimuli ensuring perfusion of oxygenated blood throughout the capillary bed [107, 124], lacking though a discussion of the actual capabilities of the embedding tissue. Therefore it is interesting to note, that detailed studies of network morphogenesis for optimal solute uptake have just recently been conducted. Currently there seem to be two frameworks in particular, celebrating a comeback in this discipline of complex network theory: the Taylor dispersion model [130] and the Krogh model [66].

Taylor dispersion has been discussed as a valid metabolite transport model for slime molds in recent literature [6, 76], but has since been utilized to account for the phenomena found in plants and blood capillaries. In this context Meigel et al [82] argued that the overall solute uptake of flow networks, which have their volume flow independent of the metabolite concentration, is determined by the Peclet number and local absorption rate of the vessel surface alone. In their studies [81] they demonstrated the compatibility of the Taylor dispersion model with the Kirchhoff ansatz. Subsequently they formulated the conditions for optimal flow injection when homogeneous absorption throughout the vessel networks is required. Further they suggested tuning of vessel radii, for constant sink-source conditions. In neither case do they find uptake driven radius adaption to lead to vessel pruning. A plexus will always stay a plexus in this framework.
On the other hand, Garvrilchenko et al [45] suggested an adaptation model on the grounds of the Krogh model. In this framework metabolites (primarily oxygen) are diffusing on a given length scale into the tissue, determined by the tissue's uptake rate. Subsequently it is possible to distinguish a supplied volume element for example by the sets of vessel lining it. In order to achieve homogeneous uptake, no radial adaptation but a respective channel length adaptation was performed, reshaping the respective volume elements in the process.
In this thesis we intend to focus in particular on systems with extended metabolic cost functions in order to derive the individual vessel dynamics from gradient descent methods. Furthermore we shall focus our efforts on metabolite transport using predominantly Taylor dispersion and radial adaptation mechanisms. We shall elaborate on the ansatz of volume element supply as well though. We will discuss the mathematical basics of these model frameworks in chapters 2 and 3.

1.2.2 Metrics for biological flow networks

In order to characterize real biological flow networks, a variety of invasive and non-invasive techniques is abundant nowadays. For our purposes though we are in need of methods providing the graph structure of capillary networks and their hydrodynamic ramifications. Unfortunately, the applicability of any method is often limited by tissue-depth resolution and tied to specific model organisms. Nevertheless, many researchers have succeed in generating spatial graphs from microscopy data allowing the standard tools for spatial networks to be applied, such as degree sequences, betweenness [12], Rentian Scaling[101] etc.
Few metrics provide the means to fit or estimate the applied effective parameters of adaptation models for real systems, even though time-lapse experiments [72], counting pruning events and topology analysis on pruned structures [122, 86] allow for qualitative insights into the mechanism at hand for certain model organisms. In this thesis we will focus on two network characteristics which are particularly useful for comparison of the spatial and topological structure of biological networks to simulated optimal networks: Scaling and Redundancy.

Scaling in spatial networks

Why are the vessels organized the way they are? Is it possible to predict branching patterns of real flow networks?
In order to address these questions West et al [141] operated on the following assumptions, with particular regard to fractal-like flow networks:
"First, in order for the network to supply the entire volume of the organism, a space-filling fractal-like branching pattern [...] is required. Second, the final branch of the network (such as the capillary in the circulatory system) is a size-invariant unit [...]. And third, the energy required to distribute resources is minimized [...] Scaling laws arise from the interplay between physical and geometric constraints implicit in these three principles."
Among other things they concluded that the size ratio of consecutive vessels on different levels of the vascular hierarchy would scale with a power law of the form

$$\frac{r_{i+1}}{r_i} = n^{-1/\alpha} \tag{1.6}$$

where r_i is the radius of the parent vessel branching into its n children with r_{i+1}. Scaling of geometric properties on the basis of metabolic constraints has become increasingly popular over recent decades [131], the notion to do is far older though.
First discussed nearly a hundred years ago by Murray [92] and W. Hess [55], they proposed a Hagen-Poiseulle flow system minimizing its power dissipation while being constrained by its overall volume, resulting in $\alpha = 3$. Ever since, extensive studies of radial distributions in real vessels trees [2, 79, 94, 3] have indeed shown that a vessel generation is often linked to the next in the form of

$$r_i^{\alpha} = \sum_j r_{i+1,j}^{\alpha} \tag{1.7}$$

Generally it is suggested to account for α variations on the grounds of different hydrodynamical approaches and optimization constraints:
For example, dealing with the more elaborate theory of compliant vessels carrying pulse waves, the case of $\alpha = 2$ corresponds to an impedance matching for consecutive vessels, reducing wave reflections [24]. Likewise, one would acquire this exponent for a purely diffusive system [127]. Recently it has been discussed that insect trachea, which display $\alpha < 2$, may scale differently due to the existence of air sacs as gas reservoirs altering the flux [2]. Naturally there have been additional studies suggesting even more elaborate hydrodynamics involving turbulence, non-Newtonian effects or hemodynamical phenomena [144, 113, 91] In the formulation (1.7) it becomes readily apparent that one may classify these networks as area preserving for $\alpha = 2$, area-increasing for $\alpha > 2$ or area decreasing for $\alpha < 2$, i.e. whether the overall cross section area of a vessel generation changes over the vascular tree, see Figure 1.4. As pointed out, optimally designed networks, such as introduced in the previous section, supposedly leave fingerprints behind in their radial distribution that allow for the prediction of α. For example, Murray's law corresponds almost directly to the solution of equation (1.2), (1.5) for a single branching with $\gamma = 0.5$. Generally for such dynamical systems, it can be shown that (1.7) becomes,

$$r_i^{2(\gamma+1)} = \sum_j r_{i+1,j}^{2(\gamma+1)} \tag{1.8}$$

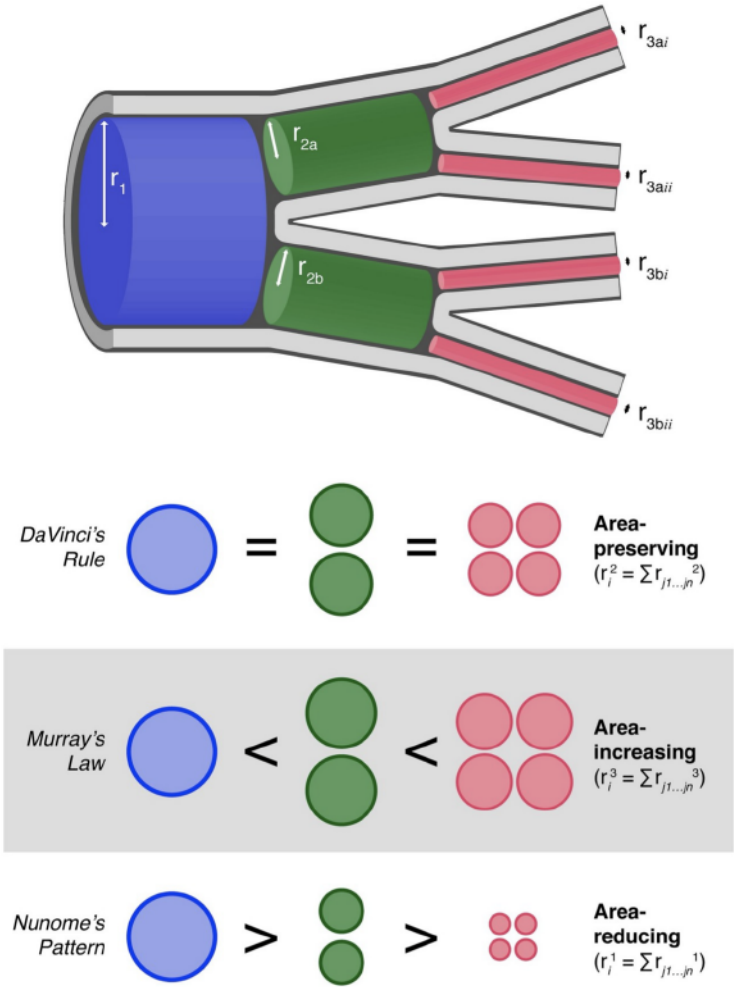

Figure 1.4: Branching patterns in vessel systems, reprinted from [2]: DaVinci's Rule, Murray's Law, Nunome's Pattern representing most prominent cases found in vaculature.

using the optimization models for alternative γ variations. Note that the relations (1.7),(1.8) are generally only formulated for tree-like branching patterns where a clear definition of parent to child is possible on the basis of edge weights, e.g using a Horton-Strahler ordering scheme for the vessel radii. There have been suggestions to extend this scheme toward reticulated networks by applying weight based (i.e.using radii, length) distinctions [85]. The problem with this identification processes will become apparent as soon as we try to apply complex flow patterns onto such reticulated networks, which do not necessarily coincide with radii based ordering schemes.

Redundancy of flow networks

It seems somehow redundant to mention how important redundancy is. Yet for biological flow networks this becomes particularly apparent as soon as occlusions or damages occur [17]. For example, assume that a vessel gets clogged: now in a capillary bed this might not matter much as fluid can be redirected almost instantaneously via other

channels, thereby ensuring the general perfusion of large section of tissue. A phenomenon that is partly possible as one does not have 'directed' links in biological flow networks. We cant really make this statement when considering aortas, where the same blockade cuts off any supply to the subsequent arterial tree.
Which implies the questions: What is the best measure for arbitrary flow network robustness? And is it possible to quantify the topological transition introduced in section 1.2.1 with these? Recently, a couple of different methods have been proposed:
First, there are measures based on finding a percolation threshold [95, 101]. They are well established for spatial networks and provide information on the topological robustness of the network in case of integrated failure of links, marking the split of a graph's giant component into multiple sub components. In general it is computed how many edge removals a graph can take before breaking into two sub components, then this may be repeated for the larger components and so on until a set threshold size is reached. This technique is comparatively heavy on the numeric side as many realizations of the percolation have to be computed [101].

$$R \propto \left\langle \frac{\#\text{removed edges till breakdown of giant component}}{\#\text{edges of graph}} \right\rangle \tag{1.9}$$

Flow entropy seems another appealing measure [30, 9]. Though primarily established for stationary diffusion problems, one may quickly generalize this for any current problem on a Kirchhoff network. Considering the volume flow rate in a vessel as f_0 which splits at a branching point into m new vessels, we know that the i-th vessel will carry the fraction $p_i = \frac{f_i}{f_0} \leq 1$ of the initial flow. Subsequently we may define this as the probability of a fluid particle taking the i-th branch at the junction. This may naturally be extended for an arbitrary path of consecutive edges q, denoted here as p_q . This enables us to a estimate the redundancy of the actual flow pattern as it evaluates the probabilities of fluid particles transitioning along certain connections. Along a spanning tree one will only have one certain path from root to leave, while it becomes rather uncertain which route we took in a mesh. Hence the flow entropy reads

$$S \propto \sum_{q \in \text{path}} p_q \log [p_q] \tag{1.10}$$

The computation is rather expensive as the probabilities of all possible particle trajectories through the network have to be computed, scaling problematically for highly reticulated networks. The by far easiest computable measure is the graph nullity (often referred to as loop density). Basically one counts the number of smallest cyclic paths in a graph, thereby directly giving a measure of the amount of redundant pathways. Interestingly these cycles form the basis of a vector space. Their linear combinations build up all further cyclic pathways possible, thereby preventing the need to evaluate all pathways. Trivially, for a simple graph of E edges and V vertices, one simply finds the dimension of this cycle space(amount of linearly independent cycles) as [143]

$$z = E - V + 1 \tag{1.11}$$

This measure doesn't provide any information though on the actual flow or robustness against targeted link removal. All these proposals allow an order parameter to be

constructed by defining a null graph for comparison. For simplicity's sake one usually utilizes the plexus of the graph or constructs a null graph via greedy algorithms [101]. Most recent studies on network adaptation, .e.g such based on the Hu-Cai model, tend to use nullity as an efficient way to present the emergence of complexity in a network, see Figure1.5b In this thesis we will focus on the nullity as the primary redundancy

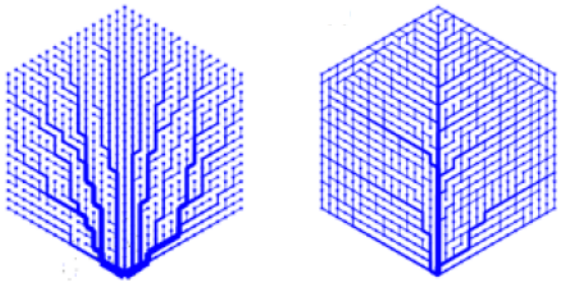

(a)

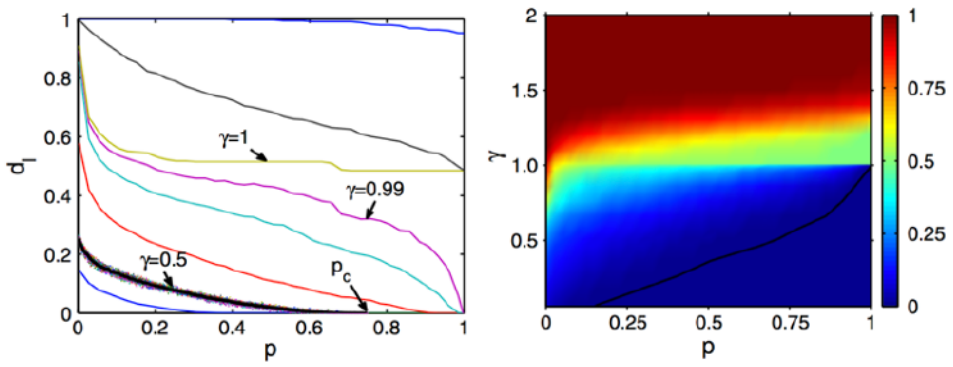

(b)

Figure 1.5: Quantifying redundancy: (a) : Redundancy changes in Hu-Cai model by closing sinks with open probability $1-p$ for $\gamma = 0.5$, with left $p = 0.$ and right $p = 0.025$. (b) Nullity transition in self-organizing flow networks is dependent of cost scaling γ and p, with $d_l = z/z_0$, reprinted from [56]

measure due to its trivial computation even in topologically dynamical systems that we intend to study. It has become apparent that a primary task of self-organization models such as introduced in the previous section is to account for complex reticulated patterns.

1.3 Problem statement

As previously illuminated, we find the study of the basic principles of remodeling dynamics to be crucial to understand vascular development during embryogenesis, wound healing and vessel pathology. Further it has been shown that these biologically inspired algorithms present precious insights into the wider field of optimal network design. Reviewing previous studies we find this often done by applying metabolic constraints to simulate dynamics on Kirchhoff networks for a set of desired flow patterns. And in the context of metabolic cost models it has been proposed to derive scaling relationships for the radii and lengths of consecutive vessel hierarchies in such networks.
Yet, most works disregard the key characteristic common to all fluid transport systems: spatial embedding, which matters especially in the case of capillary systems as these directly interact with the surrounding tissue via transfer of metabolites. These systems have to maintain a robust structure while being embedded in a possibly stiff tissue environment potentially perturbing the shear stress driven adaptation mechanism. Further, no attempts have been made to incorporate the findings of adaptation models with fluctuating flows or more complex metabolic costs into scaling relations such as Murray's law.
This thesis thus intends to address these current challenges: Network theoretical characterization of reticulated three dimensional networks and modeling adaptation for spatially embedded networks in terms of geometric restrictions & optimal metabolite transport.

1.3.1 Spatial embedding in metabolic costs models

As laid out previously, we intend to focus on the development and function of multicomponent flow networks, which influence each other based on their spatial architecture. In living organisms, one finds these intertwined structures on any organ level, as these systems often consist primarily of blood vessels and a secondary entangled network, e.g. most prominent in liver, kidney and pancreas. It should be noted that the networks studied here are not planar, nor can they be in order to ensure an intertwined embedding, which facilitates the function of the organ. Complex vessel systems are known to be three-dimensional, space-filling structures, which is why we will study predominantly network skeletons of triply periodic surfaces, see Figure 1.6. Though such multilayer network approaches have been becoming increasingly popular [19], we find the explicit coupling of multiple adapting transport networks not well studied. In particular we shall study how geometric interactions impose topological changes onto the partnered networks in combination with the conventional wall-shear stress driven adaptation models. The ansatz we choose shall also explore the phenomenon of a flow network being 'caged' by another complementary structure, e.g. capillaries embedded in bone marrow [129] or other stuff tissues. For this study we will extended the metabolic cost function ansatz to incorporate interactions between adjacent edges of the multilayer system.

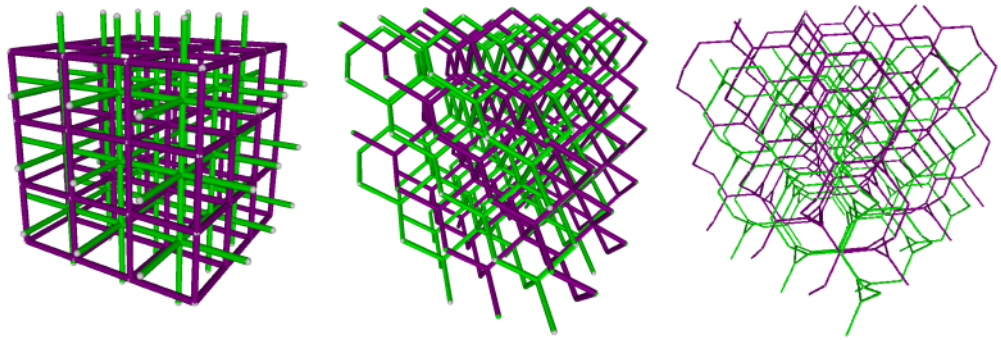

(a) (b) (c)

Figure 1.6: Graph skeletons of triply periodic surfaces: (a) Cubic lattices as skeletons of the P-surface (a) Diamond lattices as skeletons of the D-surface (a) Laves graphs of opposing chirality as skeletons of the G-surface

We further revisit the fluctuation induced reticulation model presented in [61, 30, 56] in order to discuss its interplay with the coupling mechanism. The theoretical framework and numerical results of this study are presented in section 3.1, 3.2. Note, that part of these results have been published recently in [65].

1.3.2 Characterizing three-dimensional reticulated networks

The analysis of three dimensional vessel systems on the organ level is inevitably connected with the analysis of intertwined vessel structures, as mentioned previously in section 1.1.1. In this thesis we discuss any measure of such intertwined structures on the example case of the liver lobule (the smallest conventional tissue unit of the liver) as our primary model system.
The architecture of the liver lobule ultimately results in two highly entangled flow networks, sinusoids and bile canaliculi which have their load transported in opposite directions, along the characteristic lobule's axis, central vein to portal triad. Neither of these networks has direct contact with the other, potentially contaminating its flux. Any mediation of solutes is performed by the hepatocytes, which actively transport from the sinusoids toward the canaliculi. Now, thanks to recent advances in microscopy and image segmentation, meaningful graph extractions have become possible [88, 89]. So far, the hydrodynamic specifics have also been studied indicating typical features of capillaries for the sinusoids and complex osmotically driven fluid flows in the bile canaliculi [59, 100, 83]. The latter model frameworks will briefly be discussed in chapter 4 in comparison to this thesis' results. This has been done to the extent that studies on the topological organization of the two respective networks have been conducted [90].

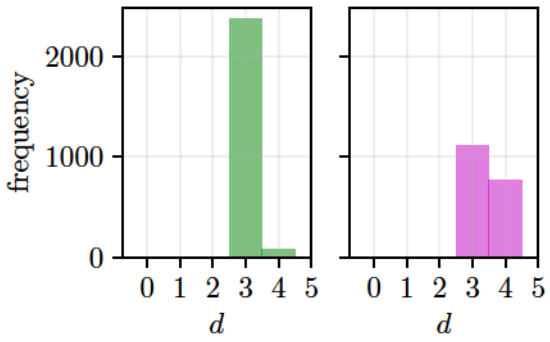

(a)

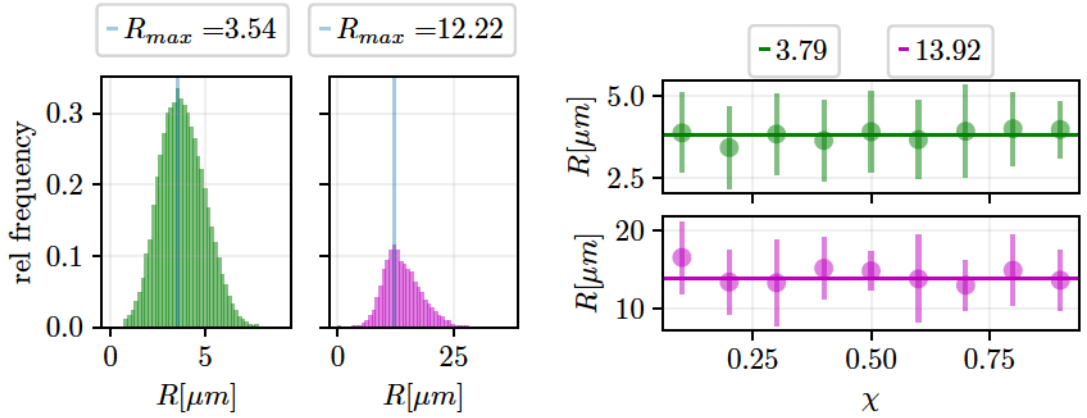

(b)

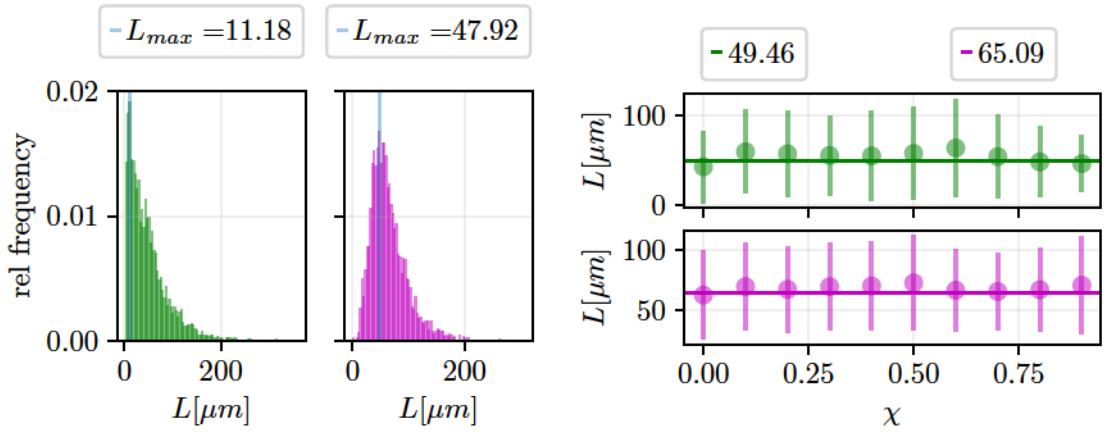

(c)

Figure 1.7: Radii and path length distributions in the mouse liver networks, sinusoids (magenta) and bile canaliculi (green). The χ represents the relative zonation in the acinus, with $\chi = 0$ at the central vein and $\chi = 1$ at the portal triad: (a) Degree distribution in the reticulated networks (b) Radii distribution in liver capillaries with modes and median indicated in the legend. (c) Length distribution in liver capillaries with modes and median indicated in the legend.

In Figure 1.7 we display basic geometric and network theoretical features of these meshed networks which have been well studied so far: Both network have very confined degree distributions, and display no significant changes of radii and path lengths throughout the lobule. Paths are defined as the walks through the graph between two branching points. Sinusoids tend to display larger vessel sizes are in comparison to bile canaliculi. In neither network one observes distinct vessel hierarchies as seen typically in spanning trees. Further, as the acquirement of these data sets is highly invasive, no detailed flow patterns are known.
All taken together, this poses a particular problem when attempting to formulate scaling relationships in the spirit of Murray's law. Scaling of the geometric properties of vascular networks has been rigorously discussed in terms of metabolic cost models, generally trying to determine power law relations (1.7). Now these attempts are usually done for tree-like network, displaying a clear vessel hierarchy and parent-to-child branching pattern, which coincide with the flow pattern. As indicated above, capillary systems do not necessarily have such a defined structure, as they are dense meshes with relatively narrow vessel size distributions, see Figure 1.1b. We were provided the corresponding network skeletons of these vessel systems, extracted from grown mice by our collaborators (Zerial Lab, MPI CBG), see section 3.3.1 for details. We tested Murray's law for these skeletons by fitting the exponent α in equation (1.7) for every Y-branching. Here, the locally largest vessel is identified as the branching's parent and its children are considered to split the flow of their parent, such has found in a tree branching. The resulting distributions for α are presented in Figure 1.8, displaying broad, long-tail distributions for either network.

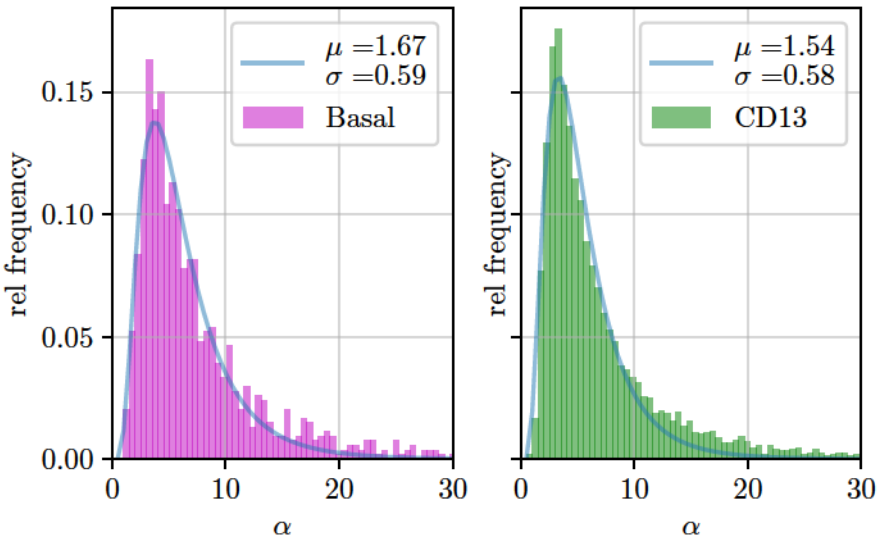

Figure 1.8: Experimental falsification of Murray's law for capillary vessels in liver lobuli: Exponent distributions found for (1.7) and respective log-normal fits. The distributions modes are used to estimate the exponents α. Sinusoidal systems (basal marker) with mode $\alpha = e^{\mu^2-\sigma^2} \approx 3.75$ and bile canaliculi systems (cd13 marker) with mode $\alpha = e^{\mu^2-\sigma^2} \approx 3.33$.

The modes of the acquired, log-normally distributed fit exponents are $\alpha \approx 3.75$ for sinusoids and $\alpha \approx 3.33$ for bile canaliculi. It has been known for quite some time that capillary systems defy the cubic relationship found by Murray [127]. We suspect this mismatch to be correlated with the reticulated nature of these network types, where the weight based parent-child classification is non-applicable. Yet, one may argue the deviation of $\alpha = 3$ is readily solved by adjusting Murray's cost model with the exponent γ which would be able to account for reticulation and $\alpha > 3$ simultaneously, see (1.8). Nevertheless applying (1.8) one would deduce $\gamma < 1$ for the given liver lobule data sets, which is in direct contradiction with the rescaled cost model [20], which predicts an exponent γ-induced nullity transition only for $\gamma \geq 1$. On the other hand, this could potentially be circumvented if fluctuation-induced loops are considered as well [61, 30]. However, to our knowledge it has not yet been discussed how such fluctuations alter Murray's law.
Further, any more complicated cost approaches (with more cost terms than currently in (1.2)) will inevitably leave model parameters behind in (1.7). What we suggest here is to reformulate Murray's law as:

$$\sum_{j \in inc(v)} a_j r_j^{\alpha_j} = A\left(s_v\right) \tag{1.12}$$

where $a_j, \alpha_j, A\left(s_v\right)$ become nontrivial functions of the parameters of the applied adaptation model and the local network properties. All this considered, we see the need to reinterpret the value of Murray's Law for flow networks:
To our knowledge no techniques have been proposed to directly extract model parameters from adaption models from real vasculature. Subsequently not only would a qualitative comparison of features such as redundancy be possible, but also identifying eligible states in the phase space of adaptation models. For that matter we intend to interpolate model parameters for volume penalties, flow fluctuations and multi-layer interactions directly from given graph topologies and radial distributions. The theoretical framework and results of this study are presented in section 3.3.1. Note, that part of these results have been published recently in [65].

1.3.3 Optimal design for metabolite uptake

As indicated, one may remodel vascular plexi in order to achieve a multitude of network topologies and radial distributions, and most studies are focused on perfusion based adaptation in order to do so. But at present almost none of these studies discuss the actual implications for solute transport to the tissue for the refined networks. In accordance with the recent studies of [82, 44] we here propose a model that takes into account stimuli in the form of the actual metabolite uptake of the surrounding tissue, and incorporates these into the metabolic cost function scheme. In particular we intend to study the competition between wall-shear driven and metabolite uptake driven adaptation in detail, combining pre-existent cost models. We do so particularly in preparation for a combined model framework that allows for the optimization of intertwined vessel networks for metabolite transport, see Figure 1.9. We further intend to focus on local and volume-wise adaptation procedures to find out whether the particular spatial embedding affects overall network metabolite uptake. The theoretical framework and results of this study are presented in section 3.4.

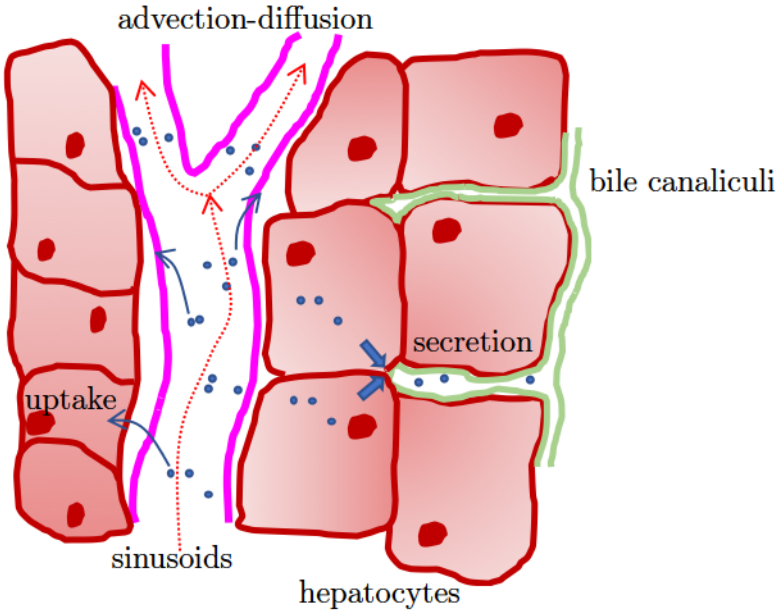

Figure 1.9: Complex metabolite transport and uptake in intertwined systems, schematically represented for sinusoids and canaliculi.

Chapter 2

Theory and Methods

2.1 Basic principles and mathematics

This section is intended to be a brief introduction to the mathematical, physical and numerical basics and methods on which any further conduct is based. In case you are familiar with these concepts, you may directly advance to section 2.2.

2.1.1 Mathematical basics

Linear equation systems

This section will briefly discuss the theory of linear equation systems, in particular the solution theory for under determined systems. This will be necessary for the following sections on graphs and Kirchhoff networks. Basic knowledge of linear algebra and functional analytics will be assumed. For detailed introductions see for example Wüst [146].
Given the Euclidean vector spaces $U \subseteq \mathbb{R}^m$, $W \subseteq \mathbb{R}^n$ with elements $\boldsymbol{x} \in U$ and $\boldsymbol{y} \in V$, the elements may be mapped with a linear operator $\boldsymbol{A} \in \mathbb{R}^{n \times m}$ as,

$$\boldsymbol{A} \cdot \boldsymbol{x} = \boldsymbol{y} \tag{2.1}$$

In this thesis we use "$\cdot$" to denote the inner product. This linear map presented by the matrix $\boldsymbol{A}$ has a kernel ker and an image im, defined as,

$$ker\,(\boldsymbol{A}) = \{\boldsymbol{x} \in U : \boldsymbol{A} \cdot \boldsymbol{x} = \boldsymbol{0}\} \tag{2.2}$$
$$im\,(\boldsymbol{A}) = \{\boldsymbol{y} \in V : \boldsymbol{y} = \boldsymbol{A} \cdot \boldsymbol{x}, \boldsymbol{x} \in U\} \tag{2.3}$$

The kernel is also referred to as the nullspace of $\boldsymbol{A}$ as it represents all elements of U being mapped to the null element of W. The image on the other hand is the effective vector space we map onto with $\boldsymbol{A}$, with $im\,(\boldsymbol{A}) \subseteq W$. Both the kernel $ker\,(\boldsymbol{A})$ and the image $im\,(\boldsymbol{A})$ are vector spaces themselves.
When dealing with linear equation systems, we know that any solution, $\boldsymbol{x}$ of equation (2.1), can be written as the composition of its particular $\boldsymbol{x}_P$ and homogeneous $\boldsymbol{x}_H$

solutions as

$$\boldsymbol{x}_H + \boldsymbol{x}_P = \boldsymbol{x} \in U \tag{2.4}$$
$$\text{with } \boldsymbol{A} \cdot \boldsymbol{x}_H = \boldsymbol{0},\ \boldsymbol{x}_H \in ker\,(\boldsymbol{A}) \tag{2.5}$$
$$\text{and } \boldsymbol{A} \cdot \boldsymbol{x}_P = \boldsymbol{y} \tag{2.6}$$

The dimensions of the kernel and image are used to define the rank rg and defect def of a linear operator $\boldsymbol{A}$ as

$$def\,(\boldsymbol{A}) = dim\,[ker\,(\boldsymbol{A})] \tag{2.7}$$
$$rg\,(\boldsymbol{A}) = dim\,[im\,(\boldsymbol{A})] \tag{2.8}$$

Hence a defect of zero means that only the null element of U maps onto the null element of W. The defect is also referred to as nullity. The rank $rg\,(\boldsymbol{A})$ is equivalent to the maximal number of linear independent rows or columns of the matrix $\boldsymbol{A}$. The rank and defect of a map $\boldsymbol{A}$ are linked via the nullity-rank theorem as follows:

$$dim\,(U) = rg\,(\boldsymbol{A}) + def\,(\boldsymbol{A}) \tag{2.9}$$

We will refer to this theorem later on when dealing with the basic concepts of graph theory in section 2.1.1, as it allows us to deduce certain characteristics for linear operators of graphs. For now, let us consider the concept of invertible matrices. In the special case where $m = n$, we call the operator $\boldsymbol{A}$ a square matrix. If it were to have full rank $rg\,(\boldsymbol{A}) = n$ it would further be called regular. This means there exists an inverse element $\boldsymbol{A}^{-1} \in \mathbb{R}^{n\times n}$ solving the problem (2.1) uniquely as,

$$\boldsymbol{x} = \boldsymbol{A}^{-1}\boldsymbol{y} \tag{2.10}$$
$$\boldsymbol{A}^{-1}\boldsymbol{A} = \boldsymbol{A}\boldsymbol{A}^{-1} = \boldsymbol{I}_n \tag{2.11}$$

with identity matrix $\boldsymbol{I}_n \in \mathbb{R}^{n\times n}$. In the case of a non-trivial kernel, i.e. $rg\,(\boldsymbol{A}) < n$ and $def\,(\boldsymbol{A}) > 0$, the matrix would be called singular, meaning it is non-invertible. Any non-square matrix $\boldsymbol{A} \in \mathbb{R}^{n\times m}$ is by default singular.
Non-invertibility of matrices is precisely the problem one is faced with when dealing with graphs and Kirchhoff networks: The most important linear operators derived from graphs are generally represented by non-invertible matrices.
Fortunately, in the case of such a non-full-rank problem $\boldsymbol{A} \in \mathbb{R}^{n\times m}$, one may utilize so called generalized-inverses (also called the Moore-Penrose inverses [102]) to solve (2.1). Hence a solution to (2.1) may be constructed with $\boldsymbol{A}^{\dagger} \in \mathbb{R}^{m\times n}$,

$$\boldsymbol{x} = \boldsymbol{A}^{\dagger}\boldsymbol{y} + \left[\boldsymbol{I}_m - \boldsymbol{A}^{\dagger}\boldsymbol{A}\right]\boldsymbol{z} \tag{2.12}$$
$$\boldsymbol{A}\boldsymbol{A}^{\dagger}\boldsymbol{A} = \boldsymbol{A} \tag{2.13}$$
$$\boldsymbol{A}^{\dagger}\boldsymbol{A}\boldsymbol{A}^{\dagger} = \boldsymbol{A}^{\dagger} \tag{2.14}$$
$$\left(\boldsymbol{A}\boldsymbol{A}^{\dagger}\right)^{T} = \boldsymbol{A}\boldsymbol{A}^{\dagger} \tag{2.15}$$
$$\left(\boldsymbol{A}^{\dagger}\boldsymbol{A}\right)^{T} = \boldsymbol{A}^{\dagger}\boldsymbol{A} \tag{2.16}$$

with an arbitrary $\boldsymbol{z} \in U$ and identity matrix $\boldsymbol{I}_m \in \mathbb{R}^{m\times m}$. The particular solution is given by $\boldsymbol{A}^{\dagger}\boldsymbol{y}$ paired with the homogeneous solution $\left[\boldsymbol{I}_m - \boldsymbol{A}^{\dagger}\boldsymbol{A}\right]\boldsymbol{z}$. Unlike for regular matrices, one actually has to define these properties for right-sided and left sided

scenarios respectively. Here, we will stick to the left-side notation.
It should be noted that the generalized inverse comes with its own special derivative [47]. This means in particular,

$$\begin{aligned}\partial_t \boldsymbol{A}^\dagger = &-\boldsymbol{A}^\dagger \partial_t \boldsymbol{A} \boldsymbol{A}^\dagger \\ &+ \left[\boldsymbol{I}_m - \boldsymbol{A}^\dagger \boldsymbol{A}\right] \partial_t \boldsymbol{A} \boldsymbol{A}^{T\dagger} \boldsymbol{A}^\dagger \\ &+ \boldsymbol{A}^\dagger \boldsymbol{A}^{T\dagger} \partial_t \boldsymbol{A} \left[\boldsymbol{I}_n - \boldsymbol{A}\boldsymbol{A}^\dagger\right]\end{aligned} \tag{2.17}$$

We will encounter this framework once again when dealing with remodeling dynamics in network morphogenesis, see section 2.2.2.

Dynamical systems and optimization

Dynamical systems are mathematical tools used to describe the temporal development of real biological or physical processes. This section gives a brief overview of the applied terminology and techniques, for further details see Reitmann [112]. A dynamical system is defined by a phase space $M \subseteq \mathbb{R}^m$ of possible states or system configurations and a one-parametric family of mappings $\boldsymbol{\phi}^t : M \to M$ with continuous parameter $t \in T \subseteq \mathbb{R}$, such that,

$$\boldsymbol{\phi}^0 (\boldsymbol{x}) = \boldsymbol{x}, \forall \boldsymbol{x} \in M \tag{2.18}$$

$$\boldsymbol{\phi}^t (\boldsymbol{\phi}^s (\boldsymbol{x})) = \boldsymbol{\phi}^{t+s} \boldsymbol{x} \tag{2.19}$$

$$\boldsymbol{\phi}^{(\cdot)} (\cdot) : T \times M \to M \tag{2.20}$$

The mapping $\boldsymbol{\phi}$ is also called flux and describes the temporal evolution of the system through the phase space M. In practice, many evolving processes may be modeled with an autonomous ordinary differential equation (ODE)

$$\partial_t \boldsymbol{x} (t) = \boldsymbol{f} (\boldsymbol{x} (t)) \tag{2.21}$$

with locally Lipschitz continuous vector field $\boldsymbol{f}$. The trajectory of such a system can then be formulated as $\boldsymbol{\alpha} : T \to M$ and is called the integral curve if $\boldsymbol{\alpha} (0) = \boldsymbol{p} \in M$ and $\partial_t \boldsymbol{\alpha} (t) = \boldsymbol{f} (\boldsymbol{\alpha} (t))$.
The local flux theorem states that, given an autonomous system as above, there is a subset $D \subseteq T \times M$ and flux $\boldsymbol{\phi} : D \to M$, such that [112],

$$\boldsymbol{\phi} (t, \boldsymbol{\phi} (s, \boldsymbol{p})) = \boldsymbol{\phi} (t + s, \boldsymbol{p}) \tag{2.22}$$

$$\boldsymbol{\phi} (0, \boldsymbol{p}) = \boldsymbol{p}, \forall \boldsymbol{p} \in M \tag{2.23}$$

$$\forall \boldsymbol{p} \in M \ , \ t \to \boldsymbol{\phi} (t, \boldsymbol{p}) \ \text{ with } t \in T \text{ is the integral curve of (2.21)} \tag{2.24}$$

Any system (2.21) effectively defines a dynamic system. The respective trajectories (or so called orbits) usually characterize the state of a dynamical system.
For the biological systems at hand we are particularly interested in stationary states, $\boldsymbol{f} (\boldsymbol{x} (t)) = \boldsymbol{0}$. In particular, simulating the dynamics of network morphogenesis, we intend to construct dynamical systems as introduced in chapter 1. There, we described how vasculature tends to refine over time from plexi to flow networks, which will be

considered as stationary states. Finding these states and characterizing their stability shall be thoroughly treated here in the sense of Lyapunov.
Let us consider a point $\boldsymbol{p} \in M$, a radius $\delta \in \mathbb{R}$ and the open sphere defined as $B_\delta(\boldsymbol{p}) = \{\boldsymbol{x} \in M | d(\boldsymbol{x}, \boldsymbol{p}) < \delta\}$ in the metric space (M, d) (d being for example the Euclidean metric). Given arbitrary thresholds $\epsilon \in \mathbb{R}$ one may refer to $\boldsymbol{p}$ as Lyapunov stable if

$$\forall \epsilon > 0 \; \exists \delta \; \forall \boldsymbol{q} \in B_\delta(\boldsymbol{p}) \forall t \geq 0, t \in T \text{ such that } d(\boldsymbol{\phi}(t, \boldsymbol{p}), \boldsymbol{\phi}(t, \boldsymbol{q})) < \epsilon \tag{2.25}$$

Further, a point $\boldsymbol{p}$ is called asymptotically Lyapunov stable if it is Lyapunov stable and additionally holds,

$$\exists \Delta \; \forall \boldsymbol{q} \in B_\Delta(\boldsymbol{p}) \text{ such that } \lim_{t \to \infty} d(\boldsymbol{\phi}(t, \boldsymbol{p}), \boldsymbol{\phi}(t, \boldsymbol{q})) = 0 \tag{2.26}$$

Finally, a point $\boldsymbol{p}$ is considered Lyapunov unstable if

$$\exists \epsilon > 0 \forall \delta > 0 \exists \boldsymbol{q} \in B_\delta(\boldsymbol{p}) \exists t_0 \text{ such that } d(\boldsymbol{\phi}(t_0, \boldsymbol{p}), \boldsymbol{\phi}(t_0, \boldsymbol{q})) \geq \epsilon \tag{2.27}$$

In order to construct dynamical systems with stable stationary points $\boldsymbol{p} \in M$, with $\boldsymbol{f}(\boldsymbol{p}) = \boldsymbol{0}$, the concept of Lyapunov functions will be employed extensively in this thesis.
Given an environment U of a point $\boldsymbol{p} \in M$, a positive-definite function Γ is a Lyapunov function of the system $\{\boldsymbol{\phi}(t, \boldsymbol{p})\}_{t \in T}$ in U when

$$\Gamma : U \to \mathbb{R} \text{ is continuous} \tag{2.28}$$

$$\Gamma(\boldsymbol{p}) = 0 \text{ and } \Gamma(\boldsymbol{p}) > 0 \; \forall \boldsymbol{x} \in U / \{\boldsymbol{p}\} \tag{2.29}$$

$$d\Gamma(\boldsymbol{\phi}(t, \boldsymbol{p})) \leq 0 \; \forall \boldsymbol{\phi}(t, \boldsymbol{p}) \in U \tag{2.30}$$

Hence, for any autonomous system (2.21) it follows in combination with (2.28) - (2.30) that the temporal development of the dynamic system fulfills

$$\partial_t \Gamma(\boldsymbol{x}(t)) = \nabla \Gamma^T(\boldsymbol{x}(t)) \cdot \boldsymbol{f}(\boldsymbol{x}(t)) \leq 0 \tag{2.31}$$

for all $\boldsymbol{x}(t) \in U$. With this in mind, if such a function Γ exists, any one of its stationary points $\boldsymbol{p}$ is (asymptotically) stable in the sense of Lyapunov. Therefore one may specifically construct an autonomous ODE system of the form (2.21) by defining a function $\Gamma(\boldsymbol{x}) \geq 0 \; \forall \boldsymbol{x} \in U$ and setting

$$\boldsymbol{f}(\boldsymbol{x}(t)) = -\nabla \Gamma(\boldsymbol{x}(t)) \tag{2.32}$$

Proceeding this way it becomes apparent that Γ is yet again a Lyapunov function with a stable stationary point.
This framework may readily be connected to the general concept of constrained optimization problems. Let us consider a continuous cost function on $U \subset \mathbb{R}^m$ and $\Lambda : U \to \mathbb{R}$ with $\boldsymbol{p} \in U$ and

$$\Lambda(\boldsymbol{p}) = \Lambda^* \leq \Lambda(\boldsymbol{x}) \; \forall \boldsymbol{x} \in U \tag{2.33}$$

Hence Λ^* is the minimum of Λ. For practical purposes, it might be useful to require relation (2.33) to hold only for a local environment W of $\boldsymbol{p}$ as,

$$\Lambda^* \leq \Lambda(\boldsymbol{x}) \; \forall \boldsymbol{x} \in U \cap W \tag{2.34}$$

One may refer to $\boldsymbol{p}$ as global solution if (2.33) or as local solution if (2.34). Furthermore, we define sets of constraining functions $g : U \to \mathbb{R}^p$, $h : U \to \mathbb{R}^q$ with components

$$g_i(\boldsymbol{x}) \leq 0 \text{ for } i \in \{1, ..., p\} \tag{2.35}$$
$$h_j(\boldsymbol{x}) = 0 \text{ for } j \in \{1, ..., q\} \tag{2.36}$$

Subsequently, we may then define the continuous, constrained optimization problem as

$$\begin{aligned} &\Lambda(\boldsymbol{x}) \to min \text{ for } \boldsymbol{x} \in U \\ &\text{and } \boldsymbol{g}(\boldsymbol{x}) \leq 0, \boldsymbol{h}(\boldsymbol{x}) = 0 \end{aligned} \tag{2.37}$$

In practice, one reformulates this problem with its Lagrange function $: \mathbb{R}^{m+p+q}$ as

$$\mathcal{L}(\boldsymbol{x}, \boldsymbol{u}, \boldsymbol{v}) = \Lambda + \boldsymbol{u}^T \cdot \boldsymbol{g} + \boldsymbol{v}^T \cdot \boldsymbol{h} \tag{2.38}$$
$$u_i \geq 0 \tag{2.39}$$
$$\boldsymbol{u}^T \cdot \boldsymbol{g} = \boldsymbol{0} \tag{2.40}$$

with $\boldsymbol{g}$ and $\boldsymbol{h}$ as defined in (2.35), (2.36). Such a constrained optimization problem was previously discussed for network morphogenesis models in 1.2.1. For that matter, any metabolic cost function problem classifies as such a constrained minimization problem (2.37). Although there is a plethora of possible numerical methods to find the local or global minima available [97, 138], we just focus on one specific class: gradient descent approaches . The gradient descent approach is mostly utilized for continuous optimization problems, readily applicable to (2.37), and allows for intuitive derivation of self-organized dynamics in biological systems. Roughly put, one chooses an initial $\boldsymbol{x}_0$ and then iteratively evaluates Λ by calculating a series of consecutive $\boldsymbol{x}_n$ as

$$\boldsymbol{x}_{n+1} = \boldsymbol{x}_n - \boldsymbol{\delta}_n^T \cdot \nabla\Lambda(\boldsymbol{x}_n) \tag{2.41}$$

where the specific calculation of $\boldsymbol{\delta}$ depends on the chosen algorithm. In this case it is assumed that the gradient $\nabla\Lambda(\boldsymbol{x}_n)$ represents a valid direction for descent, yet the iteration (2.41) may be modified due to the given constraints $\boldsymbol{g}$, $\boldsymbol{h}$ [97]. It should be noted here that one may only find a global minimum this way if Λ is globally convex. Otherwise, if Λ is only locally convex, applying (2.41) will generally result in the detection of local minima when successful.
At this point, one might already see how this connects to the dynamical systems of interest in this thesis: Solving the dynamical system (2.21), where the gradients are derived from a Lyapunov function, numerical integration naturally uses such iterative methods when relying on explicit solvers. Subsequently, we may have the cost function Λ correspond to the Lyapunov function Γ in this framework and have the constraints (2.35),(2.36) incorporated into the backend computation of $\boldsymbol{x}$. We will illustrate this process in greater detail in section 2.2.2.

Graph theory

This section provides a brief introduction to graph theory, mainly based on the terminology of [67, 95]. A simple graph G is a discrete mathematical construct consisting of

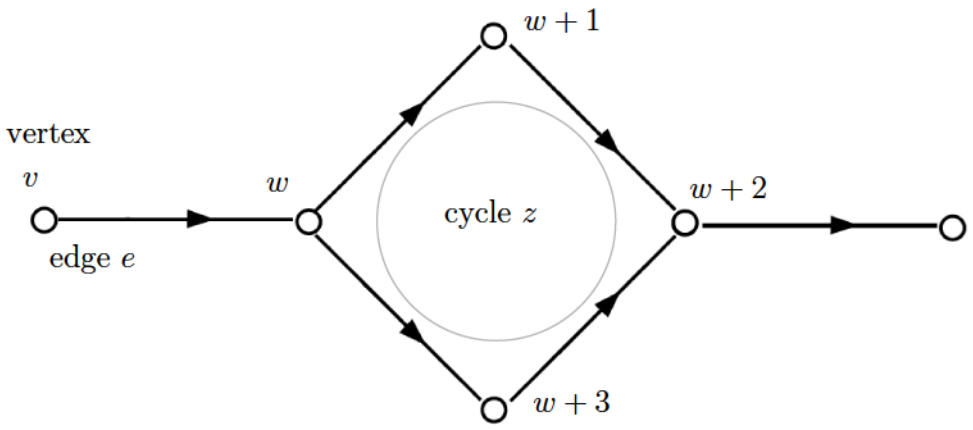

Figure 2.1: Simple graph G and its components marked as vertices v, w, edges $e = (v, w)$ and cycles $z = \{(w, w+1), (w+1, w+2), (w+2, w+3), (w+3, w)\}$. Edge direction indicated by arrows going as $\alpha \to \omega$.

a set of vertices V and a set of edges E and $E \cap V = \varnothing$, see Figure 2.1a. Further, there are two maps α, ω with $\alpha : E \to V$ and $\omega : E \to V$, uniquely defining each edge $e \in E$ as a tuple of vertices $(\alpha(e), \omega(e))$, and $\alpha(e) \neq \omega(e)$. Two vertices are called adjacent if they are connected by an edge. Two edges are called incident if they connect to the same vertex. This term may also be applied to a vertex and an edge. A path is a sequence of consecutively incident edges $\{e_0, ..., e_i, ..., e_j\}$. A subset $V' \subseteq V$ of nodes connected to each other via a set of edges $E' \subseteq E$ is called a connected component, if there exists a path between any two vertices of V'. A graph may consist of several such components (at max $|V|$ if there are no edges, min 0 if $V = \varnothing$). The degree of a vertex, i.e. the number of edges d they are incident to can be written as $\boldsymbol{D} \in \mathbb{N}^{|V| \times |V|}$,

$$D_{uv} = \begin{cases} d_v & \text{if u=v} \\ 0 & \text{else} \end{cases} \tag{2.42}$$

Moreover, each edge may to be characterized by a set of attributes. In the case of spatial transport networks, these attributes may encompass any useful descriptor such as radius, length, conductivity, flow, etc. Hence we may formulate a mapping $\gamma : E \to \mathbb{R}^{|E|}$ with the field γ being an arbitrary edge attribute. Graphs $G(V, E, \alpha, \omega)$ may be represented in matrix form by their incidence matrix. The incidence matrix $\boldsymbol{B} \in \mathbb{Z}^{|V| \times |E|}$ displays which vertices and edges are incident, and in which direction they do so

$$B_{ve} = \begin{cases} 1 & \text{if vertex v is incident with edge e and } \omega(e) = v \\ -1 & \text{if vertex v is incident with edge e and } \alpha(e) = v \\ 0 & \text{else} \end{cases} \tag{2.43}$$

In this thesis, edge directionality shall be randomly assigned to edges, as it will only be used for the definition of an arbitrary but consistently set orientation. This is important when walking along circular paths, or whether edge flow is entering or leaving a node. In a graph consisting of one connected component, this matrix has certain characteristics

such as

$$def\left(\boldsymbol{B}^T\right) = 1 \tag{2.44}$$
$$rg\left(\boldsymbol{B}^T\right) = rg\left(\boldsymbol{B}\right) = |V| - 1 \tag{2.45}$$
$$im\left(\boldsymbol{B}^T\right) \perp ker\left(\boldsymbol{B}\right) \tag{2.46}$$

where $\boldsymbol{B}^T$ is non-invertible as it has a one-dimensional kernel. In addition, it is of interest whether the graph displays any redundancies, effectively the existence of multiple, non over-lapping paths between two vertices, forming a cycle. Loosely, one may identify the number of cycles in a network in the following way: Assuming that the network is a simple graph with one connected component of $|V|$ vertices and $|E|$ edges, then one only needs $|V|-1$ edges to connect every vertex and thereby create a spanning tree, i.e. a graph without a single cycle. Moreover, any additional edge added will form a new cycle. Thus, the total amount of such cycles in a network z, is the number of excess edges:

$$z = |E| - |V| + 1 \tag{2.47}$$

These redundancies may be written in the form of a cycle matrix $\boldsymbol{Z} \in \mathbb{N}^{z \times |E|}$, given one identified z cycles, with

$$Z_{ie} = \begin{cases} 1 & \text{if cycle i contains edge e} \\ 0 & \text{else} \end{cases} \tag{2.48}$$

In a simple, connected graph the cycle matrix $\boldsymbol{Z}$ is inherently involved with the incidence matrix $\boldsymbol{B}$. One can show for a connected graph of one component that

$$def\left(\boldsymbol{Z}\right) = |V| - 1 \tag{2.49}$$
$$def\left(\boldsymbol{B}\right) = rg\left(\boldsymbol{Z}\right) = |E| - |V| + 1 \tag{2.50}$$
$$im\left(\boldsymbol{Z}^T\right) = ker\left(\boldsymbol{B}\right) \tag{2.51}$$
$$im\left(\boldsymbol{B}^T\right) = ker\left(\boldsymbol{Z}\right) \tag{2.52}$$
$$im\left(\boldsymbol{Z}^T\right) \perp ker\left(\boldsymbol{Z}\right) \tag{2.53}$$
$$\tag{2.54}$$

This is interesting insofar as any walk along a cycle generates a null vector, if one adds up nodal characteristics considering the edge orientation, as

$$\boldsymbol{Z} \cdot \boldsymbol{B}^T \cdot \boldsymbol{x} = \boldsymbol{0} \tag{2.55}$$

which will be crucial when dealing with Kirchhoff networks. It also becomes clear that z equals the rank of the cycle matrix, indicating that there are maximally z *independent* cycles. The independence refers to the fact that these cycles form the basis of a vector space, namely over the field $\mathbb{Z}^2$. Hence, one may deduct any other cycle found as a linear combination of the z basis cycles, see [86]. This makes z the dimension of this vector space, and any changes in the redundancy of a graph will affect it. The number of cycles may be calculated for any simple multicomponent graph as

$$z = |E| - |V| + P \tag{2.56}$$

where P is the number of connected components of the graph [143]. This cycle dimension is often referred to as nullity as it is equivalent to the dimension of the incidence's matrix null space. Note that we shall use the $m = |E|$ for the number of edges in the graph and $n = |V|$ for the number of nodes in the graph from here on to improve readability.

2.1.2 Basic hydrodynamics

This section gives a brief introduction basic concepts of hydrodynamics. Overall, this section covers passive transport models such as Hagen-Poiseuille flow and Taylor dispersion and how these models are applicable to extended channel networks. For further detail and terminology, see Landau et al [68].
In any continuum model of hydrodynamics, one requires a proper dynamical description of key characteristics such as mass and momentum. Further, the medium at hand may be bearer of secondary specifications, i.e. temperature and metabolite concentrations. These characteristics will be briefly introduced in the following.

Momentum and mass balance

For the proper mathematical treatment, a fluid is primarily described by two fields, the fluid's velocity $\boldsymbol{v}(\boldsymbol{r},t)$ and mass density $\rho(\boldsymbol{r},t)$. The mass transported through any infinitesimal volume element is then given by the continuity equation,

$$\partial_t \rho(\boldsymbol{r},t) + \nabla \cdot (\rho(\boldsymbol{r},t)\,\boldsymbol{v}(\boldsymbol{r},t)) = 0 \tag{2.57}$$

This means that any change of mass inside a given volume will result from dynamics in the density and effective mass advection. This particularly holds for the case of a source-free system were the overall volume is fixed. Naturally, this may be extended to complex mass transports for dynamically changing volume elements by applying the Reynold's transport theorem [114]. As we intend to focus on modeling long-term dynamics of capillary beds, we consider short-term size fluctuations and compliance to be negligible, meaning that (2.57) is sufficient for our purposes. Following the trajectory of an infinitesimal fluid element as it is advected, one may further consider its momentum density $\rho\boldsymbol{v}$. The momentum will change due to forces $\boldsymbol{F}$ acting on the volume elements surface S, i.e. due to spatial pressure gradients, shearing against adjacent fluid layers etc. This may subsequently be formulated with the stress tensor $\boldsymbol{\sigma}$ expressing the force density as in [68],

$$\boldsymbol{F} = \int_S \boldsymbol{\sigma} \cdot d\boldsymbol{A} = \int_V \nabla \cdot \boldsymbol{\sigma} dV \tag{2.58}$$

where V is the fluid elements volume. Then, we may state the dynamic equation for the momentum density as

$$\rho\left[\partial_t \boldsymbol{v}(\boldsymbol{r},t) + (\boldsymbol{v}(\boldsymbol{r},t)\cdot\nabla)\,\boldsymbol{v}(\boldsymbol{r},t)\right] = \nabla \cdot \boldsymbol{\sigma}(\boldsymbol{r},t) \tag{2.59}$$

Now the stress tensor may be customized to encapsulate any complex interaction of the fluid elements with each other. This is usually done via non-linear viscosity terms for

blood and other colloid-like suspensions. The specifics of the viscosity profiles will be neglected here as we intend to coarse-grain most of the network morphogenesis problem into a lumped parameter model anyway. Subsequently, we consider the special case of an incompressible ($\rho = const$), Newtonian fluid, i.e. turning (2.59) into the Navier-Stokes equation as [68],

$$\rho\left[\partial_t \boldsymbol{v}\left(\boldsymbol{r},t\right) + \left(\boldsymbol{v}\left(\boldsymbol{r},t\right)\cdot\nabla\right)\boldsymbol{v}\left(\boldsymbol{r},t\right)\right] = -\nabla p + \eta\Delta\boldsymbol{v}\left(\boldsymbol{r},t\right) \tag{2.60}$$

Here, η is the fluid's viscosity and p is the hydrostatic pressure. The first term on the right-hand side describes the force densities due to pressure gradients and the second term refers to the fluid's inner friction due to shearing of neighboring fluid elements along a velocity gradient. This equation may effectively be non-dimensionalized by identifying relevant reference scales for velocity $\bar{v}$, length L, viscosity η and density ρ such that we write

$$L\boldsymbol{r}^* = \boldsymbol{r} \tag{2.61}$$

$$\bar{v}\boldsymbol{v}^* = \boldsymbol{v} \tag{2.62}$$

$$\tau t^* = t \text{ with } \tau = \frac{L}{\bar{v}} \tag{2.63}$$

$$\phi p^* = p \text{ with } \phi = \frac{L}{\bar{v}\eta} \tag{2.64}$$

$$Re\left[\partial_{t^*}\boldsymbol{v}^*\left(\boldsymbol{r}^*,t^*\right) + \left(\boldsymbol{v}^*\left(\boldsymbol{r}^*,t^*\right)\cdot\nabla^*\right)\boldsymbol{v}^*\left(\boldsymbol{r}^*,t^*\right)\right] = -\nabla^* p^* + \Delta^*\boldsymbol{v}^*\left(\boldsymbol{r}^*,t^*\right) \tag{2.65}$$

with the Reynolds number $Re = \frac{\bar{v}L\rho}{\eta}$. With this formulation, one may easily assess whether inertia or viscosity is the predominant phenomenon for either $Re \gg 1$ or $Re \ll 1$. This is particularly useful as capillary beds may in general be found in the low Reynold number regime. Hence most transport phenomena, such as flow in thin, long vessels, may be evaluated for the stationary case as

$$0 \approx \nabla^* p^* - \Delta^*\boldsymbol{v}^*\left(\boldsymbol{r}^*,t^*\right) \tag{2.66}$$

which is usually referred to as the Stokes equation.

Diffusion-Advection

Additional properties such as temperature and concentration often need to be included into the tool set of transport equations. This is true particularly for biological flow networks, as the entire system is constructed to transport these quantities. In the simplest way this is done via the continuity equation, i.e. describing the macroscopic dynamics of the concentration c of an arbitrary solute as

$$\partial_t c\left(\boldsymbol{r},t\right) + \nabla\cdot\boldsymbol{j}\left(\boldsymbol{r},t\right) = 0 \tag{2.67}$$

Here, once again, we assume that the volume perfused is static. The solute flux $\boldsymbol{j}$ is given in the simplest case as Fick's law,

$$\boldsymbol{j}\left(\boldsymbol{r},t\right) = -D\nabla c\left(\boldsymbol{r},t\right) + \boldsymbol{v}\left(\boldsymbol{r},t\right)c\left(\boldsymbol{r},t\right) \tag{2.68}$$

with D being the diffusion constant. Hence, when describing the transport properties of molecules dissolved in the fluid, one needs to consider diffusion due to concentration gradients and due to advection of the medium as

$$\partial_t c(\boldsymbol{r},t) - D\Delta c(\boldsymbol{r},t) + \nabla \cdot [\boldsymbol{v}(\boldsymbol{r},t)\, c(\boldsymbol{r},t)] = 0 \tag{2.69}$$

Here we would like to point out that diffusion-advection problems are generally characterized by the time-scale $\tau = \frac{L^2}{D}$ and Peclet number $Pe = \frac{\bar{v}L}{D}$, so we rewrite the continuity equation (2.85) as

$$\partial_{t^*} c(\boldsymbol{r}^*,t^*) - \Delta^* c(\boldsymbol{r}^*,t^*) + Pe\nabla \cdot [\boldsymbol{v}^*(\boldsymbol{r}^*,t^*)\, c(\boldsymbol{r}^*,t^*)] = 0 \tag{2.70}$$

With this non-dimensional parameter we are able to distinguish between purely diffusive or advective problems, and thereby determine which transport mechanism is dominant, see Figure 2.2. This becomes interesting especially when dealing with transport

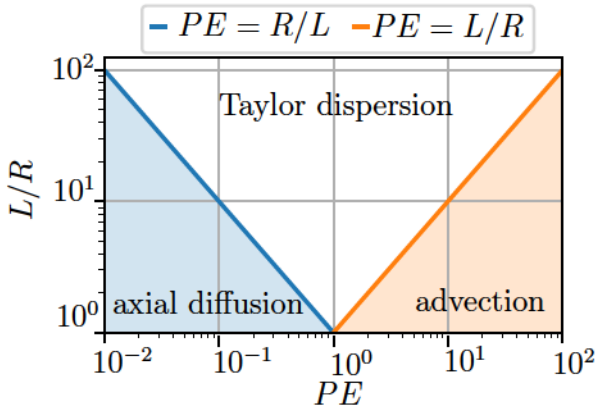

Figure 2.2: Peclet number $PE = \frac{\bar{v}L}{D}$ dependency of solute transport in a thin channel, marking dominant regimes for axial diffusion, Taylor dispersion and advection.

in thin channels, which naturally arises when modeling capillary beds, see section 2.2.1. We would like to note that we are dealing with passive fluids, i.e. it is assumed that there are no explicit dependencies between $\boldsymbol{v}$ and c. This might not necessarily be the case in some biological flow networks though. For instance, it has been discussed how flows $\boldsymbol{v}$ may be driven and controlled by the active deposition of a metabolite [21, 100]. We will briefly consider such a case at the end, in chapter 4.

Flow in a thin channel

As the intention of this thesis is to model the flow in vascular networks, the simplest way to do so is by abstracting any vessels as rigid cylindrical pipes perfused by a passive, incompressible, viscous fluid For our purposes, the cylinder is oriented along the z-axis. Due to its rotation-symmetry one has this channel characterized by its length L, radius R and flow velocity $\boldsymbol{v} = v(r)\,\boldsymbol{e}_z$. These channels are assumed to be thin, i.e. $L/R \gg 1$ and the Reynolds number to be small, i.e. $Re = \frac{vL\rho}{\eta} \ll 1$. One may readily solve the resulting Stokes equation (2.66) with the 'no slip boundary', i.e.

$v(R) = 0$, and pressure difference $\Delta p = p(z = L) - p(z = 0)$, to acquire the velocity profile as

$$v(r) = v_0 \left(1 - \frac{r^2}{R^2}\right) \tag{2.71}$$

$$v_0 = \frac{R^2}{4\eta l}\Delta p \tag{2.72}$$

Further, one may calculate the entirety of the convected fluid volume through the channel, of cross section S, per unit of time as

$$f = \int_S \boldsymbol{v}(r) \cdot d\boldsymbol{A} = \frac{\pi R^4}{8\eta L}\Delta p \tag{2.73}$$

where we call f the volume flow rate. Equation (2.73) is also referred to as the Hagen-Poiseuille flow law. As the fluid is viscous, one naturally has friction of the adjacent fluid layers, which vary radially in speed. In particular, one may calculate the stress exerted by this fluid onto the boundary layer, at the inner coating surface of the channel, which corresponds to the mechanical sensation cells may respond to. This component is also referred to as wall shear stress, which corresponds to a single component of the stress tensor $\boldsymbol{\sigma}$ as [68],

$$\sigma_{rz}|_{r=R} = -\frac{R\Delta p}{2L} \tag{2.74}$$

2.1.3 Kirchhoff networks

This section intends to give a brief overview of Kirchhoff networks, which are linear graph abstractions of the real biological vessel networks of interest for this thesis. In this framework, any transport is conducted via the edges E and linked together by nodes V. The vertices have no capacity to store fluid and represent the branching points of the network. With this in mind, each edge carries a volume flow f such that at any vertex the sum of all flows equals a nodal function s,

$$\sum_{e \in I(v)} f_e = s_v \tag{2.75}$$

where $I(v)$ indicates the set of edges incident to vertex v. The function s is referred to as a sink or source when s is non-zero, otherwise the node is called source-free. Equation (2.75) is called Kirchhoff's current law, which represents mass conservation at every vertex. One can easily show that by adding up all s_v as

$$\sum_v s_v = 0 \tag{2.76}$$

displaying the entirety of injected and extracted flows to balance [36]. Further, in such a network, one may formulate the flow as a linear function, Ohm's law, as

$$f_e = C_e \Delta p_e \tag{2.77}$$

where C_e is the conductance of an edge and Δp_e its respective potential gradient. One may thus characterize the flow in every vessel as a direct response to a gradient of potential energy and have it scale linearly with the conductance which incorporates the geometry and physical nature of the transport problem. The equation systems formulated in (2.75) and (2.77) may be bundled in vector notation as

$$\boldsymbol{B} \cdot \boldsymbol{f} = \boldsymbol{s} \tag{2.78}$$

$$\boldsymbol{f} = \boldsymbol{C} \cdot \Delta \boldsymbol{p} \tag{2.79}$$

Here, $\boldsymbol{B}$ designates the incidence matrix as introduced in section 2.1.1 and $\boldsymbol{C}$ is a diagonal matrix with C_e on the diagonal. The potential gradients can be calculated from nodal potentials as $\Delta \boldsymbol{p} = \boldsymbol{B}^T \cdot \boldsymbol{p}$. Now, combining this fact with equations (2.78) and (2.79), one finds the transformation between the sinks/sources and the potentials as

$$\boldsymbol{B} \cdot \boldsymbol{C} \cdot \boldsymbol{B}^T \cdot \boldsymbol{p} = \boldsymbol{s} \tag{2.80}$$

The incidence matrix is non-invertible, see sections 2.1.1, and therefore one needs the generalized inverse $[\cdot]^\dagger$, see section 2.1.1, to solve equation (2.80) as:

$$\Delta \boldsymbol{p} = \boldsymbol{B}^T \left[\boldsymbol{B} \cdot \boldsymbol{C} \cdot \boldsymbol{B}^T\right]^\dagger \boldsymbol{s} \tag{2.81}$$

This solution already corresponds to the least-square solution of equation (2.80) which is due to the fact that previously $\Delta \boldsymbol{p} = \boldsymbol{B}^T \cdot \boldsymbol{p}$ was assumed. This actually corresponds to the concept of a conservative potential field. Hence, all circular walks add up to a zero potential difference, see section 2.1.1, and subsequently no circular potential flows exist.
So far, we have treated these networks like boundary problems which needed defined nodal sources $\boldsymbol{s}$ or alternatively nodal pressures $\boldsymbol{p}$. One also refers to given nodal sources as a Dirichlet problem and to nodal pressures as a Neumann problem [16]
Interestingly, one may show (2.81) to correspond to the flow pattern with minimal dissipation, by applying the Thomson principle [62, 50]. Following this variational principle, one considers the system to be characterized by a cost function, i.e. the energy dissipation defined as $\Lambda = \sum_e f_e^2/\tilde{c}_e$, with positive coefficients $\tilde{c}_e > 0$. Further, one may use this cost function to formulate a constrained optimization problem with Lagrange multipliers p_v and the boundary conditions (2.75) such that

$$\mathcal{L} = \sum_e f_e^2/\tilde{c}_e + \sum_v p_v \left(s_v - \sum_{e' \in I(v)} f_{e'} \right) \tag{2.82}$$

The aim is to find the set of flows f_e which minimize the system's cost, Λ, with respect to the constraints given by the Kirchhoff current law. Doing so, one ends up naturally with Ohm's law, with the conductance $C_e = \tilde{c}_e$ for the coefficients and the Lagrange parameters p_v representing the nodal potentials. These p_v define the potential gradients as $\Delta p_e = \left(p_{\omega(e)} - p_{\alpha(e)}\right)$, where $\alpha(e), \omega(e)$ designate the initial and final vertex of any edge e, see 2.1.1. This cost function ansatz enables one to find a unique solution for the potential differences Δp in equation (2.80) as

$$\Delta \boldsymbol{p} = \boldsymbol{C}^{-1/2} \left[\boldsymbol{B} \cdot \boldsymbol{C}^{1/2}\right]^\dagger \boldsymbol{s} \tag{2.83}$$

This solution is equivalent to (2.81) and represents the optimal potential landscape, which minimizes the overall power dissipation for a given landscape of conductance and sinks [15, 103].
Note that this formalism may be applied to any stationary transport process following the Thomson principle as well as random walks of particles on a lattice. This class of systems is often referred to as lumped or linear systems, in analogy to simple electric circuits [34, 37]. Even complex transport phenomena including pulsatile flow waves and vessel compliance may be approximated in the Kirchhoff framework by adding capacities and inductivities [139, 4]. The framework may further be expanded to non-linear networks, e.g. including turbulent flows, with

$$\boldsymbol{f} = \boldsymbol{C}\left(\boldsymbol{p}\right) \tag{2.84}$$

and even generalize the Thomson principle accordingly [16]. For the rest of this thesis, we assume that any given network is linear, and its flow rate will be treated according to the Hagen-Poiseuille law, where the edge conductance is given by $C_e = \frac{\pi R_e^4}{8\eta L_e}$, see equation (2.73). Henceforth, it will be assumed in accordance with [24] that no turbulence or dissipation losses need to be considered at branching points.

2.2 Complex transport problems

This section deals with the background of commonly applied theories which combine multiple concepts discussed in section 2.1.1. It is strongly advised that the reader has an understanding of these theoretical frameworks before proceeding to the thesis' findings and discussions.

2.2.1 Taylor dispersion

As stated before in chapter 1 models involving complex adaptive flow networks have been only recently deployed to capture metabolite transport and uptake phenomena. In this section, we would like to review a specific model for metabolite transport in thin channels with laminar flow, so called Aris-Taylor dispersion. To introduce readers to the concept, consider the following thought experiment:
Two channels are to be perfused by a liquid carrying a species of molecules of concentration c at time t in a predefined volume element, as illustrated in Figure 2.3. The first channel is to be perfused by a plug flow, i.e. all radial fluid layers move at the same speed, and our concentration 'package' will not be distorted by its advection over the time span dt, see Figure 2.3a. Further, we observe that the metabolite diffuses in axial direction as only an axial concentration gradient is present. On the other hand this is not the case in the second channel displaying Hagen-Poiseuillle flow, see Figure 2.3b. First, as radial layers move at different speed, one will see a parabolic distortion of the concentration profile due to the advection. Second, axial and radial diffusion occurs due to the axial concentration gradient (as before) and a radial concentration gradient (due to the flow distortion). Therefore, it seems that the flow profile itself interferes with the concentration gradient, thereby coupling the metabolite's effective diffusion to the fluid's advection. Now, as we are dealing with passive fluids, we consider that

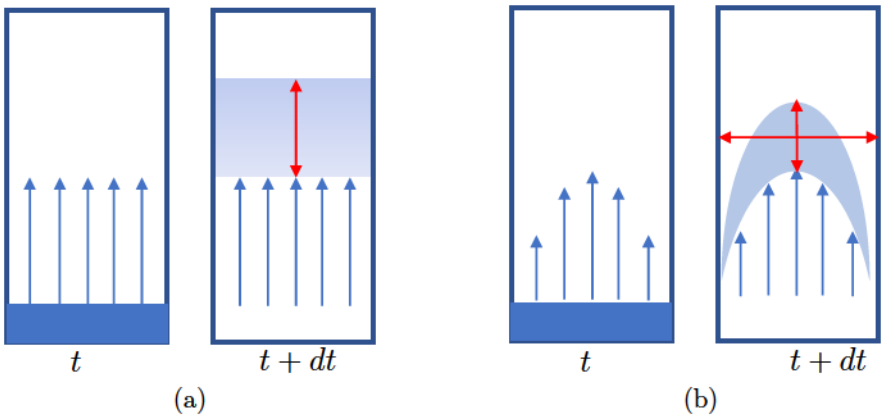

Figure 2.3: Diffusion of metabolite in a thin channel is altered by the flow profile: (a) Plug flow with axially diffusing solute. (b) Hagen-Poiseuille flow with axially and radially diffusing solute due to the parabolic velocity profile.

the flow velocity v is decoupled from the metabolite concentration c. Further, in a rotation symmetrical channel, the metabolite concentration is given as $c(z, r, t)$, as is

the carrier liquid's velocity profile $v(z,r,t)$. So, we get from (2.67), (2.68)

$$\partial_t c(z,r,t) - D\Delta c(z,r,t) + \nabla \cdot (\boldsymbol{v}(z,r,t)\, c(z,r,t)) = 0 \tag{2.85}$$

Moreover, as radial diffusion occurs on time scales much smaller than axial diffusion or advection, one may decouple these effects. In particular, we intend to describe any transport via its cross-section average $\bar{c}$ and radial perturbation δc as,

$$c(z,r,t) = \bar{c}(z,t) + \delta c(z,r,t) \tag{2.86}$$
$$v(z,r,t) = \bar{v}(z,t) + \delta v(z,r,t) \tag{2.87}$$

The cross-section averages are to hold for the relations

$$\bar{c}(z,t) = \frac{1}{\pi R^2}\int c(z,r,t)\, dA \text{ and } \bar{\delta c} = 0 \tag{2.88}$$
$$\bar{v}(z,t) = \frac{1}{\pi R^2}\int v(z,r,t)\, dA \text{ and } \bar{\delta v} = 0 \tag{2.89}$$

It is generally assumed that the flow profile is Hagen-Poiseuille. However, we haven't considered any boundary effects for the metabolite on the vessel surfaces. Following the ansatz in [82], we consider a channel of length L and radius R, whose surface is absorbing at rate ν, see Figure 2.4 . It should be noted here that we do not intend to incorporate any explicit z or c dependency into the rate ν.

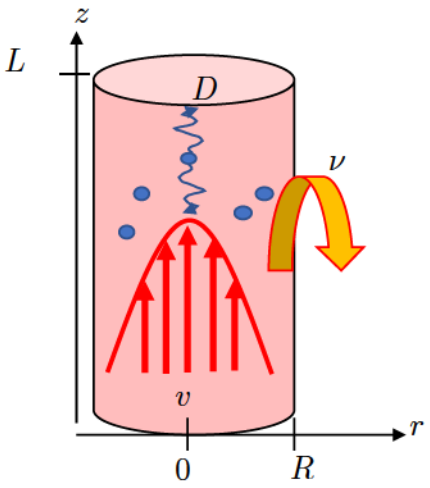

Figure 2.4: Capillary toy model: Advanced Taylor dispersion model as proposed in [82]. Fluid is advected by a parabolic profile while a metabolite of concentration c is diffusing with rate D and absorbed at the vessel's surface with rate ν.

Here, this ansatz reflects a constant solute removal, untouched by complex saturation or back-flow effects which we will discuss in chapter 3. We write this boundary condition down as :

$$\partial_r c|_{r=R} = \nu c(z,R,t) \tag{2.90}$$

One may follow the elaborate derivation in [82] in order to approximate the continuity equation similar to (2.85) for the stationary case as,

$$D\left(1 + \frac{\bar{v}^2 R^2}{48D^2}\right)\partial_{zz}\bar{c}(z) - \bar{v}\partial_z \bar{c}(z) - \left(\frac{2D\nu}{R}\right)\bar{c}(z) = 0 \tag{2.91}$$

which enables us to describe the metabolite as a quasi one-dimensional problem. In particular this approximation assumes small radial perturbations $\bar{c}(z) \gg \delta c(z,r)$ and low uptake rate $\nu R \ll 1$. It readily becomes apparent that the concentration profile (2.91) is analytically solvable and expandable to complex Kirchhoff networks, for which a discussion and ansatz is presented in [82]. Here, we would point out that the system is distinguished by a new effective axial diffusion as

$$D_{eff} = D\left(1 + \frac{\bar{v}^2 R^2}{48 D^2}\right) = D\left(1 + \frac{Pe^2}{48}\left(\frac{R}{L}\right)^2\right) \tag{2.92}$$

which represents the essence of Taylor dispersion in thin channels. As we increase the Peclet number Pe or the radius-to-length ratio, we will increase effective diffusion in the system, giving us a non-trivial coupling of the diffusion to the flow landscape inside a channel.
We will deploy this model with the intention to simulate salt and protein uptake in the sinusoids of the liver lobule in the framework of an extended network morphogenesis model, see chapter 3. Note that we intend to do a rigorous analysis of this model for the case $D_{eff} \to D$ corresponding to $\frac{1}{48}\left(\frac{PeR}{L}\right)^2 \ll 1$, in section 3.4.1. Subsequently, we set $\beta = \left(\frac{2D\nu}{R}\right)$ and we may describe the metabolite transport via the ODE

$$D\partial_{zz}\bar{c} - \bar{v}\partial_z\bar{c} - \beta\bar{c} = 0 \tag{2.93}$$

2.2.2 Flow-driven pruning

The concept of characterizing any transport network by a cost, e.g. by applying the Thomson principle, see equation (2.82), may readily be transferred to dynamic biological systems. The cells which are forming the walls of vascular networks are able to respond and adapt to a given set of stimuli, such as wall shear stress or hydrostatic pressure [106]. This enables such systems to continuously change their own topology and edge conductance in order to reach refined structures. The general framework of this network morphogenesis model will be laid out here for discrete systems only. The reader may refer to the overview given in [1], discussing continuum approaches.

Metabolic cost functions

To capture the biological behavior mentioned above, one may formulate a cost function for a vessel system as for example proposed in [20]:

$$\Gamma = \sum_e \frac{f_e^2}{C_e} + aC_e^\gamma \tag{2.94}$$

where the first term is the power dissipation as in equation (2.82) and the second a metabolic cost term C_e^γ, with proportionality factor a. This second term encapsulates the notion that a biological organism is constrained by its metabolic costs to deploy and sustain a vessel of a certain conductance. In detail this assumes that in order to

build larger vessels, with increased volume or surface area, one needs more cells, which have to be supplied with oxygen and nutrients. The exponent $\gamma > 0$ represents a degree of freedom to vary the relative importance of vessels of low or high conductance.
The minimization of the function (2.94) is performed by finding the set of conductances C_e which minimizes (2.94) for a given boundary condition, $\boldsymbol{s}$. Following the ansatz in [56] one may formulate the minimization of (2.94) in the form of temporal adaptation rules for each vessel, where each element reacts to a local stimulus instead of a single global optimization procedure. Now for that purpose let us rewrite (2.94) slightly as

$$\Gamma = \sum_e L_e \left\{ \frac{f_e^2}{K_e} + a K_e^\gamma \right\} \tag{2.95}$$

where we have the length reduced conductance as $K_e = \frac{\pi r_e^4}{8\eta}$. Here, we have the central terms of the cost function in dependence of the radii distribution r_e. We shall use this particular form to derive an ODE system for the radii dynamics of the network's channels via gradient descent. This capitalizes on the idea of deriving an asymptotically stable dynamical system from a Lyapunov function, as introduced in section 2.1.1. First, we switch to the vector notation for the dissipation-volume terms, using (2.79) and (2.81), to formulate it in terms of the nodal sinks/sources as,

$$\begin{aligned}
\Gamma &= \Delta \boldsymbol{f}^T \cdot \boldsymbol{K}^{-1} \cdot \boldsymbol{L} \cdot \Delta \boldsymbol{p} + a\, Tr\left(\boldsymbol{K}^\gamma \cdot \boldsymbol{L}\right) && (2.96)\\
&= \Delta \boldsymbol{p}^T \cdot \boldsymbol{K} \cdot \boldsymbol{L}^{-1} \cdot \Delta \boldsymbol{p} + a\, Tr\left(\boldsymbol{K}^\gamma \cdot \boldsymbol{L}\right) && (2.97)\\
&= \boldsymbol{s}^T \left[\boldsymbol{B}^T \boldsymbol{K} \cdot \boldsymbol{L}^{-1} \boldsymbol{B}\right]^\dagger \boldsymbol{s} + a\, Tr\left(\boldsymbol{K}^\gamma \cdot \boldsymbol{L}\right) && (2.98)
\end{aligned}$$

with L_e as entries of the diagonal $\boldsymbol{L}$. We calculate the (pseudo-)time derivatives of Γ

$$\begin{aligned}
\frac{d\Gamma}{dt} &= \boldsymbol{s}^T \partial_t \left[\boldsymbol{B} \cdot \boldsymbol{K} \cdot \boldsymbol{L}^{-1} \cdot \boldsymbol{B}^T\right]^\dagger \boldsymbol{s} \\
&\quad + 2\boldsymbol{s}^T \left[\boldsymbol{B} \cdot \boldsymbol{K} \cdot \boldsymbol{L}^{-1} \cdot \boldsymbol{B}^T\right]^\dagger \partial_t \boldsymbol{s} + a \partial_t Tr\left(\boldsymbol{K}^\gamma \cdot \boldsymbol{L}\right) && (2.99)
\end{aligned}$$

The derivative of the generalized inverse $\boldsymbol{B} \cdot \boldsymbol{K} \cdot \boldsymbol{L} \cdot \boldsymbol{B}^T = \boldsymbol{A}$ being [47],

$$\begin{aligned}
\partial_t \boldsymbol{A}^\dagger &= -\boldsymbol{A}^\dagger \left(\boldsymbol{B} \cdot \partial_t \boldsymbol{K} \cdot \boldsymbol{L}^{-1} \cdot \boldsymbol{B}^T\right) \boldsymbol{A}^\dagger \\
&\quad + \left[\boldsymbol{I} - \boldsymbol{A}^\dagger \cdot \boldsymbol{A}\right] \left(\boldsymbol{B} \cdot \partial_t \boldsymbol{K} \cdot \boldsymbol{L}^{-1} \cdot \boldsymbol{B}^T\right) \boldsymbol{A}^{T\dagger} \cdot \boldsymbol{A}^\dagger \\
&\quad + \boldsymbol{A}^\dagger \cdot \boldsymbol{A}^{T\dagger} \left(\boldsymbol{B}^T \cdot \partial_t \boldsymbol{K} \cdot \boldsymbol{L}^{-1} \cdot \boldsymbol{B}\right) \left[\boldsymbol{I} - \boldsymbol{A} \cdot \boldsymbol{A}^\dagger\right] && (2.100)
\end{aligned}$$

Fortunately the projector terms vanish as we have,

$$\boldsymbol{s}^T \left[\boldsymbol{I} - \boldsymbol{A}^\dagger \cdot \boldsymbol{A}\right] = 0 \text{ and } \left[\boldsymbol{I} - \boldsymbol{A} \cdot \boldsymbol{A}^\dagger\right] \boldsymbol{s} = 0 \tag{2.101}$$

Together with the identity $\boldsymbol{A}^\dagger = \left(\boldsymbol{A}^T\right)^\dagger$ the total time-derivative of Γ becomes,

$$\begin{aligned}
\frac{d\Gamma}{dt} &= -\boldsymbol{s}^T \boldsymbol{A}^{T\dagger} \left(\boldsymbol{B} \cdot \partial_t \boldsymbol{K} \cdot \boldsymbol{L}^{-1} \cdot \boldsymbol{B}^T\right) \boldsymbol{A}^\dagger \boldsymbol{s} \\
&\quad + 2\boldsymbol{s}^T \boldsymbol{A}^\dagger \partial_t \boldsymbol{s} + a \partial_t Tr\left(\boldsymbol{K}^\gamma \cdot \boldsymbol{L}\right) && (2.102)
\end{aligned}$$

With partial derivatives simplifying this formula as:

$$\begin{aligned}
\partial_t Tr\left(\boldsymbol{K}^\gamma \cdot \boldsymbol{L}\right) &= \gamma Tr\left(\boldsymbol{K}^{\gamma-1} \cdot \boldsymbol{L} \cdot \partial_t \boldsymbol{K}\right) && (2.103)\\
\partial_t \boldsymbol{s} &= 0 && (2.104)
\end{aligned}$$

As we also have $\Delta \boldsymbol{p} = \boldsymbol{B}^T \cdot \boldsymbol{A}^\dagger \boldsymbol{s}$, we may write the total time-derivative as

$$\frac{d\Gamma}{dt} = -\Delta \boldsymbol{p}^T \cdot \partial_t \boldsymbol{K} \cdot \boldsymbol{L}^{-1} \cdot \Delta \boldsymbol{p} + a\gamma Tr\left(\boldsymbol{K}^{\gamma-1} \cdot \boldsymbol{L} \cdot \partial_t \boldsymbol{K}\right) \tag{2.105}$$

$$= -\Delta \boldsymbol{f}^T \cdot \partial_t \boldsymbol{K}^{-2} \cdot \boldsymbol{L} \cdot \Delta \boldsymbol{f} + a\gamma Tr\left(\boldsymbol{K}^{\gamma-1} \cdot \boldsymbol{L} \cdot \partial_t \boldsymbol{K}\right) \tag{2.106}$$

Using this, we may rewrite the dynamical equations of K_e derived from Γ as:

$$\partial_t K_e \propto -\bigtriangledown_{K_e} \Gamma \tag{2.107}$$

The dynamics in equation (2.107) allow for a continuous local adaptation of the vessel's state by consideration of its local flux, current conductance and metabolic parameters a, γ. In accordance with [56] one may rewrite equation (2.107) to have the final adaptation rules as,

$$\partial_t K_e = b_0 \left(\frac{f_e^2}{K_e^{\gamma+1}} - b_1\right) K_e \tag{2.108}$$

with positive coefficients b_0 , b_1.

Adaptation and topological transitions

Any adaptation of a given Kirchhoff network may simply be performed by initializing it with a source vector $\boldsymbol{s}$ and any conductance distribution $\boldsymbol{K}_0$, [1]. Then we integrate (2.108) using explicit numerical solvers, incorporating the following steps:

1. Compute the pressure and current landscape $\boldsymbol{p}_n$, $\boldsymbol{f}_n$ according to (2.78), (2.81)
2. Compute $\partial_t K_e$ according to (2.108)
3. Check if $\sum_e \partial_t K_{e,n}^2 \leq \delta \geq 0$, if true: stop the loop
4. Compute increment and next time step $\boldsymbol{K}_{n+1}$, using for example Runge-Kutta or LSODA [138]
5. Check for pruning events, if $K_{e,n+1} \leq K_{crit}$, edge e is removed from the graph
6. Return to first step

During each adaptation step, the flow landscape $\boldsymbol{f}_n$ is re-evaluated for the current $\boldsymbol{K}_n$ with equation (2.94) and all conductances updated according to equation (2.94). Integrating (2.94) one minimizes the cost Γ reaching a minimum which is asymptotically stable. Doing so, we may follow the dynamics of each single vessel and subsequent topological changes as part of this self-organization, see Figure 2.5.
Yet, for a complex system as such, all fixed points reached this way are in general only local minima of Γ depending on the initial conditions, such as $\boldsymbol{K}$ and $\boldsymbol{s}$. In order to reach a state to be a global minimum, one would most likely need to partially abandon deterministic methods and refer to stochastic or hybrid methods, such as basin hopping or annealing [61]. In this thesis only deterministic optimization is performed, while averaging over a multitude of systems initialized with randomized $\boldsymbol{K}_0$. Once reached, any stationary states may now be analyzed for their respective network topology, e.g. checking the number of independent cycles as discussed in section 2.1.1. This is useful

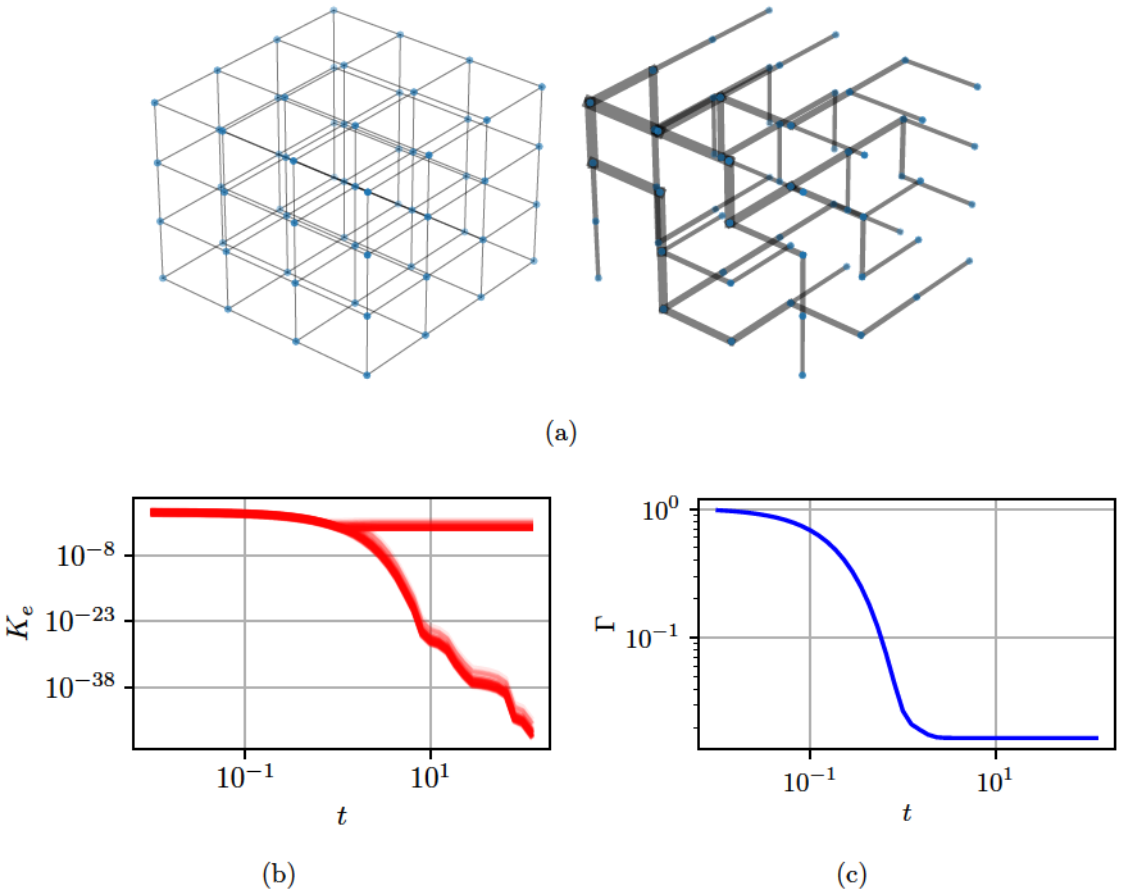

Figure 2.5: Network morphogenesis as a dynamical problem according to the Hu-Cai model [56]: A plexux is refined over time into its optimal form, adjusting the vessel conductivity according to a set level in the wall shear stress, see (a) , (b) . The algorithm is incorporating vessel pruning as $K_e \to 0$ reaching a local minimum of the metabolic cost function Γ in the process, see (c)

as it gives a first insight into the redundancy of transport networks and their capability to circumvent broken links.
Interestingly, stationary points of (2.94) are always spanning trees for $\gamma < 1$ [20], connecting sinks and sources by direct pathways, while cutting down any weakly perfused links, never leaving any loops intact. This topological transition is for all we know independent of the underlying plexus topology. Reticulation may be restored in this framework by considering $\gamma \geq 1$ [20], which will restore the initial plexus. Further, introducing noisy flow patterns by breaking links or varying the spatial correlations of sinks and sources [121, 61] may also restore reticulation. We will discuss these procedures in particular in chapter 3 and 4.
In general, the field has become a playground for testing adequate flow patterns and metabolic cost functions for their potential of topological complex stationary points [25, 81].

In this thesis, we formulate any metabolic cost function as

$$\Gamma = \sum_i \Gamma_i \tag{2.109}$$

where each Γ_i represents a cost and its constraints as in (2.94). For multi-component systems featuring several networks interacting with each other we write,

$$\Gamma = \sum_i \Gamma_i + \sum_{i,j} \Gamma_{ij} + \sum_{i,j,k} \Gamma_{ijk} + ... \tag{2.110}$$

although we will restrict ourselves to pairwise interactions in this thesis.

Chapter 3

Results

In this section, we present the results of the studies on fluctuation driven remodeling, network coupling, parameter estimation and metabolite transport in complex networks as indicated in section 1.3. In section 3.1, we revisit the fluctuation induced topological transitions and merge this framework with the intertwined network model, see section 3.2. Afterwards, we discuss the ramification for Murray's law based on these deductions and estimate model parameter distributions for real flow networks, see section 3.3.1. Note, that part of these results have been published recently in [65]. In the final section, 3.4, we discuss an extended metabolite uptake and adaptation model for topologically arbitrary flow networks.

3.1 On single network adaptation with fluctuating flow patterns

Ever since biological flow network models have been studied for their pruning behavior it has been clear that any algorithm proposed had to deal with the shunting phenomenon. It seemed particularly unclear how reticulated structures could be preserved in order to account for the self-organized emergence of capillary beds, complex leaf venation or slime mold networks. It was possible to account for gradually shifting complex reticulated hierarchies [61, 30, 56] by introducing noisy flow patterns, due to load variation and rerouting of flow in the vessel networks. In general, one may observe that capillary load rapidly changes due to blockage or short-term vaso-constriction and relaxation [24]. Here we refer to events where red blood cells clog capillaries or sphincters at supplying arterioles regulate the total inflow into the capillary bed. Furthermore, one finds the capillary bed to exchange liquid with the surrounding tissue due to spatial transmural pressure variations. That is not to say that elaborated metabolic demands can not generate reticulation [107], but we shall discuss these models and their key arguments later on.
In this section, we would like to discuss and analyze the concept of fluctuation driven topological transitions. In doing so, we will in particular discuss the model extensions made by Corson and Hu et al [30, 56], see chapter 1. In these studies it was proposed that the pressure landscape would continuously be disturbed between two adaptation steps, leaving the vessel to integrate the given stimuli for an effective update. At the same time, the capillaries themselves would not vary significantly in size.

First, we will discuss how the fluctuation model proposed in [56] can be derived from the ansatz in [30]. Subsequently we will test this model ansatz discussing the topological transition behavior, to verify claims made in [56] on parameter dependency and demonstrate explicit topological dependencies in the system. We shall later discuss a broken-link model in accordance to [61] in chapter 3.4.1.

3.1.1 Incorporating flow fluctuations: Noisy, uncorrelated sink patterns

Let us consider a Kirchhoff network as presented in chapter 2, with defined edge conductance $\boldsymbol{C}$ and Dirichlet boundary condition $\boldsymbol{s}$. Further, we follow here the self-organization approach as laid out in chapter 2, equation (2.108), as

$$\partial_t K_e = b_0 \left(\frac{f_e^2}{K_e^{\gamma+1}} - b_2 \right) K_e \tag{3.1}$$

We switch to a radial formulation for this ODE system, setting $\gamma = 0.5$, using $K_e = \frac{\pi r_e^4}{8\eta}$ and $f_e = \frac{K_e}{L_e}\Delta p_e$, resulting in

$$\partial_t r_e = c_0 \left(\Delta p_e^2 \left(\frac{r_e}{L_e} \right)^2 - c_2 \right) r_e \tag{3.2}$$

with coefficients $c_0 = \left(\frac{\eta}{2\pi}\right)^{1/2} b_0$ and $c_2 = \left(\frac{\pi}{8\eta}\right)^{-1/2} b_2$ as the resultant model parameters. Now we follow the narrative of the previous studies: Assuming a network is undergoing rapid changes in the sink distribution $\boldsymbol{s}$, any long-term adaptation simulated by an incremental r_e variation shall first integrate over these instantaneous realizations to arrive at an effective stimulus, see Figure 3.1a. For that, an ensemble average of all the instantaneous realizations of the wall-shear stress, dissipation etc. would be evaluated and used for adaptation. Here we do so by replacing the respective pressure term in equation (3.2) with the ensemble averages $\langle . \rangle$

$$\partial_t r_e = c_0 \left(\langle \Delta p_e^2 \rangle \left(\frac{r_e}{L_e} \right)^2 - c_2 \right) r_e \tag{3.3}$$

The fluctuations causing Δp to actually vary are formulated the following way: Consider an ensemble of $\boldsymbol{s}$-configurations in which there exists one source-node (here $v_{\text{source}} = 0$) and all other nodes are randomly initialized sinks with the following characteristics

$$\langle s_v \rangle = \mu_v \text{ with } v > 0 \tag{3.4}$$

$$\langle s_v s_w \rangle = \rho_{vw}\sigma_v\sigma_w + \mu_v\mu_w \text{ with } v, w > 0 \tag{3.5}$$

with sink mean value μ_v, standard variation σ_v and correlation coefficient ρ. Note, though the strength of individual sinks is varying, their distributions are uncorrelated to each other. To simplify the matter at hand, these sinks are to follow the same probability distribution, generating the same mean and standard deviations. Hence we

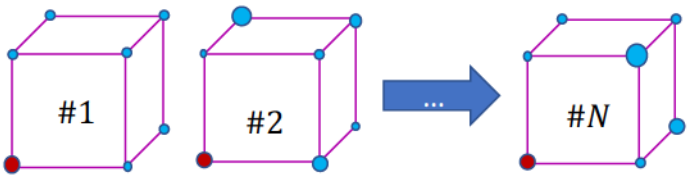

(a)

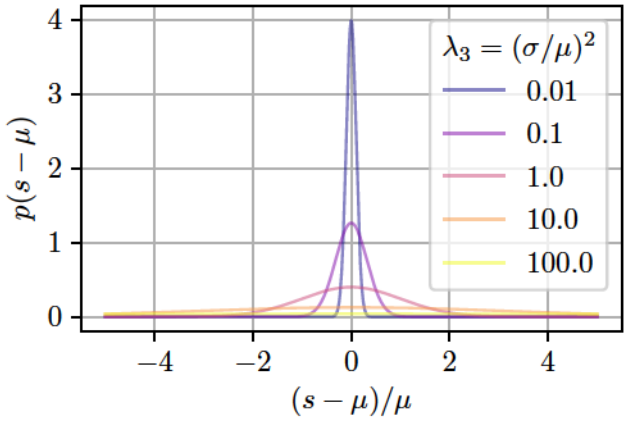

(b)

Figure 3.1: Flow fluctuations in Kirchhoff networks: (a) Schematic representation of the sink fluctuations (blue) for random realizations of the flow system, with a fixed root position (red). (b) Mean to standard deviation ratios in the squared format $\lambda_3 = \left(\frac{\sigma^2}{\mu^2}\right)$ for normal distributed sources.

set $\mu_v = \mu$, $\sigma_w = \sigma$, and $\rho_{vw} = \delta_{vw}$. From the Kirchhoff law (2.75) and Ohm's law (2.77) we know that the sum of all in- and outflows of the system vanishes, i.e. $\sum_v s_v = 0$ [36]. Further, we denote the number of nodes in the system as $|V| = n$. When considering the sink conditions as well as the source constraint one may write further moments as

$$\langle s_0 \rangle = -\left\langle \sum_{v>0} s_v \right\rangle = (1-n)\,\mu \tag{3.6}$$

$$\left\langle s_0^2 \right\rangle = \left\langle \sum_{v,w>0} s_v s_w \right\rangle = (n-1)\,\sigma^2 + (n-1)^2\,\mu^2 \tag{3.7}$$

$$\langle s_0 s_w \rangle = -\left\langle \sum_{v>0} s_v s_w \right\rangle = -(n-1)\,\mu^2 - \sigma^2 \tag{3.8}$$

It is assumed that the conductances (radii) are constant for each instantaneous realization. Hence one may calculate the squared-mean pressure Δp^2 by applying (2.83) and formulating an auxiliary conductance tensor $A^e_{vw} = C_e^{-1} \left[\boldsymbol{B} \cdot \boldsymbol{C}^{1/2}\right]^\dagger_{ev} \left[\boldsymbol{B} \cdot \boldsymbol{C}^{1/2}\right]^\dagger_{ew}$

as

$$\left\langle \Delta p_e^2 \right\rangle = \left\langle \left[\sum_v C_e^{-1/2} \left[\boldsymbol{B} \cdot \boldsymbol{C}^{1/2} \right]_{ev}^{\dagger} s_v \right]^2 \right\rangle = \sum_{vw} A_{vw}^e \left\langle s_v s_w \right\rangle \tag{3.9}$$

$$= A_{00}^e \left\langle s_0^2 \right\rangle + 2 \sum_{v>0} A_{v0}^e \left\langle s_0 s_v \right\rangle + \sum_{v,w>0} A_{vw}^e \left\langle s_v s_w \right\rangle \tag{3.10}$$

$$= A_{00}^e (n-1) \left[(n-1)\mu^2 + \sigma^2 \right] - 2 \sum_{v>0} A_{v0}^e \left[(n-1)\mu^2 + \sigma^2 \right] + \sum_{v,w>0} A_{vw}^e \left[\delta_{vw}\sigma^2 + \mu^2 \right] \tag{3.11}$$

$$= \sum_{v,w} A_{vw}^e \left\{ (n-1) \left[(n-1)\mu^2 + \sigma^2 \right] \delta_{0v}\delta_{0w} - \left[(n-1)\mu^2 + \sigma^2 \right] \left[(1-\delta_{0w})\delta_{0v} \right] \right.$$
$$\left. - \left[(n-1)\mu^2 + \sigma^2 \right] \left[(1-\delta_{0v})\delta_{0w} \right] + \left[\delta_{vw}\sigma^2 + \mu^2 \right] (1-\delta_{0v})(1-\delta_{0w}) \right\} \tag{3.12}$$

Ordering the terms for μ and σ respectively, we get auxiliary coefficient matrices $\boldsymbol{U}$ and $\boldsymbol{V}$,

$$\left\langle \Delta p_e^2 \right\rangle = \mu^2 \sum_{v,w} A_{vw}^e U_{vw} + \sigma^2 \sum_{v,w} A_{vw}^e V_{vw} \tag{3.13}$$

$$\text{with } U_{vw} = \left[1 + \delta_{0v}\delta_{0w} n^2 - n \left(\delta_{0v} + \delta_{0w} \right) \right] \tag{3.14}$$

$$\text{and } V_{vw} = \left[\delta_{vw} + (n + 1 + \delta_{vw}) \delta_{0v}\delta_{0w} - (1 + \delta_{vw}) \left(\delta_{0v} + \delta_{0w} \right) \right] \tag{3.15}$$

We may subsequently calculate the average squared pressure as

$$\left\langle \Delta p_e^2 \right\rangle = \mu^2 \phi_e + \sigma^2 \delta\phi_e \tag{3.16}$$

where the squared pressure functions are computed as

$$\phi_e = \sum_{v,w} A_{vw}^e U_{vw} \tag{3.17}$$

$$\delta\phi_e = \sum_{v,w} A_{vw}^e V_{vw} \tag{3.18}$$

The first term ϕ_e reflects the squared pressure in the case of a constant source-sink landscape, in the absence of any variance σ^2. Further, the term $\delta\phi_e$ describes the pressure perturbation caused by fluctuations with variation σ^2 analogous to the Hu–Cai model [56]. It may be useful to understand the general impact of these terms and why a topological transition is inevitable for any network using this ansatz. Rewriting equation (3.13) in terms of $\left(\frac{\sigma^2}{\mu^2}\right)$, we see that

$$\left\langle \Delta p_e^2 \right\rangle / \mu^2 = \sum_{v,w>0} \left(A_{00}^e - A_{0w}^e - A_{v0}^e + A_{vw}^e \right) + \frac{\sigma^2}{\mu^2} \sum_{v>0} \left(A_{00}^e - 2A_{0v}^e + A_{vv}^e \right) \tag{3.19}$$

We may further rewrite this as

$$A_{vw}^e = \left(C_e^{-1/2} \left[\boldsymbol{B} \cdot \boldsymbol{C}^{1/2} \right]_{ev}^{\dagger} \right) \left(C_e^{-1/2} \left[\boldsymbol{B} \cdot \boldsymbol{C}^{1/2} \right]_{ew}^{\dagger} \right) = \alpha_v^e \alpha_w^e \tag{3.20}$$

$$\Rightarrow \left\langle \Delta p_e^2 \right\rangle / \mu^2 = \sum_{v,w>0} \left(\alpha_0^e - \alpha_v^e \right) \left(\alpha_0^e - \alpha_w^e \right) + \left(\frac{\sigma^2}{\mu^2} \right) \sum_{v>0} \left(\alpha_0^e - \alpha_v^e \right)^2 \tag{3.21}$$

$$= \left\langle \Delta p_e \right\rangle^2 / \mu^2 + \left(\frac{\sigma^2}{\mu^2} \right) \sum_{v>0} \left(\alpha_0^e - \alpha_v^e \right)^2 \tag{3.22}$$

demonstrating the impact of the fluctuations in the form of $\left(\frac{\sigma^2}{\mu^2}\right)$ quite directly: All the elements of the $\sum_{v>0}\left(\alpha_0^e-\alpha_v^e\right)^2$ are positive semi-definite. Any uncorrelated fluctuations of this kind will increase the positive feedback provided by the squared pressure term (3.3). It is therefore inevitable that large enough ratios $\left(\frac{\sigma^2}{\mu^2}\right)$ will generate reticulated structures by stabilizing otherwise unnecessary links. We will subsequently restrict ourselves to an analysis of equivalent probability distributions characterized by the ratios $\left(\frac{\sigma^2}{\mu^2}\right)$, see Figure 3.1b. Note that, even though the distribution's mean might have a distinct sign, seemingly defining a source or sink, one may increasingly result in identity changes of the boundary for $\left(\frac{\sigma^2}{\mu^2}\right)>0$, when sampling over non-restricted distributions. For a matter of fact, this is a useful feature when it comes to modeling fluctuation fluid exchange between capillaries and the surrounding tissue. Respectively, one returns to the deterministically correlated state for $\left(\frac{\sigma^2}{\mu^2}\right)\to 0$ leaving us with the identity $\langle\Delta p_e^2\rangle=\langle\Delta p_e\rangle^2=\Delta p_e^2$. This form of correlation based feedback was recently demonstrated in an alternative way by Ronellenfitsch et al [121] : In their study, a spatially defined sub-population of vertices (inside a given region with diameter d around a root vertex) has correlated sinks and sources. By increasing the diameter d more and more sinks are deterministically correlated to each other, sub-sequentially breaking down any redundancy in the network previously generated. In general, one may introduce arbitrary sink configurations. For arbitrary sinks, thanks to the linearity of the problem, one may calculate any effective pressure configuration as

$$\begin{aligned}\langle\Delta p_e^2\rangle&=\left[\boldsymbol{D}\cdot\langle\boldsymbol{s}\otimes\boldsymbol{s}\rangle\cdot\boldsymbol{D}^T\right]_{ee}\\ \text{with }\boldsymbol{D}&=\boldsymbol{B}^T\left(\boldsymbol{B}\boldsymbol{C}\boldsymbol{B}^T\right)^\dagger.\end{aligned}\tag{3.23}$$

This allows us to handle averages more quickly using just one arithmetic mean over a set of sink-source realizations $\boldsymbol{s}_x$ as

$$\langle\boldsymbol{s}\otimes\boldsymbol{s}\rangle=\frac{1}{N}\sum_x\boldsymbol{s}_x\otimes\boldsymbol{s}_x\tag{3.24}$$

In [121] it was discussed to compute (3.24) utilizing an eigenvalue analysis. The ansatz (3.5) may be readily extended to include additional sources, which act as clones of the very first one, i.e. we will have $s_p=s_q$ using the indices p,q for sources and m,n for sinks. Then the conditions (3.6), (3.7) and (3.8) will become for a sources and b sinks (with $a+b=n$)

$$\left\langle\sum_p s_p\right\rangle=-\left\langle\sum_u s_u\right\rangle=-b\mu\to\langle s_p\rangle=-\frac{b}{a}\mu\tag{3.25}$$

$$\langle s_p s_q\rangle=\frac{1}{a^2}\left\langle\sum_{u,v}s_u s_v\right\rangle=\frac{1}{a^2}\left(b\sigma^2+b^2\mu^2\right)\tag{3.26}$$

$$\langle s_p s_u\rangle=-\frac{1}{a}\left\langle\sum_v s_v s_u\right\rangle=-\frac{1}{a}\left(b\mu^2-\sigma^2\right)\tag{3.27}$$

Hence we may calculate the mean squared pressure and its coefficient matrices respectively as

$$\langle \Delta p_e^2 \rangle = \sum_{v,w} A^e_{vw} \mu^2 \left[\frac{b^2}{a^2} \sum_{p,q} \delta_{pv}\delta_{qw} - \frac{b}{a} \sum_{p,m} (\delta_{pv}\delta_{mw} + \delta_{mv}\delta_{pw}) + \sum_{m,n} \delta_{mv}\delta_{nw} \right] \tag{3.28}$$
$$+ \sum_{v,w} A^e_{vw} \sigma^2 \left[\frac{b}{a^2} \sum_{p,q} \delta_{pv}\delta_{qw} - \frac{1}{a} \sum_{p,m} (\delta_{pv}\delta_{mw} + \delta_{mv}\delta_{pw}) + \sum_{m,n} \delta_{mv}\delta_{nw}\delta_{mn} \right]$$

This formalism will be applied in section 3.3.1 for parameter estimation in real network data sets. In the next section we will study in detail the implications of (μ^2, σ^2) variations and resulting topological transitions.

3.1.2 Fluctuation induced nullity transitions

In this section we numerically evaluate (3.3) in order to study topological transitions during network morphogenesis, following the general update algorithm in section 2.2.2. To do so, we derive a non-dimensional form of (3.2), by setting

$$L_e^* = L_e/L \tag{3.29}$$
$$r_e* = r_e/L \tag{3.30}$$
$$C_e^* = C_e \frac{\eta}{L^3} \tag{3.31}$$
$$s_v^* = s_v/\mu \tag{3.32}$$
$$t^* = t\frac{\mu}{L^3} \tag{3.33}$$

We set the system's characteristic time scale as $\tau = \frac{L^3}{\mu}$. Further we incorporate the flow fluctuations (3.16) discussed in the previous section with an effective fluctuation strength $\lambda_3 = \frac{\sigma^2}{\mu^2}$ and therfore rewite (3.3) in total as

$$\partial_{t^*} r_e^* = \lambda_0 \left[\left(\phi_{e_i}^* + \lambda_3^i \delta\phi_e^* \right) \left(\frac{r_e}{L_e} \right)^2 - \lambda_2 \right] r_e^* \tag{3.34}$$

Subsequently we have the dynamical system reduced to three non-dimensional parameters. The first one, $\lambda_0 = \left(\frac{\tau\mu^2\eta^2}{L^6} \right) c_0$, is the effective growth rate. Second, we have $\lambda_2 = \left(\frac{L^6}{\eta^2\mu^2} \right) c_2$ for the volume penalty (or anticipated wall-shear stress). The last parameter, λ_3, scales the strength of pressure perturbations, which effectively impose an increase in the wall shear stress term in equation (3.34). In this section, we would like to demonstrate two particular phenomena: First, to confirm the robustness of the model for a plexus represented by non-planar graphs, similar to [51]. Second, to test the independence of the fluctuation-induced nullity transition from the volume penalty λ_2, as claimed by [56]. To do so, we calculate the adaptation with a single corner source node (sinks otherwise) for a systematic scan of λ_2 and λ_3 (see Figure 3.4).
In order to quantify any potential topological transition of stationary states of (3.34)

we will use the relative nullity as order parameter

$$\varrho = \frac{m - n + 1}{z_0} \tag{3.35}$$

where $m - n + 1$ is the number of independent cycles in the network with m edges and n vertices, as discussed in chapter 1. The number of cycles, z_0, in the plexus from which we start will be used for reference, as to measure the relative loss of redundancy. Further, we will track the relative dissipation, D, of the system and its relative cross section area, S, as

$$D = \sum_e \left\langle f_e^{*2} \right\rangle / C_e^* \tag{3.36}$$

$$S = \sum_e r_e^{*2} \tag{3.37}$$

We initialize any plexus with a randomly chosen landscape, C_e^*, and therefore with a random distribution of r_e^*. Moreover, we intend to consider only highly symmetric networks for this study, i.e. considering only the case $L_e = L$. Any plexus tested here will be based on a three-dimensional lattice, namely the cubic or diamond lattices as well as Laves graphs, see Figure 3.2. We choose these lattices in particular as they represent well-known periodically expandable structures with distinct degree distributions and girth (topological cycle length) characteristics. Will shall discuss the impact of the chosen lattice topology on the order parameter ϱ in detail in section 3.1.3. When

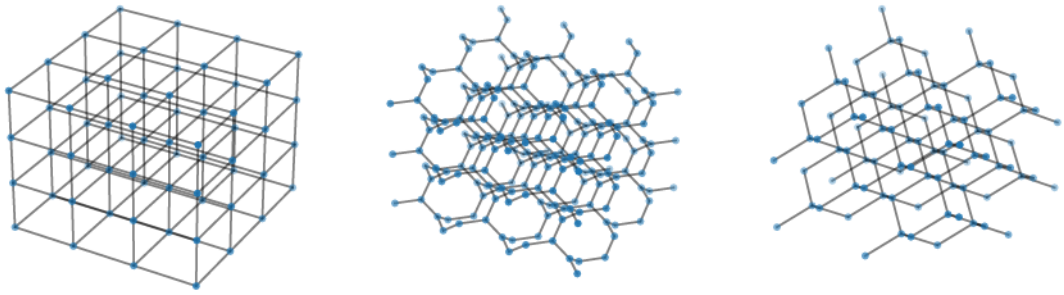

(a) (b) (c)

Figure 3.2: Three dimensional plexi as test grounds for fluctuation induced nullity transition: (a) Cubic lattice, with degree $d_{max} = 6$ and girth $l_c = 4$ (b) Laves graph, with degree $d_{max} = 3$ and girth $l_c = 10$ (c) Diamond lattice, with $d_{max} = 4$ and girth $l_c = 6$.

integrating (3.34) we observe for any graph type the transition from tree-like configurations for fluctuations $\lambda_3 \leq 1$ toward states exhibiting fluctuation induced loops for large λ_3. This transition, as well as its characteristic vessel dynamics is explicitly displayed for a cubic lattice in Figure 3.3. All data presented in this section was acquired for cubic lattices. The results for Laves graphs and diamond lattices behave the same qualitatively. Next, we turn toward a systematic scan of the model parameters λ_2 and λ_3, see Figure 3.4. In Figure 3.4a we display the color-mapped nullity (3.35) for the

stationary states of the system. It becomes clear that there is no impact of λ_2 on the nullity. Only an increase in λ_3 results in an increase in the nullity, as indicated in earlier studies [56]. Note, however, that the final vessel diameter as well as the time scale for relaxation into a stable stationary state does depend primarily on the parameter λ_2. In

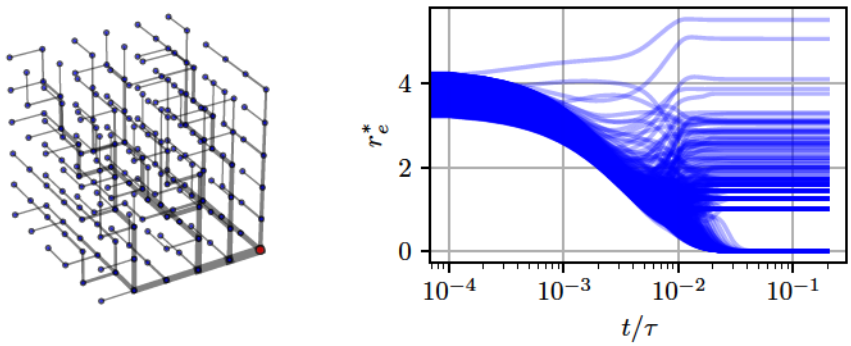

(a)

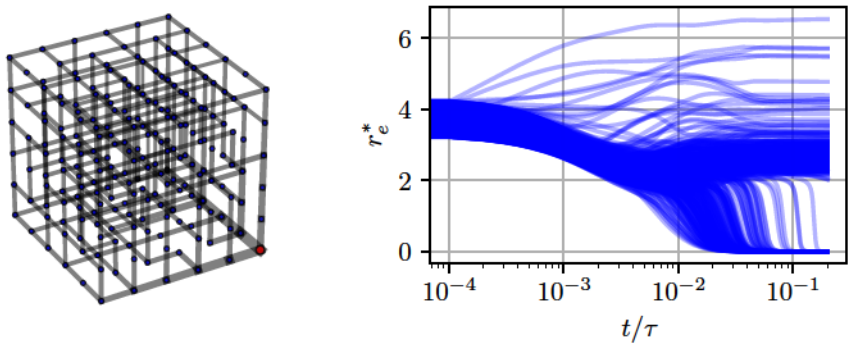

(b)

Figure 3.3: Adaptation dynamics and pruned network skeletons. The edge thickness is representative of the relative tube radius. Sinks are marked as blue dots, the source as a large red circle: (a) Spanning tree configuration for $\lambda_2 = \lambda_3 = 1$. (b) Saturation of fluctuation induced loops for $\lambda_2 = 1$ and $\lambda_3 = 10^3$.

Figure 3.4b we display horizontal cuts through the previous nullity diagram, displaying the λ_3-dependency of ϱ explicitly. For all λ_2 variations we find this transition to start for $\lambda_3 \geq 1$ progressing logarithmically until a saturation level is reached. We find that the logarithmic transition is approximately described by

$$\varrho\left(\lambda_3\right) = \kappa log_{10}\left(\lambda_3 - \lambda_c\right) + \varrho_0 \tag{3.38}$$

for any $\varrho > 0$. Thereby we define the critical fluctuation, λ_c, as the onset point for which $\varrho > 0$ is fulfilled. The parameters κ, ρ_0 may be easily obtained by interpolation of the curves in Figure 3.4b. Note here that the saturation level as well as the coefficients κ, ρ_0 are indeed dependent on the network's topology and overall size. We discuss different scenarios pertaining to that matter in section 3.1.3. Though the topological structure of these networks is indistinguishable in terms of nullity for different levels λ_2, we find significant differences in the network's geometric and hydrodynamic features, which

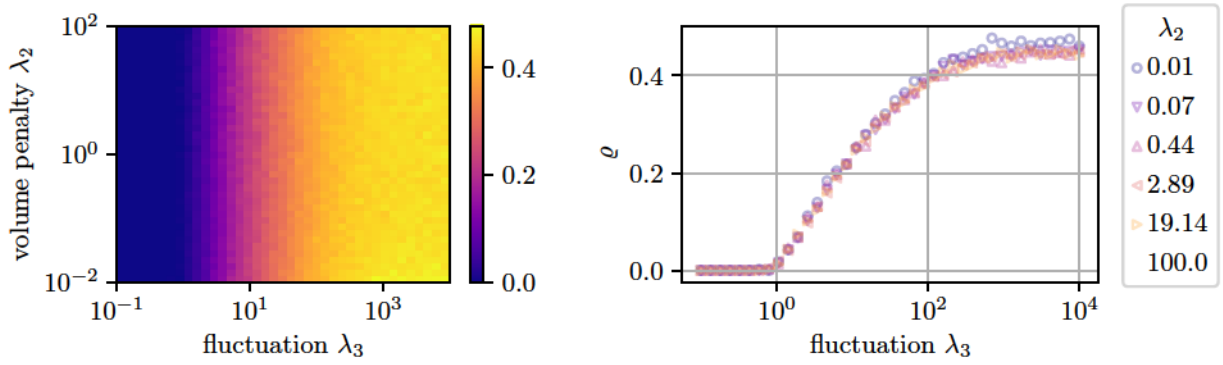

(a) (b)

Figure 3.4: Nullity ϱ state diagram and transition trajectories indicate fluctuation, λ_3, induced nullity transition to be independent of volume penalty, λ_2, as:
(a) + (b) Uncoupled adapting networks display continuous, logarithmic λ_2-independent nullity ϱ transitions in an uncoupled system.

were directly incorporated in the metabolic cost function (2.95). In particular, we see changes in the overall dissipation and cross section area of the system's stationary states, see Figure 3.5. In Figure 3.5a, we display the network,s overall cross-section area, S, as defined in equation (3.37). While an increase in volume penalty λ_2 reduces S we find fluctuations λ_3 to increase S significantly, for $\lambda_3 \gg \lambda_2$. Highly reticulated networks only have an increased cross section area when volume penalty is low. On the other hand, we display the overall dissipation, D, in Figure 3.5b. One may easily see that overall dissipation increases significantly for combined increases in λ_2 and λ_3. Therefore it appears that from a physiological standpoint, one would like to avoid this particular regime of $\lambda_2, \lambda_3 \gg 1$ for capillary beds. Not only is it unfavorable to have such an energetically inefficient network, but this regime also corresponds to the case of low overall cross section area. In our framework, with fixed channel length L, the square-root of the metric S is indicative for the overall surface area of the network. Such a surface-minimizing regime would therefore likely effect the primary function of real networks such as capillaries: the overall metabolite supply of the tissue. We shall discuss models regarding this particular impairment of metabolite filtration in section 3.4.1. In the next section, we would like to point out finite size effects of the model framework, in particular on quantitative changes in the topological transition behavior

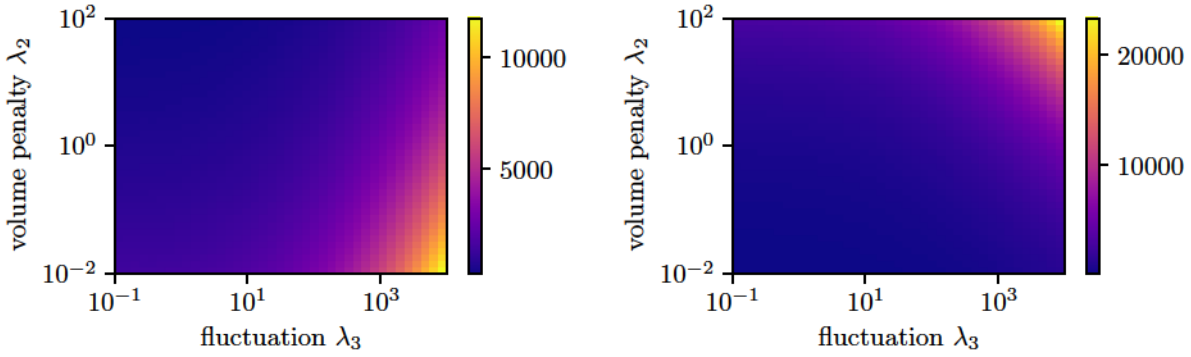

(a) Power dissipation D

(b) Cross section area S

Figure 3.5: Network geometric and hydrodynamic features: (a) Overall vessel cross section area S, as defined in equation (3.37). (b) Overall network dissipation D, as defined in equation (3.36).

3.1.3 Finite size effects and topological saturation limits

In the previous section, we numerically evaluated the fluctuation induced nullity transition in alignment with the Hu-Cai model [56]. Whilst the algorithm generally seems robust against a change of the general degree sequences of the plexus, we find detailed quantitative differences in the nullity transition curves (3.38). Subsequently, we rewrite the transition (3.38) to incorporate these network characteristics as

$$\varrho_{n,m}(\lambda_3) = \kappa(n,m)\log_{10}(\lambda_3 - \lambda_{c,n,m}) + \varrho_0(n,m) \tag{3.39}$$

To explore this phenomenon we first turn toward the explicitly acting stimuli of the model. We shall analyze the size dependencies of this ansatz, by looking into the positive feedback terms in equation (3.34). Adding up $\boldsymbol{U}$ and $\boldsymbol{V}$ and rearranging the terms around $\lambda_3 = \frac{\mu^2}{\sigma^2}$, we rewrite $\langle \Delta p_e^2 \rangle$ as

$$\frac{\langle \Delta p_e^2 \rangle}{\mu^2} = \sum_{vw} A^e_{vw} X_{vw}(\lambda_3) \tag{3.40}$$

$$\begin{aligned} \text{with } X_{vw} &= (1 + \delta_{0v}\delta_{0w} - \delta_{0v} - \delta_{0w}) + \lambda_3(\delta_{vw} - \delta_{0v}\delta_{0w}) \\ &\quad + (n-1)((n+1)\delta_{0v}\delta_{0w} - \delta_{0v} - \delta_{0w})\left[1 + \frac{\lambda_3}{n-1}\right] \end{aligned} \tag{3.41}$$

Introducing further abbreviations, to improve readability, we rewrite (3.40) as

$$\begin{aligned} X_{vw} &= X_{0,vw} + X_{1,vw}\lambda_3 + X_{2,vw}h(\lambda_3, n) \\ \text{with } X_{0,vw} &= (1 + \delta_{0v}\delta_{0w} - \delta_{0v} - \delta_{0w}) \\ X_{1,vw} &= (\delta_{vw} - \delta_{0v}\delta_{0w}) \\ X_{2,vw} &= (n-1)[(n+1)\delta_{0v}\delta_{0w} - \delta_{0v} - \delta_{0w}] \\ h(\lambda_3, n) &= 1 + \frac{\lambda_3}{n-1} \end{aligned} \tag{3.42}$$

Hence we have $h(\lambda_3, n) \longrightarrow 1$, for large networks with small fluctuations $\lambda_3 \ll n$, so the solution in (3.42) becomes

$$X_{vw} \approx (X_{0,vw} + X_{2,vw}) + X_{1,vw}\lambda_3 \tag{3.43}$$

Subsequently, only the size-independent elements $X_{1,vw}$ impact the fluctuations of the pressure term, while $(X_{0,vw} + X_{2,vw})$ corresponds to the constant unperturbed solution of the system, involving the size dependency of the system quadratically. This is not surprising, as we scale the numbers of sinks with $\langle s_v \rangle = \mu$ with the number of nodes. This result indicates that large networks are less likely to be affected by this type of fluctuations.
Next, we simulated the nullity transition for different sizes of cubic and diamond lattices and Laves graphs, see Figure 3.6. With network size we refer here to vertex and edge numbers. The intention here is to display the effect of size changes for each network type as well as type-dependent differences of the nullity saturation level. Hence, one will ultimately change the overall complexity of ϱ transitions by varying the impact of each individual edge removal, which might explain the differences in transition steepness and saturation levels as a gauging artifact. Why does the algorithm not reproduce the full plexus for any arbitrary graph topology though? Generally one finds

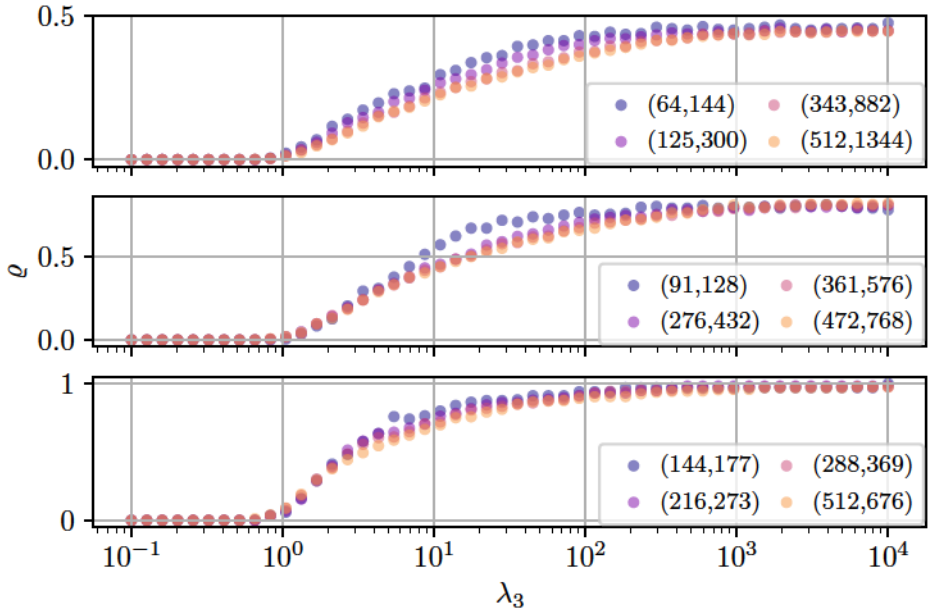

Figure 3.6: Size and topology dependency of nullity transitions in three-dimensional (periodic) graphs. The respective number of nodes and edges is indicated in the legend as tuple (n, m): *Top:* Cubic lattice, *Middle:* Diamond lattice, *Bottom:* Laves graph.

the fluctuation induced nullity transition saturating for $\lambda_3 \approx 10^4$ in cubic and diamond lattices at $\varrho < 1$. As indicated in Figure 3.6, we find this to be the case for any network size, and the particular saturation level appears to be independent of plexus size. No full recovery of the plexus seems possible, even for $\lambda_3 \gg 10^4$. On the other hand, Laves graphs display full plexus recovery behavior. Unfortunately, we do not yet know the cause of this particular pruning phenomenon, despite the presented arguments.

Nevertheless, these findings may lead to another conclusion all together: Graphs representing three-dimensional embedded plexi with junctions of degree $d > 3$ consist of inherently redundant edges when considering fluctuation driven pruning processes. This implies that the initial build of any such network is wasteful from the very start as many of the vessels deployed will be removed eventually, regardless the flow.

3.2 On geometric coupling between intertwined networks

Though network morphogenesis has been extensively studied for individual networks, it becomes clear that these models lack the level of complexity necessary to describe development in an environmental context. We find such a context to be crucial to consider when dealing with entangled vessel systems which are common in mammalian organs, as pointed out in chapter 1. In this study, we propose a toy model for two intertwined networks, such as those in the liver, pancreas or kidneys. This model framework may even be extended to one network being embedded in a rigid scaffold, as in the case of bone marrow. These vessel networks are entangled to an extent where no system can be removed without breaking the other, topologically and functionally, see Figure 1.1b. In particular we shall consider here a model that describes the pruning behavior of intertwined vessel networks on the basis of simple geometric relations, such as local neighborhoods and Euclidean distances. We shall evaluate the impact of additional negative or positive growth feedback as compared to fluctuation driven pruning processes, which were described in the previous section.

3.2.1 Power law model of interacting multilayer networks

As indicated in the previous sections, we focus on radial adaptation of rudimentary vessel networks. For this study we will do so for a multilayer system consisting of two non-overlapping Kirchhoff networks. The representative subgraphs $G_1(V_1, E_1)$, $G_2(V_2, E_2)$ shall be intertwined lattices, such as found for the network skeletons of triply periodic minimal surfaces, see Figure 1.6, or other complex net formations [13]. These graphs do not have any vertices or edges in common, $V_1 \cap V_2 = \varnothing$ and $E_1 \cap E_2 = \varnothing$, but are coupled by locally defined interactions between them. This local interaction is defined pair-wise between two vessels of different graphs, positioned in a common neighborhood. Subsequently, for this problem, we shall define a characteristic metabolic cost function Γ in accordance with monolayer systems, taking into account the local neighborhood of vessels in either system. We define each neighborhood as the set of nearest adjacent vessels of one network, for any given vessel of the other structure, as indicated in Figure 3.7. Focusing once again on symmetric lattices as plexi, we find this definition easily allowing for trivial distance criteria between two adjacent links e_1 and e_2 (shortest Euclidean distance between their representing lines). Hence for each type of intertwined networks we have a characteristic length scale set by the lattice constant, L, and a characteristic number of adjacent vessels. Furthermore, approximating vessels yet again to be cylindrical with radius r_e, we define the vessel surface distance as

$$\Delta r_{e_1 e_2} = L - (r_{e_1} + r_{e_2}) \tag{3.44}$$

where L as the lattice constant equals the distance in case of simultaneously vanishing radii. In this toy model we still consider the two respective networks to underlay basic wall shear stress based pruning, as discussed in chapter 2. We use the cost ansatz

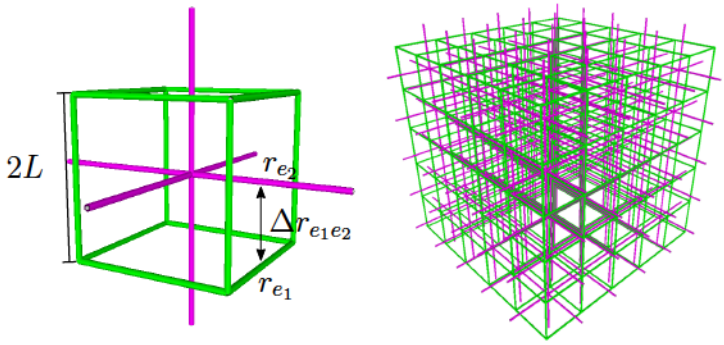

(a) (b)

Figure 3.7: Modeling biological intertwined structures: (a) Cubic unit cell and indication of spatial constraint for tube surfaces. (b) Complementary cubic lattices as a model for a space filling intertwined networks.

in (2.110) in combination with (2.95) and $K_e = \frac{\pi R_e^4}{8\eta}$ and $\gamma = 0.5$, as

$$\Gamma = \Gamma_{12} + \sum_{i\in\{1,2\}} \Gamma_i \tag{3.45}$$

$$\text{with } \Gamma_i = a_{0,i} \sum_{e_i} L_{e_i} \left(\frac{f_{e_i}^2}{K_{e_i}} + a_{2,i} K_{e_i}^{1/2} \right) \tag{3.46}$$

where $a_{0,i} \geq 0$ and $a_{2,i} \geq 0$ are proportionality coefficients for either network. From here on we use the indices $i \in \{1, 2\}$ for the two networks. Each network would independently become dissipation minimized, constrained by its overall volume, as discussed in chapter 2, if we performed a minimization of the cost (3.45) without considering any interactions, represented by the term Γ_{12}. We shall discuss the interaction term Γ_{12} in more detail in the next section, as we have not specified the nature of any distance-based interaction.

Let's assume here (without loss of generality, but for the sake of distinct terminology) to be modeling a liver lobule with its sinusoids and bile canaliculi. To model such a system of blood vessels entangled with a secondary, secreting vessel network, we require that the respective tube surfaces must not fuse or get in contact with one another, i.e. $\Delta r_{e_1e_2} \geq 0$. Subsequently, as a first level approximation, we construct the interaction term Γ_{12} for the combined system as a power law of the vessel surface distance $\Delta r_{e_1e_2}$

$$\Gamma_{12} = \frac{a_1}{2} \sum_{e_1e_2} F_{e_1e_2} \Delta r_{e_1e_2}^{\varepsilon} \tag{3.47}$$

$$\text{with } F_{e_1e_2} = \begin{cases} 1 & \text{if edges } e_1 \text{ and } e_2 \text{ affiliated} \\ 0 & \text{else} \end{cases} \tag{3.48}$$

with positive coefficient $a_1 \geq 0$ and exponent $\varepsilon \in \mathbb{R}$ allowing us to switch between a repulsive or attractive behavior of the interaction, see section 3.2.2. A repulsive interaction is representing either the competition for space or a mechanism to decrease mutual contact by increased pruning. An attractive interaction may be presented by a tissue-facilitated proliferation signal, resulting in a positive feedback to increase the

number of adjacent vessels. We have therefore arrived at the total cost function for the system:

$$\begin{aligned}\Gamma =& \frac{a_1}{2}\sum_{e_1e_2} F_{e_1e_2}\Delta r_{e_1e_2}^{\varepsilon} \\ &+ a_{0,1}\sum_{e_1} L_{e_1}\left(\frac{f_{e_1}^2}{K_{e_1}} + a_{2,1}K_{e_1}^{1/2}\right) + a_{0,2}\sum_{e_2} L_{e_2}\left(\frac{f_{e_2}^2}{K_{e_2}} + a_{2,2}K_{e_2}^{1/2}\right)\end{aligned} \tag{3.49}$$

which we may now use to derive a self-organizing dynamical system in the next section.

3.2.2 Adaptation dynamics of intertwined vessel systems

In this section, we discuss the dynamical systems in detail by a applying a gradient descent approach on the basis of the cost function shown in equation (3.49). As discussed in chapter 2 and section 3.1.2 we do so by calculating the radial dynamics as

$$\partial_t r_{e_1} \propto -\nabla_{r_{e_1}}(\Gamma_1 + \Gamma_{12}) \tag{3.50}$$

$$\partial_t r_{e_2} \propto -\nabla_{r_{e_2}}(\Gamma_2 + \Gamma_{12}) \tag{3.51}$$

Now, using the definitions of Γ_i, Γ_{ij} of the previous section as well as the derivation results of section 2.2.2 we may readily calculate the dynamics. To improve readability we rescale the proportionality factors as $b_{0,i} = \frac{\pi}{2\eta_i}a_{0,i}$ and $b_{2,i} = \sqrt{\frac{2\eta_i}{\pi}}a_{2,i}$. Considering all these factors we obtain the equations of motion as

$$\partial_t r_{e_1} \propto \left(\left(\frac{\Delta p_{e_1} r_{e_1}}{L_{e_1}}\right)^2 - b_{2,1}\right) r_{e_1} + \left(\frac{a_1\varepsilon}{b_{0,1}L_{e_1}}\right)\sum_{e_2} F_{e_1e_2}\Delta r_{e_1e_2}^{\varepsilon-1} \tag{3.52}$$

$$\partial_t r_{e_2} \propto \left(\left(\frac{\Delta p_{e_2} r_{e_2}}{L_{e_2}}\right)^2 - b_{2,2}\right) r_{e_2} + \left(\frac{a_1\varepsilon}{b_{0,2}L_{e_2}}\right)\sum_{e_1} F_{e_1e_2}\Delta r_{e_1e_2}^{\varepsilon-1} \tag{3.53}$$

The interaction terms react to the relative vessel distance Δr and impose a feedback term connected to the local neighborhood of each vessel which can be either positive (attractive coupling) or negative (repulsive coupling) depending on the choice of ε. Furthermore, we shall scale the impact of this interaction in terms of the wall-shear stress driven adaptation process in either network, namely $\left(\frac{a_1\varepsilon}{b_{0,i}L_{e_i}}\right)$.
To perform a numerical evaluation of ODE system (3.52),(3.52), we define the unit system as in the previous section 3.1.2: the radii and edge lengths in units of the grid distance $r_{e_i} = Lr_{e_i}^*$, the nodal in- and outflow $s_{v_i} = \mu_i s_{v_i}^*$, the conductance $C_{e_i} = \eta_i^{-1}L^3 C_{e_i}^*$ hence pressure $\Delta p_{e_i} = \frac{\mu_i\eta_i}{L^3}\Delta p_{e_i}^*$ and the networks' surface distance $\Delta r_{e_1e_2'} = L\Delta r_{e_1e_2}^*$. We define the time scale via the volume flow rates in the primal network as $t = \frac{L^3}{\mu_1}t^*$. Given positive proportionality constants $\chi_i \geq 0$ in the equations (3.52), (3.53), we define the effective temporal response parameters in either network as $\lambda_0^i = \frac{\chi_i L^3}{\mu_1}\left(\frac{\mu_i\eta_i}{L^3}\right)^2$. We define the effective volume penalties as $\lambda_2^i = 4b_{i,2}\left(\frac{L^3}{\mu_i\eta_i}\right)^2$.

Further, we introduce the effective network coupling coefficients $\lambda_1^i = \frac{a_1|\varepsilon|L^{\varepsilon-3}}{b_{i,0}} \left(\frac{\mu_i \eta_i}{L^3}\right)^{-2}$ and an effective coupling function $g_{e_i}^*$ term as

$$g_{e_1}^* = \frac{sgn(\varepsilon)}{L_{e_1}^*} \sum_{e_2} F_{e_1 e_2} \Delta r_{e_1 e_2}^{*\varepsilon-1} \tag{3.54}$$

$$g_{e_2}^* = \frac{sgn(\varepsilon)}{L_{e_2}^*} \sum_{e_1} F_{e_1 e_2} \Delta r_{e_1 e_2}^{*\varepsilon-1} \tag{3.55}$$

using the sign function $sgn(\varepsilon)$. For simplification, we consider the special case of $L_{e_i} = 2L$ for all vessels in either network.
All considered, we arrive at the dimensionless form of the dynamical equations (3.52), (3.53) for each network:

$$\partial_{t^*} r_{e_i}^* = \lambda_0^i \left(\Delta p_{e_i}^{*2} r_{e_i}^{*3} - \lambda_2^i r_{e_i}^* + \lambda_1^i g_{e_i}^*\right) \tag{3.56}$$

As previously mentioned, we have the coupling term $g_{e_i}^*$ change qualitative behavior of the interaction with variation of the exponent ε. In this thesis, we shall discuss the special cases of an attractive coupling $\varepsilon > 1$ and a repulsive coupling $\varepsilon < 0$, see Figure 3.8. Note that for $\varepsilon = 1$ we will obtain $g_{e_i}^*$ corresponding to a positive constant background stimulus, as proposed in earlier studies [120]. Quite in contrast to this, we intend to consider the development of a vessel surrounded by dynamically sizable vessels, with previously mentioned ε considerations. Unfortunately, one has the case $0 < \varepsilon < 1$ resulting in a diverging attraction for nearby vessels, whereas it is negligible for $\Delta r_{e_1 e_2}^* \longrightarrow 1$. These numerically unfavorable cases of $0 < \varepsilon < 1$ as well as the trivial case $\varepsilon = 1$ will not be considered hereafter. It should be noted that this model ansatz

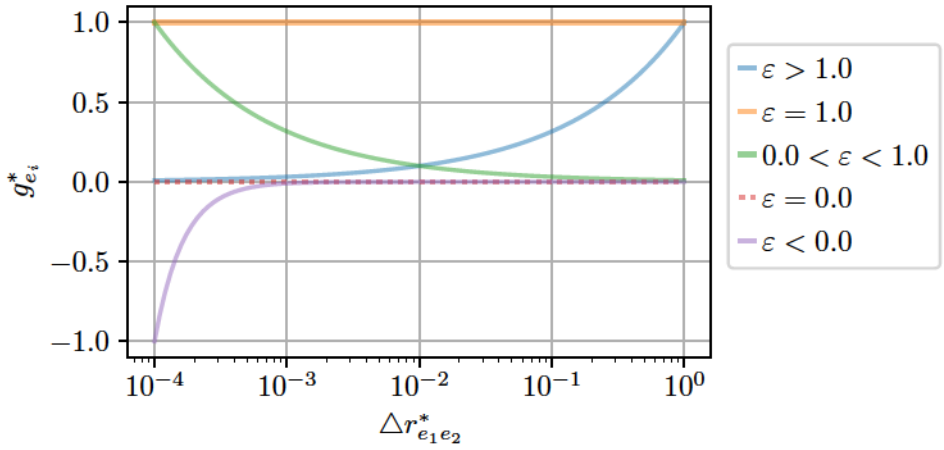

Figure 3.8: Qualitative behavior of the coupling term $g_{e_i}^*$ as defined in equations (3.54),(3.55): The interaction poses a positive growth feedback for $g_{e_i}^* > 0$ and a negative feedback for $g_{e_i}^* < 0$. Function values of $g_{e_i}^*$ are presented here in dependence of the distance of a single arbitrary vessel pairing. Curves are normalized to facilitate comparison.

could be used in the same manner to introduce distance-dependent self-interactions Γ_{ii} for vessels of the same network. Yet, a critical difference is the potential of congenial vessel membranes to merge upon contact. In real biological organisms, this actually

presents an alternative vascular pruning mechanism, in the endothelium referred to as reverse intussusception [72]. Furthermore, we will introduce noisy sinks and sources to our approach, as previously discussed in section 3.1.1. We find this ansatz particularly fitting to model the liver lobule system, as sinusoids are fenestrated structures, i.e. the vessel wall is perforated, allowing for rapid fluid exchange with the tissue. On the other hand, one may argue that the fluid leak in the sinusoidal system is negligible in comparison to the overall throughput rate, and an additional sink would have to be placed at the opposing end of the plexus, extracting the majority of the fluid. Here, we do not consider this factor, as one major sink would merely generate one (or a small number of) distinct large vessel(s), without any further impact on the topological complexity of the rest of the networks. Additionally, bile and water is frequently secreted by hepatocytes (cells forming the bulk of the tissue and the basic metabolic unit in the liver) into bile canaliculi, representing another noisy flow landscape. We incorporate these flow fluctuations with an effective fluctuation strength $\lambda_3^i = \frac{\sigma_i^2}{\mu_i^2}$ in equation (3.56) :

$$\partial_{t^*} r_{e_i}^* = \lambda_0^i \left[\left(\phi_{e_i}^* + \lambda_3^i \delta\phi_{e_i}^* \right) r_{e_i}^{*3} - \lambda_2^i r_{e_i}^* + \lambda_1 g_{e_i}^* \right] . \tag{3.57}$$

We shall discuss the numerical evaluation of this ODE system (3.57) in detail in the next section for the special cases $\varepsilon = 3$ (attractive) and $\varepsilon = -1$ (repulsive). Any numerical evaluation will be performed as indicated in the scheme in chapter 2 by integrating and monitoring the system (3.57) until a stationary state is reached in both networks.

3.2.3 Repulsive coupling induced nullity breakdown

In this section, we will focus on the ODE system (3.57) for the case of repulsive interactions, i.e. setting the coupling exponent to $\varepsilon = -1$. Doing so we simulate two vessel networks whose surfaces are seemingly repelling each other, prohibiting any direct contact between them. This effectively constrains the network's radial expansion, which is why one may interpret this ansatz also as one network being embedded in a stiff medium with excess pressure arsing from its compression. In order to differentiate the impact of spatially-coupled network morphogenesis from flow-driven effects, we systematically scan the effective network coupling, λ_1, and flow-fluctuation parameter, λ_3, as defined in the previous section. Of particular interest is the influence of the negative feedback $g_e \leq 0$ which the network interaction introduces to the dynamical system (3.57). As in the previous section 3.1.2, we characterize the network structure by its redundancy via the relative amount of independent loops, ϱ, see equation (3.35). Moreover, we compute the corresponding total cross section area, S, and power dissipation, D, for each network according to the definition given in (3.36) and (3.37). For all simulations shown, we set the temporal response $\lambda_0^1 = \lambda_0^2 = 10^{-4}$ and volume penalty $\lambda_2^1 = \lambda_2^2 = 10^6$ (providing reasonable computation times for reaching fix points and preventing stiffness).

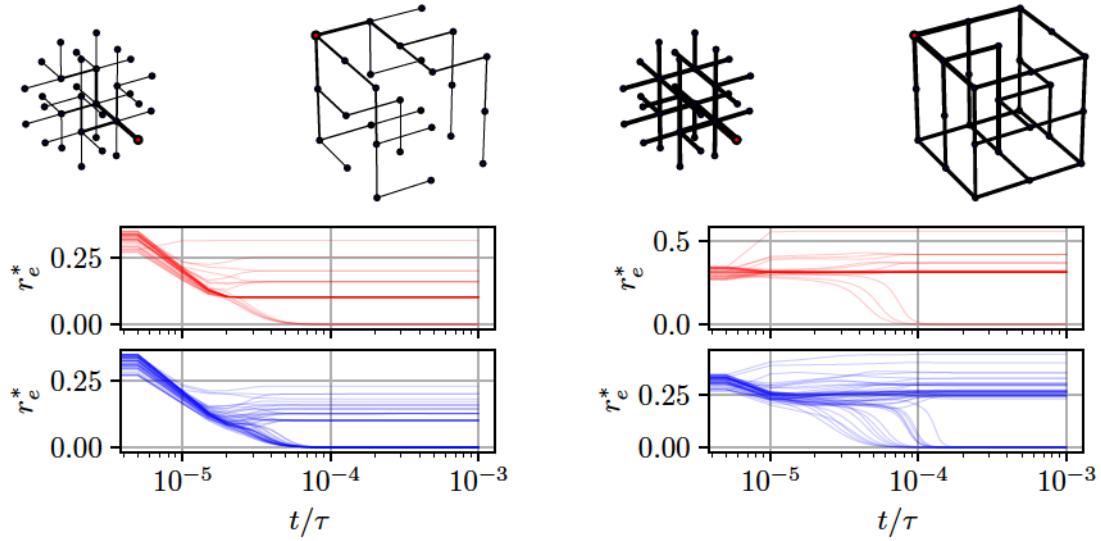

(a) $\lambda_1 = 1$ and $\lambda_3 = 10^{-1}$

(b) $\lambda_1 = 1$ and $\lambda_3 = 10^{3}$

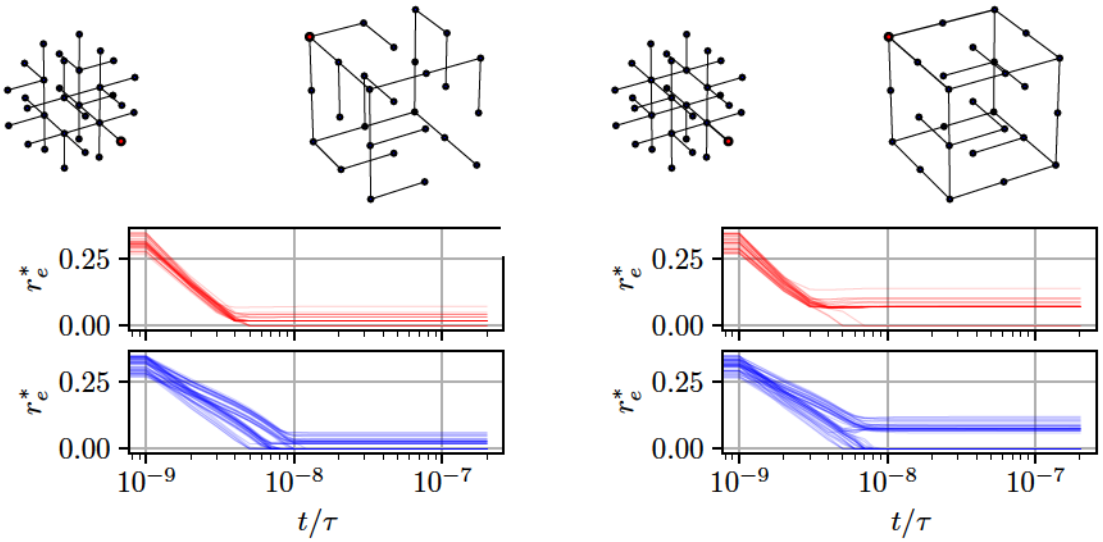

(c) $\lambda_1 = 10^{8}$ and $\lambda_3 = 10^{-1}$

(d) $\lambda_1 = 10^{8}$ and $\lambda_3 = 10^{3}$

Figure 3.9: Adaptation Dynamics for a cubic lattice system and pruned network skeletons. The edge thickness is representative for the relative tube radius, r_e^*, and sources are marked in red. The model parameters, coupling λ_1 and fluctuation λ_3, which set the dynamic behavior, are depicted in the individual sub-captions.

The initial edge radii are chosen randomly and are continuously monitored to fulfill

$$0 < r_{e_1}^* + r_{e_2}^* < 1 \text{ and } r_{e_i}^* \geq 0 \tag{3.58}$$

in order to prevent negative radii, or radii combinations corresponding to intersections. Sources are initialized as distant as possible form each other, placing them in diagonally opposing corners of the two graphs; any other vertices are initialized as fluctuating sinks, as described in section 3.1.1. To demonstrate the most basic behavior of this

model system we have the parameters λ_1^i, λ_3^i set symmetrically for this study as

$$\lambda_1^i \equiv \lambda_1 \tag{3.59}$$
$$\lambda_3^i \equiv \lambda_3 \tag{3.60}$$

All data presented here was acquired for cubic lattices, but the model has been further evaluated for diamond lattices and Laves graphs, see appendix A. The qualitative behavior is preserved, regardless of the lattice chosen. That is further true for repeated initialization of the coupled networks with slight displacement of the sources and randomly initialized edge radii.
In Figure 3.9 we display the dynamics and stationary network structures resulting for various selected parameters. We display here archetypal scenarios of the model (3.57), ranging from fluctuation and coupling free adaptation, see 3.9a, toward excessively coupled networks which are exposed to large fluctuations, see 3.9d. The cases of either coupling or fluctuation dominated adaptation, are displayed in Figure 3.9b and 3.9c. As discussed in the previous section, reticulated networks will emerge for fluctuation dominated networks λ_3, as illustrated in Figure 3.9b. This is to be expected as this scenario corresponds to the adaptation to two uncoupled cubic lattices, see section 3.1.2). Coupling dominated regimes, as illustrated in Figure 3.9b, only display spanning tree configurations. It can be seen that the nullity transition is altered for both parameters λ_1, λ_3 increased, going hand in hand with a shift in transition times and vessel hierarchies.

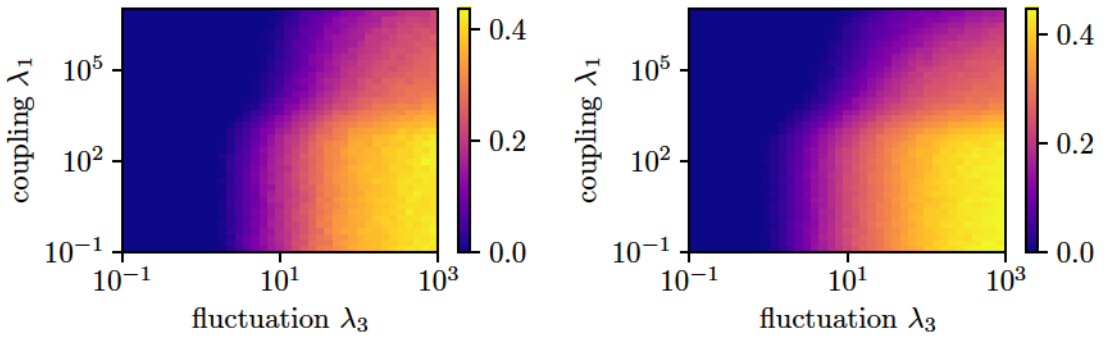

Figure 3.10: Nullity ϱ state diagrams for stationary states of the coupled ODE systems (3.57) for $\varepsilon < 0$. Displayed are the symmetric scans for coupling λ_1 and fluctuation λ_3, indicating coupling induced nullity breakdown for both networks.

We see that the topological transition disturbed by increased coupling strengths λ_1. And elevated coupling levels λ_1 actually decrease the transition time to reach a stationary state while it simultaneously seems to eradicate the distinct root-to-leaf vessel hierarchy found in conventional wall-shear stress driven pruning models, see section 2.2.2 and section 3.1.2. Taken together, all these findings indicate that we have found a mechanism for retrieving spanning trees even in the presence of large flow fluctuations. In other words, the repulsive coupling and fluctuation driven nullity onset seem to be competing against one another: On the one hand, we have a wall-shear stress driven pruning mechanism which is expanding vessels experiencing high stresses and degenerating poorly perfused ones.

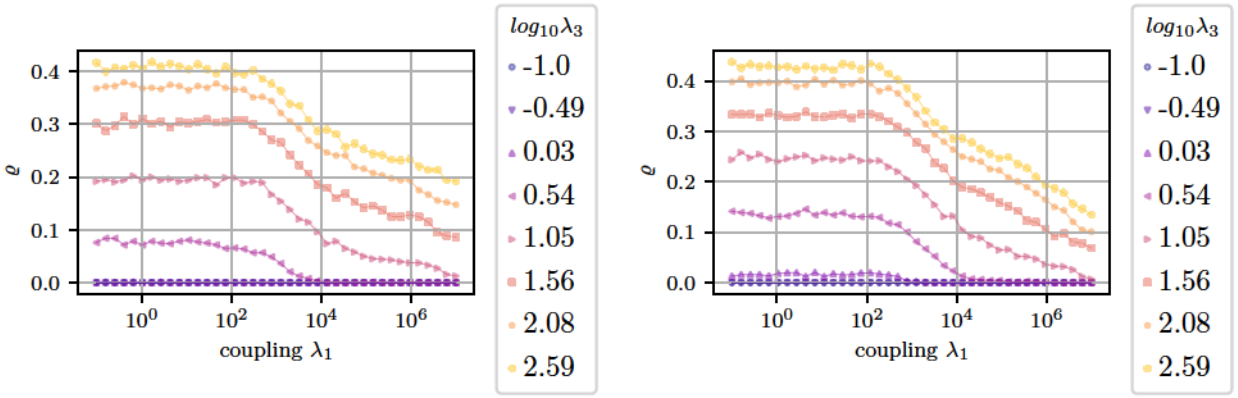

(a)

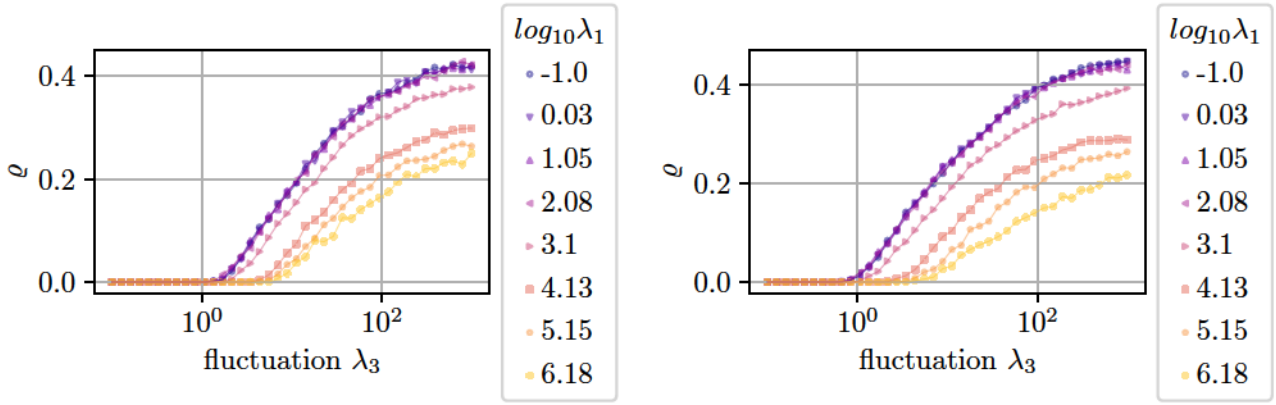

(b)

Figure 3.11: Detailed nullity trajectories from state diagram 3.10 with network 1 on the right-hand side and network 2 on the left-hand side: (a) Coupling λ_1 induced nullity breakdown for varying fluctuation λ_3. (b) Fluctuation λ_3 induced nullity onset for varying coupling λ_1.

On the other hand, any repulsive interaction tends to shrink adjacent vessels whose surfaces get close to each other. Doing so we automatically put a size cap on vessels near the root-vertices and create high shear stresses in the nearly collapsing vessels near the other graph's leaves. Yet, as the dynamical system (3.57) does not have an inherent handling of collapsing vessels due to this repulsion, i.e. negative radii are mathematically possible, we include a freezing mechanism as previously suggested in section 2.2.2. This means potentially negative vessel radii are caught as exceptions, the respective vessel radii are set to $r_e = 10^{-20}$ and not updated anymore. For the remainder of our analysis these particular edges count as pruned. In Figure 3.10, we present the resulting nullity state diagrams for both networks in stationary states for a systematic scan of the parameters λ_1 and λ_3. The colormap displays the nullity ϱ (3.35) in either network, and indicates a complex transition landscape. First, we see the fluctuation-induced nullity transition to be preserved for weak couplings, roughly below a threshold of $\lambda_1 < 10^4$. This directly corresponds to the uncoupled case of two separate monolayer systems, as mentioned before. Above this threshold, the system's nullity may not only be influenced by the rate of fluctuations, λ_3, but also by

the mutual repulsion of the two networks. Due to the non-periodic construction of the two intertwined lattices we do see boundary effects which become visible for the different network skeletons in terms of the transition trajectory. One generally finds the remaining reticulation in the case of high coupling and fluctuation to be present on the surfaces of the cubic structures, as the local neighborhoods consist of fewer edges, see 3.9. In Figure 3.11 we display these nullity transitions in detail for each network. We do so for different parameter layouts in order to extract the explicit λ_1 and λ_3 interdependencies. The general trends displayed suggest that the influence of the repulsion is less significant by comparison, needing coupling parameters to be orders of magnitude larger than the fluctuation rates to break down cycles. We also find the fluctuation-induced nullity onset to be continuous, as it was for the monolayer system, yet with the clear distinction that the onset becomes shifted and the total nullity is reduced significantly. Starting as tree-like states at small fluctuations and having ϱ increase monotonically in a logarithmic manner beyond a critical $\lambda_3 \geq \lambda_c$, we have the ϱ-trajectory eventually saturating for large fluctuation rates $\lambda_3 > 10^3$ toward a maximal nullity $\varrho_{\max}$. This leaves the network in a reticulated state, still displaying a visible vessel hierarchy towards the source. From there, we may recover tree-like network states for increased repulsion rates, λ_1. We would like to point out that the negative feedback caused by the repulsion of the two networks does not cause any shunting (i.e. collapse and disconnection of large sections of the networks) whatsoever.

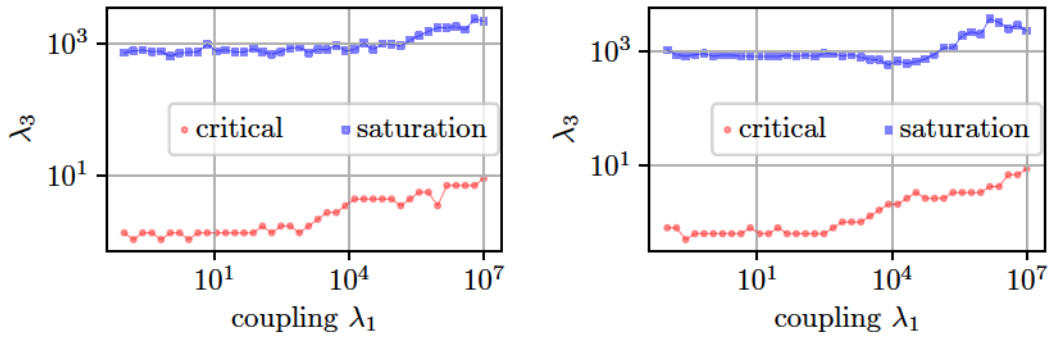

Figure 3.12: Critical and saturation values for nullity transitions for both repulsively coupled networks, with network 1 on the right-hand and network 2 on the left-hand side.

To quantify these shifts we acquire the critical λ_c by identifying the trajectories' departure from zero in Figure 3.11b. The critical point λ_c seems to monotonically shift with the coupling parameter λ_1. Following up on this observation, we extrapolate the onset of saturation in Figure 3.11b by means of sigmoidal fits. The shifts of these indicators are shown in Figure 3.12 for each network, displaying a slight increase of both, the critical value and the saturation, for increasing λ_1. As pointed out before, there seems to be a competition of the adaptation mechanisms, although the scales on which the interplay of these mechanisms unfold indicate a general dominance of fluctuation driven mechanisms. Furthermore it seems that the saturation point slight shift does not compare to the drop of the saturation level, meaning a trend for the overall nullity to be diminished utterly for rising coupling levels. As we find the individual transitions

to follow similar trajectories for either parameter scan we intend to derive an empirical form of it as done before so in section 3.1.2. Using the critical values, λ_c, we rescale the trajectories of Figure 3.11 between the onset of the nullity transition and its saturation, as shown in Figure 3.13. Introducing the reduced fluctuation parameter $\frac{\lambda_3-\lambda_c}{\lambda_c}$ we find the trajectories to collapse onto a single master curve, following a trivial logarithmic law as

$$\varrho\left(\lambda_1, \lambda_3\right) \approx \kappa\left(\lambda_1\right)\left[\log_{10}\left(\frac{\lambda_3-\lambda_c}{\lambda_c}\right)-1\right] \tag{3.61}$$

with the coupling dependent scaling factor, $\kappa\left(\lambda_1\right)$, obtained by interpolation of the data using equation (3.61). We find κ to be a decreasing function of the coupling λ_1 as shown in Figure 3.13b. This demonstrates that the nullity breakdown and shift can be tuned by the coupling alone for any given fluctuation rate.

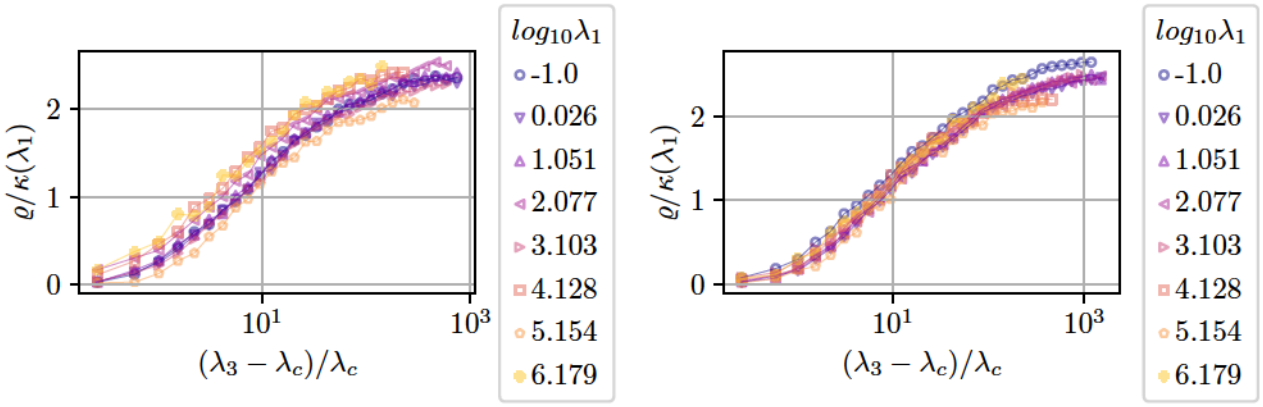

(a)

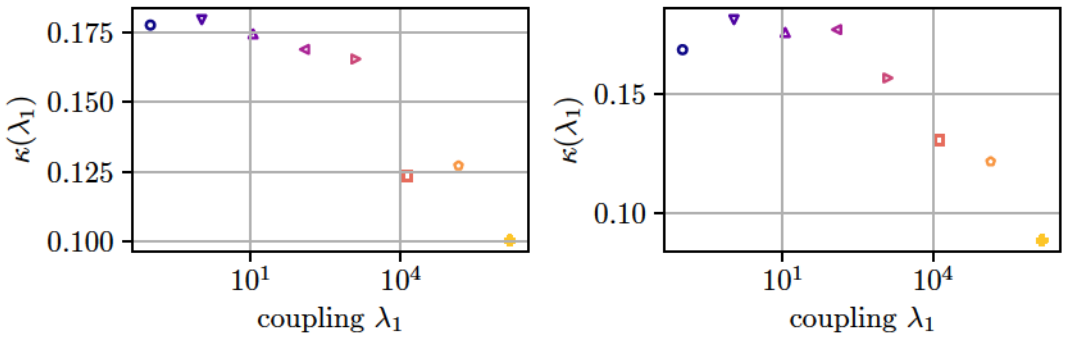

(b)

Figure 3.13: Rescaled transition curves from Figure 3.11 with network 1 on the right-hand side and network 2 on the left-hand side: (a) Single curve collapse near fluctuation induced nullity onset λ_c and scaled nullity $\varrho/\kappa(\lambda_3)$. We find the transition to be approximated by $\varrho\left(\lambda_1, \lambda_3\right) \approx \kappa\left(\lambda_1\right)\left(\log_{10}\left(\frac{\lambda_3-\lambda_c}{\lambda_c}\right)-1\right)$ (b) Coupling dependent scaling factor $\kappa\left(\lambda_1\right)$, as derived from linear interpolation of rescaled transition curves.

Let us turn toward the network area cross section, S, and power dissipation, D, for intertwined systems, see Figure 3.14. Note that the system's dissipation in Figure 3.14a

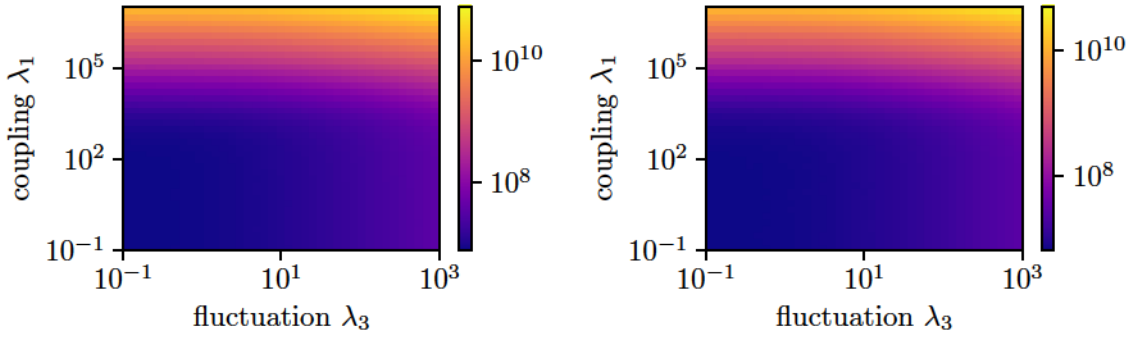

(a) Network power dissipation D

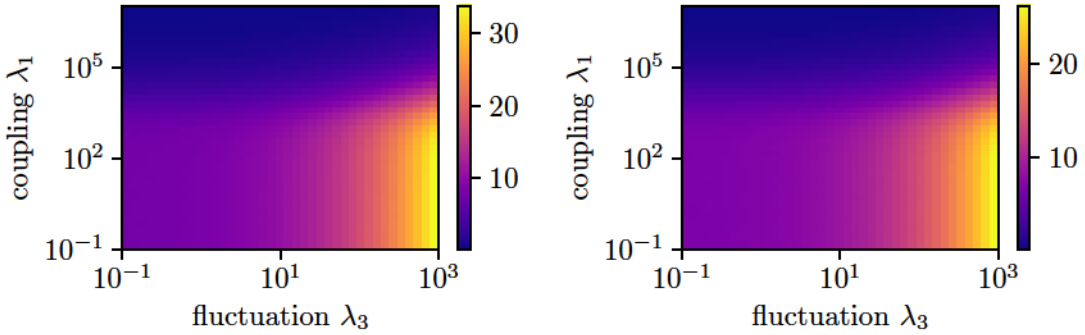

(b) Network overall cross section S

Figure 3.14: Dissipation, D, and area cross section diagrams, S, for repulsively coupled networks, with network 1 on the right-hand side and network 2 on the left-hand side.

is not significantly raised by an increase of the coupling until significant values for $\lambda_1 \geq 10^5$ are reached, indicating once again that systems for smaller λ_1 may be considered as uncoupled for the given λ_2 configuration. In Figure 3.14b we show the network's overall cross section area S. We observe here that the tube system collapses for $\lambda_1 > 10^5$ as opposed to the fluctuation induced increase of the system's overall cross section areas, which is in line with the overall rise in dissipation. Here, we once again see that the typical vessel hierarchy is eradicated and the formerly wall-shear stress optimized spanning trees or meshes become ineffective in that respect. We would like to point out that similar results may be obtained when leaving one network as a static cage, implying that the results found are based on the mere introduction of an repulsive scaffold for either network.

We have shown in this section that a complex nullity transition may be generated, even in case of symmetrically coupled and perfused networks. In particular we have found the nullity onset due to fluctuation driven positive feedback to be retarded and the saturation to be significantly reduced for increased repulsive coupling rates. Nevertheless we find the fluctuation driven adaptation mechanism to be robust against vast ranges of pertubations such as negative feedback due to spatial competition. On the other hand, we interpret the trend of effective saturation levels $\lim_{\lambda_1 \to \infty} \kappa \to 0$ to indicate the theoretical existence of a critical point, i.e. a level of coupling for which no more

reticulated networks possibly exist. Given the reticulation is fluctuation based. Currently it proves challenging from a computational point of view as the ODE system is turning stiff for this regime of λ_1, which calls for a reformulation of the current unit system. Asymmetrically coupled networks are not discussed here, but preliminary studies suggest that coupled networks with different levels of reticulation can be generated. Once again, note that this ansatz only intends to capture the qualitative behavior of a scenario, where vessel surfaces are repelled from each other, a heuristic guess so to say. We are still pending here between a mechanotransductive approach due to mutual tissue compression and complex morphogen signaling between the endothelium and the parenchyma. It is to expect that a more detailed discussion of the mechanical properties of the elastic compound of capillaries-tissue, could give us insight on the form of appropriate repulsion term as will a closer look into each organs specific biochemical milieu.

3.2.4 Attractive coupling induced nullity onset

In this section, we consider intertwined networks with an attractive spatial coupling. The system is initialized with a positive coupling exponent, $\varepsilon = 3$. Remember that this ansatz is supposed to capture additional positive feedback arising from the entanglement of the networks, without having them touch directly or pass through each other. We are particularly interested in how the positive feedback, $g_e^* \geq 0$, alters the behavior of the dynamical system (3.57) and how it compares with the fluctuation induced nullity transition. We proceed as before: In order to distinguish the impact of spatially coupled network morphogenesis from flow-driven effects, we systematically scan the effective network coupling, λ_1, and flow-fluctuation parameter, λ_3. As in section 3.1.2 we characterize the network structure by its redundancy via the relative amount of independent loops, ϱ, see equation (3.35), and compute the corresponding total cross section area S and power dissipation D for each network according to the definitions given in (3.36) and (3.37). For all simulations shown, we set the temporal response $\lambda_0^1 = \lambda_0^2 = 10^{-4}$ and volume penalty $\lambda_2^1 = \lambda_2^2 = 10^6$ (providing reasonable computation times for reaching fix points). The initial edge radii are chosen randomly and are continuously monitored to fulfill the criterion (3.58) to prevent radii combinations corresponding to intersections. Once again, sources are initialized as distant as possible, placing them in diagonally opposing corners of the two graphs. Any other vertices are initialized as fluctuating sinks. To demonstrate the most basic behavior of this model system we have the parameters λ_1^i, λ_3^i set symmetrically for this study as

$$\lambda_1^i \equiv \lambda_1 \tag{3.62}$$

$$\lambda_3^i \equiv \lambda_3 \tag{3.63}$$

As in the previous section, all data presented here is for cubic lattices only, for simulations on diamond and Laves structures, which display the same qualitative behavior, see the appendix A. Note that as in the previous section we find the stationary states (3.57) to display no significant variance in their quantitative and qualitative behavior of different edge weight initialization and source displacement.

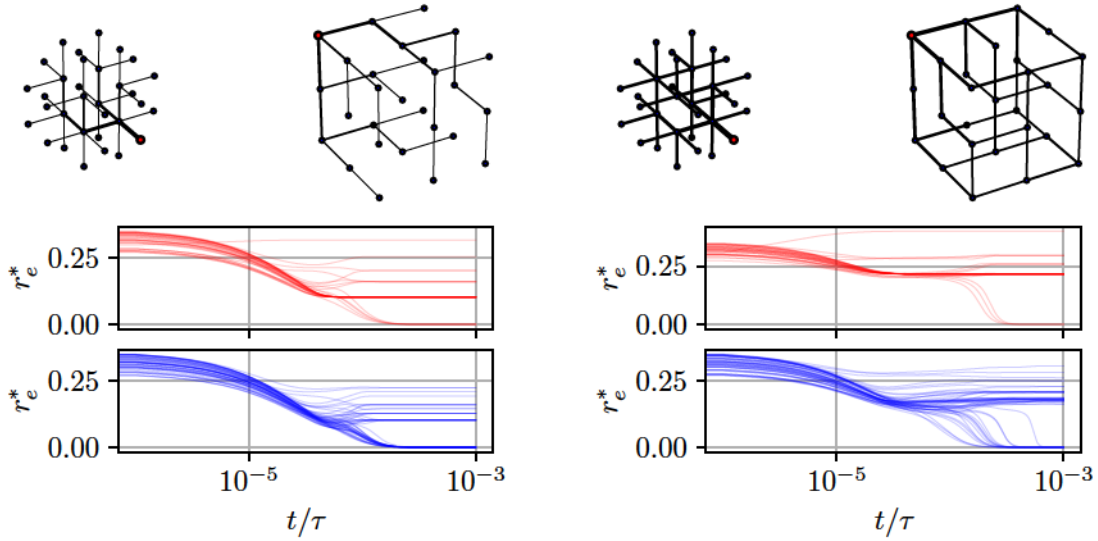

(a) $\lambda_1 = 1$ and $\lambda_3 = 10^{-1}$

(b) $\lambda_1 = 1$ and $\lambda_3 = 10^{2}$

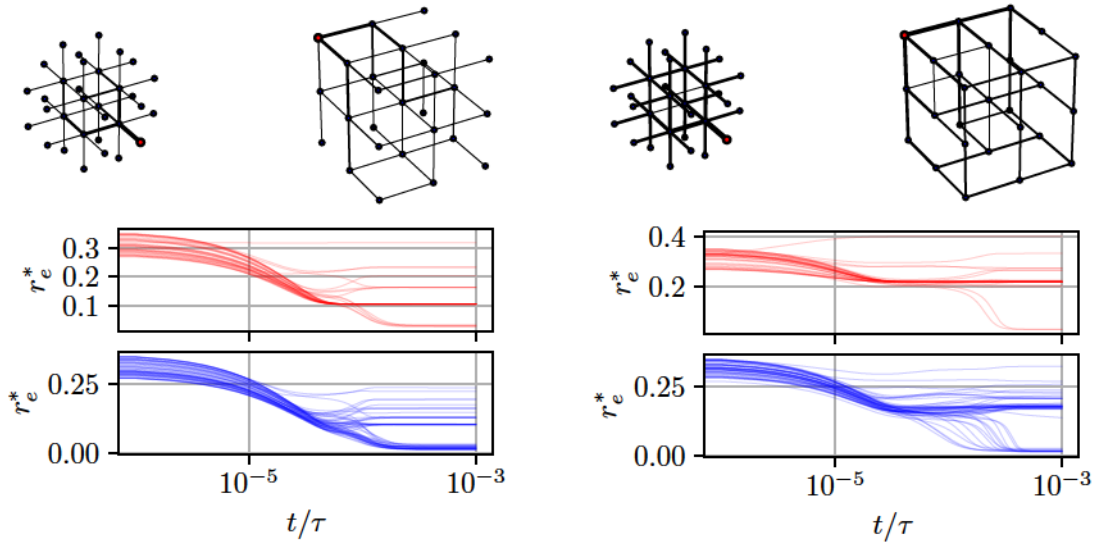

(c) $\lambda_1 = 10^{4}$ and $\lambda_3 = 10^{-1}$

(d) $\lambda_1 = 10^{4}$ and $\lambda_3 = 10^{2}$

Figure 3.15: Adaptation Dynamics for a cubic lattice system and pruned network skeletons. The edge thickness is representative for the relative tube radius r_e^* and sources are marked in red. The model parameters setting the dynamic behavior are depicted in the sub-captions with coupling λ_1 and fluctuation λ_3.

In Figure 3.15 we display the dynamics and stationary points resulting for archetypal coupling and fluctuation scenarios. Varying the fluctuation and attractive coupling in (3.57) we find once again a nullity transition, ranging from fluctuation and coupling free adaptation, see 3.15a, toward excessively coupled networks which are exposed to large fluctuations, see 3.15d. The cases either coupling or fluctuation dominated adaptation, are displayed in Figure 3.15b and 3.15c. As discussed in the previous sections, reticulated networks will emerge for fluctuation dominated networks λ_3, as illustrated

in Figure 3.15b. Interestingly, we find a new nullity transition for increased coupling levels λ_1. Coupling dominated regimes, as displayed in Figure 3.9b, display nearly full plexus recovery. The transition times and vessel hierarchies do not significantly vary in comparisons to the case of repulsive coupling. All these findings indicate that we have found a new mechanism for generating reticulated networks. Moreover, it seems to enable full recovery of the initial plexus, which should be impossible for certain graph topologies in the context of fluctuation driven reticulation.

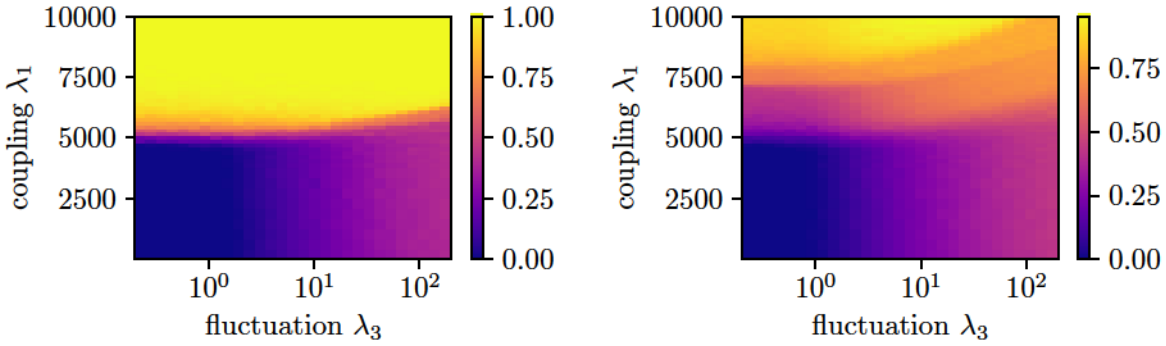

Figure 3.16: Nullity ϱ state diagrams for stationary states of the coupled ODE systems (3.57) for $\varepsilon > 1$. Displayed are the symmetric scans for coupling λ_1 and fluctuation λ_3 indicating coupling induced plexus recovery, with network 1 on the right-hand side and network 2 on the left-hand side.

In Figure 3.16, we show the resulting nullity state diagrams for this symmetric scan of the couplings and fluctuation rates, indicating a fully reversed transition behavior compared to the case of repulsive interactions, as discussed the previous section. First, we observe that a new nullity transition emerges for increased λ_1, turning from tree states of the pruned plexus into nearly full recovery of the initial graphs. This behavior is generally preserved for other network topologies, but is particularly expressed for cubic lattices. We see here a significant difference for this transition for either network, which we presume to be a surface effect. The two entangled initial plexi have different affiliation patterns for edges on the cube surfaces, leading inherently more complex nullity behavior for the second network. Further we find the coupling transition to occur on a linear scale rather than the known logarithmic scale from before. This coupling mechanism represents therefore a rather sharp switch of the network's entire complexity. It should be noted here that combined increase in fluctuation and coupling levels repeatedly fails in terms of the vessel contact criterion. The details of these nullity transitions are illustrated in Figure 3.17. For increasing coupling strength, λ_1, we see the emergence of a new nullity transition for $\lambda_1 > 4000$. Moreover we observe significant differences in the transition trajectories for either network. While the nullity trajectory for the first network depicts a step-like transition for either λ_3 variation, we find it washed out for the second network, depicting step like increments. In either case we find recovery of virtually the entire initial plexus for $\lambda_1 \to 10^4$.

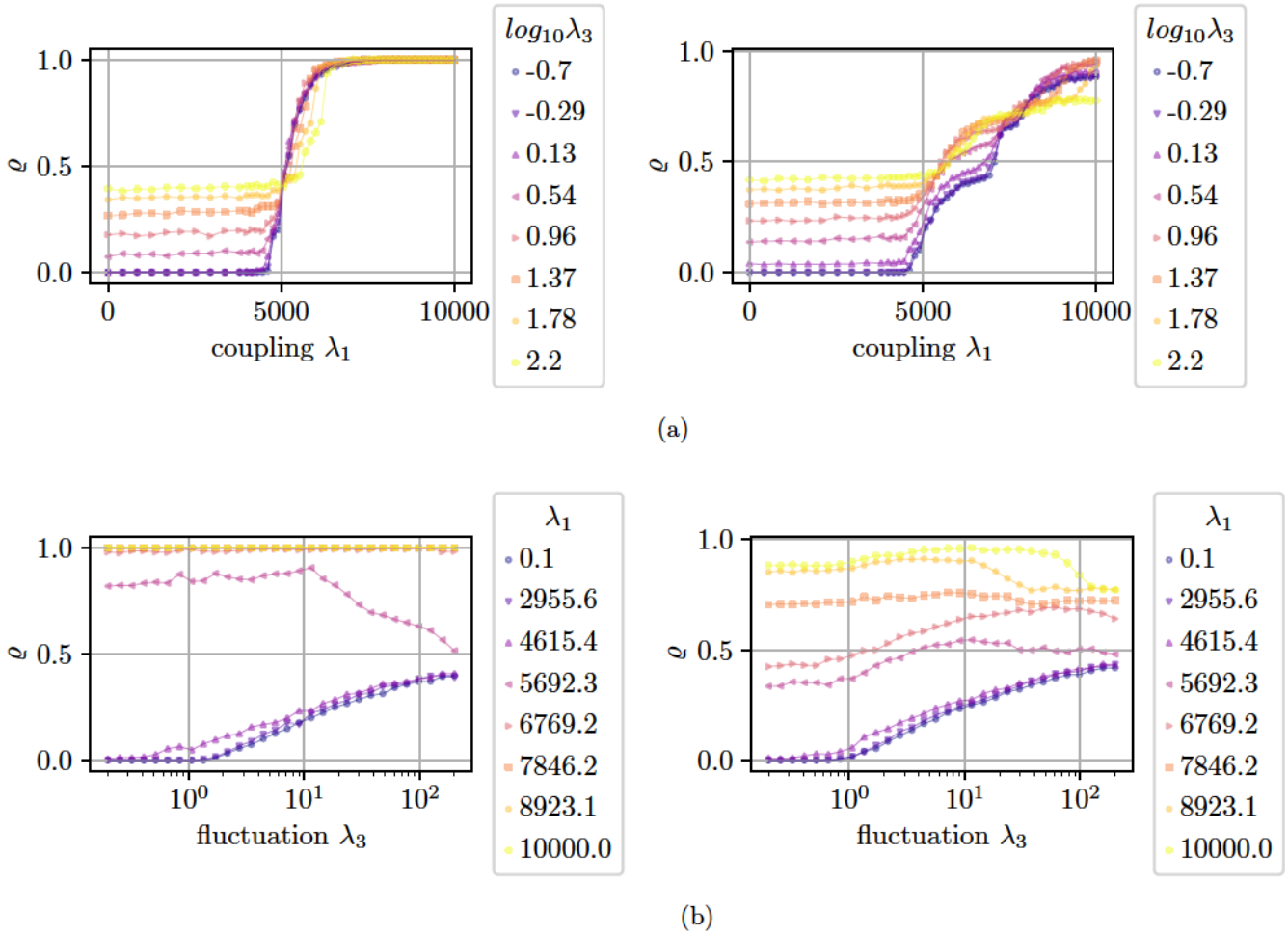

Figure 3.17: Detailed nullity trajectories from state diagram 3.16 with network 1 on the right-hand side and network 2 on the left-hand side: (a) Coupling λ_1 induced nullity onset for varying fluctuation λ_3. (b) Fluctuation λ_3 induced nullity onset and breakdown in dependence of coupling λ_1.

Any increase in fluctuations, λ_3, generates a positive offset of the nullity curve, indicating a constructive superposition of the mechanisms at hand, see Figure 3.17b. Yet, the trajectory's general form seems well preserved, while the saturation level is reduced for increased λ_3. Simultaneously, one has the fluctuation induced nullity trajectory lose its logarithmic growth behavior of increased coupling λ_1. We also observe a nullity reduction in the fluctuation dominated region for $\lambda_1 \leq 4000$. Here, the wall-shear stress driven adaptation towards a noisy flow landscape actually seems to reduce the overall positive feedback. This would suggest that even in the presence of stimuli offering nearly full recovery, we have fluctuations reducing the effective nullity. Once again, we determine the transition's onset and saturation regime, see Figure 3.18. To do so for the onset, we calculate the trajectories' root of the onset after subtracting the trajectories' offset. The saturation regime is extrapolated via a sigmoidal fit. We see in Figure 3.18 a slight shift of the onset and saturation points of the coupling induced transition. Moreover we see the coupling induced transition to preserve its form rather well for a large variation of λ_3, occurring on a linear scale.

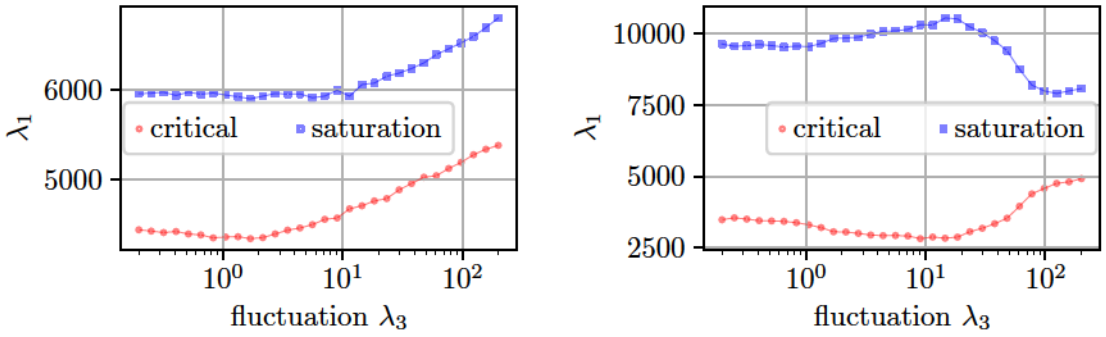

Figure 3.18: Critical λ_1 for onset of nullity transition for λ_3 variation and extrapolated saturation of nullity transition, with network 1 on the right-hand side and network 2 on the left-hand side.

As in the previous section, we are able to collapse the onset of the trajectories onto a single master curve by following a simple linear law

$$\varrho\left(\lambda_1, \lambda_3\right) \approx \kappa\left(\lambda_3\right)\left(\frac{\lambda_1 - \lambda_c}{\lambda_c}\right) + \varrho_0\left(\lambda_3\right) \tag{3.64}$$

with rescaled axis $\frac{\lambda_1 - \lambda_c}{\lambda_c}$ and coefficients κ, ϱ_0 to be acquired from interpolation, see Figure 3.19. It should be noted that we had to restrict simulations to $\lambda_3 < 300$ as affiliated edge pairs will violate the contact condition (3.58) beyond this range for increased coupling levels. Eventually the network's total cross section area, S, and power dissipation, D, turn out rather trivial, as displayed in Figure 3.20. We find here that neither S nor D depict any significant λ_1 dependency. More so, we observe an increase in either metric for an increase in λ_3. This would be somewhat, surprising as an increase in reticulation does not result in a significant rise of the cross section area. Nevertheless, as indicated in Figure 3.15c, we find the majority of newly abundant vessels to be negligibly small in comparison to the vessel of the inherent spanning tree backbone. It is to assume that these vessels do not contribute significantly to the transport of fluid as this would be indicated by a massive peak in the dissipation diagram. We have shown in this section, that positive coupling between locally affiliated edges of entangled networks display a new kind of nullity transition, while having their overall cross section areas and power dissipation virtually unaffected. Coupling induced nullity can account for full plexus recovery, no matter the underlying topology. This algorithm tends to generate a vessel hierarchy consisting of the original spanning tree backbone, known from wall shear stress driven pruning processes, in combination with poorly perfused secondary vessels.

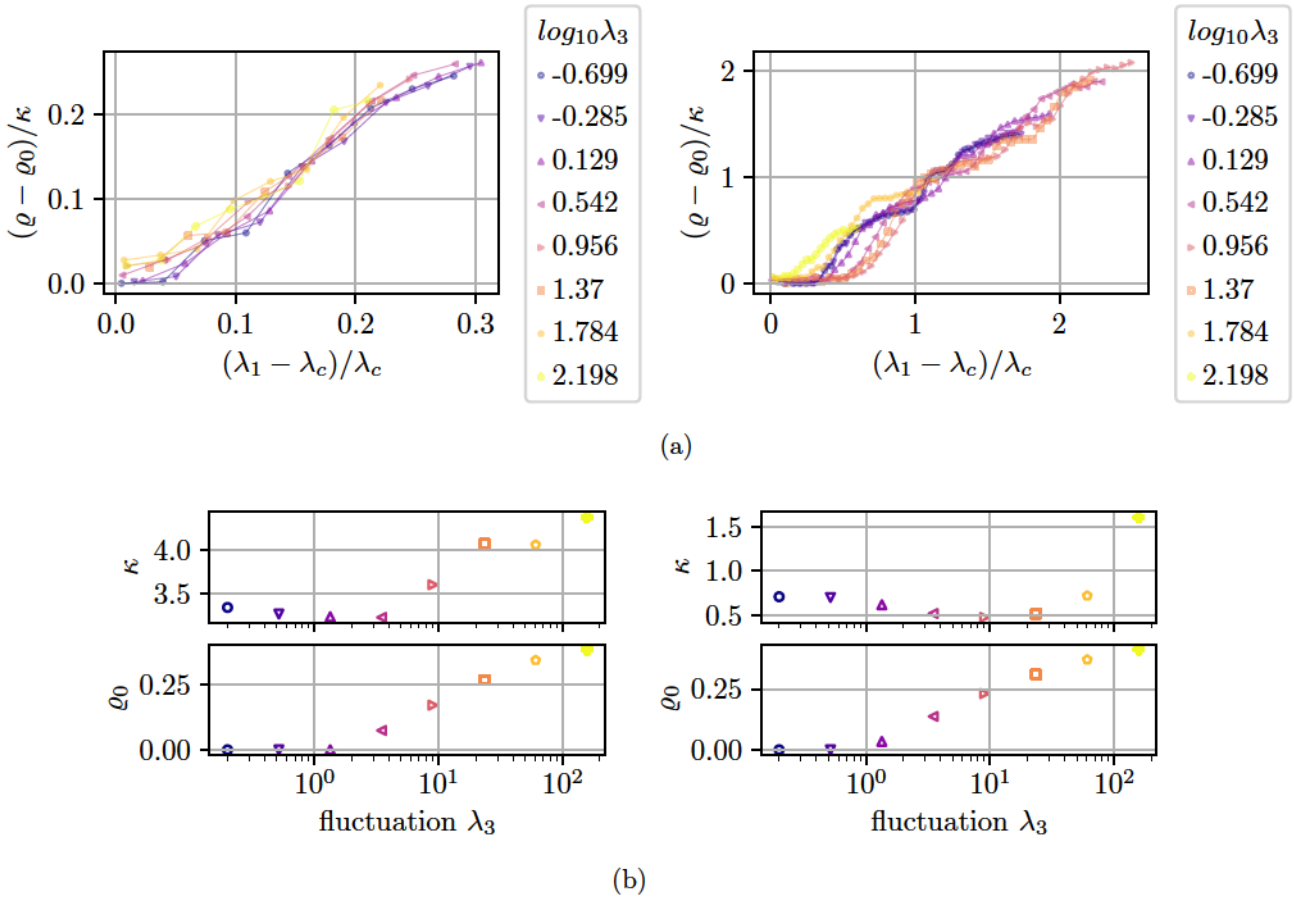

Figure 3.19: Rescaled transition curves from Figure 3.11 with network 1 on the right-hand side and network 2 on the left-hand side: (a) Single curve collapse near coupling induced nullity onset λ_c and scaled nullity $(\varrho - \varrho_0(\lambda_3))/\kappa(\lambda_3)$. We find the transition to be approximated by $\varrho\,(\lambda_1, \lambda_3) \approx \kappa\,(\lambda_3)\left(\frac{\lambda_1 - \lambda_c}{\lambda_c}\right) + \varrho_0\,(\lambda_3)$ (b) Coupling dependent scaling factor and fluctuation induced nullity offset $\kappa\,(\lambda_3)$, $\varrho_0\,(\lambda_3)$, as derived from linear interpolation of rescaled curves.

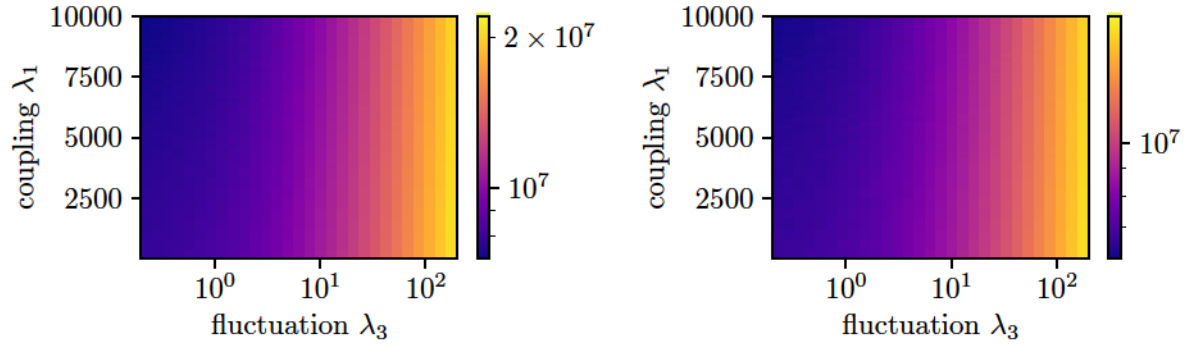

(a) Network power dissipation D

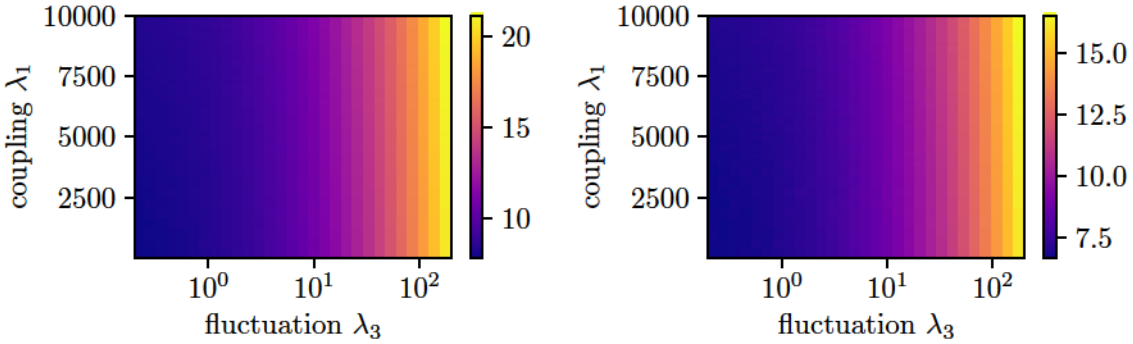

(b) Network overall cross section S

Figure 3.20: Dissipation D and cross section diagrams S for attractively coupled networks ($\varepsilon = 3$), with network 1 on the right-hand side and network 2 on the left-hand side.

3.3 On generalizing and applying geometric laws to complex transport networks

As introduced in chapter 1, metabolic cost function models, which operate on linear networks are particularly useful in predicting the exponents in radial scaling relationships. Most prominent of all: Murrays's law, is derived from such minimization principles but has been done so only for source-free, hierarchical branchings with non-stochastic flow patterns. In this section we would like to discuss our ansatz to incorporate fluctuating sinks, as discussed in section 3.1.1, and complex multilayer interactions, see section 3.2.2. In section 3.3.1, we propose a framework that allows for the direct interpolation of effective model parameters of metabolic cost functions, from the branching pattern alone. Moreover, we do so for any type of reticulated graph, not just tree like structures for which the original Murray relation was conceived. We demonstrate how parameter interpolation may be performed for lumped parameter networks with high accuracy, see section 3.3.2 Eventually we test this framework for real data sets of intertwined vessel structures, namely the liver lobule, see section 3.3.3.

3.3.1 Generalizing Murray's law for complex flow networks

In this section, we discuss a generalized version of Murray's Law, previously introduced in chapter 1. Remember that in hierarchical networks, one has this particular scaling relationship as

$$r_i^3 = \sum_j r_{i+1,j}^3 \tag{3.65}$$

where the ith level of a vessel network is splitting into j offsprings on the $(i+1)$th level. Here, we revisit the derivation of equation (3.65) in order to incorporate the presence of fluctuating sources as well as to demonstrate the effect of complex metabolic cost functions.
In the original publication of Murray [92], one considers the Kirchhoff current law (2.75) at an arbitrary node v with all its incident edges e carrying a Hagen-Poiseuille flow as

$$\sum_{e \in inc(v)} \frac{\pi r_e^4}{8\eta L_e} \Delta p_e = s_v \tag{3.66}$$

In the original study, only sink-free vertices are considered, yet we will generally assume in this section that $s_v \neq 0$. Now, one would derive a relation for Δp_e from the minima of a metabolic cost function ansatz, see for example (2.95). As these minima are the stationary points of the corresponding dynamical system, see equations (2.108), we may utilize these ODEs directly. Rewriting (2.108) by replacing the flow rates with

their respective pressure gradients we get

$$\partial_t K_e = b_0 \left(\frac{K_e^{1/2}}{L_e^2} \Delta p_e^2 - b_2 \right) K_e \tag{3.67}$$

$$\frac{\partial_t K_e}{K_e} = 0 \Rightarrow \Delta p_e^2 \left(\frac{r_e}{L_e} \right)^2 = \left(\frac{8\eta}{\pi} \right)^{1/2} b_2 \tag{3.68}$$

This framework leads directly to equation 3.65 if the vertex is sink-free and flow directions are known. The flow directions are indicated here as the resulting sign of Δp_e, which is usually derived from the vessel hierarchy of Y-junctions, splitting from large parent vessels into smaller children components.
Now,there remains the case when this is simply not possible, because such a clear vessel hierarchy is not present, as is the case for most mesh-like capillary beds? Moreover, these might be systems where it is not experimentally possible to measure flow direction or velocity. We argue that representative vertices in such capillary networks should not be considered sink-free, as discussed in section 3.1.1. This furthermore implies that there might not be a set direction of flow as re-routing frequently occurs. We intend thus to present here a generalization of (3.65) for uncorrelated fluctuation s_v and suggest a workaround for unknown flow directionality.

Murray's law for fluctuating flows

First, let us operate on the premise that the vessel system is adapting according to the previously discussed ODE system (3.2)

$$\partial_t r_e = c_0 \left(\langle \Delta p_e^2 \rangle \left(\frac{r_e}{L_e} \right)^2 - c_2 \right) r_e$$

with $\langle \Delta p_e^2 \rangle = \phi_e + \lambda_3^i \delta\phi_e$, if $\mu_v = \mu$ and $\sigma_v = \sigma$, see section 3.1.1. We define the effective sink-source fluctuation as λ_3 and the volume penalty λ_2 as done in section 3.1.1. Let us begin the derivation for the more general case of arbitrary fluctuation patterns, possibly deviating from those patterns previously introduced. Formulate a non-dimensional form of (3.2) and derive the stationary states as

$$\frac{\partial_{t^*} r_e^*}{r_e^*} \propto \left(\langle \Delta p_e^2 \rangle \left(\frac{r_e}{L_e} \right)^2 - \lambda_2 \left(\frac{8\eta}{\pi} \right)^2 \right) \tag{3.69}$$

$$\frac{\partial_{t^*} r_e^*}{r_e^*} = 0 \Rightarrow \left(\frac{\pi}{8\eta} \right) \frac{r_e}{L_e} = \sqrt{\frac{\lambda_2}{\langle \Delta p_e^{*2} \rangle}} \tag{3.70}$$

with the effective volume penalty $\lambda_2 = \left(\frac{\pi}{8\eta}\right)^{3/2} \frac{L^3}{\mu^2} b_2$. In order to combine this result with the current law (2.75) we take the ensemble average over all configurations occurring due to changes in the sink configurations and obtain

$$\sum_{e \in inc(v)} \frac{\pi r_e^4}{8\eta L_e} \langle \Delta p_e \rangle = \langle s_v \rangle \tag{3.71}$$

$$\Leftrightarrow \sum_{e \in inc(v)} \Theta_{ve} \frac{\pi r_e^4}{8\eta L_e} | \langle \Delta p_e \rangle | = \langle s_v \rangle \tag{3.72}$$

$$\text{with } \Theta_{ve} = \pm 1$$

with an effective incidence factor Θ_{ve} distinguishing between in- and outgoing flows on the relevant edges, see Figure 3.21.

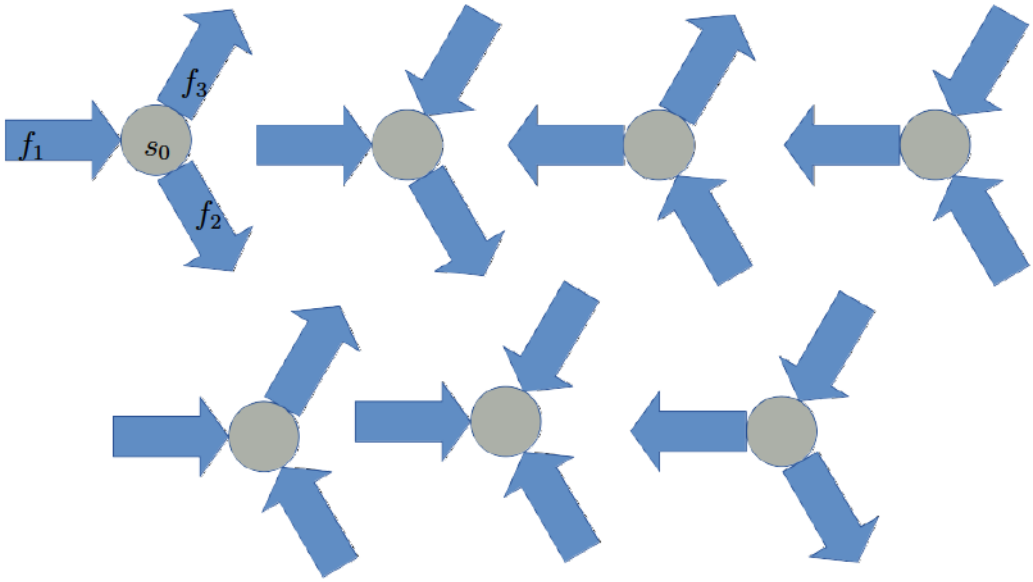

Figure 3.21: Scheme of different flow combinations at a sink, determining the respective sign of Θ_{ve}, here shown for a Y-junction. We define an incidence triplet $\boldsymbol{\Theta} = (\Theta_{01}, \Theta_{02}, \Theta_{03})$, where the sink is indexed as $v = 0$ and the edges as $e \in \{1, 2, 3\}$, doing so one can define up to seven distinct incidence triplets for Y branch.

Next, we switch to a dimensionless formulation of (3.72) using the unit system proposed in section 3.1.2

$$\sum_{e \in inc(v)} \Theta_{ve} \frac{\pi r_e}{8\eta L_e^*} r_e^{*3} | \langle \Delta p_e^* \rangle | = \langle s_v^* \rangle \tag{3.73}$$

Combining equations (3.70) and (3.73) and rewriting $| \langle \Delta p_e^* \rangle | = \sqrt{\langle \Delta p_e^* \rangle^2}$ we get

$$\sum_{e \in inc(v)} \Theta_{ve} \sqrt{\lambda_2 \frac{\langle \Delta p_e^* \rangle^2}{\langle \Delta p_e^{*2} \rangle}} r_e^{*3} = \langle s_v^* \rangle \tag{3.74}$$

Let us now deduct the ratio term $\frac{\langle \Delta p_e^* \rangle^2}{\langle \Delta p_e^{*2} \rangle}$ and sink averages $\langle s_v^* \rangle$ in equation (3.74). Note that we derived explicit expressions for the pressure averages in section 3.1.1,

with $\langle \Delta p_e^2 \rangle = \sum_{vw} A_{vw}^e \langle s_v s_w \rangle$ and $\langle \Delta p_e \rangle^2 = \sum_{vw} A_{vw}^e \langle s_v \rangle \langle s_w \rangle$. One may rewrite the ratio of these pressure terms in the form of the covariance of the sink fluctuations as

$$\frac{\langle \Delta p_e^{*2} \rangle}{\langle \Delta p_e^* \rangle^2} = \frac{\sum_{vw} A_{vw}^e \langle s_v s_w \rangle}{\sum_{vw} A_{vw}^e \langle s_v \rangle \langle s_w \rangle} \tag{3.75}$$

$$= \frac{\sum_{vw} A_{vw}^e \left[\langle s_v \rangle \langle s_w \rangle + \langle (s_v - \langle s_v \rangle)(s_w - \langle s_w \rangle) \rangle \right]}{\sum_{vw} A_{vw}^e \langle s_v \rangle \langle s_w \rangle} \tag{3.76}$$

$$= 1 + \frac{\sum_{vw} A_{vw}^e \langle (s_v - \langle s_v \rangle)(s_w - \langle s_w \rangle) \rangle}{\sum_{vw} A_{vw}^e \langle s_v \rangle \langle s_w \rangle} \tag{3.77}$$

We see that due to the linear nature of the problem, any pressure ratio is primarily dependent on the squared mean to variance ratio. Substituting this into (3.74) we acquire for any vertex,

$$\sum_{e \in inc(v)} a_e r_e^{*3} = \langle s_v^* \rangle \tag{3.78}$$

$$\text{setting } a_e = \Theta_{ve} \sqrt{\frac{\lambda_2}{1 + \frac{\sum_{vw} A_{vw}^e \langle (s_v - \langle s_v \rangle)(s_w - \langle s_w \rangle) \rangle}{\sum_{vw} A_{vw}^e \langle s_v \rangle \langle s_w \rangle}}} \tag{3.79}$$

Here we have formulated a first generalized, and dimensionless form of Murray's law for arbitrary noisy flow patterns of arbitrary mean directionality. At this point we would like to discuss several strategies to make this approach fit for applications on real flow networks. First one may simplify the equations (3.78), (3.79) significantly by considering the following: When all randomly fluctuating sinks are uncorrelated yet identically distributed, we have $\langle s_v \rangle = \mu$ and $\langle s_v s_w \rangle = \delta_{vw} \sigma^2 + \mu^2$, as discussed in section 3.1.1. Making this assumption simplifies the term (3.77),

$$\frac{\sum_{vw} A_{vw}^e \langle (s_v - \langle s_v \rangle)(s_w - \langle s_w \rangle) \rangle}{\sum_{vw} A_{vw}^e \langle s_v \rangle \langle s_w \rangle} = \lambda_3 \frac{\delta \phi_e}{\phi_e} \tag{3.80}$$

with the fluctuation strength λ_3 as defined before. Furthermore we chose our unit system such that then we have $\langle s_v^* \rangle = 1$ which leads to the final result,

$$\sum_{\in inc(v)} a_e r_e^{*3} = 1 \tag{3.81}$$

$$\text{with } a_e = \Theta_{ve} \sqrt{\frac{\lambda_2}{1 + \lambda_3 \frac{\delta \phi_e}{\phi_e}}}$$

It is interesting to note at this point that increased fluctuation ratios λ_3 tend to decrease the magnitude of the coefficients a_e as $\frac{\delta \phi_e}{\phi_e} \geq 0$. This naturally transits back to Murray's law for vertices with sinks as the noise perturbation become small $\lambda_3 \to 0$. In this particular case we have all edges entering equation (3.81) with the same weighting. But for any $\lambda_3 > 0$ we find the network's source-sink distribution and radii distribution to impact the branching relation due to $\frac{\delta \phi_e}{\phi_e}$. Now, this ansatz might not seem of much an advance at first as we have increased the complexity of the original problem by two additional, abstract coefficients, rendering the original power law fitting method useless unless all model parameters are known. We find this not to be a bug but a feature

though, as we have the previously abstract and non-approachable model parameters λ_2, λ_3 encapsulated in a purely geometric relation, allowing for their direct interpolation, given we know the radial distribution. We will discuss this subject in further detail in section 3.3.2, and subsequently demonstrate the effectiveness of this approach for Kirchhoff networks.

Murray's Law for extended metabolic costs models

As we have shown in the previous section it is possible to incorporate complex flow landscapes into Murray's law in the form of non-trivial coefficients a_e. In this section we would like to discuss a generalization of Murray's Law when considering complex metabolic cost functions (without fluctuations) as proposed in section 2.2.2 for the case $\gamma = 0.5$,

$$\Gamma = \sum_e a_0 L_e \left(\frac{f_e^2}{K_e} + a_2 K_e^{1/2} \right) + a_1 \Gamma_0 \tag{3.82}$$

$$\text{with } \Gamma_0 = \sum_i \Gamma_i + \sum_{ij} \Gamma_{ij} + ... \tag{3.83}$$

where Γ_i, Γ_{ij} are additional arbitrary metabolic costs for monolayer and multilayer systems. Without loss of generality we may choose those here to be dimensionless and have a_1 act as proportionality factor. There are no fluctuations included in this framework. In order to establish the branching relations we first have to construct the dynamical system again and look for it's stationary points in the familiar manner proposed in section 3.2,

$$\partial_t r_e \propto a_0 \left(\left(\frac{f_e}{r_e^3} \right)^2 - \left(\frac{\pi}{8\eta} \right)^{3/2} a_2 \right) r_e - a_1 \frac{4\eta L_e}{\pi} \left[\nabla_r \Gamma_0 \right]_e \tag{3.84}$$

$$\Leftrightarrow \frac{\partial_t r_e^*}{r_e^*} \propto \left(\left(\frac{f_e^*}{r_e^{*3}} \right)^2 - \lambda_2 \right) - \lambda_1 \left(\frac{L_e}{r_e} \right) \left[\nabla_{r^*} \Gamma_0 \right]_e \tag{3.85}$$

$$\frac{\partial_{t^*} r_e^*}{r_e^*} = 0 \Rightarrow f_e^* = r_e^{*3} \sqrt{\lambda_2 + \lambda_1 \left(\frac{L_e}{r_e} \right) \left[\nabla_{r^*} \Gamma_0 \right]_e} \tag{3.86}$$

with volume penalty $\lambda_2 = \left(\frac{\pi}{8\eta} \right)^{3/2} \frac{L^3}{\mu^2} a_2$ and $\lambda_1 = \frac{4\eta L^4}{\pi \mu^2} \frac{a_1}{a_0}$. We use the unit system proposed in the previous section 3.1.2. We refer to λ_1 as coupling parameter as it corresponds for our purposes to the coefficients introduced in section 3.2.2. Subsequently we may insert equation (3.86) into the Kirchhoff current law (2.75) and get

$$\sum_{\in inc(v)} a_e r_e^{*3} = s_v^* \tag{3.87}$$

$$\text{with } a_e = \Theta_{ve} \sqrt{\lambda_2 + \lambda_1 \left(\frac{L_e}{r_e} \right) \left[\nabla_{r^*} \Gamma_0 \right]_e}$$

This provides us once again with a framework similar to the one derived in (3.81), preserving the volume penalty as parameter and adding a second interaction coefficient

to the parameter sets a_e, which scales any additional metabolic cost introduced to the Hu-Cai model. Furthermore, equation (3.87) naturally transits back to Murray's law for vertices with sinks as the couplings become very small $\lambda_1 \to 0$. Now we have to look out for the nature of Γ_0, as surging negative gradients may lead to solvability problems of (3.87). As demonstrated, it is consistently possible to incorporate complex cost function models and hydrodynamics into geometric scaling relations. In particular, assuming a Hagen-Poiseuille flow we find the exponents of Murray's Law untouched and the relation generalized by adding sink terms and weighting coefficients. Now let us combine these approaches for multilayer networks as presented and discussed in section 3.2. Fortunately, combining the results in equations (3.81) and (3.87) is straightforward, so that we derive for either network the set of relations

$$\sum_{e_i} a_{e_i} r_{e_i}^{*,3} = 1 \tag{3.88}$$

$$\text{with } a_{e_i} = \Theta_{ve_i} \sqrt{\frac{\lambda_2 - \lambda_1 r_{e_i}^{*,-1} g_{e_i}^*}{1 + \lambda_3 \frac{\delta\phi_{e_i}^*}{\phi_{e_i}^*}}}$$

The effective coupling $g_{e_i}^*$ as defined in equations (3.54), (3.55). Here we see that fluctuations λ_3 and coupling λ_1 are seemingly antagonistically influencing the weighting coefficients a_{e_i}. We find the effective coupling term $g_{e_i}^*$ to considerably influence the solvabilty of the problem as it is the primary cause for sign changes in the root term in dependence of the exponent ε, see Figure 3.8. Furthermore we know the coupling term $g_{e_i}^*$ to incorporate the relation of each vessel to its local environment which is now encapsulated in the geometric scaling of the intertwined multilayer system proposed. In the next section we will test our ansatz in order to extract the parameter triplets $(\lambda_1, \lambda_2, \lambda_3)$ for a given set of Kirchhoff networks, with the radius distribution and sink placement being the only information available.

3.3.2 Interpolating model parameters for intertwined networks

In this section we intend to use the generalized version of Murray's law (3.88) to estimate model parameters such as effective coupling λ_1, volume penalty λ_2 and fluctuation λ_3 from given network structures.
Given any intertwined graph system, we shall apply equation (3.88) to all branching points of degree $d \geq 3$. Further, we identify the edge radii distributions in both networks, relevant length scales, the vertices' positions and a consistent placement of sink-sources in the system. As applying the fluctuation model of section 3.1.1, we only need information on whether a vertex is a sink or a source, not their actual mean values or variances of the flow. We further rewrite (3.88) for any junction as a root finding problem:

$$1 - \sum_{e_i} \Theta_{ve_i} r_{e_i}^{*,3} \sqrt{\frac{\lambda_2 - \lambda_1 r_{e_i}^{*,-1} g_{e_i}^*}{1 + \lambda_3 \frac{\delta\phi_{e_i}^*}{\phi_{e_i}^*}}} = \chi\left(\lambda_1^i, \lambda_2^i, \lambda_3^i\right) \tag{3.89}$$

Having acquired the radii, nodal positions and source-sink locations, we may evaluate the coupling terms g_{e_i} and effective pressure ratios $\frac{\delta\phi_{e_i}^*}{\phi_{e_i}^*}$ according to their definitions

given in (3.54), (3.54) and (3.17), (3.18). Then, we numerically find the roots of $\chi\left(\lambda_1^i, \lambda_2^i, \lambda_3^i\right)$ as formulated in (3.89), for a set of positive definite $\lambda_j^i \geq 0$, for every eligible junction in the system.
As we do not necessarily have information on the direction of the currents at the sink nodes, we do not have any specific information on Θ. Therefore we evaluate (3.89) for all relevant sign permutations at each branching, e.g. as depicted in Figure 3.21. Successfully acquired parameter triplets of the form

$$\boldsymbol{\lambda} = \left(\lambda_1^i, \lambda_2^i, \lambda_3^i\right) \tag{3.90}$$

are subsequently compared for their quality of fulfilling the root problem $\chi \to 0$. The triplet $\boldsymbol{\lambda}$ providing the smallest χ is forwarded for further analysis, while the rest is discarded.
Doing so we acquire the distributions of interpolated model parameters from static, geometric data of the graphs alone. These parameters may then tell us which state or interaction type a requested network system corresponds to, or whether the applied model is any good at all. As $\boldsymbol{\lambda}$ consists of effective dimensionless quantities one would need further information, e.g the fluid's viscosity or actual flow rates to interpolate the coefficients from the original metabolic cost functions (3.49).

Testing ideal Kirchhoff networks

Due to the highly non-linear nature of the problem (3.89) one might argue that a consistent derivation of model parameters from static data might prove fatal, as multitude of solutions and numerical artifacts occur. Therefore we suggest a test on ideal Kirchhoff networks for which this approach is designed in the first place. With this test we intend to demonstrate that consistent parameter estimation is indeed possible for linear networks and may be performed with high accuracy.
We initialize intertwined system, utilizing the framework discussed in section 3.2. The parameter triplets (3.90) $\boldsymbol{\lambda}$ are set symmetrically and fixed points of (3.34) are numerically acquired. We do so for repulsive and attractive coupling, as well as varying fluctuation levels. The sources were positioned in random vertices of the system. Here, all tests are performed on the intertwined Laves graphs, representing the network skeletons of the gyroid, resulting in an abundance of Y-junction by default. In Figure 3.22 and 3.22 we represent such numerically acquired parameter distribution for archetypal realizations of entangled networks. Generally we use a logarithmic rescaling of the parameter axis in order to find a symmetric representation of the histogram data, allowing us to perform a peak identification similar to [3]. Doing so we fit a normal distribution $\mathcal{N}(\mu, \sigma)$ to the histogram's maxima. Subsequently, we the terms $\mu_i\left(\log_{10}\lambda_i\right) \pm \sigma_i\left(\log_{10}\lambda_i\right) = \mu_i \pm \sigma_i$ to denote the characteristics of the distributions of $\log_{10}\lambda_i$ and evaluate the quality of the interpolation. In Figure 3.22 we present the results for repulsively coupled networks, with coupling exponent $\varepsilon = -1$.

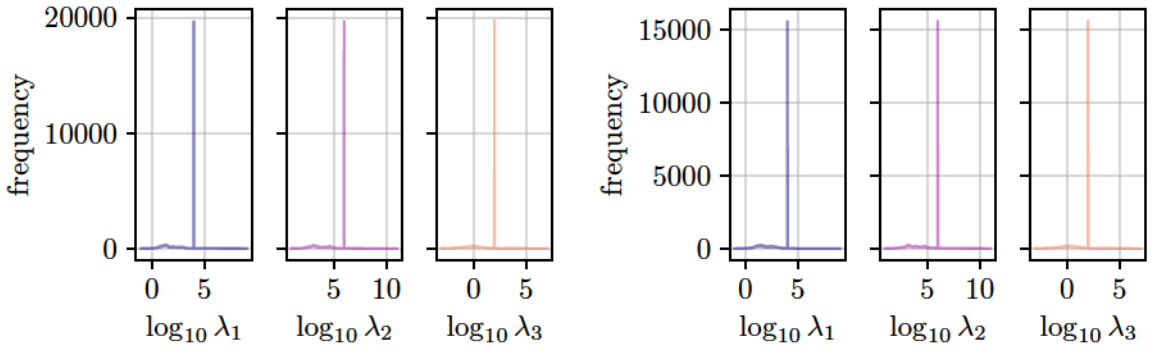

(a) $\boldsymbol{\lambda} = (10^4, 10^6, 10^2)$

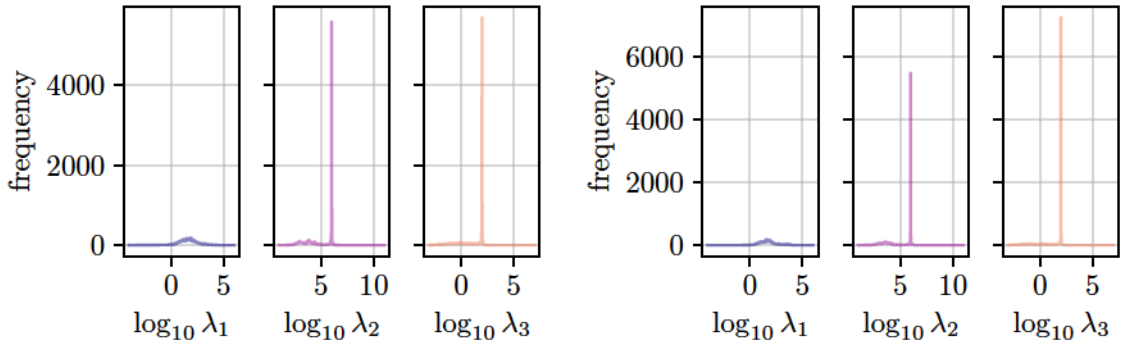

(b) $\boldsymbol{\lambda} = (10^1, 10^6, 10^2)$

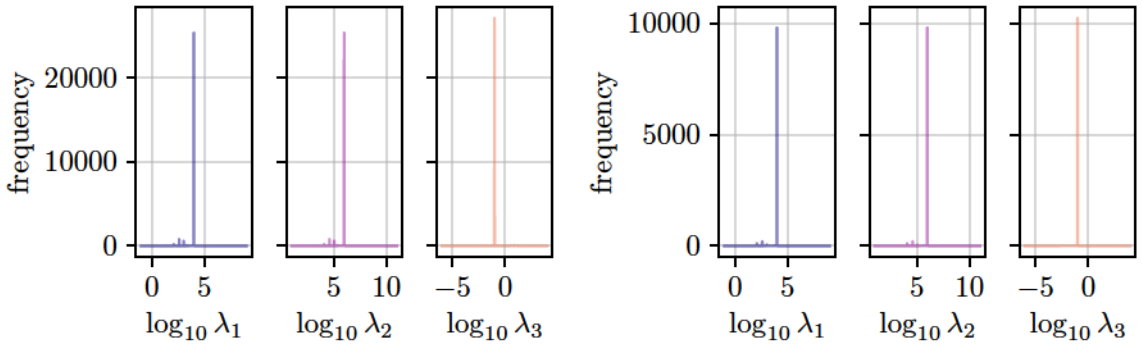

(c) $\boldsymbol{\lambda} = (10^4, 10^6, 10^{-1})$

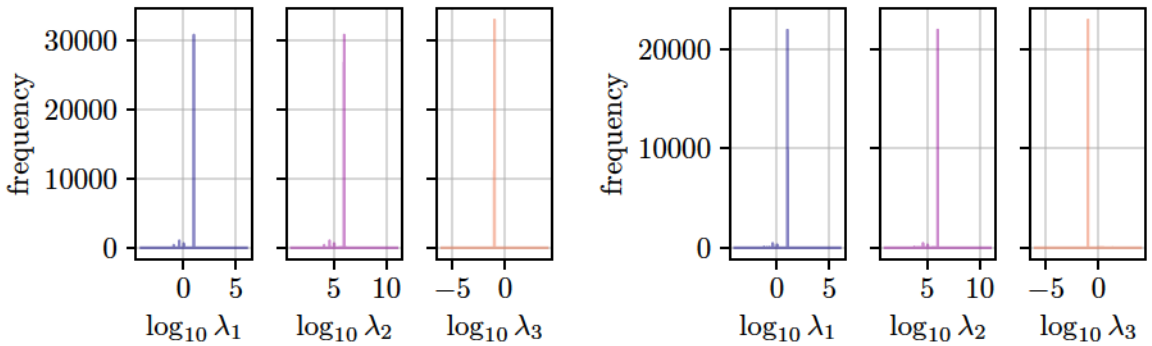

(d) $\boldsymbol{\lambda} = (10^1, 10^6, 10^{-1})$

Figure 3.22: Numerically extracting model parameters for repulsively coupled mono-source Kirchhoff networks, according to (3.89). Sub-captions indicate the model parameters as $\boldsymbol{\lambda} = (\lambda_1, \lambda_2, \lambda_3)$.

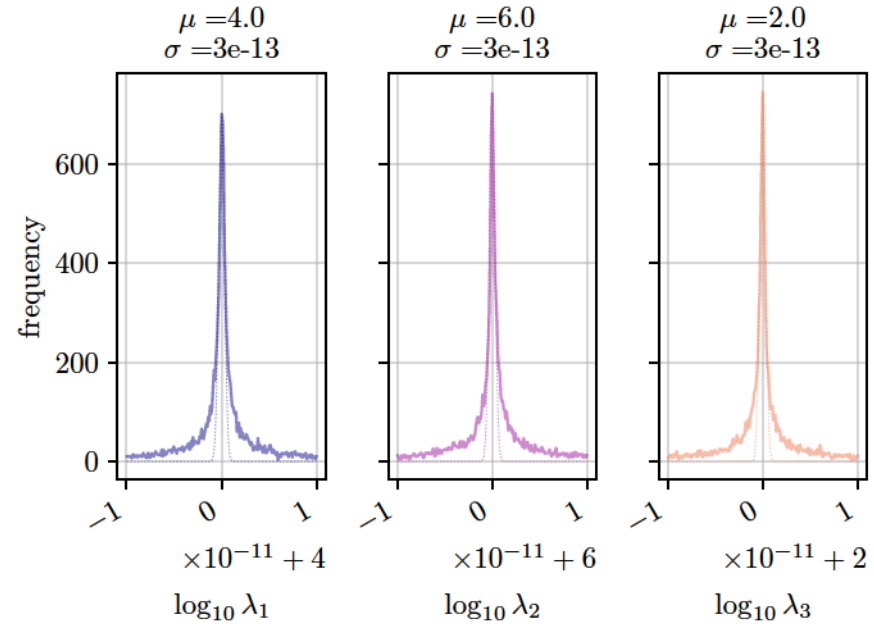

(a)

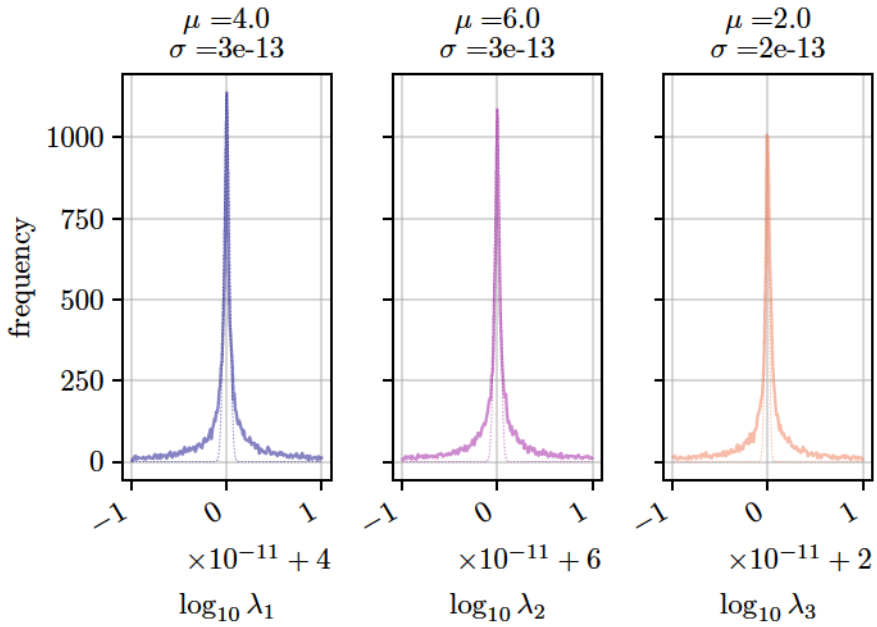

(b)

Figure 3.23: Under the microscope: Estimating distribution accuracy of main peak in 3.22a, for initialized parameters $\boldsymbol{\lambda} = (10^4, 10^6, 10^2)$. For repulsively coupled systems we find accurate estimates of the initial model parameters and find the variance for either network as $\sigma < 10{-}12$.

In Figure 3.24, we display the acquired distributions for attractively coupled networks with $\varepsilon = 3$. For the archetypal sets shown, we vary the strengths of λ_1 and λ_3, ranging from coupling dominated networks toward fluctuation dominated ones. We also explore the cases in between, for negligible interactions and simultaneously active ones. We see the applied model parameters indeed correspond to the emerging, sharp maxima in the distributions 3.23. We find these maxima to be in good agreement for the majority of sampled parameter scenarios. Subsequently we are able to identify which adaptation mechanism seems to be dominant in the system. Yet, one observes also the emergence of side maxima, and long-tailed side shoulders in the histograms. Usually one may ignore those due to the significance of the maxima. We further find small coupling parameters λ_1 to pose a problem in case of fluctuation dominated adaptation dynamics, as the estimations deviate here considerably from the initialized value and become broadly distributed. In Figure 3.23, we display the highly resolved maxima fo the distrubtions shown in Figure 3.22a. These peaks are of marginal width, while corresponding to the initial parameter triplets that where used to realize the adaptation problem. Generally we find the parameter estimations for repulsively coupled Kirchhoff networks to be as accurate for a wide range of model parameters.
For the archetypal sets shown, we once again vary the strengths of λ_1 and λ_3, ranging from coupling dominated networks toward fluctuation dominated ones. We also explore the cases in between, for negligible interactions and simultaneously active ones. Once again we are able to identify the initial parameter distributions and find high levels of accuracy. This may be particularly seen in Figure 3.25, where the maxima of 3.24a are displayed for higher resolutions. It seems here that the level of accuracy is worse than the one found for repulsive coupling. Nevertheless it becomes clear that the interactions in attractively coupled systems can be estimated with good confidence as well.
One may argue that real complex intertwined systems will have more elaborate source-sink configurations which might not be described with one effective source in the system. We tested such model cases with the clone source-model presented in section 3.1.1 and can provide yet again distinct estimation of the model parameters. So far we have not found any limitation of this approach for lumped parameter models. In the next section we shall apply our framework to real entangled vessel system to estimate effective model parameters of (3.88). Naturally this assumes that these vessel networks are indeed characterized by a repulsive or attractive interaction. Hopefully, this parameter estimation ansatz allows a quality test of the applied toy models ,which where discussed in section 3.2 and displayed a rich variety of network complexity.

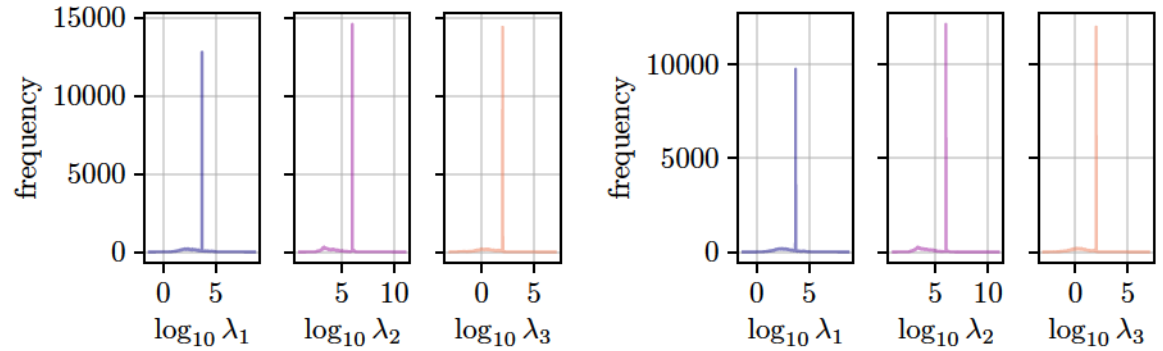

(a) $\boldsymbol{\lambda} = (5000, 10^6, 10^2)$

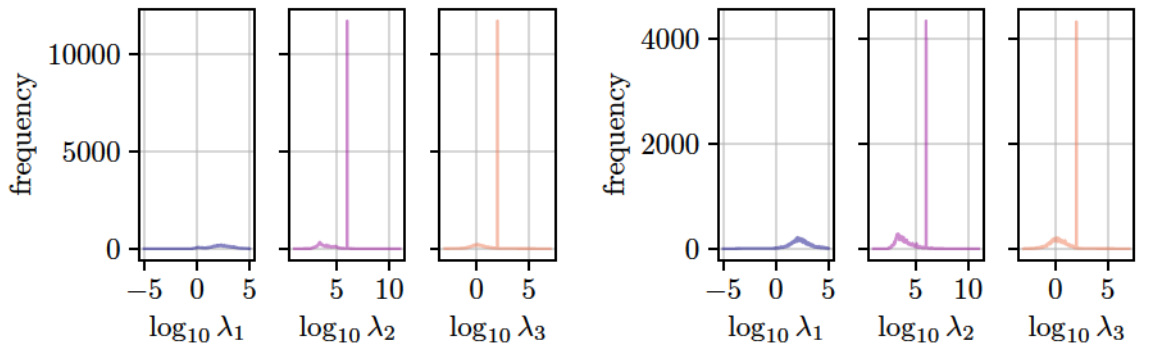

(b) $\boldsymbol{\lambda} = (10^0, 10^6, 10^2)$

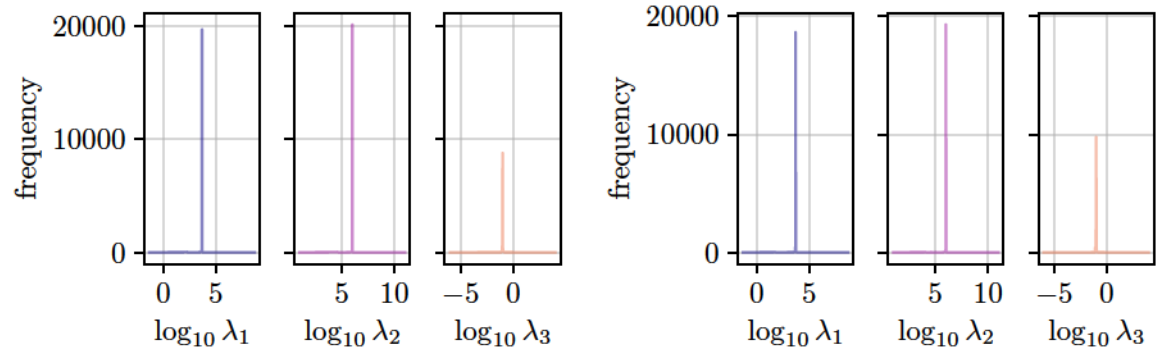

(c) $\boldsymbol{\lambda} = (5000, 10^6, 10^{-1})$

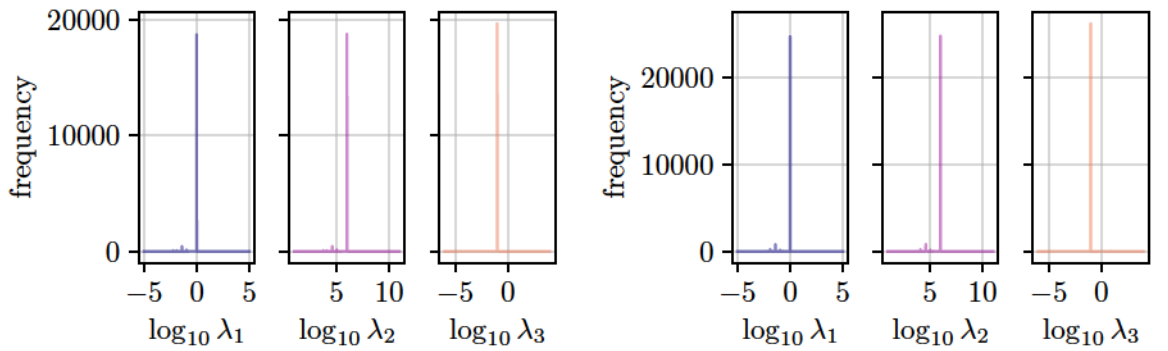

(d) $\boldsymbol{\lambda} = (10^0, 10^6, 10^{-1})$

Figure 3.24: Numerically extracting model parameters for attractively coupled mono-source Kirchhoff networks, according to (3.89). Sub-captions indicate the model parameters as $\boldsymbol{\lambda} = (\lambda_1, \lambda_2, \lambda_3)$.

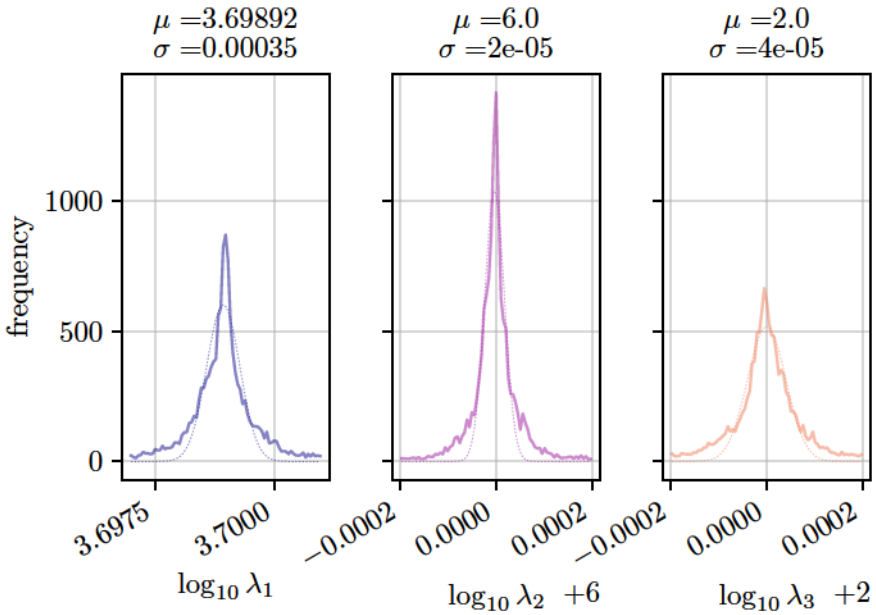

(a)

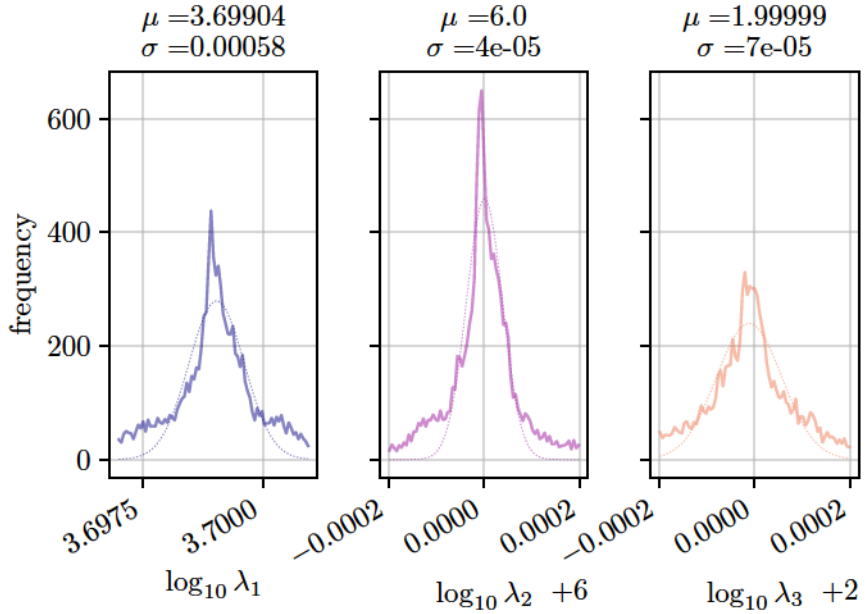

(b)

Figure 3.25: Under the microscope: Estimating distribution accuracy of main peak in 3.24a, for initialized parameters $\boldsymbol{\lambda} = (5000, 10^6, 10^2)$. For attractively coupled systems we find accurate estimates of the initial model parameters and find the variance for either network as $\sigma < 10{-}3$.

3.3.3 Identifying geometrical fingerprints in the liver lobule

In this section we intend to deploy the framework developed in the previous sections to the network skeletons of a real extracted vessel system. For that purpose we identify the relevant edge characteristics and affiliations of the extracted graphs of the sinusoids and canaliculi of the liver lobule, which we were highlighting in chapter 1.1.1. The sample we analyze is called a liver acinus, the tissue segment between the central vein and portal triad. A representation of the respective network skeletons is given in in Figure 1.1b, where the apparent cavity marks the position of the central vein. The data was provided by collaborators at the Zerial Lab, MPI-CBG in the following way: Mouse livers from adult mice were fixed by trans-cardial perfusion, sectioned into 100 mm serial slices, optically cleared and immunostained, as described in [88]. To visualize the different tissue components, the tissue sections were stained for nuclei (DAPI), cell borders (Phalloidin), bile canaliculi network (CD13), and the extracellular matrix (ECM, fibronectin and laminin) facing the sinusoidal network [90]. High-resolution images of the liver lobule (central vein, portal vein axis) were acquired by using confocal microscopy with a 63 $\times$/1.3 objective (0.3 μm voxel size). Finally, the resulting images were segmented and network skeletons containing mean vessel radii and vertex positions calculated with the *Motion Tracking* software as described in [88, 89]. We consider this vessel system, as mentioned earlier, an intertwined system and will therefore treat it as a coupled multilayer network as modeled in section 3.2. Assuming this toy model we deploy the generalized Murray law (3.89) for model parameter estimation. For a meaningful validation of (3.89) we need to establish vessel affiliations of the entangled networks as well as the source-sink distribution. For sinusoids we may consider any vertices along the central vein directly as sources. We consider any other nodes as sinks. Unfortunately we do not have detailed information about the portal triads' position so will we restrict the parameter estimation in this section to sinusoids only. As the vessel pieces form seemingly irregular grids we redefine affiliations between the two networks.

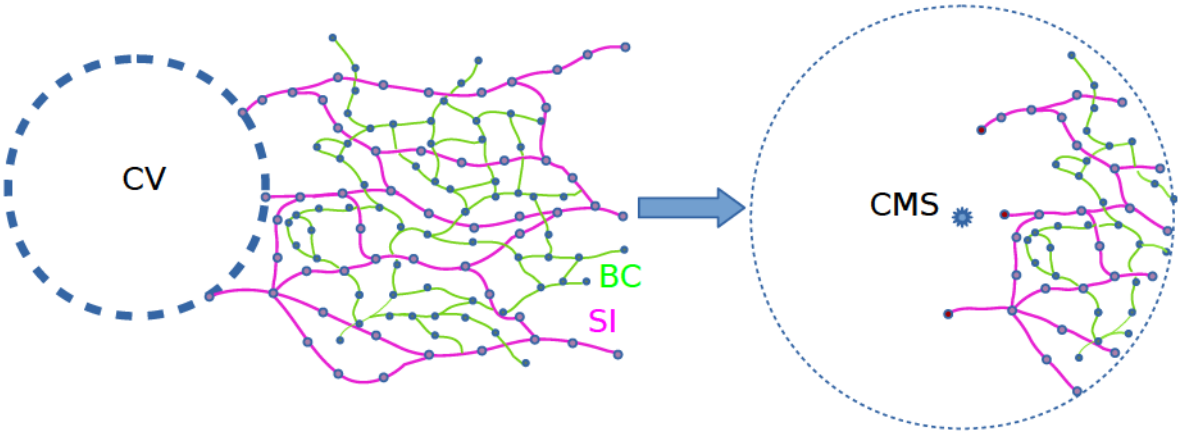

Figure 3.26: Setting the range of interest for the sinusoidal (SI) and bile canaliculi system (BC). *Left:* Vertices closest to the central vein (CV) are identified as sinks. *Right:* Determine geometric center of mass of all sinks (CMS) and discard all components, vertices, edges outside a set perimeter.

To do so efficiently we first reduce the complexity of the graph skeletons. In order to reduce the extracted skeleton's size and complexity, we only consider vessels inside a confined zone around the central vein and merge vessels along pathways. The applied reduction procedure is displayed in Figures 3.26, 3.27. First, the vertices in the sinusoidal network which are closest to the central vein are identified. Using these vertices, a geometric center of mass (CMS) is calculated and subsequently used as the center of a sphere of radius R, representing the range of interest, see Figure 3.26. Any edge consisting of two vertices outside the range of interest are discarded, leading to an effective reduction of graph size. Any further operations, such as coarse-graining, are conducted on these reduced structures. Next, all branching points in the sinusoidal network are identified and all paths $\boldsymbol{p} = (e_i, ..., e_j)$ consisting of consecutive edges e_i interconnecting these junctions. We proceed for the canaliculi the same way and check for each segment of a path $\boldsymbol{p}$ whether there is another segment of another network's path $\boldsymbol{p}'$ inside a perimeter δ, see Figure 3.27.

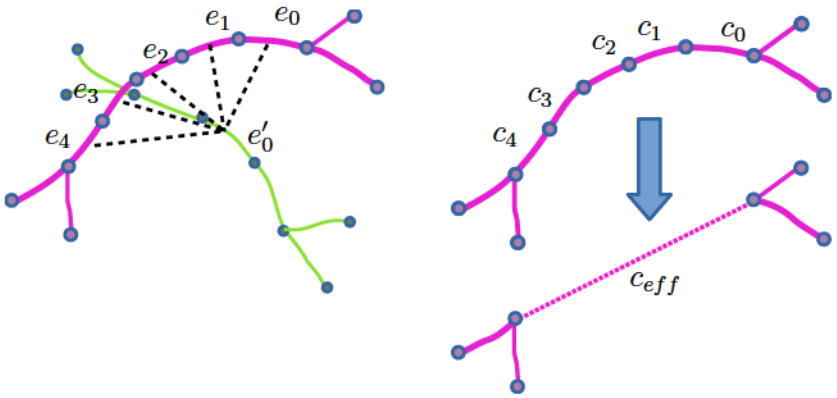

Figure 3.27: Coarse-graining the sinusoidal (SI) and bile canaliculi system (BC). *Left:* Deducting the distance of one path of a network to another path of the partner network by calculating the pair-wise distances of all path-segments and finding its minimum. *Right:* Coarse-graining paths into one effective edge, with new edge weight according to addition theorem $c^*_{eff} = \sum_e \frac{1}{c^*_e}$.

If so, these paths count as affiliated. Then we merge all edges along a path into a single edge by using the conventional addition theorems for series of resistors, as $c_{eff} = \sum_e \frac{1}{c_e}$, see Figure 3.27. The resulting analysis of these blood capillaries and secretion channels relies on the particular range of interest, namely the radius R and the affiliation perimeter δ will affect the estimation of the parameters $\log_{10} \lambda_i$. For example, see Figure 3.28, when increasing the affiliation parameter δ one will naturally increase the number of edges affiliated with each other, possibly linking vessel structures of several consecutive neighborhoods.
After all affiliations and source-sink relations are set we compute the coupling terms g^*_e and $\frac{\delta\phi^*_e}{\phi^*_e}$ for all coefficients in equation (3.89) using the multi-source to multi-sink approach as introduced in 3.1.1. We do so, as stated before, only for Y-junctions in the sinusoidal network. As there is no information on the nature of the coupling though, we attempt to screen through a range of potential coupling exponents ε. The intention is to identify potential parameter combinations for which the estimations become sufficiently narrow as was the case for ideal Kirchhoff networks.

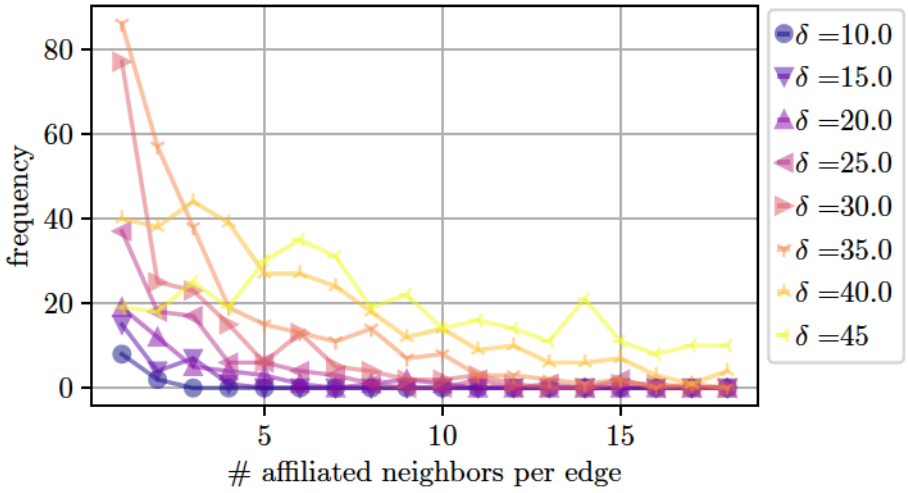

Figure 3.28: Histogram displaying the number of affiliated neighbors (edges) found for a given radius around a vessel (threshold, all values the inset in μm). Total number of pairings found overall for given threshold in the inset for set range of interest $R = 397\ \mu m$.

For the results presented here we chose the range of interest as $R = 390\ \mu$m and the affiliation perimeter $\delta = 30\ \mu$m). Proceeding like this, we end up with a reduced sinusoidal network, with $n = 318$ vertices and $m = 452$ edges. We find the parameter triplets $\boldsymbol{\lambda} = (\lambda_1, \lambda_2, \lambda_3)$ numerically by solving equation (3.89). Be reminded that we have introduced the parameters in the previous sections, with λ_1 as effective coupling, λ_2 as effective volume penalty and λ_3 as fluctuation rate. In Figure 3.29 and 3.30 we display the estimated distributions for selected ε depicting the different coupling regimes. We choose a logarithmic scale for the parameter axis, as done in the previous section, in order to simplify identification of the histograms maxima. We find the estimated parameter distribution for the attractively coupled network scenario to span several order of magnitude, see 3.29. As the distribution are further relatively noisy one find it inherently difficult to pin down a specific parameter realization of the model. We find the same to be true for the repulsive coupling scenario, where a shift of the estimated coupling λ_1 becomes apparent for smaller ε. We subsequently smooth the distributions for either case and apply Gaussian fits in order to identify the maxima positions and width. The smoothed histograms as well as the calculated means $\mu(\log_{10}\lambda_i)$ and standard deviations $\sigma(\log_{10}\lambda_i)$ are indicated in Figure 3.31. We find the parameter distributions to be considerably broadened single peak distributions, indicating relatively stable means for $\log_{10}\lambda_2$, $\log_{10}\lambda_3$ with varying means of $\log_{10}\lambda_1$ for exponent ε variations. Let us discuss the particular differences for repulsive and attractive coupling in detail.
From the previous section 3.2.4, we concluded that attractively coupled networks ($\varepsilon > 1$) are able to generate robust, reticulated structures for increased coupling rates of λ_1 and are potentially in competition with flow fluctuations λ_3.

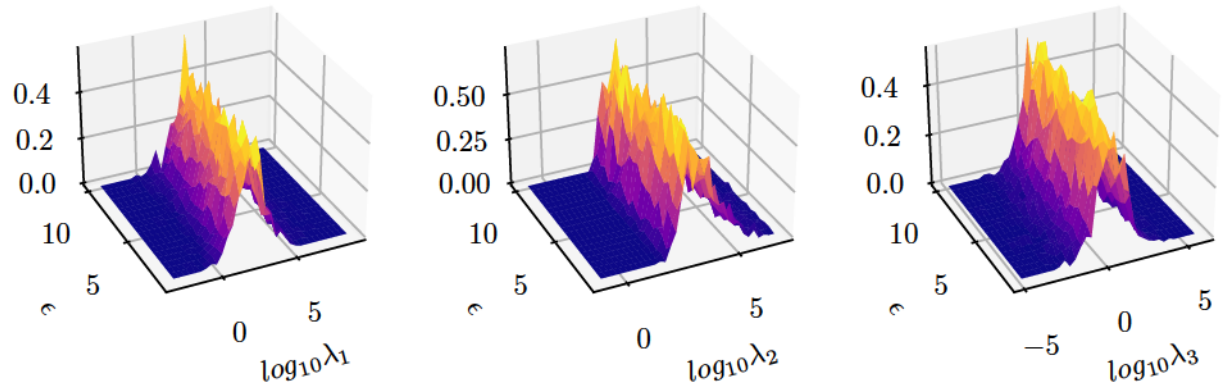

(a) (b) (c)

Figure 3.29: Estimated parameter distributions for attractive coupling $\varepsilon > 1$ utilizing (3.89): Displayed are the relative frequencies of estimated model parameters for various positive coupling exponents.

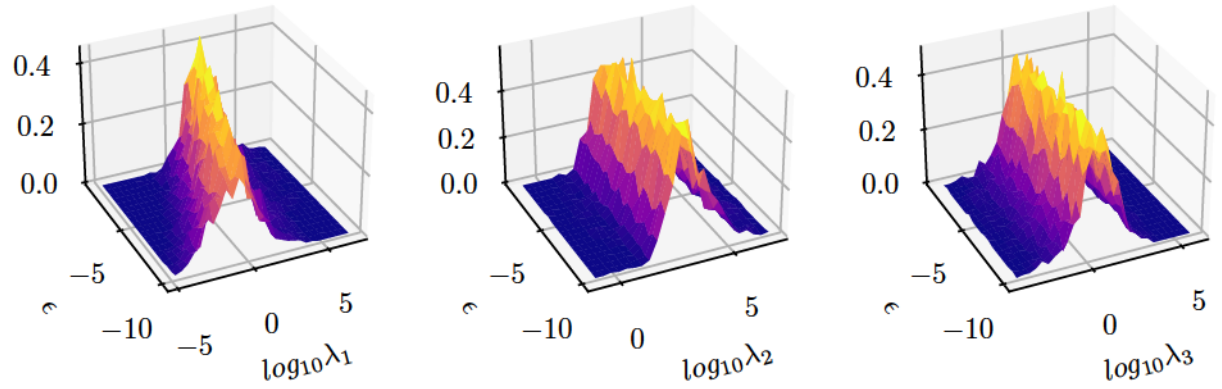

(a) (b) (c)

Figure 3.30: Estimated parameter distributions for repulsive coupling $\varepsilon < 0$ utilizing (3.89): Displayed are the relative frequencies of estimated model parameters for various negative coupling exponents.

The estimates for the attractive coupling case in Figure 3.31a indicate that increased fluctuation rates are present $\mu(\log_{10}\lambda_3) > 0$ which may account for reticulated structures in flow driven adaption. Further, we observe monotonically increasing rates of coupling for increasing ε. We find the coupling rates poised just below the actual onset of the topological transition, e.g. $\mu(\log_{10}\lambda_1) \pm \sigma(\log_{10}\lambda_1) = 2.56 \pm 1.04$, for the coupling exponent $\varepsilon = 3$.
Further we find the repulsive coupling case to reproduce the same regime of values for $\log_{10}\lambda_2$, $\log_{10}\lambda_3$, indicating reticulation by flow fluctuation. Yet the coupling parameter $\mu(\log_{10}\lambda_1)$ displays a monotonically decreasing behavior for decreasing values of ε, as depicted in Figure 3.31b. Those low values of $\log_{10}\lambda_1$ suggest repulsive interactions

to be negligible as the estimates lie far from the regimes with topological implication, e.g., $\mu(\log_{10}\lambda_1) \pm \sigma(\log_{10}\lambda_1) = 1.94 \pm 1.03$ for the coupling exponent $\varepsilon = -1$.
Unfortunately, all estimates $\mu(\log_{10}\lambda_i)$ are accompanied by large standard deviations, which in the logarithmic context correspond to orders of magnitudes. Further, we find no indication for a specific coupling scenario ε, e.g., based on a collapse of the standard deviation for a specific ε, parameter distributions contradicting topological structure, etc. We suspect these issues to originate from several sources: inherent limitations of the toy model, segmentation inaccuracies during image analysis, crude approximation of the sink-source landscape of the system, the chosen algorithm of complexity reduction, and ambiguity of numeric solutions due to the non-linearity of the problem. Nevertheless, the fact that we find a confined distribution at all is significant, as it also gives way to further interpretation: Assuming the that our toy model for intertwined networks is actually appropriate, we find this to indicate that real network morphogenesis is determined by locally valid parameters $\boldsymbol{\lambda}$, representing the specific behavior of individual vessels, rather a small set of globally valid $\boldsymbol{\lambda}$. This particularly corresponds to the arguments of Pries et al [106], which indicated locally shifting wall-shear stress levels in a vascular bed.
Ultimately, the very fact that we only make an educated guess about the adaptation mechanisms might exclude other essential principles of self-organized vessel adaptation in the liver lobule. Nevertheless, considering these findings and the restrictions of our model's approach, we assume the emergence of reticulated sinusoidal structures to be the product of flow fluctuations rather than of the newly proposed geometrical interactions. Though attractive coupling can not be totally ruled out as a factor. With this technique, we have shown that it is possible to extract order of magnitude *estimates* of otherwise inaccessible parameters of real adapting biological networks, and in doing so to make qualitative statements about the *relative* strength or importance of different feedbacks. We expect this ansatz to come in particularly handy in future work, when identifying potential cost function parameters for even more elaborate cost models.

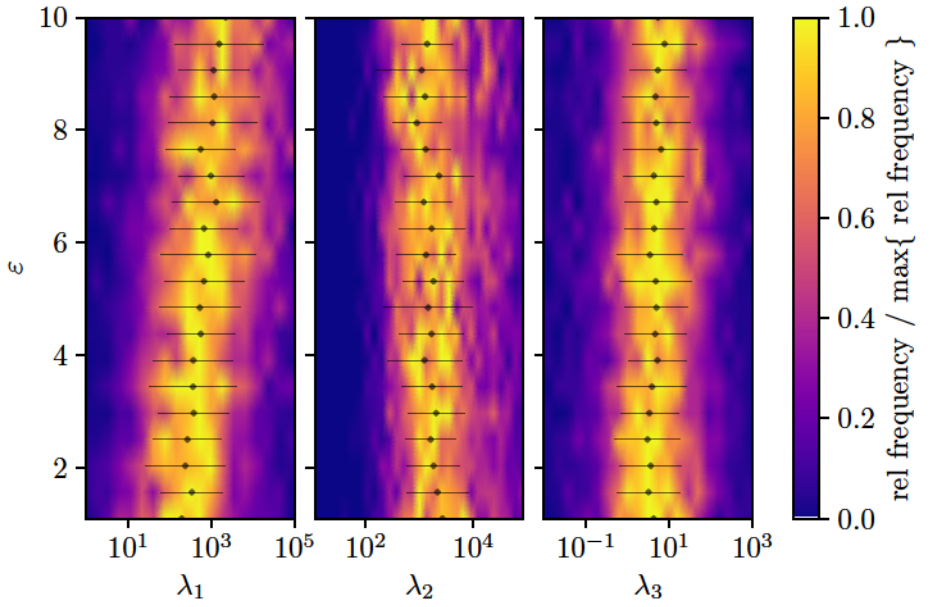

(a) Attractive coupling

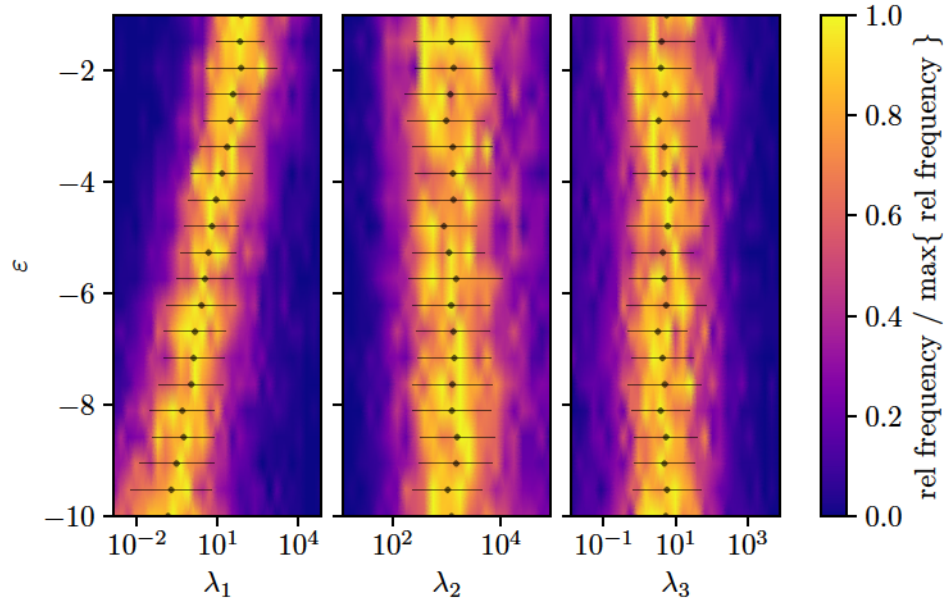

(b) Repulsive Coupling

Figure 3.31: Combining estimated parameter distributions and acquired data means and standard deviations: The normalized, smoothed histograms are indicate for the effective model parameters of (3.89) for (a) attractive coupling and (b) repulsive coupling, which both display broad distributions.

3.4 On the optimization of metabolite uptake in complex flow networks

We have pointed out in chapter 1 that the primary function of capillary systems is to supply tissues with crucial metabolites such as oxygen, glucose, salts etc. It seems therefore natural to describe this phenomenon in terms of self-organized adaptation models which have been used so far in order to account topological complexity. Many network models have been proposed discussing complex flow landscapes in order to reach robust network structures during morphogenesis. In the context of capillaries one may ask though whether networks acquired by such flow landscapes are any good at transporting solutes to the tissue sections needed. Recent studies argue that this metabolite uptake itself presents a new level of complexity which considerably changes the emerging behavior during morpohogenesis [81, 45].
As indicated in 2.2.1, we focus on the transport of metabolites in accordance to the extended Taylor framework, modeling any transport facilitated by a passive hydrodynamic model inside a channel system. These kind of transport problems may be readily extended for linear networks enabling us to incorporate them into the metabolic cost function approach discussed in the previous sections. Furthermore we intend to customize our ansatz toward sinusoid-like systems, i.e. fenestrated capillaries which are meant to facilitate the transport cascade of metabolites into its surrounding tissue components and subsequent clearance of the products into secondary secretion networks. Subsequently we study and evaluate the interplay of wall-shear stress driven morphogenesis and metabolite uptake for networks of different spatial embedding and topological ramifications.

3.4.1 Metabolite transport in thin channel systems

As mentioned before we intend to study the complex metabolite uptake behavior in self-organizing biological flow networks. To do so we treat any representative vessel network again as Kirchhoff networks perfused by Hagen–Poiseuille flows. In this case we have the volume flow rate given as $f = \frac{\pi R^4}{8\eta L}\Delta p$. This ansatz considers the approximation of thin cylindrical vessels of radius R and length L being perfused laminar by a fluid of viscosity η and setting the conductivity on each link as $C_e = \frac{\pi R_e^4}{8\eta L_e}$. Given that a solute with concentration cross section average $\bar{c}$ is diffusing and being advected through this network we may apply the quasi-one dimensional relation (2.91) to every single channel, see section 2.2.1. As we intend to evaluate the metabolite transport on the smallest capillary scale we facilitate the reduced transport ODE as given in equation (2.93).

On single channel solutions

Reintroducing the Peclet number $Pe = \frac{uL}{D}$, the rescaled z-coordinate $z^* = z/L$ and rescaling the effective surface absorption rate $\bar{\beta} = \frac{\beta L^2}{D}$, we rewrite (2.93) as

$$\partial_{zz^*}\bar{c} = Pe\partial_{z^*}\bar{c} + \bar{\beta}\bar{c} \tag{3.91}$$

Interestingly when applied to a channel system as intended, equation (3.91) mathematically corresponds to the problem described by Heaton et al [54]. Here a dynamic diffusion problem on a network with absorption is turned into a second order ODE system of analogue shape by applying a Laplace analysis. Equation (3.91) may readily be solved such that we get

$$\bar{c}\left(z^*\right) = X_0 \mathrm{e}^{Y_0 z^*} + X_1 \mathrm{e}^{Y_1 z^*} \tag{3.92}$$

$$\text{with } Y_{0,1} = \frac{1}{2}\left(Pe \pm \sqrt{Pe^2 + \bar{\beta}}\right) \tag{3.93}$$

Further one deduces from the channel boundaries $\bar{c}\left(z=0\right) = \bar{c}_0$, $\bar{c}\left(z=L\right) = \bar{c}_L$ that the coefficients X_i are given as

$$X_0 = \frac{\bar{c}_L - \bar{c}_0 \mathrm{e}^{a_1}}{\mathrm{e}^{a_0} - \mathrm{e}^{a_1}} \tag{3.94}$$

$$X_1 = \frac{\bar{c}_0 \mathrm{e}^{a_0} - \bar{c}_L}{\mathrm{e}^{a_0} - \mathrm{e}^{a_1}} \tag{3.95}$$

Now we generalize these channel equations for arbitrarily directed edge e, whose end and starting vertices we label as $\omega\left(e\right)$, $\alpha\left(e\right)$. Hence we label all nodal concentrations as $\bar{c}_{e,0} = \bar{c}_{\alpha(e)}$, $\bar{c}_{e,L} = \bar{c}_{\omega(e)}$. Using this notation we may rewrite the concentrations $\bar{c}_e\left(z\right)$ of each link e as

$$\bar{c}_e\left(z^*\right) = \frac{\mathrm{e}^{\frac{Pe_e z^*}{2}}}{\sinh\left(\frac{x_e}{2}\right)}\left\{\bar{c}_{\omega(e)} \sinh\left(\frac{x_e z^*}{2}\right)\mathrm{e}^{-\frac{Pe_e}{2}} - \bar{c}_{\alpha(e)} \sinh\left(\frac{x_e\left[z^*-1\right]}{2}\right)\right\} \tag{3.96}$$

$$\text{with } x_e = \sqrt{Pe_e^2 + \bar{\beta}_e} \tag{3.97}$$

Each link is further assigned its cross section area $A_e = \pi R_e^2$. We use the result in (3.96) in combination with the one-dimensional version of Fick's law (2.68), to calculate the edge solute flux $I_e = A_e j_e\left(z^*\right)$ as

$$\begin{aligned} I_e\left(z^*\right) = \frac{q_e \mathrm{e}^{\frac{Pe_e z^*}{2}}}{\sinh\left(\frac{x_e}{2}\right)}\Bigg\{&\bar{c}_{\omega(e)}\left[Pe_e \sinh\left(\frac{x_e z^*}{2}\right) - x_e \cosh\left(\frac{x_e z^*}{2}\right)\right]\mathrm{e}^{-\frac{Pe_e}{2}} \\ &-\bar{c}_{\alpha(e)}\left[Pe_e \sinh\left(\frac{x_e\left[z^*-1\right]}{2}\right) - x_e \cosh\left(\frac{x_e\left[z^*-1\right]}{2}\right)\right]\Bigg\} \end{aligned} \tag{3.98}$$

$$\text{with } q_e = \frac{A_e D}{2L} \tag{3.99}$$

For further purposes we use the notation $I_e\left(0\right) = I_{\alpha(e)}, I_e\left(L\right) = I_{\omega(e)}$. In general we apply Dirichlet boundaries or mixed boundaries for any such edge depending on its position in the network, i.e. whether vertices are peripheral/terminal or internal. If the vertex is a terminal, representing the inlet of fluid and solute, we will set $I_{\alpha e} = J_0$. In case it's the outlet terminal we will for all further purposes set it as an absorbing boundary $c_{\omega(e)} = 0$. As an example, Figure 3.36 displays such a solution of (3.96),(3.98) for single channel system (equivalent to any linear refinement of the channel into a chain of channels). Now we may finally calculate the total solute uptake per edge e, as

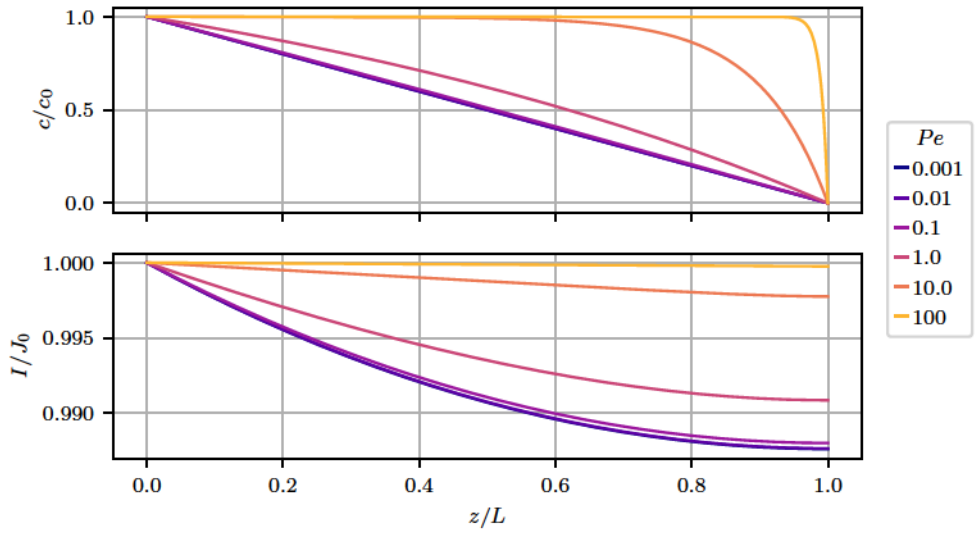

Figure 3.32: Single channel concentration and flux profile for the case of absorbing boundary according to (3.96) with relative uptake parameter $\bar{\beta} = 0.1$ and varying Peclet number Pe.

suggested in [81], as $\Phi_e = \beta L \int_0^1 \bar{c}_e(z^*)\, dz^*$ and eventually get

$$\Phi_e = q_e \left\{ \bar{c}_{\alpha(e)} \left[x_e \coth\left(\frac{x_e}{2}\right) - \frac{x_e e^{\frac{Pe_e}{2}}}{\sinh\left(\frac{x_e}{2}\right)} + Pe_e \right] + \bar{c}_{\omega(e)} \left[x_e \coth\left(\frac{x_e}{2}\right) - \frac{x_e e^{-\frac{Pe_e}{2}}}{\sinh\left(\frac{x_e}{2}\right)} - Pe_e \right] \right\} \tag{3.100}$$

The result in equation (3.100) represents the amount of solute removed per unit time by the entire absorbing surface of a single edge. To represent the effective uptake of any vessel we apply $log_{10}(\Phi/J_0)$ (fraction absorbed metabolite in comparison to the inlet flux of metabolite) of a single channel with absorbing boundary in Figure 3.33. The effective uptake Φ of a single vessel is determined by the landscape of Peclet numbers Pe and local uptake rates $\bar{\beta}$. It should be noted at this point that for any $\bar{\beta}$, Φ/J_0 tends to reach a maximum if $Pe \to 0$. Nevertheless the depicted behavior of (3.100) will naturally change if confronted with complex networks where the concentrations c_v have to be computed simultaneously for complex Pe_e landscapes and given sets of edge absorption $\bar{\beta}$.

On detailed absorption rate models

As demonstrated previously we are able to describe the metabolite uptake by consideration of an effective absorption rate $\bar{\beta}$. So far we haven't made clear how this parameter is actually dependent on the environment of the particular channel and to what microscopic absorption scenario it corresponds to. For that purpose we would like to discuss another one-dimensional toy model for a metabolite absorbing tissue (non-endocrine, no liquid exchange) as shown in Figure 3.34a. Here we consider the blood vessel (B)

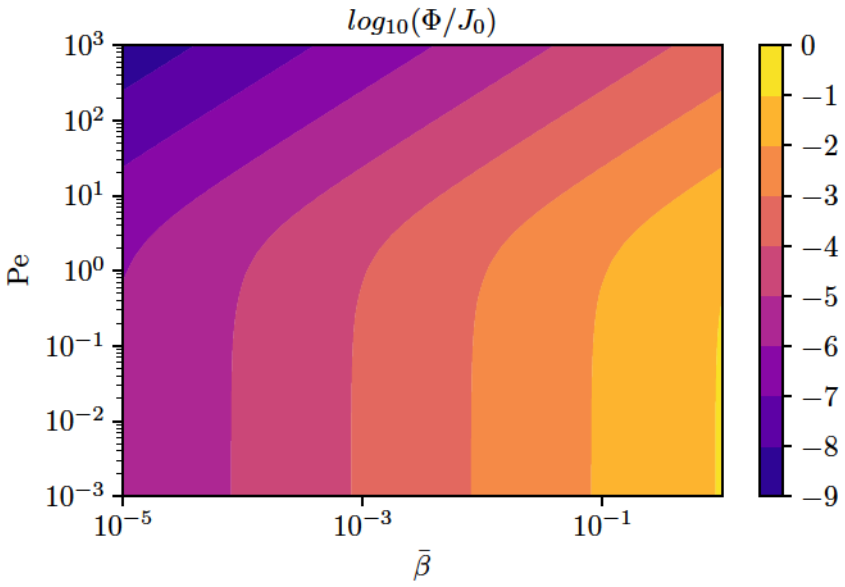

Figure 3.33: Effective solute uptake Φ/J_0 of a single channel with absorbing boundary according to (3.100).

to be evenly surrounded by a relevant section of tissue (e.g. hepatocytes, H), with a homogenous concentration of the solute of interest across the entire cross section. The solute is distributed over the length of the vessel such that we only care for its z dependency. The actual uptake process is here split into three main components: diffusion across the membrane with effective permeability p_{BH}, active transport α by membrane proteins and tissue clearance μ. With clearance we refer to metabolic processing of the particular chemical species as well as transport, i.e. diffusion or secretion, into different parts of the organ. All these parameters shall be molecule specific.

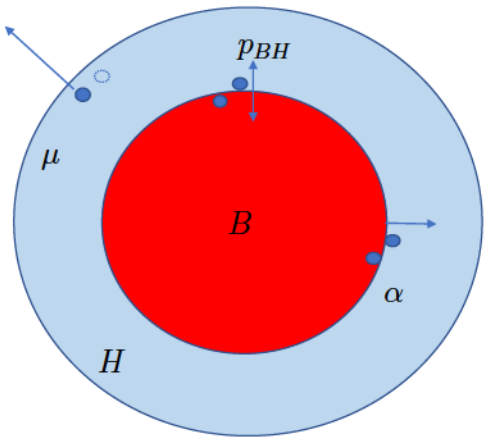

Figure 3.34: One-dimensional elimination model for uptake and clearance for solutes in blood capillaries: Conceptual cross-section with symmetric tissue environment, transport dependent on active transport α, cross-membrane diffusion p_{BH} and tissue clearance.

Considering these processes, one could formulate the concentration dynamics in the first order as continuity equations for the tissue c_H and the blood c_B as

$$\partial_t c_H(z) = p_{BH}[c_B(z) - c_H(z)] + \alpha c_B(z) - \mu c_H(z) \tag{3.101}$$

$$\partial_t c_B(z) = D\partial_{zz} c_B(z) - \bar{v}\partial_z c_B(z) - p_{BH}[c_B(z) - c_H(z)] - \alpha c_B(z) \tag{3.102}$$

Here it is assumed that the capillary is being perfused with mean velocity $\bar{v}$. The tissue itself is treated as a bath like environment where lateral transport is negligible in comparison to the solute exchange with the capillary The cross membrane transport by diffusion is here given in the first order of the concentration difference. While the solute clearance is only linearly dependent in this representation, one should be reminded as metabolic processing often is enzyme dependent. On the same note is to assume that transporter proteins in the membrane have an upper capacity. Here first approximations are usually Michaelis–Menten like kinetics of the form

$$\alpha \to \frac{\alpha_1}{\alpha_0 + c_B} = \alpha(c_B) \tag{3.103}$$

$$\mu \to \frac{\mu_1}{\mu_0 + c_H} = \mu(c_H) \tag{3.104}$$

Hence active transport and clearance is pending between two limit cases of unsaturated linear behavior and a constant capacity limit. We would like to focus in this thesis on the special case of unsaturated kinetics with $\alpha \to \frac{\alpha_1}{\alpha_0} = const$ and $\mu \to \frac{\mu_1}{\mu_0} = const.$ A more rigorous discussion on the other case of saturated kinetics is given in the appendix B.2 and outlook in chapter 4.
We solve the PDE system (3.101), (3.102) in accordance to the previous sections for the stationary case as

$$\partial_t c_H(z) = 0 \Rightarrow c_H(z) = c_B(z)\frac{p_{BH} + \alpha}{p_{BH} + \mu} \tag{3.105}$$

$$\partial_t c_B(z) = 0 \Rightarrow 0 = D\partial_{zz} c_B(z) - u\partial_z c_B(z) - \mu\frac{p_{BH} + \alpha}{p_{BH} + \mu} c_B(z) \tag{3.106}$$

So far we have required the continuity equation for the capillary concentration profile in accordance with the channel solution (3.91) and may rescale it to acquire

$$\partial_{zz^*} c_B(z) = Pe\partial_{z^*} c_B(z) + \bar{\beta} c_B(z) \tag{3.107}$$

with the effective surface absorption becoming

$$\bar{\beta} = \left(\frac{p_{BH}L^2}{D}\right)\left(\frac{\mu}{p_{BH}}\right)\left(\frac{1 + \frac{\alpha}{p_{BH}}}{1 + \frac{\mu}{p_{BH}}}\right) = \bar{p}_{BH}\left(\frac{\bar{\mu}}{1 + \bar{\mu}}\right)(1 + \bar{\alpha}) \tag{3.108}$$

Here we see from direct comparison with (3.91) that the effective absorption rate may be expressed as a non trivial factorization of the model parameters, where $\bar{\alpha} = \frac{\alpha}{p_{BH}}$, $\bar{\mu} = \frac{\mu}{p_{BH}}$ and $\bar{p}_{BH} = \frac{p_{BH}L^2}{D}$. Hence the magnitude of $\bar{\beta}$ actually depends on the interplay among membrane permeability, transporter activity and clearance as shown in Figure 3.35a. Given a fixed effective permeability $\bar{p}_{BH}$ we have the variation of transporter activity and clearance generate a variability of $\bar{\beta}$, meaning that high surface absorption rates may only be achieved for high clearance rates $\bar{\mu}$ combined with

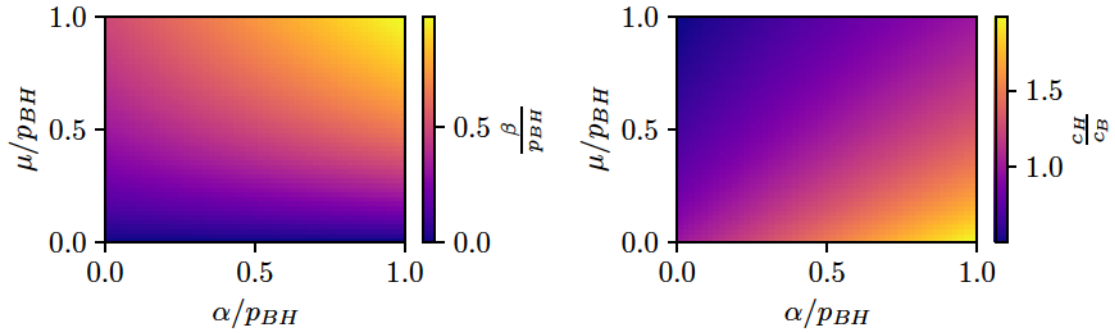

(a) (b)

Figure 3.35: One-dimensional elimination model for uptake and clearance for solutes in blood capillaries: (a) Effective absorption rate β in relation to the effective membrane permeability p_{BH} (b) Effective concentration balance for effective clearance and active transport.

high active transport. Subsequently one may interpret low $\bar{\beta} \to 0$ as regimes of low clearance rates. It is hard to pin down though by how much the concentration balance between the capillary and tissue is tilted, as can be seen in Figure 3.35b. This regime seems virtually unaffected by active transport. It should be noted that such transport models have already been discussed in different form, for extended Krogh models [44] or even multi-layer systems, e.g. regarding coarse grained hepatic elimination [117, 118], see appendix B.2. Yet, only in part have those been utilized for complex network and morphogenesis modeling. We shall generalize this ansatz for arbitrary networks and discuss the framework on the example of noisy flow landscapes. We particularly focus on the regime of small $\bar{\beta}$ for the rest of the thesis.

On linear network solutions

In this section we formulate the governing equations and solution algorithm for an arbitrary Kirchhoff network transporting a metabolite, given that the flow landscape $\boldsymbol{f}$ is known. To do so one may formulate the boundary conditions analogous to the Kirchhoff current condition, see (2.80). In particular the balance of solute in- and outflux J_v on each vertex sets the boundaries as

$$J_v = \sum_e B_{ve} I_e = \sum_{e \in out(v)} I_{\alpha(e)} - \sum_{e \in in(v)} I_{\omega(e)} \tag{3.109}$$

This set of boundary conditions determines the nodal concentration landscape $\bar{c}_v$. We solve these equations according to a method described by Koplik et al [64]: By sorting the combined equations (3.109) for the concentration terms, we bring them

to the form

$$\boldsymbol{M}\cdot\boldsymbol{c}=\boldsymbol{J} \tag{3.110}$$

$$\text{with } M_{vw}=\sum_e q_e\left[B_{ve}Pe_e+|B_{ve}|x_e\coth\left(\frac{x_e}{2}\right)\right]\delta_{vw} - \sum_{e\in out(v)} q_e\frac{x_e e^{-\frac{Pe_e}{2}}}{\sinh\left(\frac{x_e}{2}\right)}\delta_{\omega(e),w} - \sum_{e\in in(v)} q_e\frac{x_e e^{\frac{Pe_e}{2}}}{\sinh\left(\frac{x_e}{2}\right)}\delta_{\alpha(e),w} \tag{3.111}$$

We generally set $J_n\geq 0$ for any nodes with $s_n\geq 0$, thereby matching the sources and solute influx. For any $s_v=0$ we will also have $J_v=0$. In this thesis we only focus on a system with absorbing boundaries, setting a subset of nodes $c_w=0$ which coincide with the system's sinks, hence we rewrite (3.110) as

$$\tilde{\boldsymbol{M}}\cdot\tilde{\boldsymbol{c}}=\tilde{\boldsymbol{J}} \tag{3.112}$$

where $\tilde{\boldsymbol{M}}$ is the reduced matrix of $\boldsymbol{M}$, having the columns and rows $\{w\}$ removed, while $\tilde{c}_v>0$ and $\tilde{J}_v\geq 0$. The reduced system may then be solved uniquely by computing the inverse of $\tilde{\boldsymbol{M}}$. We would like to note at this point that the concentrations on the non-outlet nodes $c_v\neq 0$ become non-trivial functions of Pe_e and $\bar{\beta}$. Further, one may easily show that the total absorption of such a network is given by the balance of terminal fluxes

$$\sum_e \Phi_e=\sum_{v,J_v>0} J_v+\sum_{w,J_w<0} J_w \tag{3.113}$$

$$\Rightarrow \frac{\sum_e \Phi_e}{\sum_{v,J_v>0} J_v}=1+\frac{\sum_{w,J_w<0} J_w}{\sum_{v,J_v>0} J_v} \tag{3.114}$$

In general we will evaluate the left hand term for the system in order to characterize it. For the right-hand side we would need to evaluate $\sum_{w,J_w<0} J_w$ for which the respective J_w are yet to be computed from (3.111). In order to monitor the relative solute uptake of any complex network we define the order parameter

$$\sigma=\log_{10}\left[\frac{\sum_e \Phi_e}{\sum_{v,J_v>0} J_v}\right] \tag{3.115}$$

representing the overall fraction of solute absorbed in the network in comparison to the total amount of metabolites flushed into the system. Hence we get $\sigma\to 0$ if the network's vessel surfaces absorbs the entire injected solute and $\sigma\to-\infty$ if there is no absorption whatsoever.

On the uptake in spanning tree and reticulated networks

The framework presented so far enables us to compute the nodal concentrations and link-wise solute uptakes in the presence of a given flow landscape in a Kirchhoff network. We use this framework to point out the caveats of current flow driven adaptation models typically employed to generate topologically complex structures. To do so we shall deploy a compatible toy model for fluctuation driven reticulation in combination

with solute uptake, similar to [61]:
We utilize another time-scale separation model, i.e. in order to compute a noisy flow landscape, we construct the ensemble average of a set of individual flow realizations, which are generated by randomly removing links from the representative graph $G(V, E)$. With removing, we refer to setting the respective edge conductivity to $C_e^* \propto 10^{-20}$. During each individual realization we calculate a flow landscape according to (2.79). We iterate the entirety of edges in G, blocking any of them with probability p, corresponding to the construction of a pseudo-random graph (rejecting realizations with disconnected components). After matching all realizations with their respective conductivity tensors $\boldsymbol{C}_n$, we calculate the effective wall-shear stress as

$$\left\langle \left(\frac{\Delta p_e r_e}{L_e} \right)^2 \right\rangle = \sum_n \left(\Delta p_{e,n} \frac{r_{e,n}}{L_e} \right)^2 \tag{3.116}$$

This construct is then used to evaluate the stress driven network morphogenesis, as described in earlier sections,

$$\partial_t r_e = c_0 \left(\left\langle \left(\frac{\Delta p_e r_e}{L_e} \right)^2 \right\rangle - c_2 \right) r_e \tag{3.117}$$

Subsequently we compute the corresponding adaptation of the network for varying blockage probabilities p. Here we operate on hexagonal grids with sources and sinks strictly separated to the pins of opposing grid sites. We set the homogeneous length scale $L_e = L$ for links. All other nodes are considered source free. We acquire once again a topological transition in this model framework by varying p in accordance to the transition described in [61]. Although one may point out that our ansatz is allowing for multiple edges to be shut simultaneously, instead of realizing single edge blockage scenarios. In Figure 3.36, we display the spanning tree to mesh transition of such a network, and may be characterized by the nullity ϱ according to equation (3.35). It seems that this transition scales as $\varrho \propto p^{0.34}$, see Figure 3.37a. Once again we would like

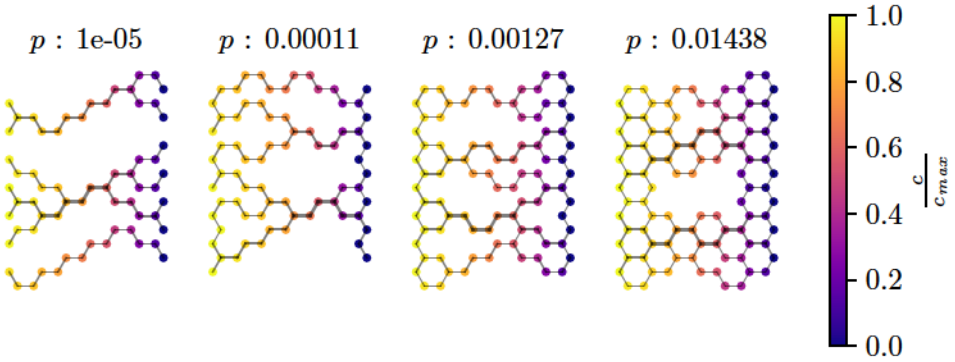

Figure 3.36: Link breakage probability $p > 0$ leads toward complex reticulated graph structures. The colormap indicates the resultant concentration profile of the case of an absorbing boundary problem, see (3.111) for $\bar{\beta} = 10^{-2}$.

to note that we only deployed this toy model to generate complex pruned networks with

characteristic noisy flow landscapes for further evaluation. We shall demonstrate now that any of these network's solute uptake capabilities are virtually independent of their p-dependent reticulation status. To do so we impose a solute influx on the source nodes and consider sinks as absorbing boundaries, as laid out in the previous section. For the final pruned networks we then recompute a noisy flow landscape due to random link blockage and evaluate the resultant concentration profiles according to (3.111). The resultant profiles for $\bar{\beta} = 10^{-2}$ are displayed in the color map of Figure 3.36. We further

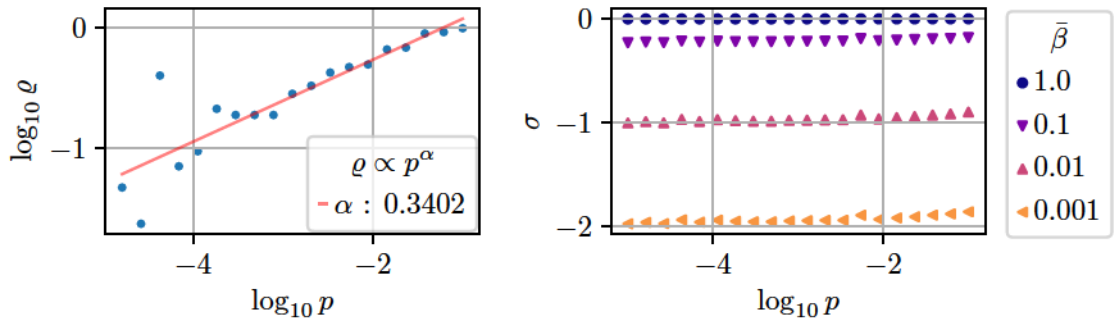

(a) (b)

Figure 3.37: Nullity transition ϱ and network filtration rate σ for link blockage variations p: (a) Link-blockage induced nullity transition follows a power law indicated by interpolation with exponent $\alpha \approx 0.3411$ (b) Overall filtration is predominantly dependent on $\bar{\beta}$ rather then the flow landscape in noisy, reticulated networks.

evaluated the concentration and uptake profiles for a range of different $\bar{\beta}$ for which the total network filtration σ, see equation (3.115), is displayed in Figure 3.37b. Here it becomes immediately clear that the topological complexity of the network, which makes it robust against random link failure and enables flow rerouting, does virtually nothing in improving the overall solute uptake capabilities. The differences of the respective flow landscapes in tree-like and mesh-like networks are negligible. We rather see a solemn dependency on the absorption rate $\bar{\beta}$ for the filtration rate σ. In Figure 3.38

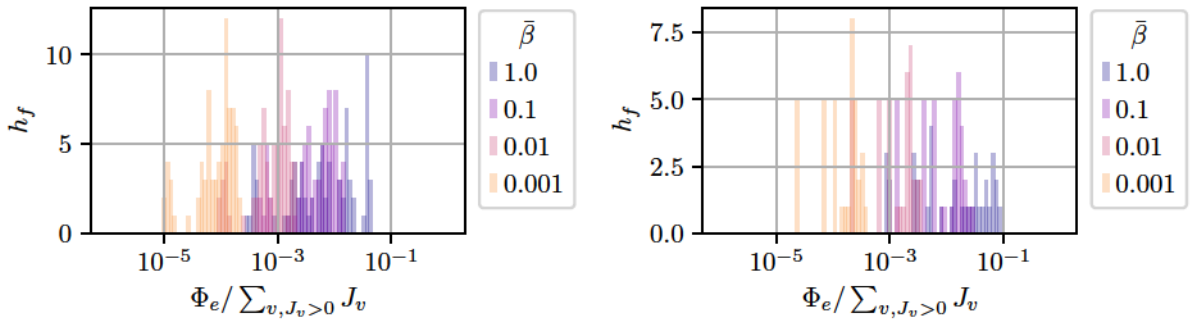

(a) Mesh, $p = 0.1$ (b) Tree, $p = 10^{-6}$

Figure 3.38: Histograms displaying single edge filtration rate $\Phi_e / \sum_{v,J_v>0} J_v$.

we display the link-wise filtration for spanning trees and reticulated systems in detail for a variation of $\bar{\beta}$. Though one observes a slight change of the uptake patterns it

is by far less significant than the changes resulting from $\bar{\beta}$. Now as mentioned in the previous sections, we consider $\bar{\beta}$ here a constant. On the other hand one should be reminded that $\bar{\beta}$ contains crucial information on the embedding as it may encapsulate the vessel membrane permeability, density of active surface transporters, clearance rates in the tissue etc. So this might suggest that robustness of biological flow networks is achieved by complex flow landscapes but its actual metabolite interaction is dependent on another level of complexity encapsulated by the absorption rate $\bar{\beta}$. But what if there is a mechanism to generate flow landscapes in order to shift σ for a given $\bar{\beta}$? Is it possible to reach arbitrary filtration σ and topological robustness simultaneously? Which topological structures, resulting from flow landscapes, reach desired filtration σ levels for any given $\bar{\beta}$? Or does one characteristic emerge independently from the other?

3.4.2 Optimizing metabolite uptake in shear-stress driven systems

As was demonstrated in [81], optimizing for homogeneous solute uptake in a flow network will not spark topological transitions or pruning events whatsoever, as long as no penalty for keeping vessels open is introduced. In this study's framework, edge radii were adapted effectively altering the flow landscape and subsequently the Peclet number distribution Pe_e of the network, thereby shifting the uptake capabilities of each vessel, e.g. see Figure 3.33. As we have demonstrated in the previous section, one does not find such adapted Peclet number distributions in the case of noise induced reticulation models and therefore only a $\bar{\beta}$ dependency on the uptake capabilities. We would like to extend these frameworks by combining the conventional wall-shear stress adaptation model with the solute uptake model discussed so far.
In this study we consider a dissipation-volume minimizing system equivalent to (2.95), in combination with the metabolic needs of the surrounding tissue. Each vessel is to be surrounded by tissue to which it is supplying a metabolite, as described in 3.4. Each element of tissue i demands a basic influx of solute $\Phi_{0,e}$ possibly mismatching the current uptake Φ_e provided by the embedded vessels. We define a mismatch cost $S(\mathbf{\Phi}, \mathbf{\Phi}_0) \geq 0$ and write

$$\Gamma = S(\mathbf{\Phi}, \mathbf{\Phi}_0) + \sum_e \alpha_1 \frac{f_e^2}{K_e} + \alpha_0 K_e^\gamma \tag{3.118}$$

This mismatch $S(\mathbf{\Phi}, \mathbf{\Phi}_0)$ we formulate as a metabolic cost which is to be minimized. Doing so we create a system for a given absorption rate $\bar{\beta}$ where vessels are allowed adjust their individual radii, which will alter the flow landscape and the local Peclet numbers. The impact of the simultaneously given dissipation-volume constraints, as in (2.94), is administered via the coupling parameters α_0, α_1. This approach assumes that individual vessels act as fair players by adapting toward a specific need and not beyond that. On the other hand it is to assume that tissues are to be saturated at a certain point with the metabolite of need. Any further supply beyond the preferred might present a toxic overdosing, and shall be treated as such here. Therefore we shall construct $S(\mathbf{\Phi}, \mathbf{\Phi}_0)$ in such a way that deviation from the demand $\mathbf{\Phi}_0$ is penalized. Generally we intend to construct the mismatch $S(\mathbf{\Phi}, \mathbf{\Phi}_0)$

such that a certain value of σ is preferred (3.115). We therefore expect the stimuli given by wall shear stress and uptake optimization to compete against each other. The radii changing optimization of equation (3.118) is performed using a gradient descent approach. For the numerical evaluations presented in the following sections, we orientate ourselves once again at the scheme presented in section 2.2.2. First we initialize a graph with a given reduced conductivity matrix $\boldsymbol{K}_0$ and boundary conditions of sources and sinks $\boldsymbol{s}$, flux boundaries on the source nodes $J_v > 0$ and absorbing boundaries on the outlets $c_v = 0$. In order to reduce the problem's complexity we focus here on the special case of constant channel length throughout the system $L_e = L$ and set $\gamma = 0.5$. We set a optimization threshold $\delta > 0$ and integrate the dynamical system derived from (3.118), using explicit numerical solvers, incorporating the following steps :

1. Compute the pressure and current landscape $\boldsymbol{p}_n$, $\boldsymbol{f}_n$ according to (2.78), (2.81)
2. Compute the concentration and uptake landscape $\boldsymbol{c}_n$, $\boldsymbol{\Phi}_n$ according to (3.100),(3.111)
3. Compute $\partial_t \boldsymbol{r}_n$, with $\partial_t \boldsymbol{r}_n \propto -\nabla_r \Gamma$
4. Check if $\sum_e \|\partial_t \boldsymbol{r}\|^2 \leq \delta$, if true: break
5. Compute increment and next time step $\boldsymbol{r}_{n+1}$, using for example Runge-Kutta or LSODA [138]
6. Check for pruning events, if $r_{e,n+1} \leq r_{crit}$, edge e is removed from the graph
7. Return to first step

Naturally this allows us only to find local minima of Γ depending on its initial $\boldsymbol{K}_0$ and boundary conditions. In appendix B.1 we give a detailed account on the derivation of the necessary Jacobian matrices for $\boldsymbol{\Phi}$, $\boldsymbol{c}$ and $\boldsymbol{Pe}$. In the next section we elaborate on the mismatch $S(\boldsymbol{\Phi}, \boldsymbol{\Phi}_0)$ for specific embedding and uptake scenarios.

Link-wise supply-demand model

Similar to previous setups in [66, 81, 107] we will focus here on a vessel network embedded in a tissue environment, where each vessel is surrounded by a service volume it supplies. Generally speaking these service volumes are ensembles of cells forming an effective bulk environment, signaling affiliated vessels to adjust absorption properly. Each such service volume demands a basic influx of solute $\Phi_{0,e}$ possibly mismatching the current uptake Φ_e provided by the embedded vessel, see Figure 3.39a. This mismatch we formulate as a cost

$$S(\boldsymbol{\Phi}, \boldsymbol{\Phi}_0) = \sum_e (\Phi_e - \Phi_{0,e})^2 \tag{3.119}$$

Hence we write for the system cost (3.118),

$$\Gamma = \sum_e \left[(\Phi_e - \Phi_{0,e})^2 + \alpha_1 \frac{f_e^2}{K_e} + \alpha_0 K_e^{\frac{1}{2}} \right] \tag{3.120}$$

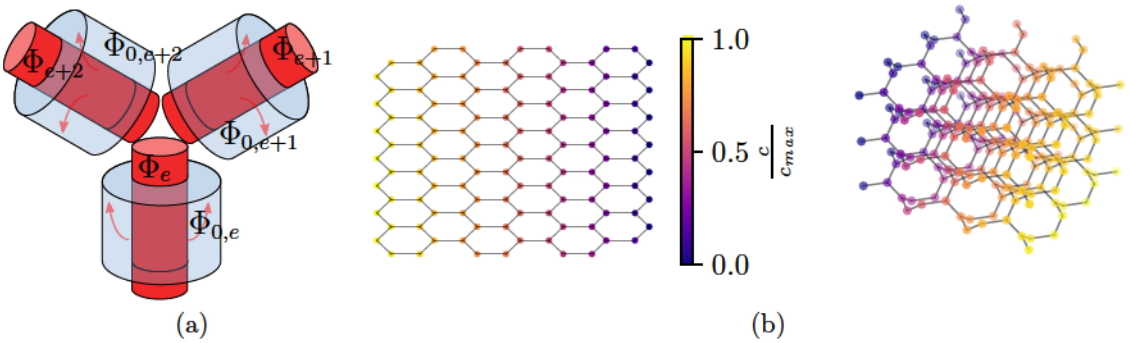

(a) (b)

Figure 3.39: Link-wise supply demand model: (a) Every edge is assigned a demand $\Phi_{0,e}$ it intends to answer by a supply Φ_e (b) Hexagonal grids and Laves graphs with multiple sources as inlet nodes for solutes and absorbing boundaries on the opposing graph side. The colormap indicates the normalized nodal concentrations.

In fact if the service volume demands are identical for the entire network we recreate the optimization framework studied in [81] extended by wall-shear stress driven pruning. It should be noted once again that in this model framework every link becomes an essential absorber and without any volume constraints, no pruning would take place whatsoever. We numerically solve the minimization problem in (3.120) by initializing a plexus in the form of planar hexagonal grids or laves lattices, see Figure 3.39b. We impose sources and solute influx on all vertices of one side of the lattice and sinks and absorbing boundaries on the opposing side. We initialize the system for different absorption rates $\bar{\beta}$ and demand ϕ_0 combinations, while scanning systematically for the impact of the dissipation feedback α_1 and the volume penalty α_0. In particular we here realize all vessels to correspond to a demand $\phi_{0,e}$ such that the network's demanded filtration rate would correspond to $\sigma_0 = \frac{\sum_e \phi_{0,e}}{\sum_{v,J_v>0} J_v}$. For the presented simulations, we initialize $\phi_{0,e}$ homogeneously across the network, we do so for $\bar{\beta}$ as well. Following the adaptation algorithm, as described in the previous section, we find the system's stationary states and analyze those for their nullity ϱ and actual filtration rate σ.
In Figure 3.40 we present the collected results, as state diagram grids for these parameter screens. These diagrams were obtained for the hexagonal lattice plexus, and we shall discuss the microscopic structures arising in such plexi later on. For the results on three-dimensional plexi see the appendix B.3.1. Note that the grid's x-axis is illustrating different cases of absorption rates $\bar{\beta}$ while the demanded filtration rate σ_0 variation is displayed on the grid's y-axis. In detail, we present the system's emerging nullity ϱ in Figure 3.40a, as defined previously in equation (3.35). In these diagrams we observe the networks reticulation to vary significantly, when exposed to the competing constraints of (3.120). For once we see that networks of high filtration demand depict a nullity transition pending between spanning trees and full plexus recovery. In accordance to previous studies on wall-shear stress driven adaptation we find that systems dominated by dissipation and volume penalty are developing into spanning trees. On the other hand we find the transition toward reticulated states shifting in dependence of the filtration demand σ_0 and absorption rate $\bar{\beta}$. Relating to the diagram grid 3.40a as a matrix, we find the upper triangle (top-left) as well as the diagonal (bottom-left to

top-right) elements, to display qualitatively similar pruning behavior in that matter. The lower triangle (bottom-right) in 3.40a, illustrates non-trivial state changes, so far unknown to us.

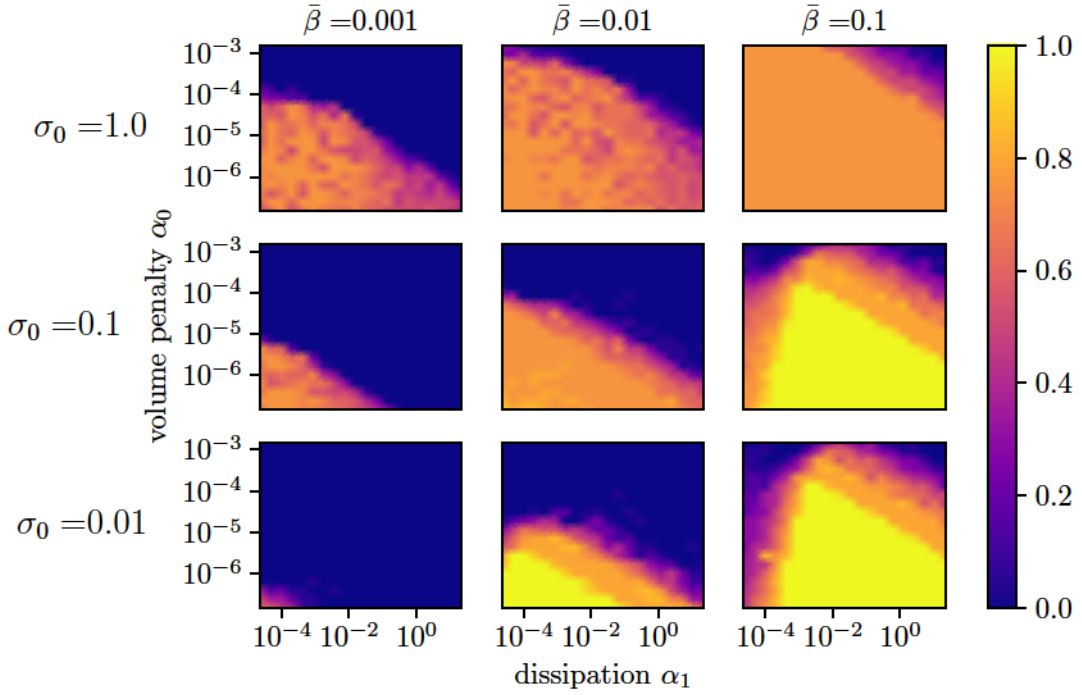

(a) Nullity ϱ

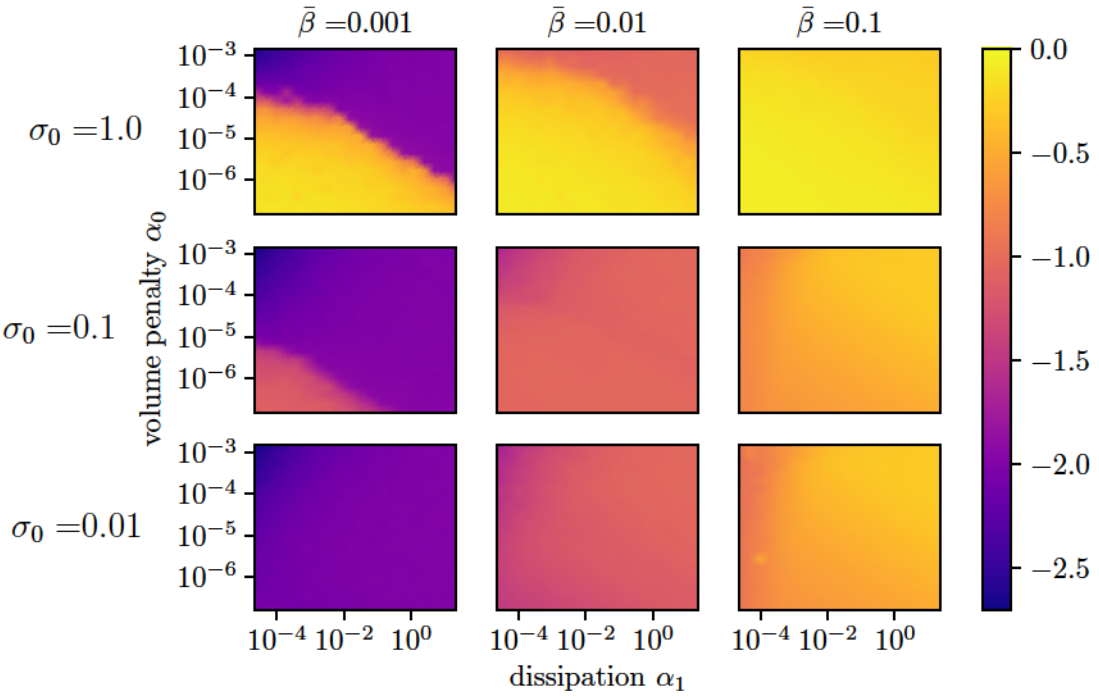

(b) Filtration σ

Figure 3.40: Nullity and filtration diagrams for stationary states of the cost problem (3.120), with boundary parameter variation $\sigma_0 = \frac{\sum_e \Phi_{0,e}}{\sum_{J_n>0} J_n} \in \{10^0, 10^{-1}, 10^{-2}\}$, $\bar{\beta} \in \{10^{-1}, 10^{-1}, 10^{-2}\}$; systematic volume penalty α_0 and dissipation α_1 are scanned systematically: (a) The nullity phase diagram indicates a topological transition and re entrant behavior. (b) Filtration diagram indicating varying quality of filtration adjustment for varying $\bar{\beta}$.

Here we observe the emergence of re-entry behavior, where we have spanning trees for low dissipation coupling α_1 turning into a full plexus recovery for an increase of α_1. Further increase in α_1 will result in the breakdown of said reticulation and enter the regime of wall-shear stress driven dominated adaptation again. We find this behavior to be limited by the volume penalty, as an increase in α_0 will ultimately result in the breakdown of the reticulated interim phase. As indicated by the grid layout, this behavior only seems to prevail in the case of small filtration demands paired with high absorption rates. In the second block, see Figure 3.40b, we display the network's collective filtration rate as defined in equation (3.115). Generally it becomes clear to see that the ability of a network to achieve its demanded filtration goal is dependent on the parameter initialization of σ_0 and $\bar{\beta}$. In analogy to 3.40a, walking through the upper triangle of the diagram grid, we find the filtration filtration to display qualitatively similar behavior. In particular we find that the initial filtration demand is quite well matched for the dissipation α_1 and volume penalty α_0 regimes which correspond to the reticulated states of the nullity diagram. We find the shift of this phase to correspond once again to the variation of σ_0 and $\bar{\beta}$. It appears that a decrease in these parameters results in a shift of the phase borders toward smaller dissipation and volume penalty. This comes somewhat intuitively, as such a decrease in σ_0, $\bar{\beta}$ generally corresponds to reduction of the demand-supply cost term in (3.120). Analyzing the diagonal we find the filtration goal to be seemingly matched for any kind of network topology, given the parameter space we explore at this point. The lower triangle displays a significant mismatch though, displaying in general the resulting filtration to be higher than initially demanded. Note that these are the data sets corresponding to the emergence of nullity re-entrant behavior discussed previously. Let us from here on discuss the resulting network topologies and uptake patterns in detail, we shall do for archetypal cases along the diagram grid's diagonal (top-left to bottom-right) elements. We shall discuss the nature of the newly emerging nullity phase transition and from there try to reason which of these states represent the behavior of actual vascular beds.
In Figure 3.41 we showcase exemplary network formations and concentration profiles, alongside detailed trajectories for nullity and filtration taken from the top-left diagrams in 3.40. This diagram's data corresponds to the case of high demand in $\sigma_0 = 1.0$ and paired with low absorption $\bar{\beta} = 0.001$. The stationary networks depicted in Figure 3.41a show that increasing α_1 will generally result in a nullity transition, displaying frustrations on the sink side for the reticulated case as well as the formation of dangling branches not connected to any sinks. This presents an interesting phenomenon, as is illustrates the ability of such a system to adjust toward the unfavorable initialization of σ_0, $\bar{\beta}$. Naturally, low $\bar{\beta}$ impair individual vessels from absorbing any significant amount of solute being advected. In the reticulated case for small α_1 we observe in general that the majority of vessel are dilated while the very peripheral connections to the sinks are degenerate and near seemingly near to collapse. As we operate on Neumann boundaries in order to calculate the volume flow rate of the Kirchhoff network we know that a constant amount of fluid is to be transported through the network per unit time. Hence by dilating the bulk of vessels one minimizes the overall Peclet numbers Pe in the system, which increases overall uptake, as previous mentioned in section 3.4.1 and illustrated in Figure 3.33a. Creating such a Peclet landscape is further resulting in a homogeneous concentration landscape, as the this scenario corresponds to a stationary diffusion problem for the bulk of network vessels.

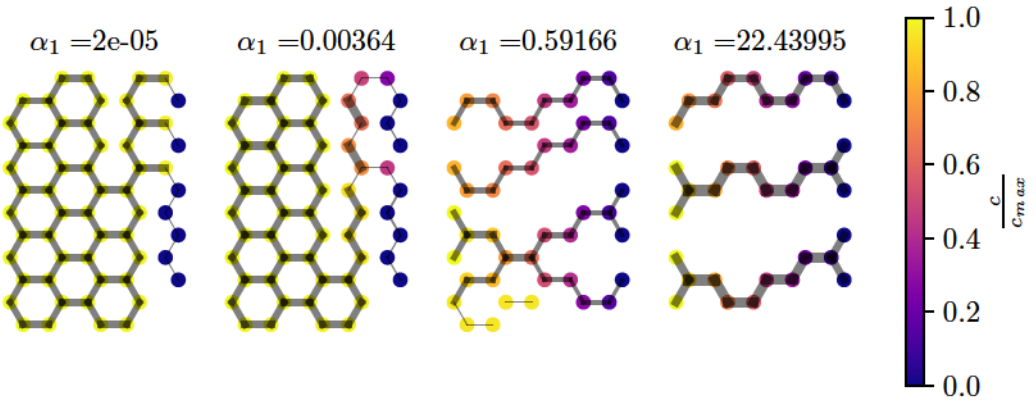

(a) Network skeletons and relative concentration profile

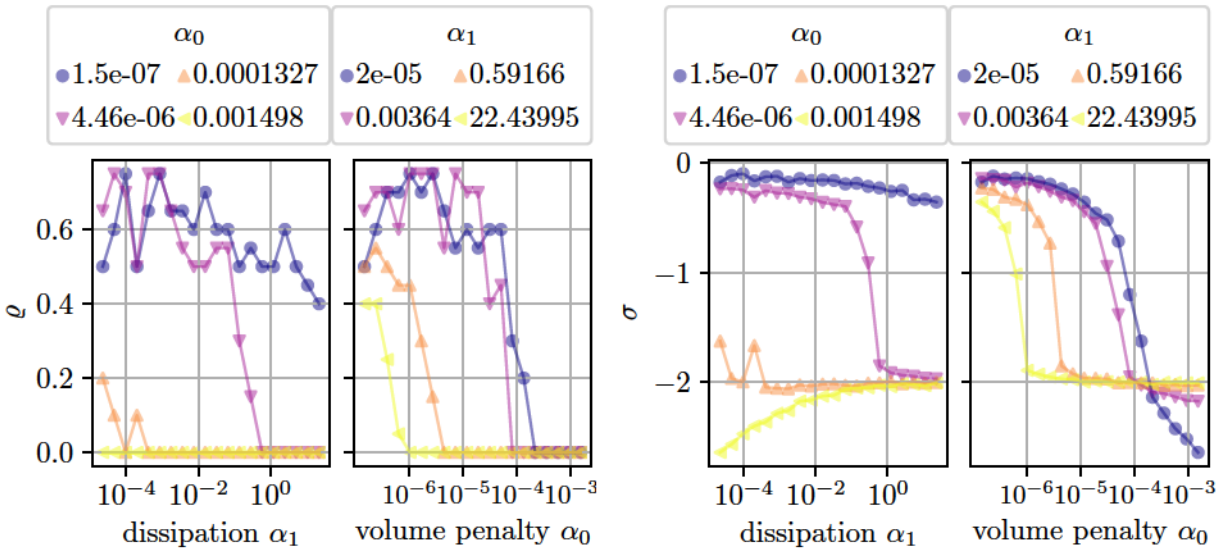

(b) Nullity ϱ (c) Filtration σ

Figure 3.41: Formations of the adaptation model (3.120) with $\sigma_0 = 1.0$ and $\bar{\beta} = 0.001$, displayed for selected dissipation α_1 and volume penalties α_0: (a) Network plots illustrating the relative concentration profiles and edge radii, depicted for $\alpha_0 = 4.4 \cdot 10^{-6}$. (b) Nullity transitions displaying α_1 and α_0 induced reticulation breakdown. (c) Filtration trajectories depicting switches in correlation to topological transitions.

The low absorption rates $\bar{\beta}$ barely crate a concentration gradient. In order to still guarantee high filtration, as many vessels as possible have to stay open, resulting in a reticulated network state. Limiting the size of peripheral vessels leads to a sudden increase of the Peclet number Pe and allow for rapid solute clearance in accordance to the boundary conditions. Naturally, these small vessels experience dramatically higher wall-shear stress than the rest of the system, but due to small α_1 this remains without much of a consequence. Subsequently, increasing α_1 breaks this pattering, as it will open up exactly these vessels, hence decreasing Pe at the periphery and incident vessel's Pe.

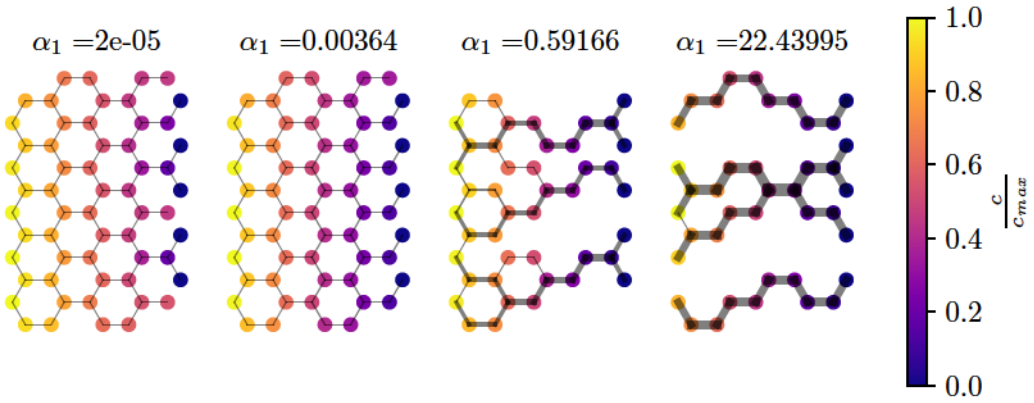

(a) Network skeletons and relative concentration profile

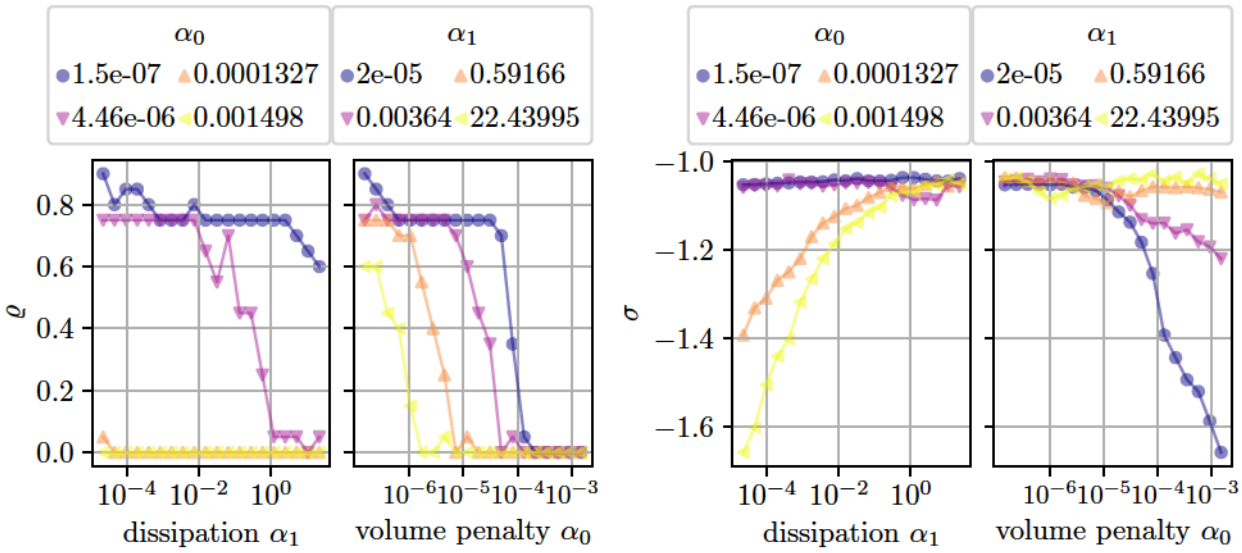

(b) Nullity ϱ

(c) Filtration σ

Figure 3.42: Formations of the adaptation model adaptation model (3.120) with $\sigma_0 = 0.1$ and $\bar{\beta} = 0.01$, displayed for selected dissipation α_1 and volume penalties α_0: (a) Network plots illustrating the relative concentration profiles and edge radii, depicted for $\alpha_0 = 4.4 \cdot 10^{-6}$. (b) Nullity transitions displaying α_1 and α_0 induced reticulation breakdown. (c) Filtration trajectories depicting demand match by increase of α_1 and mismatch by increasing α_0

This in turn changes the concentration landscape resembling more and more a network wide gradient, resulting ultimately in the breakdown of high filtration rates. Now as we still have a volume penalty we observe the break down of weakly perfused vessels, which are not anymore stabilized by the uptake mechanism. We find this behavior well reflected in the trajectory diagrams 3.41b and 3.41c. Note that this algorithm is able to generate non-perfused branches, stabilized against the volume penalty by solute uptake alone. Hence it seems indeed possible to adjust network solute uptake by adjustment of the flow pattern with the help of radial adaptation, even though this may result in seemingly unfavorable formations of peripheral vessels which have to endure extremely high wall-shear stress in turn

In Figure 3.42, we display exemplary cases of the same nature, for the central diagram of the grid 3.40, corresponding to $\sigma_0 = 0.1$ and $\bar{\beta} = 0.01$. Here we see once again a nullity breakdown due to increase of α_i, yet the corresponding filtration trajectories and concentration profiles are considerably different. We display characteristic network formations for increasing α_1 in Figure 3.42a. Here one can see, that even for small α_1 a system spanning concentration gradient is abundant, and no degeneration of peripheral vessel takes place, as previously observed. The filtration diagrams 3.42c illustrate that a seeming match of metabolite uptake is generally achieved in good approximation, yet deteriorates for small dissipation factors α_1 paired with large volume penalties α_0. Increased volume penalties naturally lead to smaller vessel structures, simultaneously increasing Pe and therefore hinder solute uptake. On the other hand, increasing the dissipation factor α_1 will generally increase vessel size and decrease Pe, therefore increase uptake. Further, we see that dissipation dominated regimes, where spanning trees emerge as the distinct graph topology, still reasonably well fulfill the initial filtration demand. It seems that these demand goals can be met for such levels of $\bar{\beta}$ for any network with increase dissipation feedback α_1. Note that seeming quantitative match is a coincidence, as even a turning the network into a spanning tree, with most vessels being pruned, still leaves the network in this particular uptake regime. From a filtration point of view, reticulation is not necessary.
In Figure 3.43, we display exemplary cases for the re-entrant behavior in the bottom-right diagram of the grid 3.40, corresponding to $\sigma_0 = 0.01$ and $\bar{\beta} = 0.1$. These sets depict a regime in which the tissue is supposedly on low demand, yet confronted with highly absorbing vessel surfaces. Naturally we should end here with a system that displays vessels degeneration and near collapse in order to increase Pe, which in turn diminishes solute uptake. Subsequently we are operating in a system that is experiencing high wall-shear stress for the majority of vessels in the network. That is indeed the case and may be observed for the network plots in Figure 3.43a. How does this lead to a re-entrant behavior in the nullity diagram though? Focusing on the nullity trajectories in Figure 3.43b, we observe fully recovered plexi to appear for small volume penalties α_0 for nearly all levels of dissipation α_1. On the other hand, increasing the volume penalty will at first lead toward the emergence of an reticulated interim zone of a certain α_1 width, which is diminished for further increasing α_0. Now we would expect the system to prune down to the minimal amount of conducting channels with high Pe, for increased volume penalties as this allows for an effective reduction of solute uptake. We reason this to be exactly the case for small α_1, where the negative feedback is not countered by any significant positive feedback. As mentioned earlier this results in a system with high wall-shear stress in the majority of vessels, now what would naturally happen when we increase α_1? The system is somewhat loaded with high shear stress in all vessels to which an interim dissipation feedback jumps eagerly, stabilizing all of the sudden a set of previously collapsing vessels, the system encounters a nullity transition. Further increasing α_1 pushes the system once again toward the wall-shear stress dominated regime, where the adaptation stimulus for solute uptake becomes negligible and we observe the emergence of large conducting channels. Looking at the filtration diagram in Figure 3.43c, we find this reasoning to be plausible. First, an increase of the dissipation feedback α_1 should only increase these channel's radii and as such counter any affords of Pe increase. This relaxation naturally pushes the filtration rate up. Surprisingly an increase in α_0 is mostly resulting in an increase in the network's solute

uptake and continues to do so until an inflection point is reached. We suspect the jump in filtration σ to correspond to the onset of nullity in the system. This comes rather intuitively as an increase in open, perfused vessels equals an increase in solute uptake at this level of $\bar{\beta}$. Below this jump we see σ to be virtually independent of α_0. But as soon as the positive dissipation feedback kicks in, we see an adjustment rather to an interplay between α_1 and α_0 rather than the demanded filtration level. The inflection point of this trajectory corresponds to a critical α_0 at which the reticulation breaks down once again.

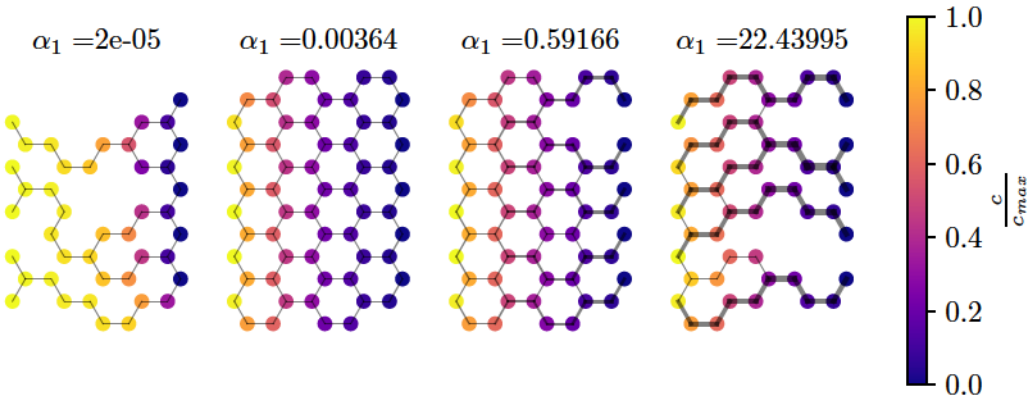

(a) Network skeletons and relative concentration profile

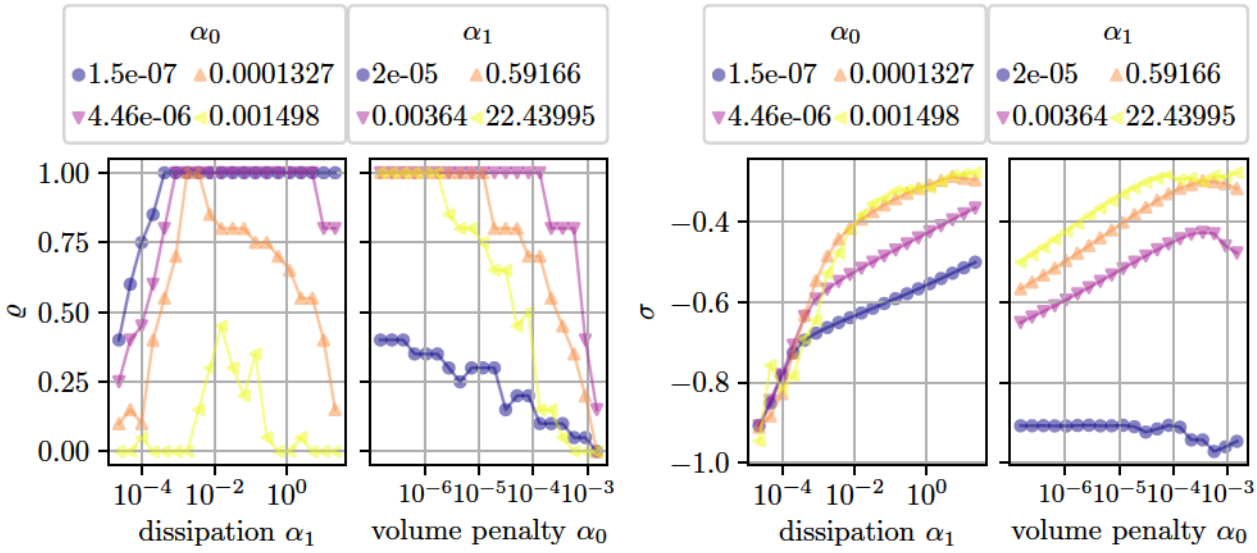

(b) Nullity ϱ

(c) Filtration σ

Figure 3.43: Formations of the adaptation model adaptation model (3.120) with $\sigma_0 = 0.01$ and $\bar{\beta} = 0.1$, displayed for selected dissipation α_1 and volume penalties α_0: (a) Network plots illustrating the relative concentration profiles and edge radii, depicted for $\alpha_0 = 1.33 \cdot 10^{-4}$. (b) Nullity transitions displaying α_1 re-entrant behavior and α_0 induced reticulation breakdown. (c) Filtration trajectories depicting uptake increase due to increase of α_1 and α_0.

In this section have shown that combining link-wise solute demand adaptation significantly perturbs the conventional wall-shear stress driven adaptation algorithm, resulting a nullity transition of varying complexity depending on the demand request and absorption capabilities of the vessels involved. We found that such systems are capable of adjusting rather efficiently toward the demanded filtration level unless exposed to high absorption rates. We expect this framework to become increasingly useful for future studies involving spatio-temporal variations of σ_0 and $\bar{\beta}$. As all phenomena found for this study, illustrated for visibility with hexagonal grids, are qualitatively equivalent to three-dimensional plexi, see appendix B.3.1. In the next section we shall discuss how a collective feeding mechanism , which couples several vessels to the same service volume will alter the complex nullity and uptake landscape.

Volume-wise supply-demand model

In this section we alter the previous setup and focus our studies on a system defined by shared volume elements rather than single vessel service volumes. Here, each service volume element V is in contact with a set of vessels supplying individually a fraction of their uptake Φ_e, see Figure 3.44a. Each volume V demands an influx of solute $\Phi_{0,v}$ potentially mismatching the summed uptake $\sum_{e\in V}\Phi_e$, provided by the attached vessels. We do so in accordance with a similar model by Gavrilchenko et al [45]. Once again we focus on radial adaptation and link removal alone. In accordance to the previous section's setup, we propose a cost for volume-service in the form

$$S\left(\mathbf{\Phi},\mathbf{\Phi}_0\right)=\sum_V\left\{\Phi_{0,v}-\sum_{e\in V}\Phi_e\right\}^2 \tag{3.121}$$

Hence we formulate the system's metabolic cost function,

$$\Gamma=\sum_V\left\{\Phi_{0,v}-\sum_{e\in V}\Phi_e\right\}^2+\sum_e\alpha_1\frac{f_e^2}{K_e}+\alpha_0K_e^{\frac{1}{2}} \tag{3.122}$$

It should be noted that in this particular model framework, not every link is essential to the absorbing volume, which technically, only needs to be in touch with at least one supplying vessel. We numerically solve the minimization problem in (3.122) by initializing a plexus in the form of planar hexagonal grids or laves lattices , see Figure 3.44b. For all planar systems we define the graph's faces as service volumes. In order to ensure the same amount of vessels per service volume and vice versa, we impose periodic boundaries on the system. In the same manner we define each shortest cycle as a service volume for any non-planar network and initialize it with periodic boundaries. With periodic boundaries we refer to the same kind of framework utilized in molecular dynamics simulations [7]. We define a conceptual box around our spatially embedded graph, whose nodes close to the box border get connected by additional edges, where adjacency is determined by finding closets neighbors, regarding the periodic displacements in the box. In any system with periodic boundaries we impose a single sources with solute influx on a random position and a single sink with absorbing boundary on one of the topologically most distant site. As before, we initialize the system for different absorption rates $\bar{\beta}$ and demand ϕ_0 combinations, while scanning

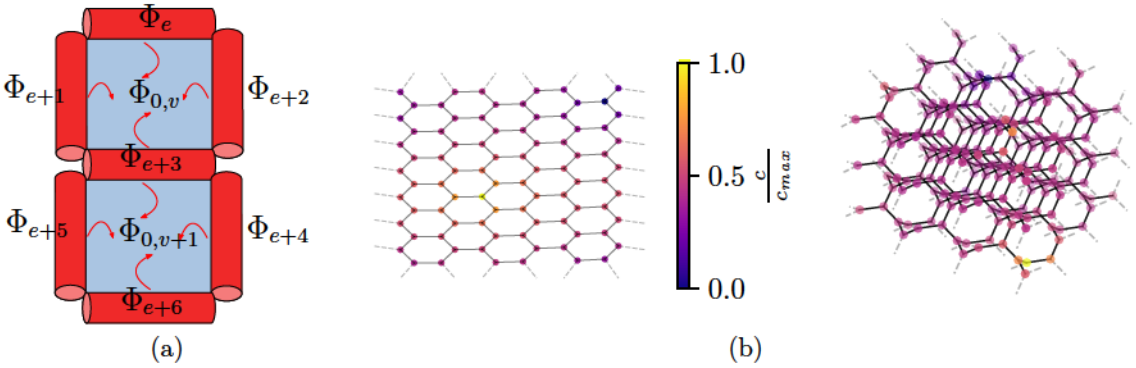

Figure 3.44: Volume-demand model setups: (a) Basic cycles are assigned a demand $\Phi_{0,v}$ which is answered by a supply of its cycle edges Φ_e. (b) Hexagonal grids and Laves graphs with dipole source-sink configuration acting as well as inlet and absorbing boundaries. The colormap is indicates the normalized nodal concentrations. Transparent, marked links are indicating periodic boundaries.

systematically for the impact of the dissipation feedback α_1 and the volume penalty α_0. In particular, we realize all vessels to correspond to a volume demand $\phi_{0,v}$ such that the network's demanded filtration rate would correspond to $\sigma_0 = \frac{\sum_v \phi_{0,v}}{\sum_{v,J_v>0} J_v}$. For the presented simulations, we initialize $\phi_{0,v}$ homogeneously across the network, we do so for $\bar{\beta}$ as well. Following the adaptation algorithm, as described in the previous section, we find the system's stationary states and analyze those for their nullity ϱ and actual filtration rate σ, as defined in the previous sections. Beware that non-zero nullity, for periodic boundaries, may correspond to the existence of topological generators (cycles created by walking through the periodic boundaries).
In Figure 3.45 we present the collected results, as state diagram grids for these parameter screens. These diagrams were acquired for the hexagonal lattice plexus, and we shall discuss the microscopic structures arising in such plexi later on. For the results on three-dimensional plexi, see the appendix B.3.2. Note that the grid's x-axis is illustrating different cases of absorption rates $\bar{\beta}$ while the demanded volume filtration rate σ_0 variation is displayed on the grid's y-axis. At first glance we find the systems to depict the same qualitative behavior as single link demand systems previously. In detail, we present the systems emerging nullity ϱ in Figure 3.45a. In these diagrams we observe the networks reticulation to vary significantly, when exposed to the competing constraints of (3.122). In accordance to previous studies we find that systems dominated by dissipation and volume penalty are developing into spanning trees. Note that spanning trees correspond here to single conducting channels between the source and sink nodes. We find the transition toward reticulated states shifting in dependence of the volume filtration demand σ_0 and absorption rate $\bar{\beta}$. Once again, we find the upper triangle (top-left) as well as the diagonal (bottom-left to top-right) elements, to display qualitatively similar pruning behavior in that matter. The lower triangle (bottom-right) in 3.45a, illustrates non-trivial state changes, analog to (3.120).

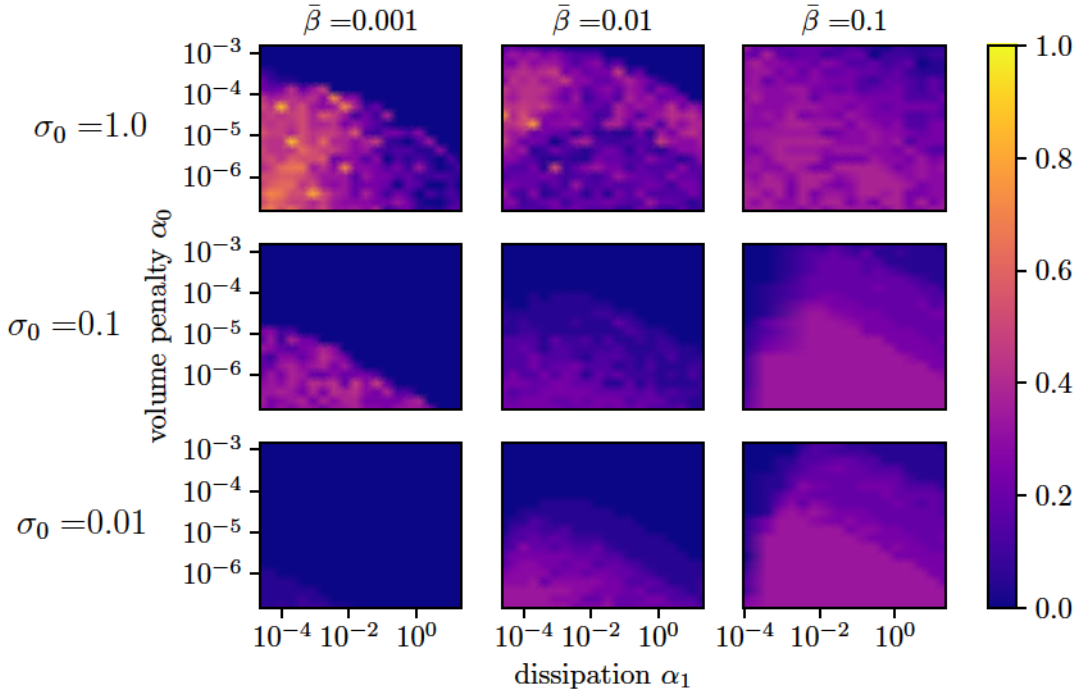

(a) Nullity ϱ

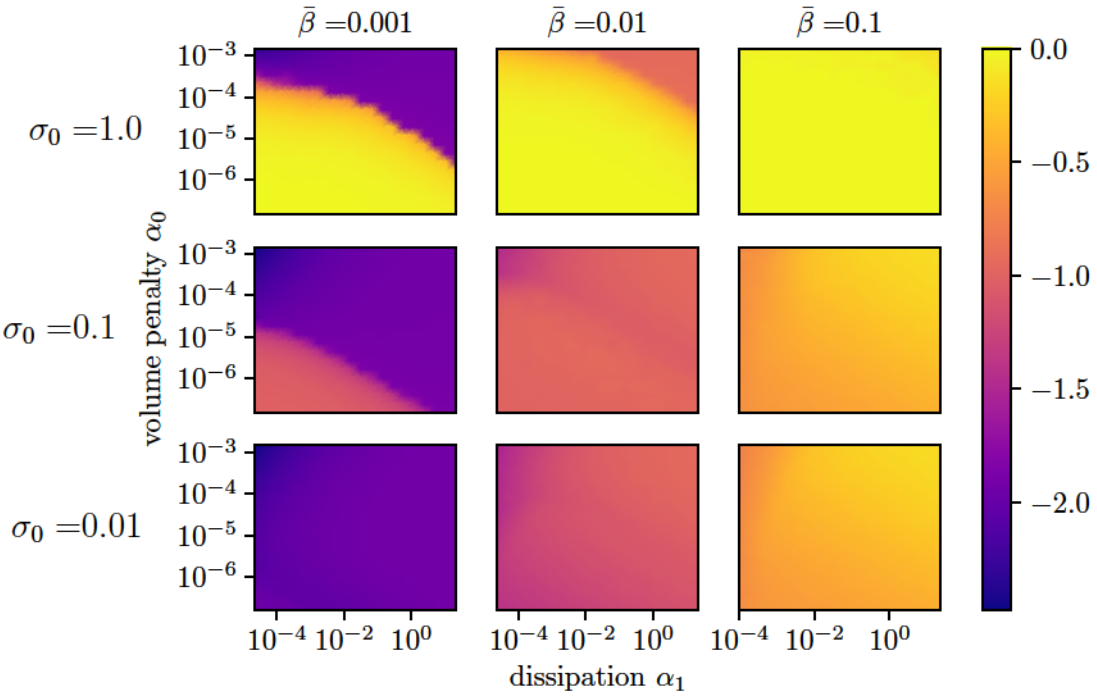

(b) Filtration σ

Figure 3.45: Nullity and filtration diagrams for stationary states of the cost problem (3.122), with boundary parameter variation $\sigma_0 = \frac{\sum_v \Phi_{0,v}}{\sum_{J_n>0} J_n} \in \{10^0, 10^{-1}, 10^{-2}\}$, $\bar{\beta} \in \{10^{-1}, 10^{-1}, 10^{-2}\}$; systematic volume penalty α_0 and dissipation α_1 are scanned systematically: (a) Nullity phase diagram indicating a topological transition and re entrant behavior. (b) Filtration diagram indicating varying quality of filtration adjustment for varying $\bar{\beta}$.

The emergence of re-entry is preserved for variations of α_i, despite the topological change of the problem as well as its initial uptake problem. As indicated by the grid layout, this behavior only seems to prevail in the case of small filtration demands paired with high absorption rates. In the second block, see Figure 3.45b, we display the filtration diagrams. In analogy to 3.45a, walking through the upper triangle of the diagram grid, we find the filtration to display qualitatively similar behavior. In particular we find that the initial filtration demand is quite well matched for the dissipation α_1 and volume penalty α_0 regimes which correspond to the reticulated states of the nullity diagram. Although the noisy nullity landscapes suggest that slightly reticulated network and spanning trees are capable of matching the supply demand. We find the shift of this phase to correspond once again to the variation of σ_0 and $\bar{\beta}$. It appears that a decrease in these parameters results in a shift of the phase borders toward smaller dissipation and volume penalty for the same reasons as in the previous section. Analyzing the diagonal we find the filtration goal to be seemingly matched for any kind of network topology. As previously discussed, we expect this quantitative match to be a coincidence. The lower triangle displays a significant mismatch though, displaying in general the resulting filtration to be higher than initially demanded. Let us from here on discuss the resulting network topologies and uptake patterns in detail, we shall do for archetypal cases along the diagram grid's diagonal (top-left to bottom-right) elements. We shall discuss the nature of the newly emerging nullity phase transition and from there try to reason which of these states represent the behavior of actual vascular beds.

In Figure 3.46 we showcase exemplary network formations and concentration profiles, alongside detailed trajectories for nullity and filtration taken from the top-left diagrams in 3.45. This diagram's data corresponds to the case of high demand in $\sigma_0 = 1.0$ and paired with low absorption $\bar{\beta} = 0.001$. Be reminded that we operate with periodic boundaries, indicated by dashed edges in 3.46a. Figure 3.46a generally shows that increasing α_1 will result in a nullity transition. As before, we observe the formation of dangling branches not connected to any sinks. We find the same mechanism at work as discussed for 3.41a: Low $\bar{\beta}$ impair individual vessels from absorbing any significant amount of solute, as a result we observe the majority of vessels dilated, while the connection to the sinks is degenerated for small α_1 Hence by dilating the bulk of vessels one minimizes the overall Peclet numbers Pe in the system, which increases overall uptake. Creating such a Pe landscape is further resulting in a homogeneous concentration landscape as low $\bar{\beta}$ barely crate a concentration gradient. In order to still guarantee high filtration the service volumes, as many vessels as possible have to stay open, resulting in the reticulated network state. Limiting the size of peripheral vessels leads to a sudden increase of Pe and allow for rapid solute clearance in accordance to the boundary conditions. Subsequently, increasing α_1 breaks this pattering, as it stabilizes and expands links with high wall-shear stress. This in turn changes the concentration landscape resembling more and more a network wide gradient, resulting ultimately in the breakdown of high filtration rates. We find this behavior well reflected in the trajectory diagrams 3.46b and 3.46c. Note that this algorithm is able to generate non-perfused branches and even non-perfused loops, stabilized against the volume penalty by the solute uptake mechanism alone. In Figure 3.47, we display exemplary cases for the central diagram of the grid 3.45, corresponding to $\sigma_0 = 0.1$ and $\bar{\beta} = 0.01$. Here we see once again a nullity breakdown due to an increase of α_0 and α_1,

yet the corresponding filtration trajectories and concentration profiles are considerably different.

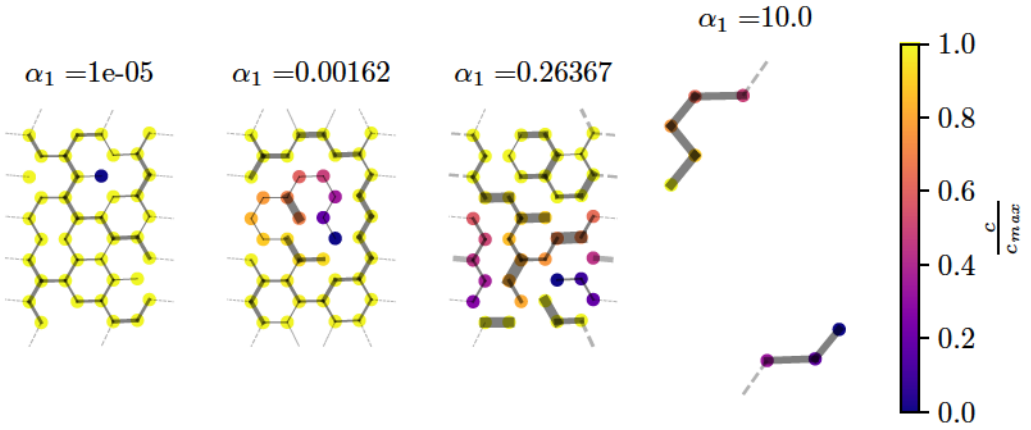

(a) Network skeletons and relative concentration profile

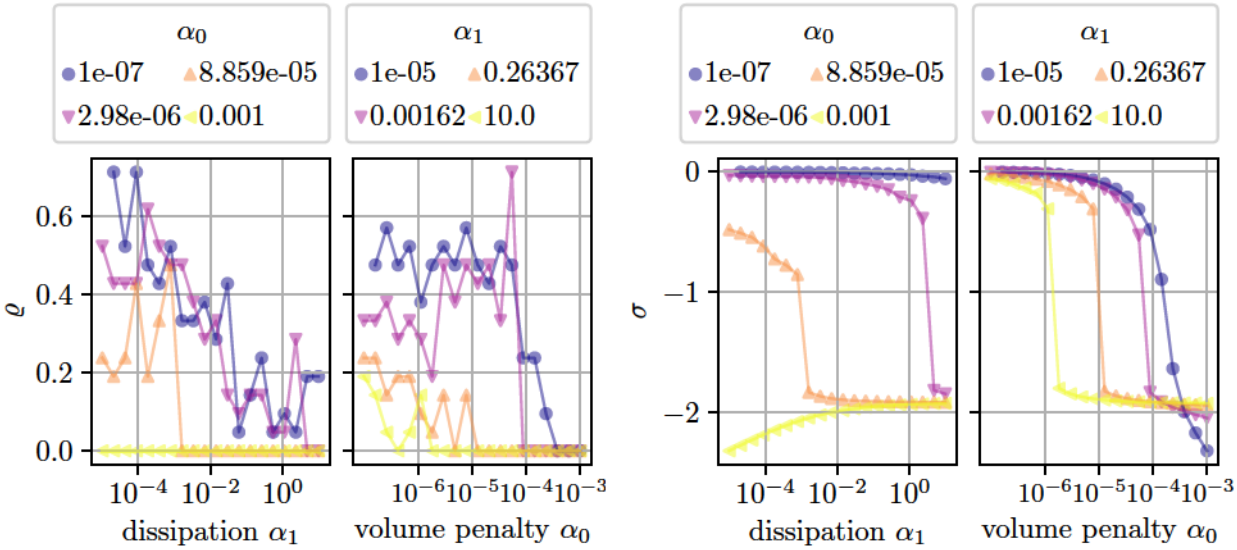

(b) Nullity ϱ

(c) Filtration σ

Figure 3.46: Formations of the adaptation model (3.120) with $\sigma_0 = 1.0$ and $\bar{\beta} = 0.001$, displayed for selected dissipation α_1 and volume penalties α_0: (a) Network plots illustrating the relative concentration profiles and edge radii, depicted for $\alpha_0 = 9 \cdot 10^{-5}$. (b) Nullity transitions displaying α_1 and α_0 induced reticulation breakdown. (c) Filtration trajectories depicting switches in correlation to topological transitions.

We display characteristic network formations for increasing α_1 in Figure 3.47a. Here one can see, that even for small α_1 a system spanning concentration gradient is abundant. The filtration diagrams 3.47c illustrate that a match of metabolite uptake is achieved in good approximation, yet deteriorates for small dissipation factors α_1 paired with large volume penalties α_0. Increased volume penalties naturally lead to smaller vessel structures, simultaneously increasing Pe and therefore hinder solute uptake.
In Figure 3.48, we display exemplary cases for the re-entrant behavior in the bottom-right diagram of the grid 3.45, corresponding to $\sigma_0 = 0.01$ and $\bar{\beta} = 0.1$. These sets

depict a regime in which the tissue is supposedly on low demand, yet confronted with highly absorbing vessel surfaces.

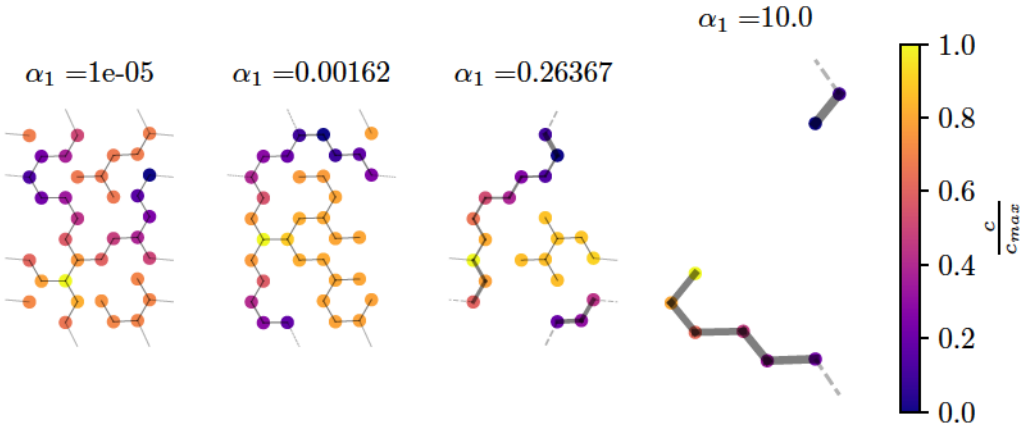

(a) Network skeletons and relative concentration profile

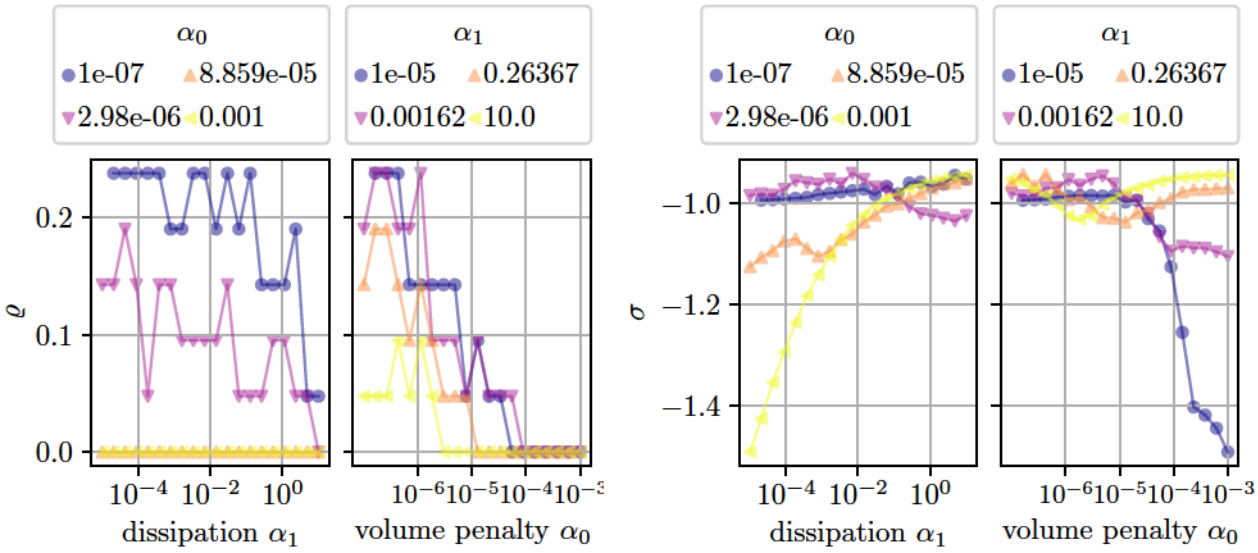

(b) Nullity ϱ

(c) Filtration σ

Figure 3.47: Formations of the adaptation model (3.120) with $\sigma_0 = 0.1$ and $\bar{\beta} = 0.01$, displayed for selected dissipation α_1 and volume penalties α_0: (a) Network plots illustrating the relative concentration profiles and edge radii, depicted for $\alpha_0 = 9 \cdot 10^{-5}$. (b) Nullity transitions displaying α_1 and α_0 induced reticulation breakdown. (c) Filtration trajectories depicting switches in correlation to topological transitions.

Hence we end up with a system that displays vessels degeneration and near collapse in order to increase Pe, which in turn diminishes solute uptake. Subsequently we are operating in a system that is experiencing high wall-shear stress for the majority of vessels in the network. That is indeed the case and may be observed for the network plots in Figure 3.48a. How does this lead to a re-entrant behavior in the nullity diagram though? Focusing on the nullity trajectories in Figure 3.48b, we observe fully recovered plexi to appear for small volume penalties α_0 for nearly all levels of dissipation α_0. Note

that we had the mechanisms for this behavior already discussed for the formations in 3.43 Looking at the filtration diagram in Figure 3.48c, we find this reasoning once again to be plausible.

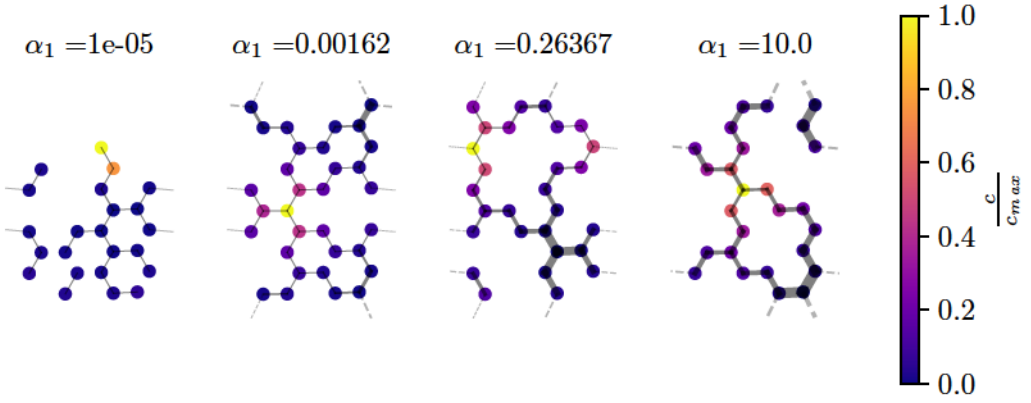

(a) Network skeletons and relative concentration profile

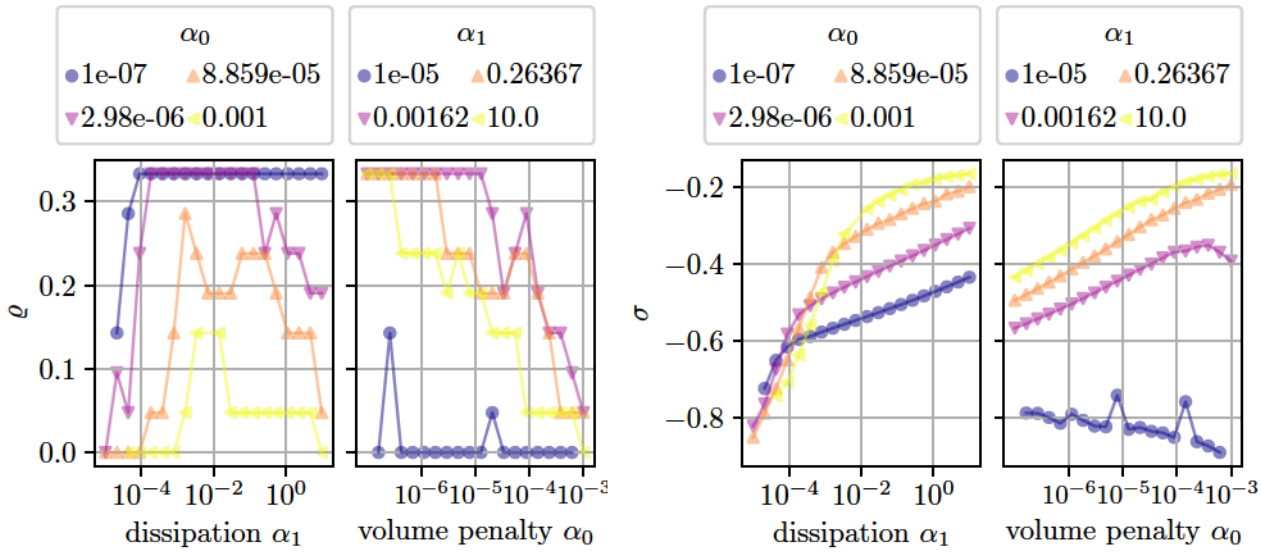

(b) Nullity ϱ

(c) Filtration σ

Figure 3.48: Formations of the adaptation model (3.120) with $\sigma_0 = 0.01$ and $\bar{\beta} = 0.1$, displayed for selected dissipation α_1 and volume penalties α_0: (a) Network plots illustrating the relative concentration profiles and edge radii, depicted for $\alpha_0 = 9 \cdot 10^{-5}$. (b) Nullity transitions displaying α_1 and α_0 induced reticulation breakdown. (c) Filtration trajectories depicting switches in correlation to topological transitions.

First, an increase of the dissipation feedback α_1 should only increase these channel's radii and as such counter any affords of Pe increase. This relaxation naturally pushes the filtration rate up. Surprisingly an increase in α_0 is mostly resulting in an increase in the network's solute uptake, beyond a α_1 continues to do so until an inflection point is reached. We suspect the jump in filtration σ to correspond to the onset of nullity in the system. This comes rather intuitively as an increase in open, perfused vessels equals an increase in solute uptake at this level of $\bar{\beta}$. But as soon as the positive dissipation

feedback kicks in, we see an adjustment rather to an interplay between α_1 and α_0 rather than the demanded filtration level. In this section have shown that combining volume-wise solute demand adaptation significantly perturbs the conventional wall-shear stress driven adaptation algorithm, but displays the same and hydrodynamical phases as link-wise demand models. We observe an inherently noisy nullity transition of varying complexity depending on the filtration request and absorption capabilities of the vessels involved. We found that such systems are capable of adjusting rather efficiently toward the demanded filtration level unless exposed to high absorption rates. As for the previous section, we expect this framework to become increasingly useful for future studies involving spatio-temporal variations of σ_0 and $\bar{\beta}$. We advise the reader to have a look a the supplementary material B.3.2, for the results on three-dimensional plexi adaptation. Though most of the flow pattern formation is analogous to what we have shown here, we find the nullity re-entry behavior to collapse when the topology is changed. Beware that the simulation results were obtained for small systems and finite-size effects can not be ruled out at this point. Therefore consecutive studies are in order.

Chapter 4

Discussion and Outlook

We would like to conclude this thesis by pointing out its key insights in comparison to the current scientific discussion. For that we shall outline the significance of the results discussed so far in the coming section, followed by an outlook on consecutive and spin-off projects.

4.1 Summary of Results

As initially stated in chapter 1.3, this thesis intended to address current challenges of network theoretical characterization, modeling the adaptation of spatially embedded networks in terms of geometric restrictions & optimal metabolite transport and derive new scaling laws for such complex constraints. Hence, we discussed current model frameworks, developed a new multilayer model for entangled systems and compared the compatibility and effectiveness in generating optimal network structures for conventional and new approaches.
In section 3.1, we showed that fluctuation induced nullity, treated according to the model framework of Corson and Hu et al [30, 56], can be formulated as a single parameter problem. Further, we verified claims stated in the latter publication on volume penalty independence and ramifications of the detailed framework. We demonstrated that the transition indeed follows a logarithmic law. We then demonstrated the influence of plexus size as well as topological dependencies on the nullity transition.
In section 3.2 we formulated a new coupling model for entangled adapting networks as a toy model approach for vasculature found in the liver lobule, pancreas, kidney etc. Here we discussed a model based on local, distance-dependent interactions between pairs of three-dimensional network skeletons, representing the cavities of triply periodic minimal surfaces. Doing so, we found unprecedented delay and breakdown of the fluctuation induced nullity transition for repulsive interactions, stabilizing spanning trees in the face of noisy flow patterns. Moreover, we found a new nullity transition emerging for attractive coupling, which account for virtually dissipation neutral and volume neutral reticulation. These new phenomena seem to be mostly independent of the initial plexus topology.
In section 3.3.1 we discussed parameter estimation from Murray's Law for ideal Kirchhoff networks and intertwined networks. In particular, we discussed how flow fluctuations and complex metabolic costs can be incorporated into Murray's Law. Then we

showed that one can derive model parameters of optimization models given experimental data alone. In the case of ideal Kirchhoff networks, for which this framework was originally developed, we indeed found high accuracy parameter reconstruction to be possible. On the other hand, when testing our framework on the skeletons of real vasculature, such as bile canaliculi and sinusoids, we observed this parameter estimation to result in broad, long tailed distributions. Yet, we were able to derive an order of magnitude estimation for the parameters, suggesting fluctuation driven adaptation to be the dominant factor in these networks.
In section 3.4 we discussed optimal metabolite uptake for Kirchhoff networks. We generalized the previous framework of Meigel et al [82] and evaluated the impact of solute uptake driven adaption in comparison to wall-shear stress driven adaptation. Here we found the emergence of a nullity transition in case of a dominant metabolite uptake machinery, which potentially led to the formation of absorption efficient bottleneck systems for small absorption rates. In addition re-entrant behavior emerged in case of high absorption rates, which displayed a complex interaction between shear-stress generation and subsequent feedback. We tested this approach for different plexus topologies and graph sizes, yet could not identify significant changes in the behavior described above.

4.2 Discussion

Here, we would like to progress with a more critical evaluation of the results presented as well as on the intended impact of this thesis. In the beginning of this thesis we found that a surprisingly small community has focused on network morphogenesis in vascular beds. Fascinating as it was to be a newcomer in this field, reading up on the theoretical frameworks and hypotheses developed up to this point, see 1.2.1, it became even more exiting to discover how many questions seemed unanswered, or had not even been posed, in particular with regard to three-dimensional, mesh-like flow networks.
In the first study in section 3.1, focused on the fluctuation induced nullity transition, we turned our attention to topology dependence to find out whether the algorithm is sensitive to changes from planar to non-planar systems. As these frameworks were originally tested in such networks, as toy models for leaf venation systems and slime molds, we were wary of complications when moving forward to three-dimensional capillary systems. Yet it turned out that, quite naturally, the algorithm was reliably generating network structures from arbitrary plexi. Further, we showed that one could do so in terms of a single parameter for arbitrary fluctuation scenarios, without needing to constrain sinks to specific probabilistic models, see for example Hu et al [56]. During that time we also became aware of the research conducted by Ronellenfitsch et al [122], suggesting arbitrary, locally correlated sink fluctuations in a single parameter model. In a sense their framework was more powerful, as it was able to explicitly demonstrate correlation dependency of fluctuations to account for reticulation in optimized flow networks, which we only suspected at this point. The remarkable topological significance we found was that graphs with degree distributions $d > 3$ seem to display an inherent saturation limit in the nullity transition, rendering such plexi intrinsically wasteful in terms of fluctuation generated reticulation.
Our second project in section 3.2 was developed within the context of liver lobule morphogenesis. As such there existed a thriving community in Dresden to gain knowledge and assistance from. In particular, the collaboration with the Zerial Lab at the MPI-CBG turned out quite fruitful as they were able provide us with data sets on liver networks and advise us in terms of modeling approaches. Subsequently we developed the power law model for intertwined networks, testing once again different graph topologies of entangled networks. Though the model turned out to be robust for different graph types, we found the interesting new nullity behavior to open up a new path in network morphogenesis modeling. We found in particular the attractive model to display interesting behavior as its coupling induced reticulation coincides with the notion of existent flow highways in capillary networks, being surrounded by seemingly auxiliary vessels, see Karschau et al [59]. It was during these studies that we found that seemingly no one had tried to match the branching patterns of liver networks to Murray's Law or similar in the context of these recent morphogenesis models. Or any three-dimensional non-hierarchical networks for that matter It was here that we started looking more closely to readable markers in the geometrical and topological footprints of these networks. As such we formulated a generalized version of Murray's Law, see section 3.3.1, introducing edge weighting coefficients and sink influence. Though we found that this approach still seems crude when applied to real liver networks we find these results actually reassuring of the potential of this ansatz. For the first time we propose a directly applicable and quantifiable method to identify effective model parameters in flow

networks. The results seem to highlight various aspects though: First, the broad distributions found could be interpreted as a local variation of model parameters across the network, which implies a new complex system on its own, as current model frameworks assume globally homogeneous adaptation parameters for all vessels involved. Second, the quality of data as well as our cost function model have to be improved significantly. That is to say segmentation is still limited by occurrence of artifacts and geometric inconsistencies, as well as difficulties of separating capillary surfaces automatically from peripheral structures to allow for consistent terminal identification. Furthermore we could were unable to falsify our cost model approach, which might be connected to the circumstance that our model does not capture which adaptation mechanisms are at hand in the first place. Therefore alternative interpolation methods might be in order. While planning this thesis, we came across the works of Meigel et al [82], in particular by personal communications with the author at the MPI-PKS. As initially intended for this thesis, we wanted to incorporate metabolite uptake and transport in the intertwined models. Then, between first attempts and numerical evaluations to coarse-grain the model framework further, colleagues of the MPI-CBG and MPI-PKS suggested different uptake strategies, one of which was volume-wise supply. Here, we were also made aware of the works of Gavrilchenko et al [44], who employed a similar morphogenesis model for solute uptake. We found that our ansatz to account for nullity transitions due to radial adaptation of the vessel systems, optimizing solute uptake by regulation of the flow pattern. Moreover we illustrated that these only partly correspond to real vascular beds as frustrated optimization attempts were creating bottleneck structures. Needless to say, such formations are unfavorable to real flow networks as they tend to create extremely high wall-shear stress peaks, localized to a few peripheral capillaries. Rather we find our results to indicate that an effective metabolite uptake should be achieved by alternative adaptation processes, e.g. having a flow-driven machinery generate robust capillary beds by fluctuation or external factors, with subsequent adjustment of local filtration and absorption rates. Therefore we think further studies on absorption rate gradients to be extremely valuable, in particular as uptake gradients were indicated in liver networks, see Meyer et al [83].
Considering these findings as well as the constructive feedback we received over time from our collaborators, we are determined to continue our work in order to identify valid adaptation mechanisms in these kind of embedded complex networks.
As a last, more personal note, let us note a rather recent revelation. From an engineering point of view alone, the difficulties of designing a complex system and keeping track of potential pitfalls are substantial. Just writing the code for theses studies was ironically creating a complex software environment to understand another, even more complicated system. Well, every programmer can sing a hymn to that [77]. Yet developing a complex system for a given purpose is in general manageable, as we all know considering the current status of modern technologies. Now you find yourself confronted with the subsequent task: to make the periphery of the object you created match and interact with other even more complicated systems, which all then are interconnected by your primary infant project. Of course, the collective efforts of mankind have proven to be fruitful regarding this kind of task creating complex machinery, cultures and ideas. As such we know that unintended complications arise for increasingly more complex concepts as well as its higher potential for failure. Therefore, it is somewhat awe-inspiring that the evolutionary process has brought about a robust set

of mechanisms to create such a thing of beauty and functionality as the vasculature system step by step [87]. Almost miraculously, any organism is realized from a genetic blueprint, which has been created over millions of years by trial and error, without any guidance on how to design such a system from scratch [35].
In that light, life actually did not turn out half bad, or at least, our vasculature did not.

4.3 Outlook

In this final section we would like to point out ongoing projects and future endeavors derived from the studies in this thesis. We would like to highlight two projects in particular with respect to intertwined systems and complex metabolic uptake scenarios: Metabolite transport in the liver lobule and optimization of complex absorption landscapes.

4.3.1 Metabolite transport in the liver lobule

Insight into the formation of the liver's microscopic tissue structure has come a long way since the first detailed physiological re-examinations [40, 41] in the 20th Century. In particular, complex and elaborated models have been produced recently, modeling the fluid dynamics inside the elementary tissue building blocks, i.e. the liver lobules [109]. There have been attempts to account for the initial formation of the respective vessel networks [29, 128, 111, 49], their individual hydrodynamics [69, 70, 110] and metabolic capabilities of the organ [80]. In particular one may observe a controversy on the matter of bile transport mechanisms, see [136] and [83]. With the framework developed in this thesis, we propose another multilayer model for further studies, incorporating the functional interplay between blood capillaries, hepatocytes and canaliculi. In this complex morphogenesis model one approximates sinusoids once again as Kirchhoff networks which are coupled toward hepatocytes representing the second layer. On the third layer we find the canaliculi approximated as a non-linear flow network, coupled with the epithelial cells, the hepatocyes. We plan to utilize an extended version of the Ostrenko model for this purpose. The peripheral networks, i.e. sinusoids and canaliculi are coupled to a bath providing the sources and sinks of fluid and metabolites. We shall elaborate on the details of the suggested framework with an eye particularly on the generalized Ostrenko model and metabolite transport coupling in between the network layers.

Expansion of the Ostrenko model

The bile canaliculi are an elaborate mesh of vessels formed by the apical surfaces of the hepatocytes. It has been hypothesized that the flux of bile is generated by the active deposition of bile salts and other chemical constituents into these channels. The cross-membrane concentration gradient triggers an osmotic influx of water from the epithelium, creating the outflow of concentrated bile. For any further purpose we treat these channels as one-dimensional channels with mean flow velocities $\bar{v}(z)$, metabolite concentration $\bar{c}(z)$, effective radius R and deposition rate g. As shown in the model framework of Ostrenko et al [100] one may model the osmotic driven flux in a single

epithelial duct via the ODE system

$$\bar{v}(z) = -\frac{R^2}{8\eta}\partial_z p(z) \tag{4.1}$$

$$\partial_z \bar{v}(z) = \frac{2\kappa}{R}\left(N_A k_B T c(z) - p(z)\right) \tag{4.2}$$

$$0 = \frac{2g(z)}{R} - \partial_z\left(\bar{c}(z)\,\bar{v}(z)\right) \tag{4.3}$$

Here we have the first equation (4.1) as the conventional stokes solution for thin channels. The second equation (4.2) is describes the increase or decrease of the flow velocity due to the inlfux of water triggered by the difference in transmural pressure and concentration between the channel and the tissue. Here we refer to κ as the permeability of the apical membrane. This means that the computation of the channel pressure becomes a nonlinear problem, as the flow velocity is now coupled to the concentration profile, unlike the passive hydrodynamics discussed in section 2.1.2. The last equation (4.3) represents the stationary continuity equation for negligible diffusion processes along the channel, merely taking into account the advection of solute and its deposition rate. One may rewrite (4.3) in its integrated form

$$G(z) = \frac{2}{R}\int_0^z g(z')\,dz' = \bar{c}(z)\,\bar{v}(z) - \bar{c}(0)\,\bar{v}(0) \tag{4.4}$$

This equation system has unique analytic solutions if the concentration profiles $\bar{c}$ are known. Otherwise for boundaries only indicating the deposition rates g one may efficiently construct a numerical solution by employing finite element methods [98]. It should be noted here that the qualitative behavior of any solution to depend on a single parameter: The Münch number M. This parameter scales as the resistances of fluid flow through the channel versus the cross membrane influx of water as,

$$M = \frac{16\eta\kappa L^2}{R^3} \tag{4.5}$$

In particular one gets $M \to 0$ for relative low channel flow resistance (wet-tip regime) while $M \gg 1$ represents the case of high resistance (dry-tip regime). This regime change is usually displayed by a shift of the spatial velocity profile, where we have significant flow throughout the channel for $M \to 0$ and a suppression of such for $M \gg 1$, see [100]. We propose here a framework generalizing the single channel solutions of (4.1)- (4.3) for arbitrary complex networks, for the case of analytic concentration profiles. We do so primarily to derive an efficient algorithm, which is compatible with the network morphogenesis models discussed in this thesis. Here we focus on solutes with profiles which are expandable with coefficients $f_m, k_n \in \mathbb{R}$ as

$$\bar{c} = \sum_n^\infty k_n \frac{z^n}{n!} \text{ with } k_{n+m} = f_m k_n, \tag{4.6}$$

The equation system (4.1)- (4.3) may then readily be solved for the channel pressure and velocity as

$$p(z) = \left[q_1 e^{\frac{\sqrt{M}z}{L}} + q_2 e^{-\frac{\sqrt{M}z}{L}}\right] + \Omega \bar{c}(z) \tag{4.7}$$

$$\bar{v}(z) = -\frac{R^2}{8\eta}\left\{\frac{\sqrt{M}}{L}\left[q_1 e^{\frac{\sqrt{M}z}{L}} - q_2 e^{-\frac{\sqrt{M}z}{L}}\right] + \Omega \partial_z \bar{c}(z)\right\} \tag{4.8}$$

$$\begin{aligned} G(z) = -\frac{R^2}{8\eta}\Bigg(&\bar{c}(z)\left\{\frac{\sqrt{M}}{L}\left[q_1 e^{\frac{\sqrt{M}z}{L}} - q_2 e^{-\frac{\sqrt{M}z}{L}}\right] + \Omega \partial_z \bar{c}(z)\right\} \\ &+ \bar{c}(0)\left\{\frac{\sqrt{M}}{L}\left[q_1 - q_2\right] + \Omega \partial_z \bar{c}(0)\right\}\Bigg) \end{aligned} \tag{4.9}$$

$$\text{with } \Omega = \frac{N_A k_B T}{1 - \frac{L^2}{M} f_2} \tag{4.10}$$

These solutions and their M dependency have been thoroughly discussed in [99]. We started working on generalizing this framework for arbitrary flow networks in the following way: Given a representative graph $G(V, E)$ with vertices v and edges e we consider concentrations $\bar{c}_e$, which are given according to (4.6) along every edge. Now we may formulate respective concentrations on the start and end nodes as $\bar{c}_e(z = 0) = c_{\alpha(e)}$ and $\bar{c}_e(z = L) = c_{\omega(e)}$ which are to match for incident edges. We proceed in the same manner for the fluid velocity $\bar{v}_e(z = 0) = \bar{v}_{\alpha(e)}$, $\bar{v}_e(z = L) = \bar{v}_{\omega(e)}$ and transmural pressure $\bar{p}_e(z = 0) = p_{\alpha(e)}$, $\bar{p}_e(z = L) = p_{\omega(e)}$. Subsequently we formulate for any such edge the integrated continuity equation (4.4) for the accumulated deposit $G_e(z = L) = G_{\omega(e)}$ as

$$G_{\omega(e)} = \bar{c}_{\omega(e)} \bar{v}_{\omega(e)} - \bar{c}_{\alpha(e)} \bar{v}_{\alpha(e)} \tag{4.11}$$

Thereby forming a system of $m = |E|$ linear independent equations. We have further the Kirchhoff law (2.75) giving $n - 1$ independent equations of the form:

$$\sum_{e \in out(v)} \pi R_e^2 \bar{v}_{\alpha(e)} - \sum_{e \in in(v)} \pi R_e^2 \bar{v}_{\omega(e)} = s_v \tag{4.12}$$

As this model is meant to capture the injection of fluid and metabolite into the system via its vessels surfaces we generally have $s_v = 0$. Further, we define one distinguished sink-node meant to represent the systems periphery (or a set as such) with the relation

$$s_0 = \pi \sum_e R_e^2 \left(\bar{v}_{\alpha(e)} - \bar{v}_{\omega(e)}\right) \tag{4.13}$$

derived from summing up all equations in (4.12). And eventually we need the transmural pressures to match at each node of degree $d \geq 2$, generating us $d - 1$ independent constituting equations at each such node as

$$\begin{gathered} \frac{2\kappa}{R_e}\left(RT \bar{c}_{\alpha(e)=v} - p_{\alpha(e)=v}\right) = \partial_z \bar{v}_{\alpha(e)=v} \\ \text{with } R_{e_i} \partial_z \bar{v}_{\alpha(e_i)=v} = \ldots = R_{e_j} \partial_z \bar{v}_{\omega(e_j)=v} \\ \text{where } i \in out(v) \text{ and } j \in in(v) \end{gathered} \tag{4.14}$$

This particular set of equations needs careful handling as to adjust for the incidence of the edges at branching points. In total we acquire $\sum_v (d-1) = 2m - n$ independent lines for the further usage. All together the equations (4.11), (4.12), (4.14) form a system of $2m$ linear independent equation for the unknown coefficients q_1^e, q_2^e allowing us to uniquely determine the pressure (4.7), flow velocity (4.8) and accumulated deposit (4.9) across an arbitrary flow network, e.g. see Figures 4.1. We display such solutions via color coding of the relative flow velocity for a homogeneous concentration profile $c_v = c_0$. Here one may see the conservation of the wet to dry tip transition for due to the change of Münch numbers M. We would like to note here that that the flux

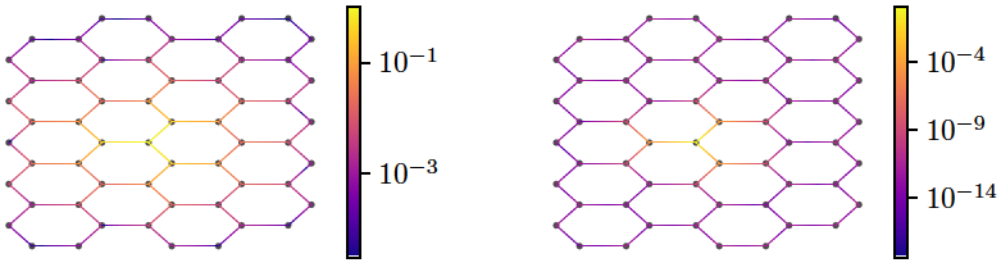

(a) (b)

Figure 4.1: Flow velocity profiles for a homogeneous concentration landscape $c_0 = 1$ and one central sink, where the color map represents $\frac{|v|}{|v_{max}|}$. We display here the iconic scenarios for different Münch numbers M: (a) Wet-tip $M = 1$ (b) Dry tip $M = 100$

in this kind of system is purely generated by the osmotic influx of water via the vessel membranes, and not by injection and drainage at terminal nodes. We propose this framework to be applied to endothelial channel systems as well, as fenestrated capillary systems are known to have a volatile exchange of fluid with the surrounding tissue, mainly due to transmural pressure differences [24]. Note, that it would be crucial for such systems to implement terminal nodes for fluid injection and drainage.

Complex multi transport probems in biology

We propose for future research to combine this extended Ostrenko model with the metabolite uptake discussed in section 3.4 in order to obtain a complex model for the morphogenesis of the sinusoids and canaliculi in the liver lobule, based on the transport and processing of bile salt or drug components in between them. Hence we consider this problem in the following multi-layer representation, see Figure 4.2a. As displayed before, we may easily compute the flux landscape and deposition rates for given concentration landscapes in the canaliculi. Taking a reasonable landscape as the baseline for any adaptation processes, we propose the vessel system to be remodeled to the point that the Münch numbers M ensure a wet-tip regime. Doing so will ultimately alter the flow $\bar{v}$ and the deposition rates G, which in turn will change the water influx and solute transport of hepatocytes. In this model framework we assume that demand will be matched by the supply of the sinusoids, in first instance we will do so for metabolites only. Hence we may deploy the framework discussed in the previous

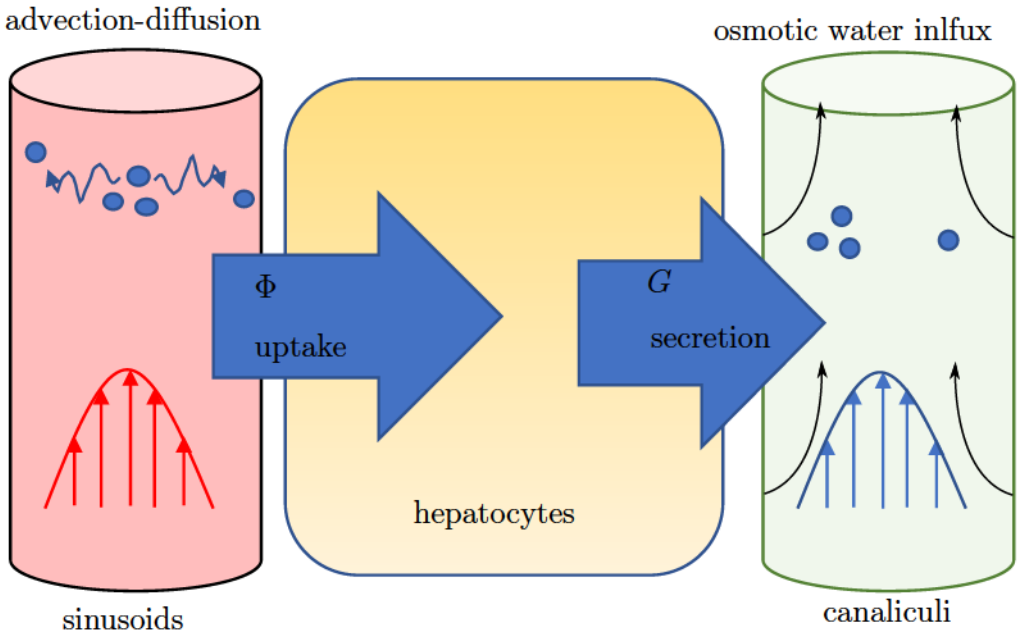

Figure 4.2: Schematic liver transport model, in order to simulate and identify optimal metabolite uptake and secretion patterns.

chapter, demonstrating the uptake dependence of the Peclet number and local absorption rate $\bar{\beta}$. Hence we could install an elaborated demand supply chain where the canaliculi as consumers will direct the morphogenesis of the sinusoids. It has further been shown that the concentration level of bile salt components in blood may alter the overall perfusion of the liver [69]. Further it was discussed that sinusoidal pressure and perfusion does not considerably alter bile output beyond a minimal perfusion threshold [23]. Therefore it is advised to take into account saturating feedback models where the actual supply of bile salt components will determine the subsequent deposition rates and the osmotic influx of water and concentration landscapes as well as the total outflux of bile. The total level of bile output is then to change the concentration in blood after passing the digestion tract and altering the subsequent perfusion of the lobules etc. We expect this scenario to require an increased numerical effort though, due to its enormous complexity. It should be pointed out here, that this ansatz, likely based on the metabolic cost function models, shall be customized for any interacting endothelial and epithelial system, e.g. kidneys or pancreas.

4.3.2 Absorption rate optimization and microscopic elimination models

As discussed previously we are planning to extend the presented framework for metabolite uptake in a chimera like ansatz: First, having topologically robust networks generated by wall-shear stress driven pruning mechanism involving noisy flow landscapes. Second, performing an uptake optimization by variation of edgewise absorption rates

$\bar{\beta}$. We demonstrated that wall shear stress driven systems are partially capable of adjusting toward metabolic needs, and subsequently generating network wide filtration levels of interest if given a specific $\bar{\beta}$ environment. Here we propose to increase the configuration space of a flow network, which is so far rather geometrical, by the number of edges in the network as $\bar{\beta} \to \boldsymbol{\beta}$. This procedure seems appealing as it emphasizes the narrative of a local organization level simultaneously to the radial adaptation processes. It seems unclear at this point whether the metabolic cost function ansatz discussed in the previous chapters is suitable for this problem as one would be required to evaluate the problem

$$d\Gamma = \nabla_r \Gamma^T \cdot d\boldsymbol{r} + \nabla_\beta \Gamma^T \cdot d\boldsymbol{\beta} \tag{4.15}$$

Now, we would consider a separation of adaptation schemes where the $\boldsymbol{\beta}$ landscape adjusts toward the finalized pruned structure for given $\boldsymbol{r}$ and $\boldsymbol{Pe}$. In case there are radial dependencies in the absorption rates to consider (which we utterly neglected in this thesis) one has to incorporate this into the ongoing adaption evaluations as well. One is to be confronted with a complexity explosion, when considering a microscopic breakdown of $\boldsymbol{\beta}$ on the basic ideas presented in section 3.4 or the appendix B.2. Here we could consider permeability changes of the membrane, clearance rates and density of active transporters leading up to

$$d\boldsymbol{\beta} = \boldsymbol{D}_r(\boldsymbol{\beta}) \cdot d\boldsymbol{r} + \boldsymbol{D}_\alpha(\boldsymbol{\beta}) \cdot d\boldsymbol{\alpha} + \boldsymbol{D}_\mu(\boldsymbol{\beta}) \cdot d\boldsymbol{\mu} + \boldsymbol{D}_p(\boldsymbol{\beta}) \cdot d\boldsymbol{p}_{BH} + \ldots \tag{4.16}$$

where $\boldsymbol{D}(\boldsymbol{\beta})$ is the Jacobian of $\boldsymbol{\beta}$ and parameters are to be added depending on the particular vessel system.

Appendix A

More on coupled intertwined networks

In this appendix we provide additional material on simulations as performed in section 3.2 for alternative plexus types, such as Laves graphs and diamond lattices. Note that no significant changes occur due to the change of the graph type. The only graph type specific characteristic seems to be the already known change in saturation levels of the nullity, which was discussed for monolayer networks in section 3.1.3.

A.1 Coupling of Diamond lattices

In this section we give an overview of the results for diamond lattices for repulsively and attractively coupled systems. The lattices were generated by repetition of unit cells, enabling us to define edge adjacencies of closest neighbors. In detail, the dual structure was generated by first repeating a unit cell (consisting of points $(0,0,0)$, $(0.5,0.5,0.5)$, $(1,0,1)$, $(0,1,1)$, $(1,1,0)$, connecting those pairs of relative distance $\delta = \sqrt{3}/2$) periodically with the three translation vectors $\boldsymbol{a} = i * (1,0,0)$, $\boldsymbol{b} = j * (0,1,0)$, $\boldsymbol{c} = k * (0,0,1)$ with $i,j,k \in \mathbb{Z}$ and $(i+j+k)mod2 = 0$. The second network is acquired by copying the first structure and shifting it by $\boldsymbol{t} = (1,1,1)$. Subsequently one has one edge in a network being affiliated with up to six edges of the other network. These six edges form a loop by themselves, as diamond lattices are of girth six.

A.1.1 Repulsive coupling

We see the same nullity transition behavior as before for cubic lattices in section 3.2.3. As the coupling, λ_1, is increased we find the nullity reduced. In general we saturate for purely fluctuation driven systems at the same nullity levels as discussed for monolayers. Further we find from the nullity state diagram in Figure A.1 the logarithmic transition to prevail. The general switch of dissipation and volume optimized systems are displayed in Figure A.2.

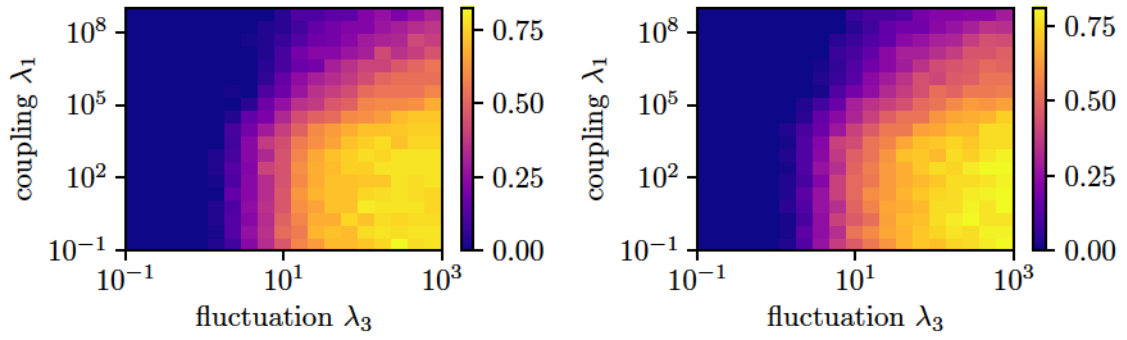

Figure A.1: Nullity ϱ state diagrams for stationary states of the coupled ODE systems (3.57) for $\varepsilon < 0$. Displayed are the symmetric scans for coupling λ_1 and fluctuation λ_3 for a dual diamond plexus, indicating coupling induced nullity breakdown for both networks.

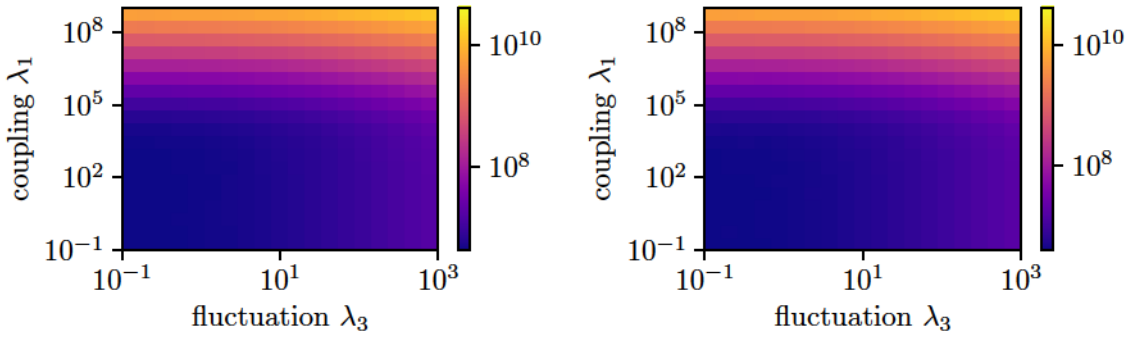

(a) Network power dissipation D

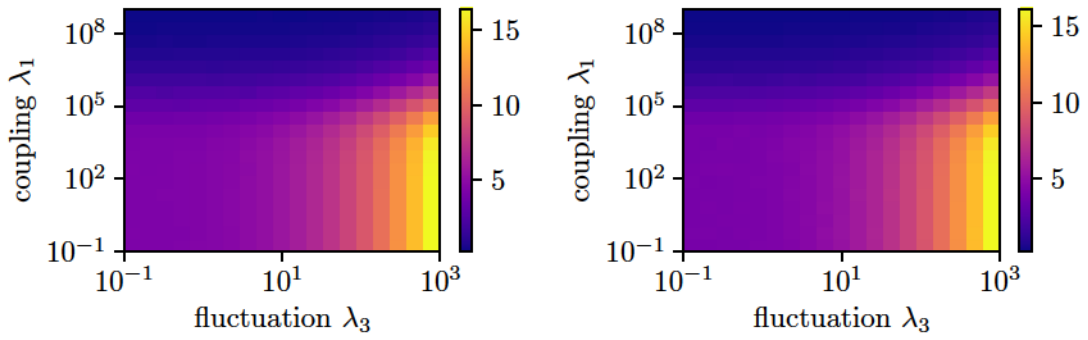

(b) Network overall cross section S

Figure A.2: Dissipation, D, and area cross section diagrams, S for a dual diamond plexus, for repulsively coupled networks, with network 1 on the right-hand side and network 2 on the left-hand side.

A.1.2 Attractive coupling

Here we see right away that the new emerging nullity transition for attractively coupled networks is preserved regardless the topology change. The nullity state diagram in Figure A.3 indicates logarithmic transition behavior as discussed in section 3.2.4. Unlike for fluctuation induced nullity we have the coupling enabling full plexus recovery. We once again find no significant change in the dissipation and volume development apart from the λ_3 generated increase.

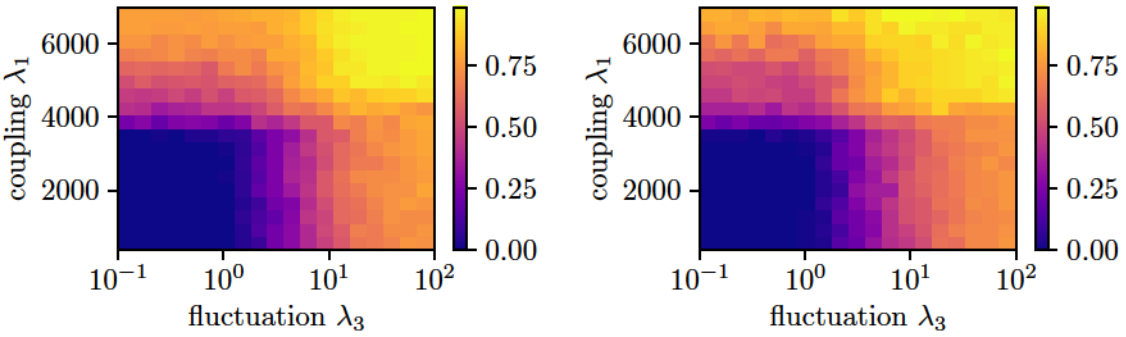

Figure A.3: Nullity ϱ state diagrams for stationary states of the coupled ODE systems (3.57) for $\varepsilon > 1$. Displayed are the symmetric scans for coupling λ_1 and fluctuation λ_3 for a dual diamond plexus, indicating coupling induced nullity onset and plexus recovery for both networks.

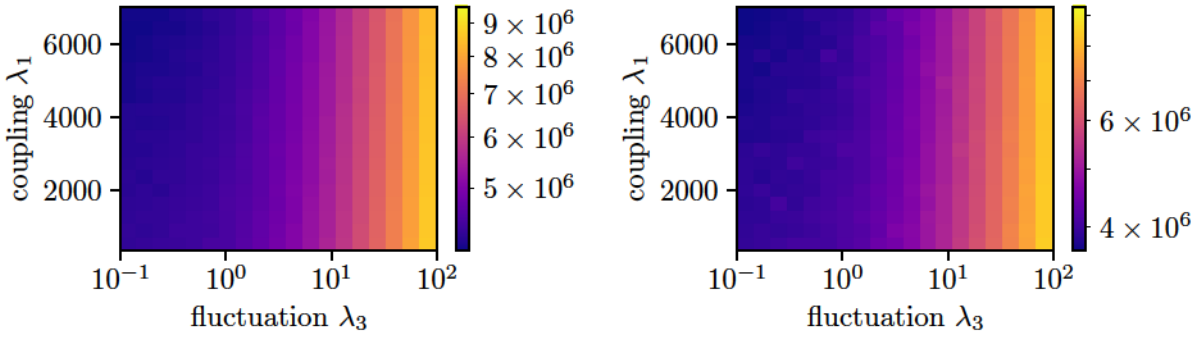

(a) Network power dissipation D

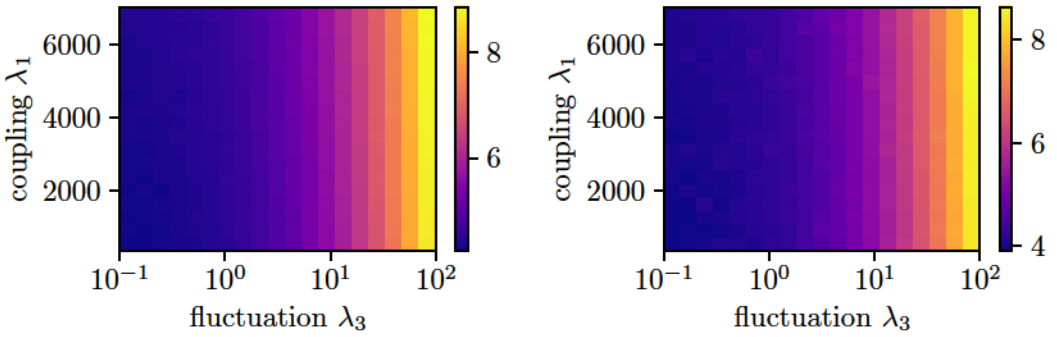

(b) Network overall cross section S

Figure A.4: Dissipation, D, and area cross section diagrams, S, for a dual diamond plexus, for attractively coupled networks, with network 1 on the right-hand side and network 2 on the left-hand side.

A.2 Coupling of Laves Graphs

In this section we give an overview of the results for laves lattices for repulsively and attractively coupled systems. The lattices were generated by repetition of unit cells, enabling us to define edge adjacencies of closest neighbors. In detail, the dual structure was generated by first repeating a unit cell (consisting of points $(0,0,0)$, $(1,1,0)$, $(1,2,1)$, $(0,3,1)$, $(2,2,2)$, $(3,3,2)$, $(3,0,3)$, $(2,1,3)$, connecting those pairs of relative distance $\delta = \sqrt{2}$) periodically with the three translation vectors $\boldsymbol{a} = i * (4,0,0)$, $\boldsymbol{b} = j * (0,4,0)$, $\boldsymbol{c} = k * (0,0,4)$ with $i,j,k \in \mathbb{Z}$. The second network is acquired by mirroring in order to create the opposing chirality of the first structure, i.e. $\boldsymbol{a} \to -\boldsymbol{a}$, and shifting it by $\boldsymbol{t} = (3,2,0)$. Subsequently one has one edge in a network being affiliated with up to eight edges of the other network. As a matter of fact one finds these eight edges do not form a complete cycle as the girth of the Laves graph is ten.

A.2.1 Repulsive coupling

We see the same nullity transition behavior as before for cubic lattices in section 3.2.3. As the coupling λ_1 is increased we find the nullity reduced. In general we saturate for

purely fluctuation driven systems at the same nullity levels as discussed for monolayers. Once again it is only the Laves graph topology enabling full plexus recovery for fluctuating flow patterns. The general breakdown behavior and saturation onset are displayed in Figure A.5, we find slight shifting of these thresholds with variation of the coupling λ_1. The general switch of dissipation and volume optimized systems are displayed in Figure A.6.

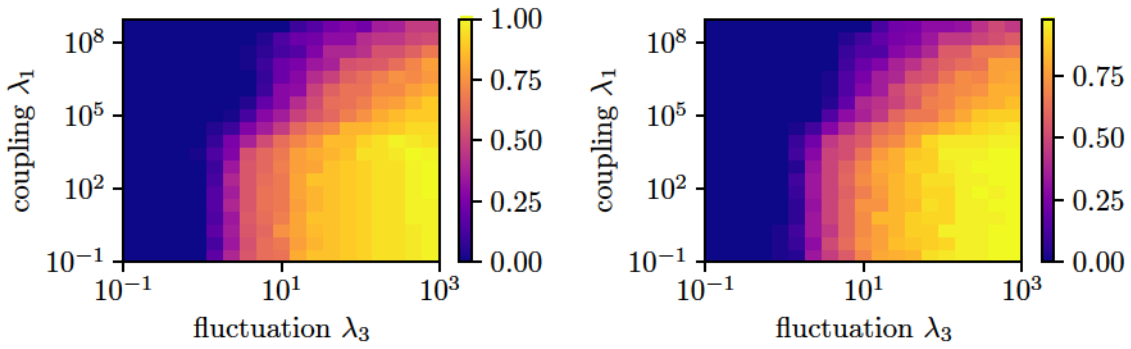

Figure A.5: Nullity ϱ state diagrams for stationary states of the coupled ODE systems (3.57) for $\varepsilon < 0$. Displayed are the symmetric scans for coupling λ_1 and fluctuation λ_3, indicating coupling induced nullity breakdown for both networks.

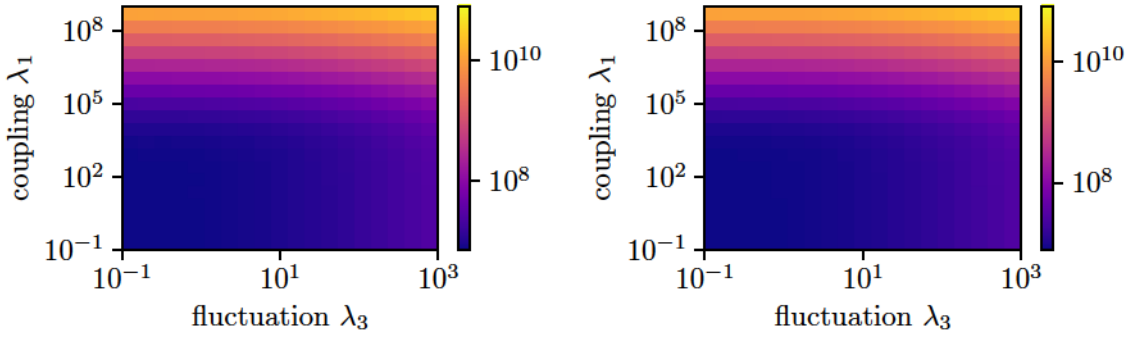

(a) Network power dissipation D

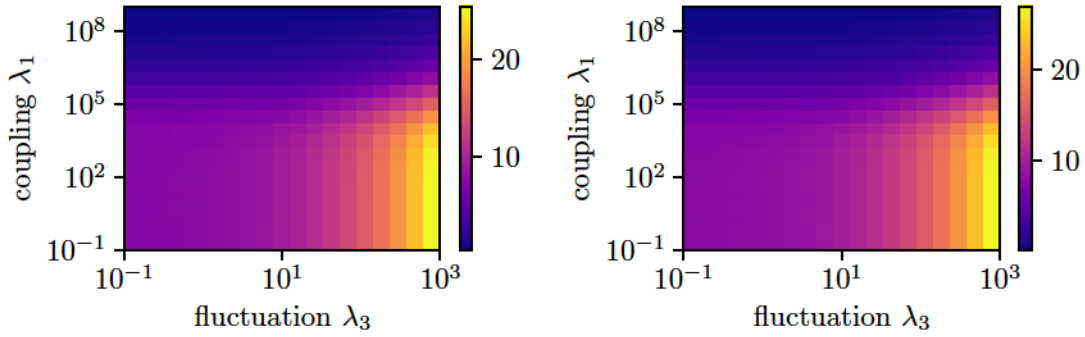

(b) Network overall cross section S

Figure A.6: Dissipation, D, and area cross section diagrams, S, for repulsively coupled Laves graphs, with network 1 on the right-hand side and network 2 on the left-hand side.

A.2.2 Attractive coupling

Here we see right away that the new emerging nullity transition for attractively coupled networks is preserved regardless the topology change. The nullity state diagram in Figure A.7 indicates logarithmic transition behavior as discussed in section 3.2.4. Once again, unlike for fluctuation induced nullity we have the coupling generating full plexus recovery. The onset and saturation of the λ_1 induced transition is displayed in Figure A.7. We once again find no significant change in the dissipation and volume development apart from the λ_3 generated increase, see Figure A.8 .

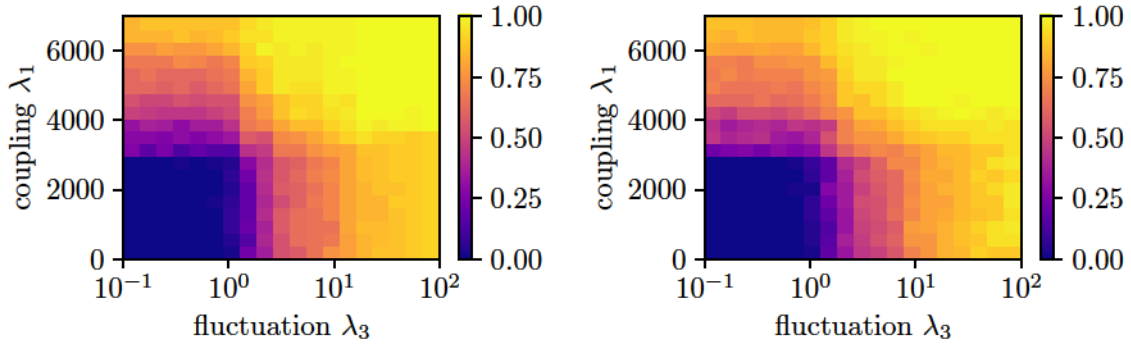

Figure A.7: Nullity ϱ state diagrams for stationary states of the coupled ODE systems (3.57) for $\varepsilon > 1$. Displayed are the symmetric scans for coupling λ_1 and fluctuation λ_3 for dual Laves graphs, indicating coupling induced nullity onset and plexus recovery for both networks.

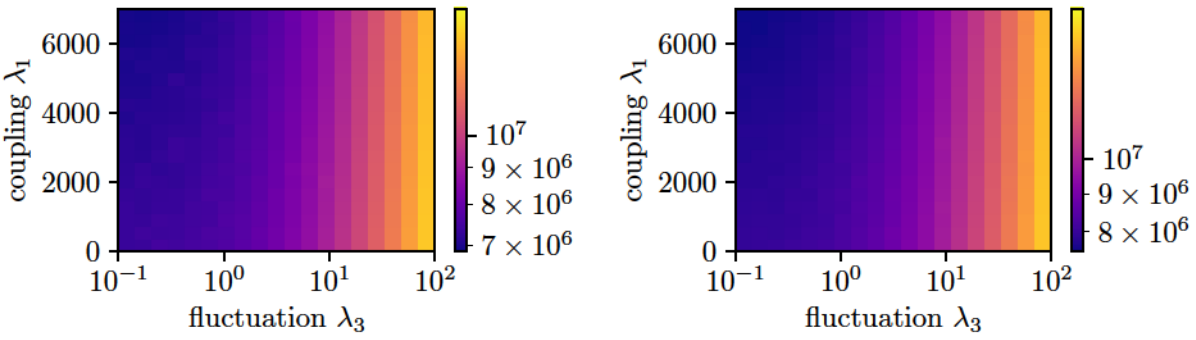

(a) Network power dissipation D

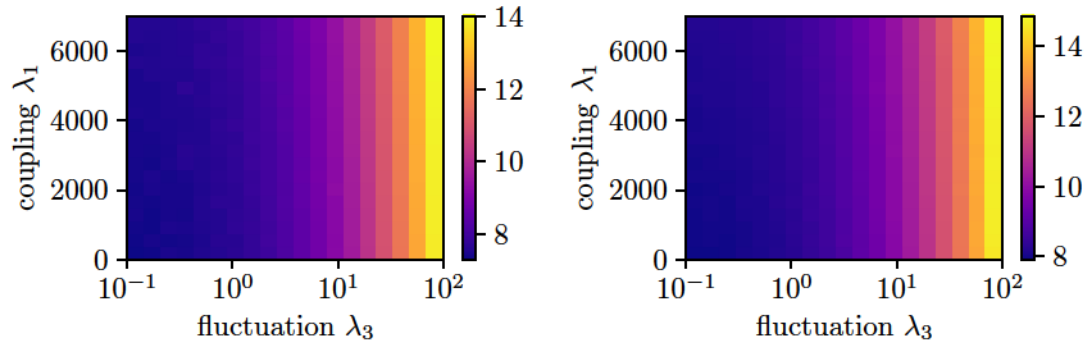

(b) Network overall cross section S

Figure A.8: Dissipation, D, and area cross section diagrams, S, for attractivvely coupled Laves graphs, with network 1 on the right-hand side and network 2 on the left-hand side.

Appendix B

More on metabolite uptake adaptation

In this appendix we provide additional information on the analytic framework discussed in section 3.4.2 and following. Here we present the detailed derivation of the dynamical system for the metabolic cost function ansatz, as well as a detailed discussion on microscopic uptake toy models compatible which our approach. Further we illustrate the resulting network structures for three-dimensional plexi, whose behavior is largely described in section 3.4.2 and 3.4.2.

B.1 Deriving dynamical systems from demand-supply relationships

In this section we would like to demonstrated the derivation of the dynamical equations from the gradient as discussed in section 3.4.2 by considering the system,

$$\Gamma = \sum_e \left(\Phi_e - \Phi_{e,0}\right)^2 = \Delta\boldsymbol{\Phi}^T \cdot \Delta\boldsymbol{\Phi} \tag{B.1}$$
$$\text{with } \Delta\boldsymbol{\Phi} = \boldsymbol{\Phi} - \boldsymbol{\Phi}_0$$

where Φ_e denotes the actual metabolite uptake per edge and $\Phi_{e,0}$ the surrounding tissue's demand. Here $\Gamma \geq 0$ represents the cost of a flow network that is supposed to deliver a metabolite at the exact rates $\boldsymbol{\Phi}_0$ and any deviation from doing so is penalized. That may be a reasonable first assumption as oversupply of glucose, proteins and salts may results in unfavorable osmotic pressures while an under-supply may end in starvation of the cells involved. Remember the framework elaborated on in section 3.4 in order to derive $\nabla_r\Gamma$ dependent radial adaptation modeling. As discussed in section 3.4.1 we have the concentration landscape defined by the injection and drainage of solute (3.110), (3.111) as,

$$\boldsymbol{M}\cdot\boldsymbol{c} = \boldsymbol{J} \tag{B.2}$$
$$\text{with } M_{vw} = \sum_e q_e \left[B_{ve}Pe_e + |B_{ve}|x_e \coth\left(\frac{x_e}{2}\right)\right]\delta_{vw}$$
$$- \sum_{e\in out(v)} q_e \frac{x_e \mathrm{e}^{-\frac{Pe_e}{2}}}{\sinh\left(\frac{x_e}{2}\right)}\delta_{\omega(e),w} - \sum_{e\in in(v)} q_e \frac{x_e \mathrm{e}^{\frac{Pe_e}{2}}}{\sinh\left(\frac{x_e}{2}\right)}\delta_{\alpha(e),w} \tag{B.3}$$

displaying $\boldsymbol{M}$ as an asymmetric matrix, with $q_e = \frac{A_e D}{2L_e}$, We rewrite the edgewise metabolite uptake (3.100) as

$$\Phi_e = q_e \left(\bar{c}_{\alpha(e)} G_e^0 + \bar{c}_{\omega(e)} G_e^1\right) \tag{B.4}$$

$$G_e^0 = \left(x_e \coth\left(\frac{x_e}{2}\right) - \frac{x_e \mathrm{e}^{\frac{Pe_e}{2}}}{\sinh\left(\frac{x_e}{2}\right)} + Pe_e\right) \tag{B.5}$$

$$G_e^1 = \left(x_e \coth\left(\frac{x_e}{2}\right) - \frac{x_e \mathrm{e}^{-\frac{Pe_e}{2}}}{\sinh\left(\frac{x_e}{2}\right)} - Pe_e\right) \tag{B.6}$$

Hence we may calculate the gradient of (B.1) as

$$\nabla_r \Gamma = 2D\left[\Delta\boldsymbol{\Phi}\right] \cdot \Delta\boldsymbol{\Phi} \tag{B.7}$$

where $D\left[\Delta\boldsymbol{\Phi}\right]$ is the Jacobian whose elements are of the form $D_{je}\left[\Delta\boldsymbol{\Phi}\right] = \partial_{r_j}\Phi_e = \partial_j \Phi_e$ reading,

$$\begin{aligned} D_{je}\left[\Delta\boldsymbol{\Phi}\right] = {} & \partial_j q_e \left(\bar{c}_{\alpha(e)} G_e^0 + \bar{c}_{\omega(e)} G_e^1\right) \\ & + q_e \left(\partial_j \bar{c}_{\alpha(e)} G_e^0 + \partial_j \bar{c}_{\omega(e)} G_e^1\right) \\ & + q_e \left(\bar{c}_{\alpha(e)} \partial_j G_e^0 + \bar{c}_{\omega(e)} \partial_j G_e^1\right) \end{aligned} \tag{B.8}$$

Calculating the components one easily acquires the first derivates of q_e as

$$\partial_j q_e = 2\pi R_e \delta_{je} \tag{B.9}$$

For derivatives of concentration terms we need to employ (3.110) in its reduced form for the absorbing boundary problem as discussed in section 3.4.1. Doing so we calculate for all $c_v > 0$ and $J_v \geq 0$ using (3.112)

$$\begin{aligned} \partial_j c_v &= \partial_j \left(\boldsymbol{e}_v^T \cdot \boldsymbol{c}\right) = \boldsymbol{e}_v^T \cdot \partial_j \left(\tilde{\boldsymbol{M}}^{-1} \tilde{\boldsymbol{J}}\right) \\ &= -\boldsymbol{e}_v^T \cdot \left(\tilde{\boldsymbol{M}}^{-1} \partial_v \tilde{\boldsymbol{M}} \tilde{\boldsymbol{M}}^{-1} \tilde{\boldsymbol{J}}\right) = -\boldsymbol{e}_v^T \cdot \left(\tilde{\boldsymbol{M}}^{-1} \partial_j \tilde{\boldsymbol{M}}\right) \cdot \boldsymbol{c} \end{aligned} \tag{B.10}$$

In detail we calculate $\partial_j \tilde{M}_{vw}$ to be

$$\begin{aligned} \partial_j \tilde{M}_{vw} = {} & \sum_e \left\{\partial_j q_e \left[B_{ve} Pe_e + |B_{ve}| x_e \coth\left(\frac{x_e}{2}\right)\right]\right\} \delta_{vw} \\ & + \sum_e \left\{ q_e \left(B_{ve} + |B_{ve}| \left\{ \frac{\coth\left(\frac{x_e}{2}\right)}{x_e} - \left[\frac{\coth\left(\frac{x_e}{2}\right)}{\cosh\left(\frac{x_e}{2}\right)}\right]^2 \right\} \right) \partial_j Pe_e \right\} \delta_{vw} \\ & - \sum_{e \in out(v)} \left\{ \partial_j q_e \frac{x_e \mathrm{e}^{-\frac{Pe_e}{2}}}{\sinh\left(\frac{x_e}{2}\right)} + q_e \frac{\mathrm{e}^{-\frac{Pe_e}{2}}}{\sinh\left(\frac{x_e}{2}\right)} \left[\frac{Pe_e}{x_e} - \frac{x_e}{2} - \frac{Pe_e}{2} \coth\left(\frac{x_e}{2}\right)\right] \partial_j Pe_e \right\} \delta_{\omega(e),w} \\ & - \sum_{e \in in(v)} \left\{ \partial_j q_w \frac{x_e \mathrm{e}^{-\frac{Pe_e}{2}}}{\sinh\left(\frac{x_e}{2}\right)} + q_e \frac{\mathrm{e}^{-\frac{Pe_e}{2}}}{\sinh\left(\frac{x_e}{2}\right)} \left[\frac{Pe_e}{x_e} + \frac{x_e}{2} - \frac{Pe_e}{2} \coth\left(\frac{x_e}{2}\right)\right] \partial_j Pe_e \right\} \delta_{\alpha(e),w} \end{aligned} \tag{B.11}$$

Every other derivative of concentrations c_w at the absorbing boundary is correspondingly set with $\partial_j c_w = 0$. Further we find the derivatives of the flow coefficients G_e^i to result in

$$\begin{aligned}\partial_j G_e^0 = \frac{\partial_j Pe_e}{\sinh\left(\frac{x_e}{2}\right)} \Bigg\{ \frac{Pe_e}{x_e} \left[\cosh\left(\frac{x_e}{2}\right) - \mathrm{e}^{\frac{Pe_e}{2}}\right] + \sinh\left(\frac{x_e}{2}\right) \\ - \frac{Pe_e}{2\sinh\left(\frac{x_e}{2}\right)} + \mathrm{e}^{\frac{Pe_e}{2}} \left[\frac{Pe_e}{2}\coth\left(\frac{x_e}{2}\right) - \frac{x_e}{2}\right] \Bigg\} \end{aligned} \tag{B.12}$$

$$\begin{aligned}\partial_j G_e^1 = \frac{\partial_j Pe_e}{\sinh\left(\frac{x_e}{2}\right)} \Bigg\{ \frac{Pe_e}{x_e} \left[\cosh\left(\frac{x_e}{2}\right) - \mathrm{e}^{-\frac{Pe_k}{2}}\right] - \sinh\left(\frac{x_e}{2}\right) \\ - \frac{Pe_e}{2\sinh\left(\frac{x_e}{2}\right)} + \mathrm{e}^{-\frac{Pe_e}{2}} \left[\frac{Pe_e}{2}\coth\left(\frac{x_e}{2}\right) + \frac{x_e}{2}\right] \Bigg\} \end{aligned} \tag{B.13}$$

And eventually we calculate the explicit derivatives for the edgewise Peclet numbers as

$$\partial_j Pe_e = \frac{2Pe_j}{R_j} \left[\delta_{je} - 2\left(\frac{R_e}{R_j}\right)^2 C_j \left(\boldsymbol{B}^T \left[\boldsymbol{B}\boldsymbol{C}\boldsymbol{B}^T\right]^\dagger \boldsymbol{B}\right)_{je}\right] \tag{B.14}$$

Now, using equations (B.9)-(B.14) we are able to evaluate the Jacobian (B.8), and may compute

$$\partial_t r_e \propto -2D\left[\Delta\boldsymbol{\Phi}\right] \cdot \Delta\boldsymbol{\Phi} \tag{B.15}$$

for any given flow and concentration landscape of a Kirchhoff network. For now any vessel adapting according to (B.15), is essentially be informed on the uptake behavior of all vessel in the network. We may apply our formalism directly for (B.1), corresponding to the special case $a_0 = 0$ and $a_1 = 0$ of the model framework presented in section 3.4.2.

B.2 Microscopic uptake models

In section 3.4.1 we discussed a toy mode for microscopic uptake of solutes for cylindrical vessels, being surrounded by a bulk of tissue it feeds into. Here we would like to give an account on alternative uptake scenarios and its respective solutions.

B.2.1 Detailed uptake estimation in single layer systems

As mentioned in 3.4.1 , we proposed the first order approximation of this transport to be modeled via the nonlinear PDE

$$\partial_t c_H(z) = p_{BH}\left[c_B(z) - c_H(z)\right] + \left[\frac{\alpha_1}{\alpha_0 + c_B(z)}\right] c_B(z) - \left[\frac{\mu_1}{\mu_0 + c_H(z)}\right] c_H(z) \quad \text{(B.16)}$$

$$\partial_t c_B(z) = D\partial_{zz} c_B(z) - \bar{v}\partial_z c_B(z) - p_{BH}\left[c_B(z) - c_H(z)\right] - \left[\frac{\alpha_1}{\alpha_0 + c_B(z)}\right] c_B(z) \quad \text{(B.17)}$$

where a Michaelis-Menten like dynamic was assumed for active transport and clearance of the molecules of interest. We showed in section 3.4 that the linear regime with, with $\alpha \to \alpha_1/\alpha_0$ and $\mu \to \mu_1/\mu_0$, actually corresponds to the limit case of the Taylor dispersion model. Now we would like to illuminate the framework (B.16), (B.17) for abritrary parameter regimes. Doing so, we once again are interested in stationary solutions, beginning with (B.16) we get:

$$\partial_t c_H(z) = 0 \Rightarrow c_H(z) = \frac{q_0}{2} \pm \sqrt{\left(\frac{q_0}{2}\right)^2 + q_1} = f\left(c_B(z)\right) \quad \text{(B.18)}$$

$$\text{with } q_0(z) = \mu_0 + \frac{1}{p_{BH}}\left[\mu_1 - \left(\frac{\alpha_1}{\alpha_0 + c_B(z)}\right) c_B(z)\right]$$

$$q_1(z) = \mu_0 c_B(z)\left[1 + \frac{1}{p_{BH}}\left(\frac{\alpha_1}{\alpha_0 + c_B(z)}\right)\right]$$

For which only the positive solution is eligible to ensure $c_H \geq 0$, Solving (B.17) for the stationary case in combination with results of (B.18)

$$\partial_t c_B(z) = 0 \quad \text{(B.19)}$$

$$\Rightarrow D\partial_{zz} c_B(z) - \bar{v}\partial_z c_B(z) - p_{BH} c_B(z) - \left[\frac{\alpha_1}{\alpha_0 + c_B}\right] c_B(z) = p_{BH} f\left(c_B(z)\right)$$

Now this look indeed like an unpleasant non-linear ODE problem. Luckily, one is generally interested the limit cases for which (B.19) simplifies significantly. We discussed the linear case for $\alpha_0 \gg c_B$ and $\mu_0 \gg c_H$ already in section 3.4.1, as it coincides with limit case of the Taylor dispersion framework. Now we also could elaborate a bit on the opposite case for $\alpha_0 \ll c_B$ and $\mu_0 \ll c_H$, Then we get for (B.18), (B.19)

$$c_H = c_B + p_{BH}(\alpha_1 - \mu_1) \quad \text{(B.20)}$$

$$0 = D\partial_{zz} c_B(z) - \bar{v}\partial_z c_B(z) - \mu_1 \quad \text{(B.21)}$$

Therefore we readily solve (B.22) using the substitution $\kappa = D\partial_z c_B$ and acquire

$$\kappa = -\frac{D\mu_1}{\bar{v}}\left(1 - \mathrm{e}^{\frac{\bar{v}z}{D}}\right) \Rightarrow c_B(z) = c_0 - \left(\frac{\mu_1 L^2}{D}\right)\left[\frac{Pe\frac{z}{L} + \left(1 - \mathrm{e}^{Pe\frac{z}{L}}\right)}{Pe^2}\right] \tag{B.22}$$

Now this result would require a completely different handling for to be generalized for arbitrary flow networks. As we do have $c_B(z=0) = c_0$ and $c_B(z=L) = c_0 - \left(\frac{\mu_1 L^2}{D}\right)\left[\frac{Pe+\left(1-\mathrm{e}^{Pe}\right)}{Pe^2}\right]$ from (B.22) one might expect conflicts regarding the nodal concentrations not matching up in reticulated networks for a given flow landscape and absorption parameters. Therefore computation of the networks nodal concentration according to (3.110) is not possible. This problem partly corresponds to the problem discussed in [82] where it is proposed that for any complex flow network, where the solute transport through any channel is to be directed with the volume flow, one may consider volume-less branching points enabling perfect mixing of incoming solute. Hence one would be able to reformulate the solute conservation (3.109) as

$$J_v = \sum_{e \in out(v)} I_{\alpha(e)}[c_v] - \sum_{e \in in(v)} I_{\omega(e)}\left[c_{\alpha(e)}\right] \tag{B.23}$$

which would be used to solve for c_v defining a consistent c_0 for vessels carrying flow out of the node.

B.2.2 Detailed uptake estimation in liver sinusoids

During the collaboration with the Zerial Lab, MPI-CBG, we were advised that the microscopic breakdown of the absorption rate is not yet elaborate enough in the case of liver lobule. Here we are confronted with the fact, that an inter-layer between the sinusoids and hepatocytes displays its own dynamic behavior: The space of Disse. In order to address this issue we propose the extension of the organ coarse-grained hepatic elimination model discussed previously [117, 118], see Figure B.1. Here we

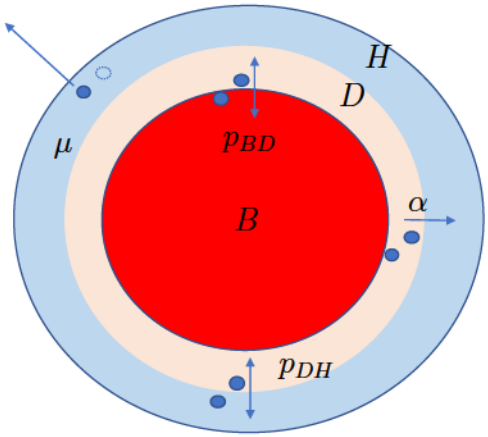

Figure B.1: One dimensional uptake model in accordance to the hepatic uptake model [117]: Interplay between Blood capillaries (B), space of Disse (D) and hepatocyte bulk (H)

introduce the continuity equation for the respective metabolite concentrations c_B, c_H and c_D and the corresponding transport processes of cross-membrane diffusion p_{BH}, p_{DH}, active transport at the basal membrane α and hepatic clearance μ, The particular characteristic involves the space of Disse, which is known to carry a flow that is generally opposed to the portal vein to central vein directionality of the blood flow. For the sake of simplicity we do not consider fluid exchange between adjacent tissue layers, i.e. transmural responses or lymphatic functions. Hence we formulate the dynamics of the problem in a first order approximation as

$$\partial_t c_H = p_{DH}\left(c_D - c_H\right) + \alpha c_D - \mu c_H \tag{B.24}$$

$$\partial_t c_D = D_D \partial_{zz} c_D - \bar{u}\partial_z c_D - p_{DH}\left(c_D - c_H\right) + p_{BD}\left(c_B - c_D\right) - \alpha c_D \tag{B.25}$$

$$\partial_t c_B = D_B \partial_{zz} c_B - \bar{v}\partial_z c_B - p_{BD}\left(c_B - c_D\right) \tag{B.26}$$

Here we introduce the advection velocities $\bar{v}$ for perfusion in the capillary and $\bar{u}$ in the space of Disse, with $\bar{v} \gg \bar{u}$, The diffusion constants D_D, D_B are not necessarily identical. Assuming here a linear regime, below the respective transport capacity and clearance limit, one may formulate this problem as a coupled ODE system for its stationary states as

$$\partial_t c_H = 0 \Rightarrow c_H = c_D \frac{p_{DH} + \alpha}{p_{DH} + \mu} \tag{B.27}$$

$$\partial_t c_D = 0 \Rightarrow 0 = D_D \partial_{zz} c_D - \bar{u}\partial_z c_D - \left[\frac{p_{BD}\left(\mu + p_{DH}\right) + \mu\left(\alpha + p_{DH}\right)}{\mu + p_{DH}}\right] c_D + p_{BD} c_B \tag{B.28}$$

$$\partial_t c_B = 0 \Rightarrow 0 = D_B \partial_{zz} c_B - \bar{v}\partial_z c_B - p_{BD}\left(c_B - c_D\right) \tag{B.29}$$

One may readily solve the system (B.28), (B.29) by writing $\boldsymbol{a} = (c_D, c_B)$ and $\boldsymbol{b} = \partial_z \boldsymbol{a}$ and solving the system

$$\partial_z \begin{bmatrix} \boldsymbol{a} \\ \boldsymbol{b} \end{bmatrix} = \begin{bmatrix} 0 & \boldsymbol{I} \\ \boldsymbol{A} & \boldsymbol{B} \end{bmatrix} \cdot \begin{bmatrix} \boldsymbol{a} \\ \boldsymbol{b} \end{bmatrix} \tag{B.30}$$

Here we have the matrices $\boldsymbol{A}$, $\boldsymbol{B}$, $\boldsymbol{I}$ with

$$\boldsymbol{I} = \begin{bmatrix} 1 & 0 \\ 0 & 1 \end{bmatrix}, \boldsymbol{A} = \begin{bmatrix} p_{BD} & -p_{BD} \\ -p_{BD} & p_{BD} + \frac{\mu(\alpha + p_{DH})}{\mu + p_{DH}} \end{bmatrix}, \boldsymbol{B} = \begin{bmatrix} \bar{u} & 0 \\ 0 & \bar{v} \end{bmatrix} \tag{B.31}$$

This framework simplifies significantly if we assume that diffusion-advection in space of Disse is negligible in comparison to the surface based exchange of solutes. In particular be would obtain a continuity equation for c_B as

$$0 \approx -\left[p_{BD} + \alpha + p_{DH}\frac{\mu - \alpha}{\mu + p_{DH}}\right] c_D + p_{BD} c_B \tag{B.32}$$

$$\partial_t c_B = 0 \Rightarrow 0 = D_B \partial_{zz} c_B - \bar{v}\partial_z c_B - \frac{\mu p_{BD}\left(\alpha + p_{DH}\right)}{p_{BD}\left(\mu + p_{DH}\right) + \mu\left(\alpha + p_{DH}\right)} c_B \tag{B.33}$$

On the other hand, it might be advisible to consider a further increase of the problems complexity by adding fluid exchange between adjacent zones due to emerging transmural pressure differences. We advise to treat this in first approximation with the extended Ostrenko model, see section section 4.3.1.

B.3 Metabolite uptake in three-dimensional plexi

In this section we present additional results of the metabolite uptake algorithm, as discussed in section 3.4. In section B.3.1 we revisit the link-wise adaptation model for three-dimensional lattices, the Laves graph in particular. In section B.3.2 we revisit the volume-wise adaptation model in the same manner. Note that the significant topological transitions are mostly preserved for changes from planar to non-planar plexi.

B.3.1 Link-wise demand adaptation

In Figure B.2 we present the collected results as state diagram grids for systematic parameter screens. Note that the grid's x-axis is illustrating different cases of absorption rates $\bar{\beta}$ while the demanded filtration rate σ_0 is displayed on the grid's y-axis. In detail, we present the system's emerging nullity ϱ in Figure B.2a, as defined previously in equation (3.35). In these diagrams we observe the networks reticulation to vary significantly, when exposed to the competing stimuli of (3.120). The results correspond largely to the ones found and discussed for hexagonal grids in section 3.4. In Figure B.3 we showcase exemplary network formations and concentration profiles, alongside detailed trajectories for nullity and filtration taken from the top-left diagrams in B.2. This diagram's data corresponds to the case of high demand in $\sigma_0 = 1.0$ and paired with low absorption $\bar{\beta} = 0.001$, Once again we find the formation of a 'bottleneck' at the peripheral links, and as we increase the dissipation feedback α_1 we observe an opening of these channels, which reorganizes the concentration landscape and the reticulation pattern. In Figure B.4, we display exemplary cases of the same nature, for the central diagram of the grid B.2, corresponding to $\sigma_0 = 0.1$ and $\bar{\beta} = 0.01$, Here we see once again a nullity breakdown due to increase of α_i. As previously discussed in section 3.4, we find the filtration diagrams B.4c to display a seeming match of metabolite uptake, which deteriorates for small dissipation factors α_1 paired with large volume penalties α_0. In Figure B.5, we display exemplary cases for the re-entrant behavior in the bottom-right diagram of the grid B.2, corresponding to $\sigma = 0.01$ and $\bar{\beta} = 0.1$, These sets depict a regime in which the tissue is supposedly on low demand, yet confronted with highly absorbing vessel surfaces. Naturally we should end here with a system that displays vessels degeneration and collapse in order to increase Pe, which in turn diminishes solute uptake. Subsequently we are operating in a system that is experiencing high wall-shear stress for the majority of remaining vessels in the network. As laid out previously, we find the interplay of wall-shear stress driven adaptation and this mechanism for generating high shear stresses to be the cause for re-entry behavior.

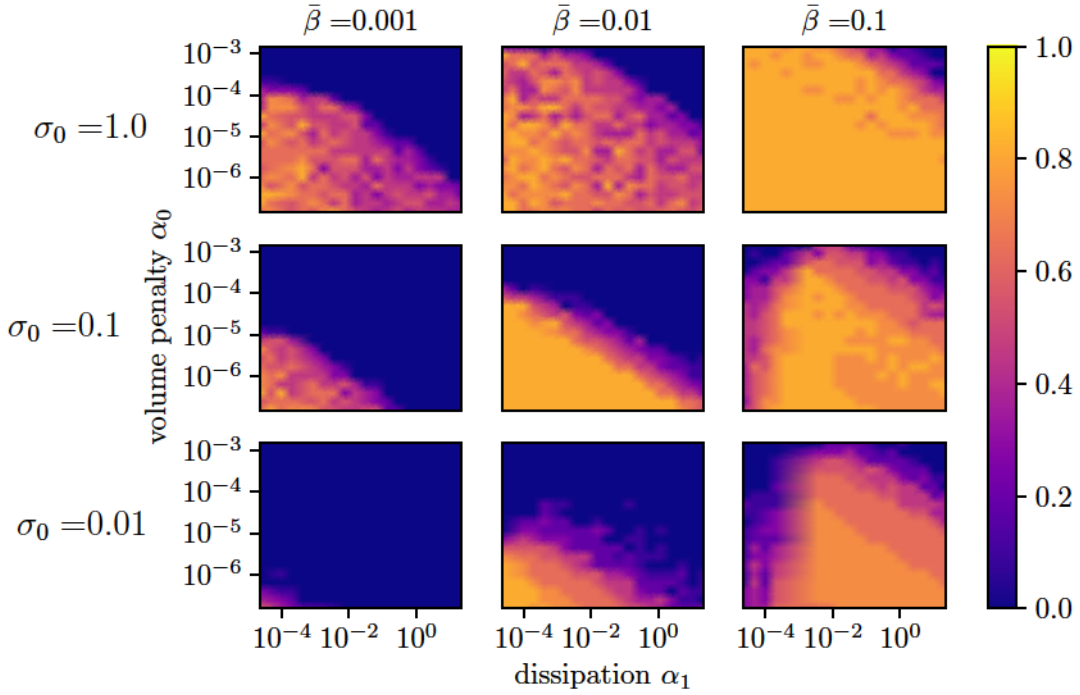

(a) Nullity ϱ

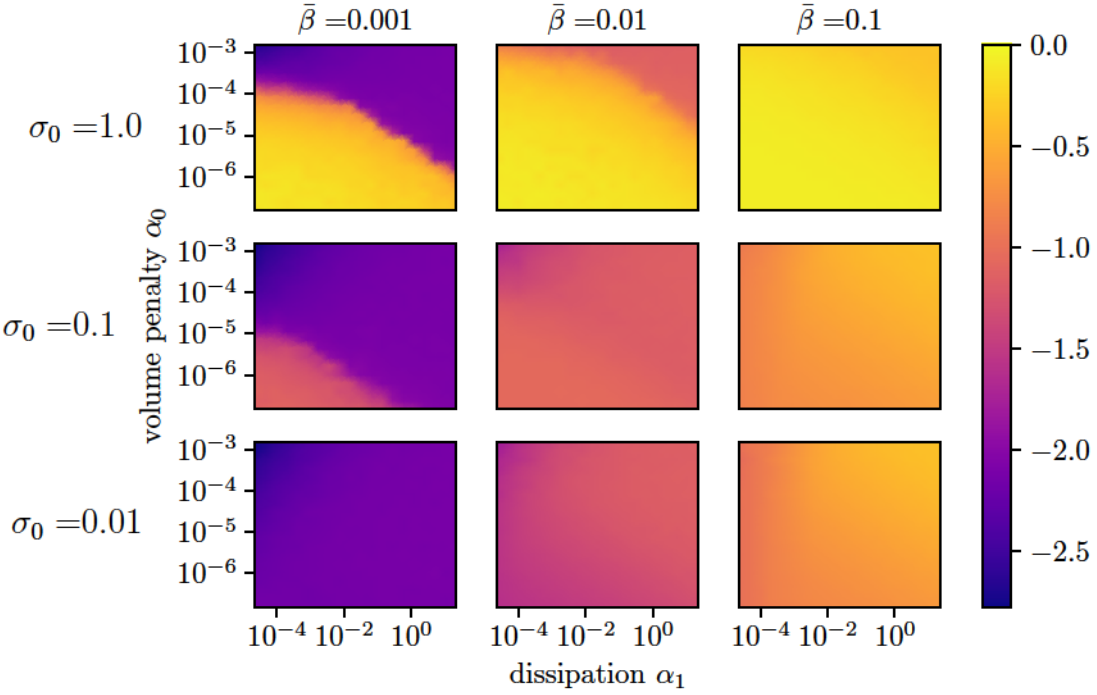

(b) Filtration σ

Figure B.2: Nullity and filtration diagrams for stationary states of the cost problem (3.120), with boundary parameter variation $\sigma_0 = \frac{\sum_e \Phi_{0,e}}{\sum_{J_n>0} J_n} \in \{10^0, 10^{-1}, 10^{-2}\}$, $\bar{\beta} \in \{10^{-1}, 10^{-1}, 10^{-2}\}$; systematic volume penalty α_0 and dissipation α_1 are scanned systematically: (a) The nullity phase diagram indicates a topological transition and re entrant behavior. (b) Filtration diagram indicating varying quality of filtration adjustment for varying $\bar{\beta}$,

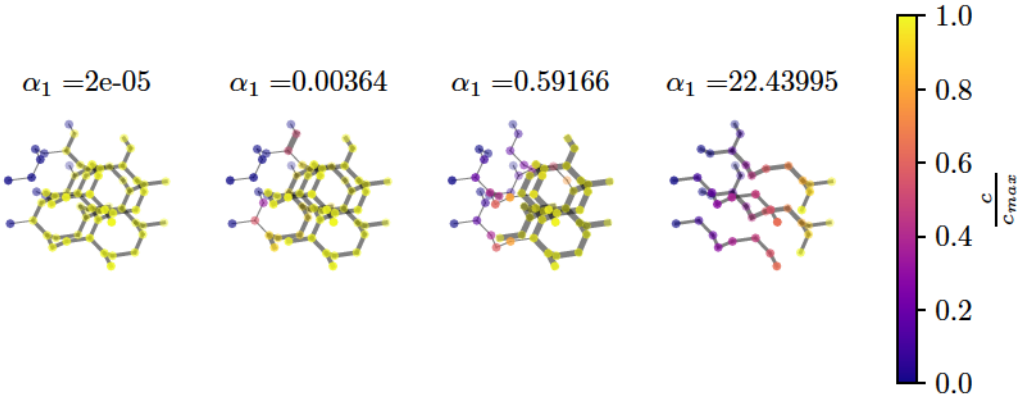

(a) Network skeletons and relative concentration profile

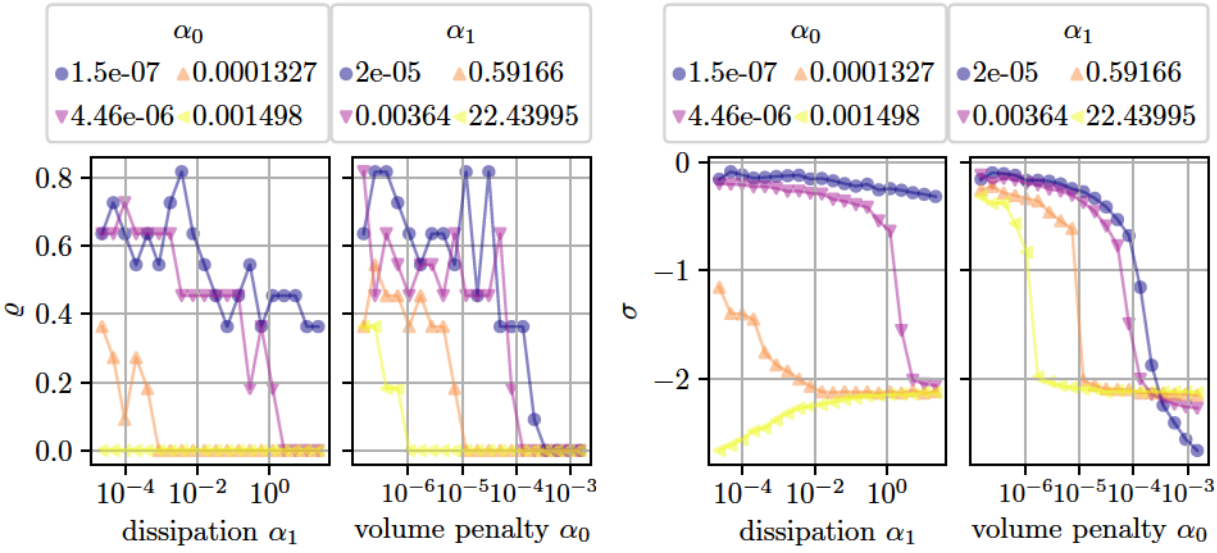

(b) Nullity ϱ

(c) Filtration σ

Figure B.3: Formations of the adaptation model (3.120) with $\sigma_0 = 1.0$ and $\bar{\beta} = 0.001$, displayed for selected dissipation α_1 and volume penalties α_0: (a) Network plots illustrating the relative concentration profiles and edge radii, depicted for $\alpha_0 = 4.4 \cdot 10^{-6}$, (b) Nullity transitions displaying α_1 and α_0 induced reticulation breakdown. (c) Filtration trajectories depicting switches in correlation to topological transitions.

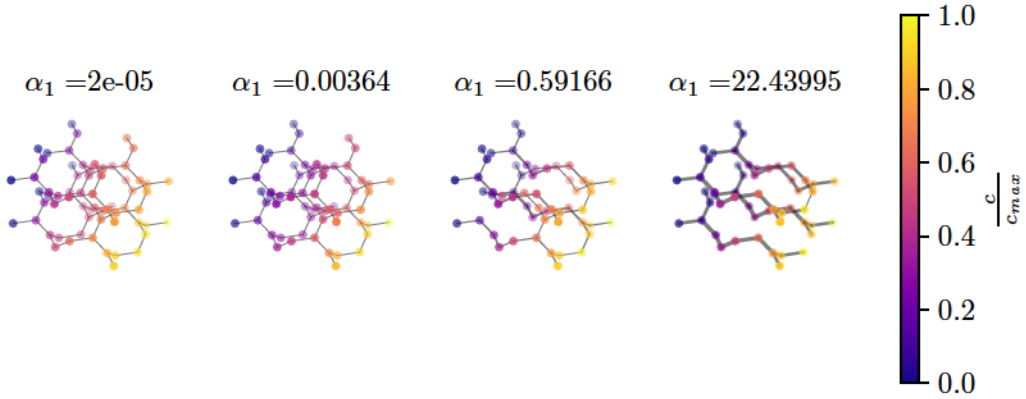

(a) Network skeletons and relative concentration profile

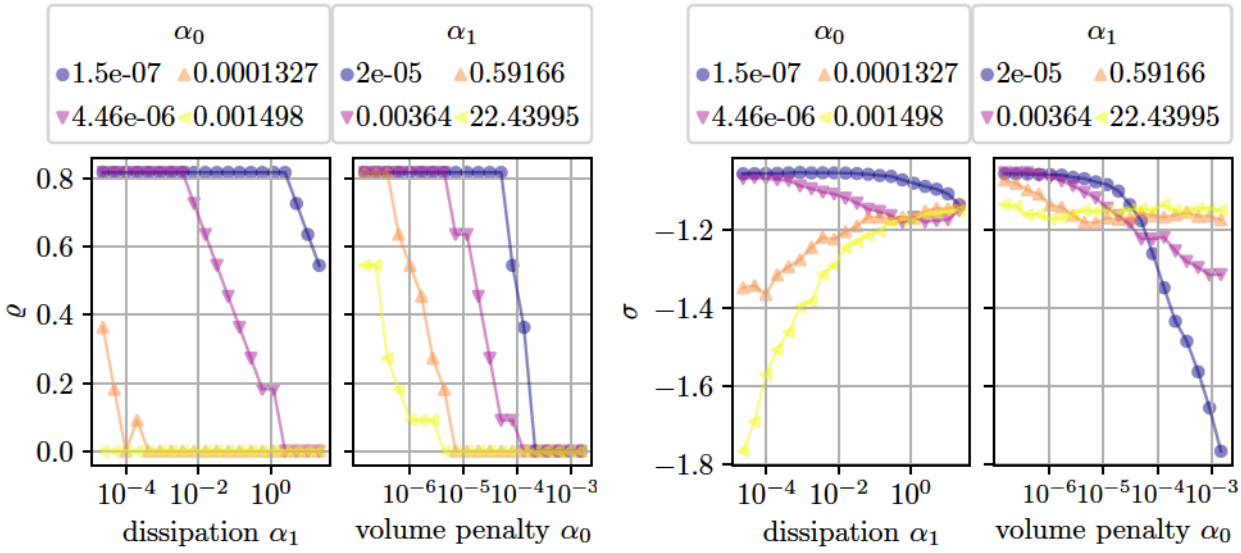

(b) Nullity ϱ

(c) Filtration σ

Figure B.4: Formations of the adaptation model (3.120) with $\sigma_0 = 0.1$ and $\bar{\beta} = 0.01$, displayed for selected dissipation α_1 and volume penalties α_0: (a) Network plots illustrating the relative concentration profiles and edge radii, depicted for $\alpha_0 = 4.4 \cdot 10^{-6}$, (b) Nullity transitions displaying α_1 and α_0 induced reticulation breakdown. (c) Filtration trajectories depicting demand match by increase of α_1 and mismatch by increasing α_0.

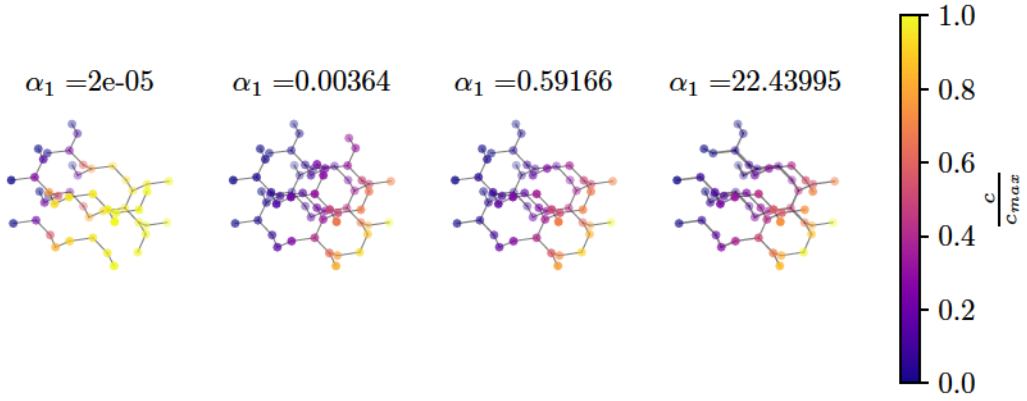

(a) Network skeletons and relative concentration profile

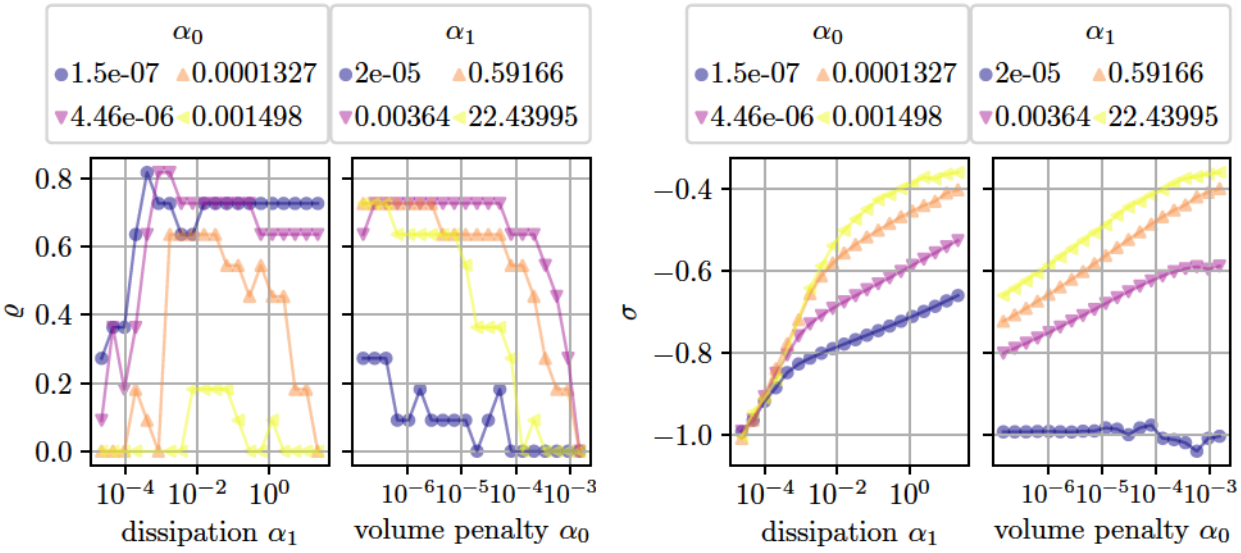

(b) Nullity ϱ

(c) Filtration σ

Figure B.5: Formations of the adaptation model (3.120) with $\sigma_0 = 0.01$ and $\bar{\beta} = 0.1$, displayed for selected dissipation α_1 and volume penalties α_0: (a) Network plots illustrating the relative concentration profiles and edge radii, depicted for $\alpha_0 = 1.33 \cdot 10^{-4}$, (b) Nullity transitions displaying α_1 re-entrant behavior and α_0 induced reticulation breakdown. (c) Filtration trajectories depicting uptake increase due to increase of α_1 and α_0.

B.3.2 Volume-wise demand adaptation

In Figure B.6 we present the collected results, as state diagram grids for systematic parameter screens. Note that the grid's x-axis is illustrating different cases of absorption rates $\bar{\beta}$ while the demanded volume filtration rate σ_0 variation is displayed on the grid's y-axis. In detail, we present the systems emerging nullity ϱ in Figure B.6a. In comparison to the previous section, we find the final reticulation to significantly change for the diagonal and lower triangle elements of the diagram grid. The re-entry behavior as well as most of the reticulation transition is lost for the scanned parameter range. In the second block, see Figure B.6b, we observe that the adaptability toward desired filtration rate is once again impaired for the lower triangle. As indicated in the upper triangle diagrams, we find the filtration matches to occur for reticulated states, which correspond to lower nullity values than before. As previously discussed, we expect the quantitative match for the diagonal elements to be a coincidence. In Figure B.7 we showcase exemplary network formations and concentration profiles, alongside detailed trajectories for nullity and filtration taken from the top-left diagrams in B.6. This diagram's data corresponds to the case of high demand in $\sigma_0 = 1.0$ and paired with low absorption $\bar{\beta} = 0.001$, Be reminded that we operate with periodic boundaries, indicated by dashed edges in B.7a. Figure B.7a generally shows that increasing α_1 will result in a nullity transition. As before, we observe the formation of dangling branches not connected to any sinks. We find the same mechanism at work as discussed for B.3a: Low $\bar{\beta}$ impair individual vessels from absorbing any significant amount of solute, as a result we observe the majority of vessels dilated, while the connection to the sinks is degenerated for small α_1, Note that this algorithm is able to generate non-perfused branches and even non-perfused loops, stabilized against the volume penalty by the solute uptake mechanism alone. In Figure B.8, we display exemplary cases for the central diagram of the grid B.6, corresponding to $\sigma_0.1$ and $\bar{\beta} = 0.01$, Note that the system becomes seemingly more fragmented, as nullity breaks down, which we display in Figure B.8a for increasing α_1, In Figure B.9, we show that no re-entrant behavior is present anymore in bottom-right diagram of the grid B.6, corresponding to $\sigma = 0.01$ and $\bar{\beta} = 0.1$, Be aware that consecutive studies on size dependency are in order to rule out finite size effects, as we can not dismiss the influence of topological generators for small systems at this point.

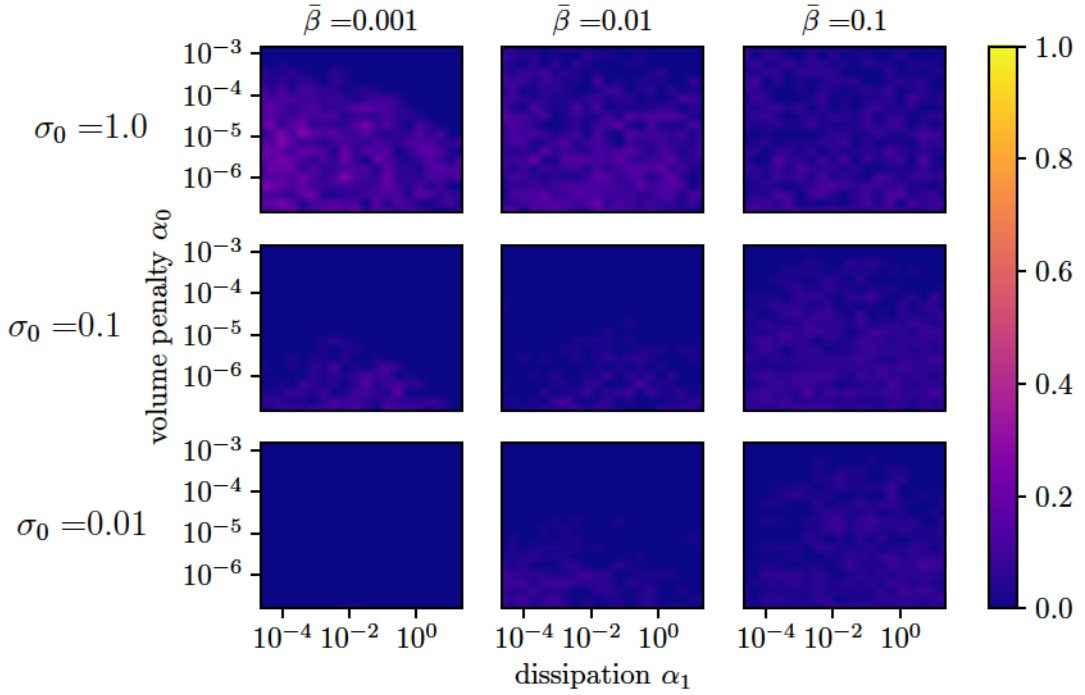

(a) Nullity ϱ

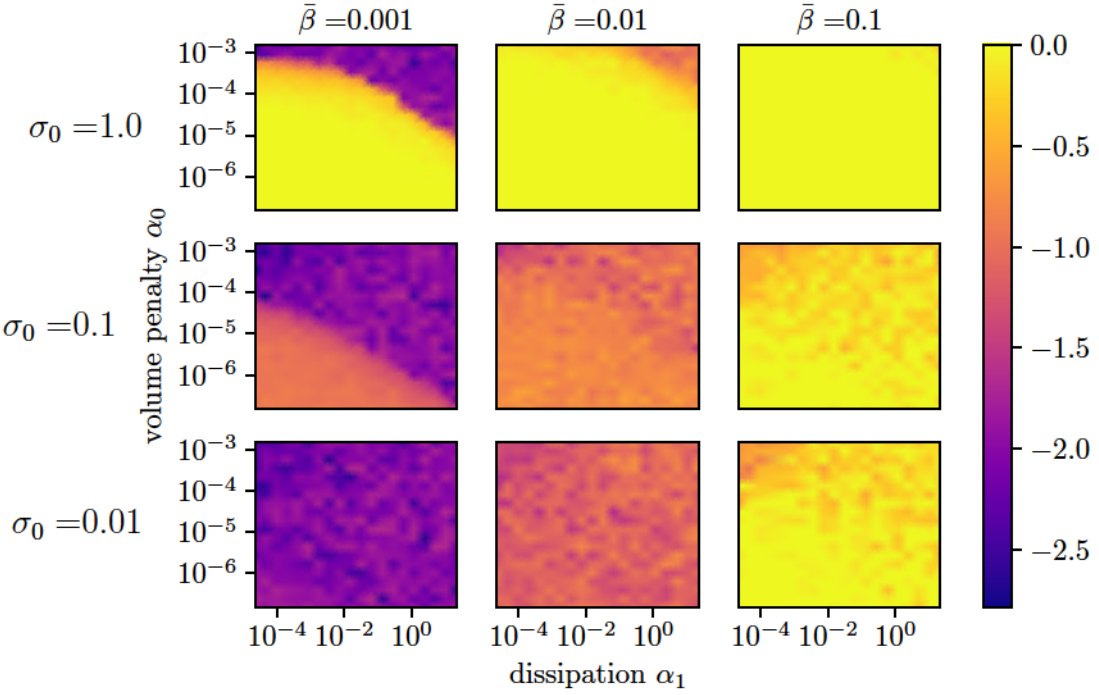

(b) Filtration σ

Figure B.6: Nullity and filtration diagrams for stationary states of the cost problem (3.120), with boundary parameter variation $\sigma_0 = \frac{\sum_e \Phi_{0,e}}{\sum_{J_n>0} J_n} \in \{10^0, 10^{-1}, 10^{-2}\}$, $\bar{\beta} \in \{10^{-1}, 10^{-1}, 10^{-2}\}$; systematic volume penalty α_0 and dissipation α_1 are scanned systematically: (a) The nullity phase diagram indicates a topological transition and re entrant behavior. (b) Filtration diagram indicating varying quality of filtration adjustment for varying $\bar{\beta}$.

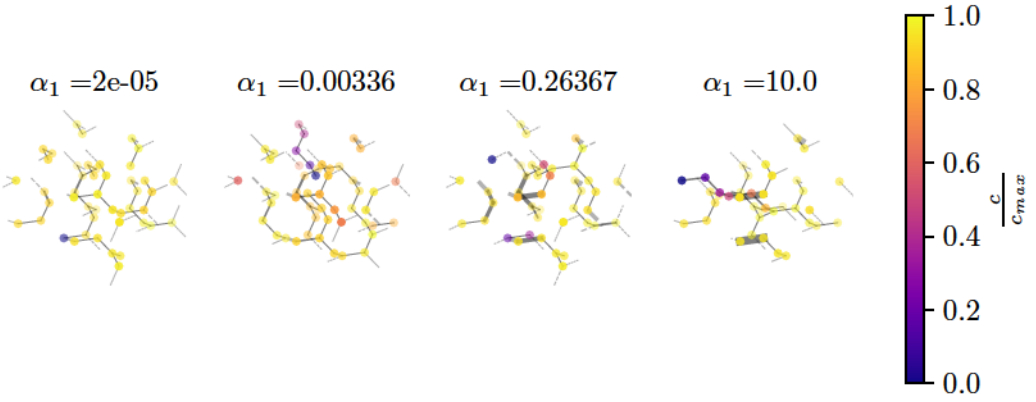

(a) Network skeletons and relative concentration profile

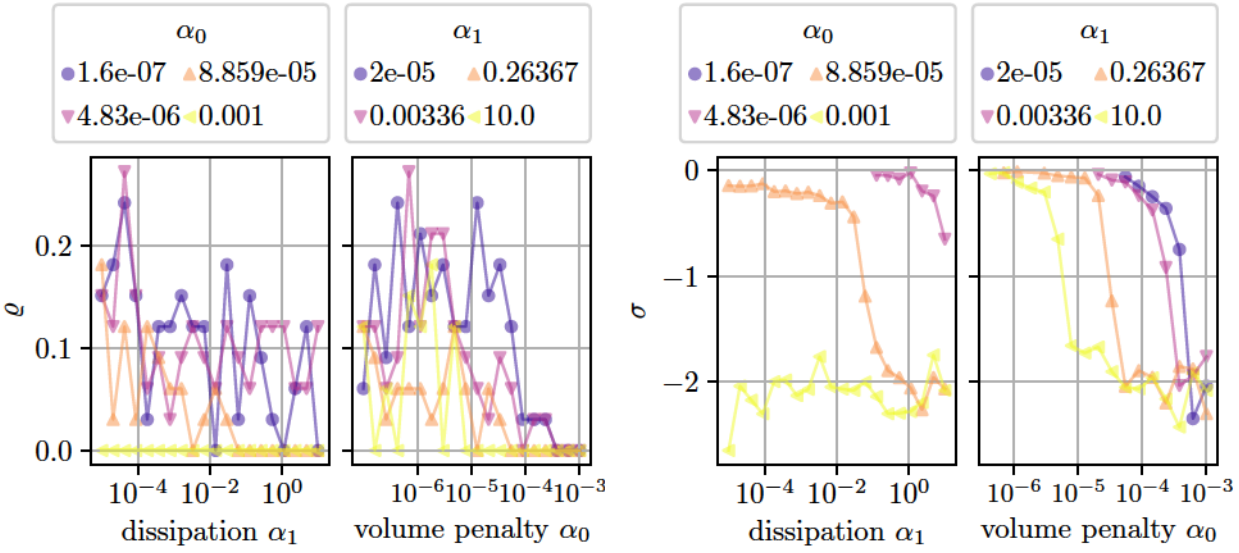

(b) Nullity ϱ

(c) Filtration σ

Figure B.7: Formations of the adaptation model (3.120) with $\sigma_0 = 1.0$ and $\bar{\beta} = 0.001$, displayed for selected dissipation α_1 and volume penalties α_0: (a) Network plots illustrating the relative concentration profiles and edge radii, depicted for $\alpha_0 = 9 \cdot 10^{-6}$, (b) Nullity transitions displaying α_1 and α_0 induced reticulation breakdown. (c) Filtration trajectories depicting switches in correlation to topological transitions.

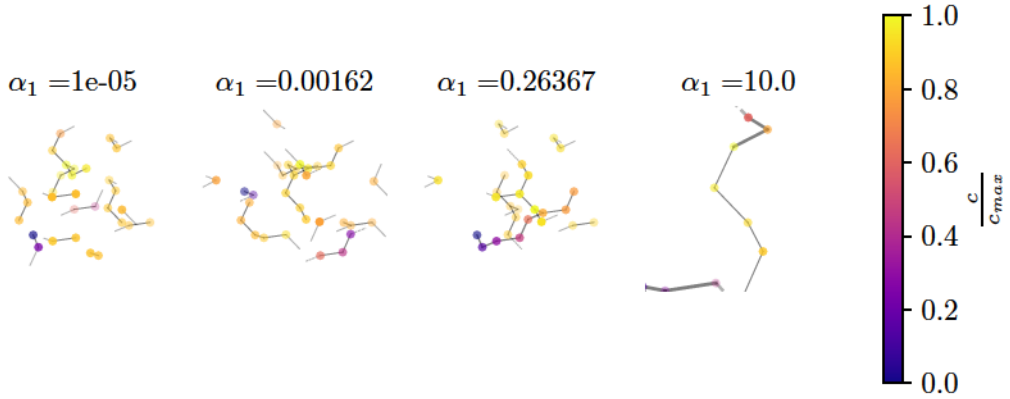

(a) Network skeletons and relative concentration profile

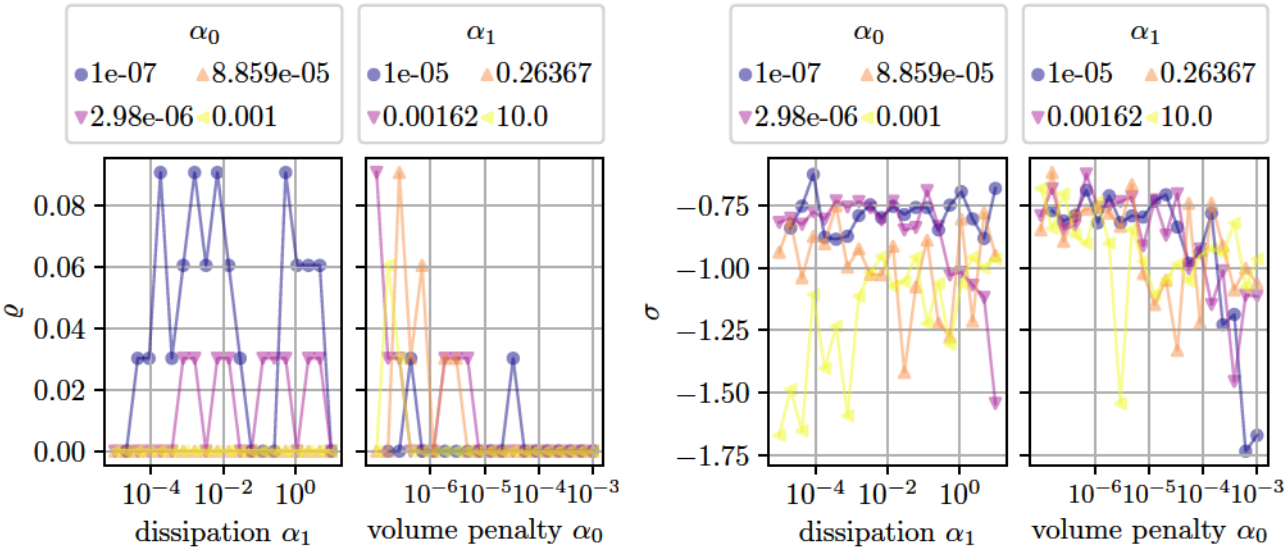

(b) Nullity ϱ

(c) Filtration σ

Figure B.8: Formations of the adaptation model (3.120) with $\sigma_0 = 0.1$ and $\bar{\beta} = 0.01$, displayed for selected dissipation α_1 and volume penalties α_0: (a) Network plots illustrating the relative concentration profiles and edge radii, depicted for $\alpha_0 = 9 \cdot 10^{-6}$, (b) Nullity transitions displaying α_1 and α_0 induced reticulation breakdown. (c) Filtration trajectories depicting demand match by increase of α_1 and mismatch by increasing α_0

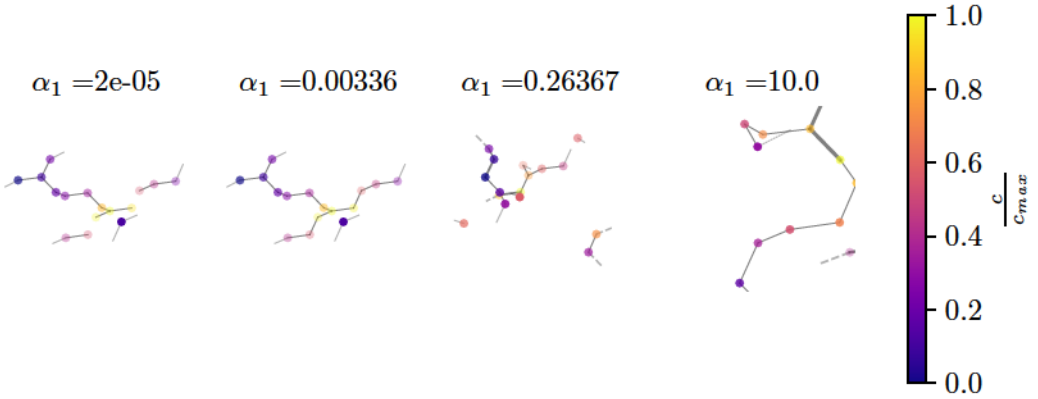

(a) Network skeletons and relative concentration profile

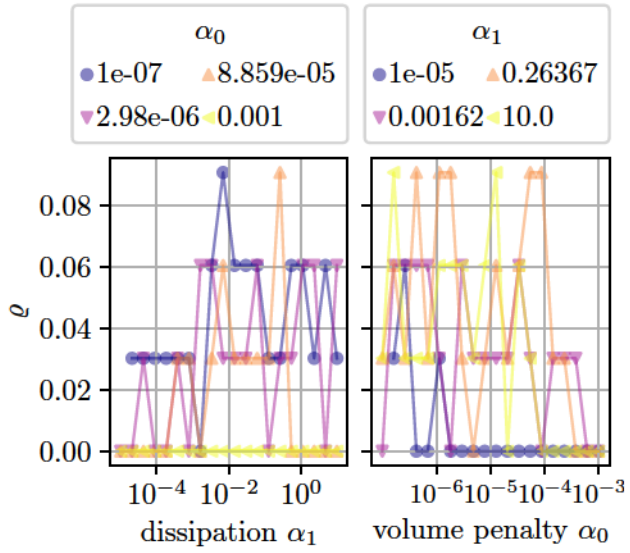

(b) Nullity ϱ

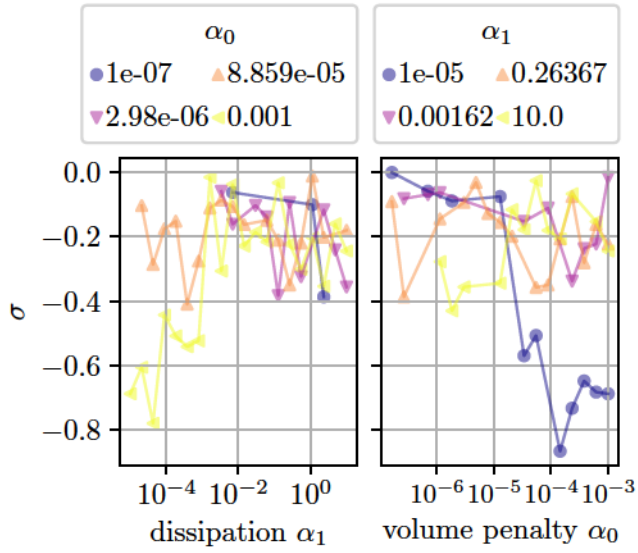

(c) Filtration σ

Figure B.9: Formations of the adaptation model (3.120) with $\sigma_0 = 0.01$ and $\bar{\beta} = 0.1$, displayed for selected dissipation α_1 and volume penalties α_0: (a) Network plots illustrating the relative concentration profiles and edge radii, depicted for $\alpha_0 = 9 \cdot 10^{-6}$, (b) Nullity transitions displaying α_1 re-entrant behavior and α_0 induced reticulation breakdown.
(c) Filtration trajectories depicting uptake increase due to increase of α_1 and α_0.

Bibliography

[1] *Active Particles, Volume 1*. Springer International Publishing. Cham, 2017.

[2] Ian J. Aitkenhead et al. "Tracheal branching in ants is area-decreasing, violating a central assumption of network transport models". In: *PLOS Computational Biology* 16.4 (Apr. 2020), e1007853–15.

[3] Dai Akita et al. "Experimental models for Murray's law". In: *Journal of Physics D: Applied Physics* 50.2 (Dec. 2016), pp. 024001–12.

[4] Jordi Alastruey et al. "Lumped parameter outflow models for 1-D blood flow simulations: Effect on pulse waves and parameter estimation". English. In: *Communications in Computational Physics* 4.2 (Aug. 2008), pp. 317–336. ISSN: 1815-2406.

[5] Karen Alim. "Fluid flows shaping organism morphology". In: *Philosophical Transactions of the Royal Society B: Biological Sciences* 373.1747 (Apr. 2018), p. 20170112.

[6] Karen Alim et al. "Random network peristalsis in Physarum polycephalum organizes fluid flows across an individual". In: *Proceedings of the National Academy of Sciences* 110.33 (2013), pp. 13306–13311.

[7] M. P. Allen, D. J. Tildesley, and Dominic J. Tildesley. *Computer simulation of liquids*. First publ. in paperback (with corr.) , reprinted. Oxford [u.a.]: Clarendon Pr., 2007. ISBN: 9780198556459.

[8] P W Anderson. "More Is Different". In: *Science* 177.4 (Aug. 1972), pp. 393–396.

[9] Wah Khim Ang and Paul W Jowitt. "Some new insights on informational entropy for water distribution networks". In: *Engineering Optimization* 37.3 (Apr. 2005), pp. 277–289.

[10] D. Berfin Azizoglu et al. "Vascular development in the vertebrate pancreas". In: *Developmental Biology* 420.1 (Dec. 2016), pp. 67–78.

[11] Yaneer Bar-Yam. *Making Things Work; Solving complex problems in a complex world*. NECSI, Jan. 2004. ISBN: 0965632822.

[12] Marc Barthélemy. *Morphogenesis of Spatial Networks*. Springer International Publishing. Cham, 2018.

[13] Stuart R. Batten and Richard Robson. "Interpenetrating Nets: Ordered, Periodic Entanglement." In: *Angewandte Chemie (International ed. in English)* 37.11 (June 1998), pp. 1460–1494.

[14] Beatrice Bedussi et al. "Paravascular spaces at the brain surface: Low resistance pathways for cerebrospinal fluid flow." In: *Journal of cerebral blood flow and metabolism : official journal of the International Society of Cerebral Blood Flow and Metabolism* 38.4 (Apr. 2018), pp. 719–726.

[15] A. Ben-Israel and A. Charnes. "Generalized inverses and the Bott-Duffin network analysis". In: *Journal of Mathematical Analysis and Applications* 7.3 (1963), pp. 428–435.

[16] Garrett Birkhoff and J. B Diaz. "Non-Linear Network Problems". In: *Quarterly of Applied Mathematics* 13.4 (Jan. 1956), pp. 431–443.

[17] Pablo Blinder et al. "Topological basis for the robust distribution of blood to rodent neocortex". In: *Proceedings of the National Academy of Sciences* 107.28 (July 2010), pp. 12670–12675.

[18] Benjamin Blonder et al. "Variation and macroevolution in leaf functional traits in the Hawaiian silversword alliance (Asteraceae)". In: *The Journal of ecology* 104.1 (2016), 219—228. ISSN: 0022-0477.

[19] S. Boccaletti et al. "The structure and dynamics of multilayer networks". In: *Physics Reports* 544.1 (Nov. 2014), pp. 1–122.

[20] Steffen Bohn and Marcelo O Magnasco. "Structure, Scaling, and Phase Transition in the Optimal Transport Network". In: *Physical Review Letters* 98.8 (Feb. 2007), pp. 088702–4.

[21] Justin S. Bois, Frank Jülicher, and Stephan W Grill. "Pattern Formation in Active Fluids". In: *Physical Review Letters* 106.2 (Jan. 2011), pp. 028103–4.

[22] Ralf Brandes et al. *Physiologie des Menschen mit Pathophysiologie : mit 850 Farbabbildungen*. 32. Auflage. Berlin: Springer, [2019]. ISBN: 9783662564677.

[23] R. W. Brauer, G. F. Leong, and R. J. Holloway. "Mechanics of Bile Secretion - Effect of Perfusion Pressure and Temperature on Bile Flow and Bile Secretion Pressure". In: *American Journal of Physiology* 177.1 (1954), pp. 103–112.

[24] C. G. Caro et al. *The Mechanics of the Circulation*. 2nd ed. Cambridge University Press, 2011.

[25] Shyr-Shea Chang and Marcus Roper. "Microvascular networks with uniform flow". In: *Journal of Theoretical Biology* 462 (Feb. 2019), pp. 48–64.

[26] Shyr-Shea Chang and Marcus Roper. "Microvscular networks with uniform flow." In: *Journal of Theoretical Biology* 462 (Feb. 2019), pp. 48–64.

[27] Shyr-Shea Chang et al. "Optimal occlusion uniformly partitions red blood cells fluxes within a microvascular network". In: *PLOS Computational Biology* 13.12 (Dec. 2017), e1005892–22.

[28] Donald S Coffey. "Self-organization, complexity and chaos: The new biology for medicine". In: *Nature medicine* 4.8 (1998), pp. 882–885.

[29] Sophie Collardeau-Frachon and Jean-Yves Scoazec. "Vascular Development and Differentiation During Human Liver Organogenesis". In: *The Anatomical Record: Advances in Integrative Anatomy and Evolutionary Biology* 291.6 (2008), pp. 614–627.

[30] Francis Corson. "Fluctuations and Redundancy in Optimal Transport Networks". In: *Physical Review Letters* 104.4 (Jan. 2010), pp. 048704–4.

[31] Svend Bertel Dahl-Jensen et al. "Deconstructing the principles of ductal network formation in the pancreas". In: *PLOS Biology* 16.7 (July 2018), e2002842–25.

[32] P. F. Davies. "Flow-Mediated Endothelial Mechanotransduction". In: *Physiological Reviews* 75.3 (July 1995), pp. 519–560.

[33] J. de Haan. "How emergence arises". In: *Ecological Complexity* 3.4 (2006). Complexity and Ecological Economics, pp. 293–301. ISSN: 1476-945X.

[34] Charles A. Desoer and Ernest S. Kuh. *Basic circuit theory*. New York [u.a.]: McGraw-Hill, 1969. ISBN: 0070165750.

[35] Theodosius Dobzhansky. "Nothing in Biology Makes Sense except in the Light of Evolution". In: *The American Biology Teacher* 35.3 (Mar. 1973), pp. 125–129. ISSN: 0002-7685.

[36] R. J. Duffin. "Distributed and Lumped Networks". In: *Journal of Mathematics and Mechanics* 8.5 (1959), pp. 793–826.

[37] R. J. Duffin. "Nonlinear Networks .2(B)." In: *Bulletin of the American Mathematical Society* 54.2 (1948), pp. 119–127.

[38] Marc Durand. "Architecture of optimal transport networks". In: *Physical Review E* 73.1 (Jan. 2006), pp. 592–6.

[39] Marc Durand and Denis Weaire. "Optimizing transport in a homogeneous network". In: *Physical Review E* 70.4 (Oct. 2004), pp. 3125–5.

[40] H Elias. "A Re-Examination of the Structure of the Mammalian Liver .1. Parenchymal Architecture". In: *American Journal of Anatomy* 84.2 (1949), pp. 311–333.

[41] H Elias. "A Re-Examination of the Structure of the Mammalian Liver .2. the Hepatic Lobule and Its Relation to the Vascular and Biliary Systems". In: *American Journal of Anatomy* 85.3 (1949), pp. 379–456.

[42] V Fleury. "Branching morphogenesis in a reaction-diffusion model". In: *Physical Review E* 61.4 (Apr. 2000), pp. 4156–4160.

[43] V. Fleury, J. F. Gouyet, and Marc Leonetti. *Branching in Nature*. Dynamics and Morphogenesis of Branching Structures, from Cell to River Networks. Springer Science & Business Media, Apr. 2013.

[44] Tatyana Gavrilchenko. *Geometry and Topology of Optimal Flow Networks*. 2020. URL: https://repository.upenn.edu/dissertations/AAI27961481.

[45] Tatyana Gavrilchenko and Eleni Katifori. "Distribution networks achieve uniform perfusion through geometric self-organization". In: (2020).

[46] Thomas J. Givnish et al. "Repeated evolution of net venation and fleshy fruits among monocots in shaded habitats confirms a priori predictions: evidence from an ndhF phylogeny." In: *Proceedings. Biological sciences* 272.1571 (July 2005), pp. 1481–1490.

[47] G. H. Golub and V. Pereyra. "The Differentiation of Pseudo-Inverses and Nonlinear Least Squares Problems Whose Variables Separate". In: *SIAM Journal on Numerical Analysis* 10.2 (Apr. 1973), pp. 413–432.

[48] Marko Gosak et al. "Network science of biological systems at different scales: A review". In: *Physics of Life Reviews* 24 (Mar. 2018), pp. 118–135.

[49] G. Gouysse et al. "Relationship between vascular development and vascular differentiation during liver organogenesis in humans". In: *Journal of Hepatology* 37.6 (Dec. 2002), pp. 730–740.

[50] Leo J. Grady and Jonathan R. Polimeni. *Discrete Calculus*. Applied Analysis on Graphs for Computational Science. Springer Science & Business Media, July 2010.

[51] Johannes Gräwer et al. "Structural self-assembly and avalanchelike dynamics in locally adaptive networks". In: *Physical Review E* 92.1 (July 2015), pp. 290–7.

[52] Jan Haskovec, Peter Markowich, and Benoît Perthame. "Mathematical Analysis of a PDE System for Biological Network Formation". In: *Communications in Partial Differential Equations* 40.5 (2015), pp. 918–956.

[53] Jan Haskovec et al. "Notes on a PDE system for biological network formation". In: *Nonlinear Analysis* 138 (June 2016), pp. 127–155.

[54] Luke L. M. Heaton et al. "Advection, diffusion, and delivery over a network". In: *Physical Review E* 86.2 (Aug. 2012), pp. 1360–10.

[55] W. R Hess. "Über die periphere Regulierung der Blutzirkulation". In: *Pflüger's Archiv für die gesamte Physiologie des Menschen und der Tiere* 168.9 (1917), pp. 439–490.

[56] Dan Hu and David Cai. "Adaptation and Optimization of Biological Transport Networks". In: *Physical Review Letters* 111.13 (Sept. 2013), H1706–5.

[57] Dan Hu, David Cai, and Aaditya V Rangan. "Blood Vessel Adaptation with Fluctuations in Capillary Flow Distribution". In: *PLoS ONE* 7.9 (Sept. 2012), e45444–.

[58] M. Luisa Iruela-Arispe and Greg J Beitel. "Tubulogenesis." In: *Development* 140.14 (July 2013), pp. 2851–2855.

[59] Jens Karschau et al. "Resilience of three-dimensional sinusoidal networks in liver tissue". In: *PLOS Computational Biology* 16.6 (June 2020), e1007965–22.

[60] Eleni Katifori and Marcelo O Magnasco. "Quantifying Loopy Network Architectures". In: *PLoS ONE* 7.6 (June 2012), e37994–14.

[61] Eleni Katifori, Gergely J. Szöllősi, and Marcelo O Magnasco. "Damage and Fluctuations Induce Loops in Optimal Transport Networks". In: *Physical Review Letters* 104.4 (Jan. 2010), pp. 522–4.

[62] F. P. Kelly. "Network Routing". In: *Philosophical Transactions of the Royal Society of London Series a-Mathematical Physical and Engineering Sciences* 337.1647 (1991), pp. 343–367.

[63] H. Kitano. "Systems biology: A brief overview". In: *Science* 295.5560 (2002), pp. 1662–1664.

[64] J. Koplik, S. Redner, and D. Wilkinson. "Transport and dispersion in random networks with percolation disorder." In: *Physical review. A, General physics* 37.7 (Apr. 1988), pp. 2619–2636.

[65] Felix Kramer and Carl D. Modes. "How to pare a pair: Topology control and pruning in intertwined complex networks". In: *Phys. Rev. Research* 2 (4 2020), p. 043171.

[66] A. Krogh. "The number and distribution of capillaries in muscles with calculations of the oxygen pressure head necessary for supplying the tissue." In: *Journal of Physiology-London* 52.6 (May 1919), pp. 409–415.

[67] Sven O. Krumke and Hartmut Noltemeier. *Graphentheoretische Konzepte und Algorithmen*. 3. Aufl. Wiesbaden: Springer Vieweg, 2012. ISBN: 9783834818492.

[68] L. D. Landau and E. M. Lifshitz. *Fluid Mechanics*. 2. Engl. ed., rev., repr. with corr. Course of Theoretical Physics (V.6). Amsterdam: Elsevier, Butterworth-Heinemann, 2012. ISBN: 9780750627672.

[69] W. W. Lautt. "Regulatory processes interacting to maintain hepatic blood flow constancy: Vascular compliance, hepatic arterial buffer response, hepatorenal reflex, liver regeneration, escape from vasoconstriction". In: *Hepatology Research* 37.11 (Nov. 2007), pp. 891–903.

[70] W. W. Lautt and C. V. Greenway. "Conceptual Review of the Hepatic Vascular Bed". In: *Hepatology* 7.5 (1987), pp. 952–963.

[71] Yuri Lazebnik. "Can a biologist fix a radio?—Or, what I. learned while studying apoptosis". In: *Cancer Cell* 2.3 (2002), pp. 179–182. ISSN: 1535-6108.

[72] Anna Lenard et al. "Endothelial Cell Self-fusion during Vascular Pruning". In: *PLOS Biology* 13.4 (Apr. 2015), e1002126–25.

[73] Liang Liu et al. "Physarum Optimization: A Biology-Inspired Algorithm for the Steiner Tree Problem in Networks". In: *IEEE Transactions on Computers* 64.3 (Mar. 2015), pp. 818–831.

[74] Karin Ljung, Rishikesh P. Bhalerao, and Göran Sandberg. "Sites and homeostatic control of auxin biosynthesis in Arabidopsis during vegetative growth". In: *The Plant Journal* 28.4 (2001), pp. 465–474.

[75] Judith Magenheim et al. "Blood vessels restrain pancreas branching, differentiation and growth." In: *Development* 138.21 (Nov. 2011), pp. 4743–4752.

[76] Sophie Marbach et al. "Pruning to Increase Taylor Dispersion in Physarum polycephalumNetworks". In: *Physical Review Letters* 117.17 (Oct. 2016), p. 178103.

[77] Robert C. Martin. *Clean codea handbook of agile software craftsmanship*. Upper Saddle River, NJ: Prentice Hall, 2009. ISBN: 9780132350884.

[78] Fulvio Mazzocchi. "Complexity in biology. Exceeding the limits of reductionism and determinism using complexity theory." In: *EMBO reports* 9.1 (Jan. 2008), pp. 10–14.

[79] Katherine A McCulloh, John S. Sperry, and Frederick R Adler. "Water transport in plants obeys Murray's law". In: *Nature* 421.6926 (2003), pp. 939–942.

[80] P. J. Meier. "Molecular mechanisms of hepatic bile salt transport from sinusoidal blood into bile". In: *American Journal of Physiology-Gastrointestinal and Liver Physiology* 269.6 (Dec. 1995), G801–G812.

[81] Felix J. Meigel and Karen Alim. "Flow rate of transport network controls uniform metabolite supply to tissue". In: *Journal of The Royal Society Interface* 15.142 (May 2018), pp. 20180075–10.

[82] Felix J. Meigel et al. "Robust Increase in Supply by Vessel Dilation in Globally Coupled Microvasculature". In: *Physical Review Letters* 123.22 (Nov. 2019), p. 228103.

[83] Kirstin Meyer et al. "A Predictive 3D Multi-Scale Model of Biliary Fluid Dynamics in the Liver Lobule". In: *Cell Systems* 4.3 (Mar. 2017), 277–290.e9.

[84] George K. Michalopoulos and Bharat Bhushan. "Liver regeneration: biological and pathological mechanisms and implications". In: *Nature Reviews Gastroenterology & Hepatology* (Dec. 2020), pp. 1–16.

[85] Yuriy Mileyko et al. "Hierarchical Ordering of Reticular Networks". In: *PLOS ONE* 7.6 (June 2012), pp. 1–9.

[86] Carl D. Modes, Marcelo O. Magnasco, and Eleni Katifori. "Extracting Hidden Hierarchies in 3D Distribution Networks". In: *Physical Review X* 6.3 (July 2016), pp. 031009–16.

[87] R. Monahan-Earley, A. M. Dvorak, and W. C. Aird. "Evolutionary origins of the blood vascular system and endothelium." In: *Journal of thrombosis and haemostasis : JTH* 11 Suppl 1 (June 2013), pp. 46–66.

[88] Hernan Morales-Navarrete et al. "A versatile pipeline for the multi-scale digital reconstruction and quantitative analysis of 3D tissue architecture". In: *Elife* 4 (2015).

[89] Hernan Morales-Navarrete et al. "Automatic recognition and characterization of different non-parenchymal cells in liver tissue". In: *2016 IEEE 13th International Symposium on Biomedical Imaging (ISBI)*. IEEE, pp. 536–540.

[90] Hernan Morales-Navarrete et al. "Liquid-crystal organization of liver tissue." In: *Elife* 8 (June 2019), p. 1035.

[91] Baptiste Moreau and Benjamin Mauroy. "Murray's law revisited: Quémada's fluid model and fractal trees". In: *Journal of Rheology* 59.6 (Nov. 2015), pp. 1419–1430.

[92] C. D. Murray. "The Physiological Principle of Minimum Work: I. The Vascular System and the Cost of Blood Volume." In: *Proceedings of the National Academy of Sciences* 12.3 (Mar. 1926), pp. 207–214.

[93] Cecil D. Murray. "The Physiological Principle of Minimum Work. II. Oxygen Exchange in Capillaries". In: *Proceedings of the National Academy of Sciences of the United States of America*. Department of Biology, Bryn Mawr College. May 1926, pp. 299–304.

[94] Mitchell G. Newberry, Daniel B. Ennis, and Van M. Savage. "Testing Foundations of Biological Scaling Theory Using Automated Measurements of Vascular Networks". In: *PLOS Computational Biology* 11.8 (Aug. 2015), e1004455–18.

[95] Mark E. J. Newman. *Networks*. Second edition. Oxford: Oxford University Press, 2018. ISBN: 9780198805090.

[96] Thi-Hanh Nguyen et al. "Dynamics of vascular branching morphogenesis: The effect of blood and tissue flow". In: *Physical Review E* 73.6 (June 2006), pp. 6–14.

[97] Jorge Nocedal and Stephen J. Wright. *Numerical optimization; 2nd ed.* Springer series in operations research and financial engineering. New York: Springer, 2006.

[98] Oleksandr Ostrenko. *Quantitative modeling of bile secretion and transport in the liver*. Dresden, 2017.

[99] Oleksandr Ostrenko, Jochen Hampe, and Lutz Brusch. "Wet-tip versus dry-tip regimes of osmotically driven fluid flow". In: *Scientific Reports* (Mar. 2019), pp. 1–15.

[100] Oleksandr Ostrenko, Jochen Hampe, and Lutz Brusch. "Wet-tip versus dry-tip regimes of osmotically driven fluid flow." In: *Scientific Reports* 9.1 (Mar. 2019), pp. 4528–15.

[101] Lia Papadopoulos et al. "Comparing two classes of biological distribution systems using network analysis". In: *PLOS Computational Biology* 14.9 (Sept. 2018), e1006428–31.

[102] R Penrose. "A generalized inverse for matrices". In: *Proceedings of the Cambridge Philosophical Society*. Cambridge University Press, July 1955, pp. 406–413.

[103] R Penrose. "On best approximate solutions of linear matrix equations". In: *Proceedings of the Cambridge Philosophical Society*. Jan. 1956, pp. 17–19.

[104] Nuno D. Pires and Liam Dolan. "Morphological evolution in land plants: new designs with old genes." In: *Philosophical transactions of the Royal Society of London. Series B, Biological sciences* 367.1588 (Feb. 2012), pp. 508–518.

[105] Lara Planas-Paz and Eckhard Lammert. "Mechanosensing in Developing Lymphatic Vessels". In: *Developmental Aspects of the Lymphatic Vascular System*. Vienna: Springer Vienna, Nov. 2013, pp. 23–40.

[106] A. R. Pries, B. Reglin, and T. W Secomb. "Structural adaptation of vascular networks - Role of the pressure response". In: *Hypertension* 38.6 (Dec. 2001), pp. 1476–1479.

[107] A. R. Pries, T. W. Secomb, and P Gaehtgens. "Structural adaptation and stability of microvascular networks: theory and simulations". In: *American Journal of Physiology-Gastrointestinal and Liver Physiology* 275.2 (Aug. 1998), H349–H360.

[108] Axel R. Pries et al. "Structural Adaptation and Heterogeneity of Normal and Tumor Microvascular Networks". In: *PLOS Computational Biology* 5.5 (May 2009), e1000394–11.

[109] Ahmadi-Badejani R, Mosharaf-Dehkordi M, and Ahmadikia H. "An image-based geometric model for numerical simulation of blood perfusion within the liver lobules". In: *Computer Methods in Biomechanics and Biomedical Engineering* 0.0 (June 2020), pp. 1–18.

[110] H. P Rani et al. "Numerical investigation of non-Newtonian microcirculatory blood flow in hepatic lobule." In: *Journal of biomechanics* 39.3 (2006), pp. 551–563.

[111] Peggy Raynaud et al. "Biliary differentiation and bile duct morphogenesis in development and disease". In: *International Journal of Biochemistry and Cell Biology* 43.2 (Feb. 2011), pp. 245–256.

[112] Volker Reitmann. *Reguläre und chaotische Dynamik*. Stuttgart: Teubner, 1996. ISBN: 9783815420904.

[113] Rémi Revellin et al. "Extension of Murray's law using a non-Newtonian model of blood flow". In: *Theoretical Biology and Medical Modelling* 6.1 (May 2009), pp. 207–9.

[114] Osborne Reynols. *Collected Works: Papers on Mechanical and Physical Subjects – The Sub-Mechanics of the Universe*. Vol. 3. Cambridge: Cambridge Univ. Press, 1903.

[115] W Risau. "Mechanisms of angiogenesis". In: *Nature* 386.6626 (1997), pp. 671–674.

[116] W. Risau and I Flamme. "Vasculogenesis". In: *Annual Review of Cell and Developmental Biology* 11.1 (1995), pp. 73–91.

[117] M. S. Roberts and M Rowland. "A dispersion model of hepatic elimination: 1. Formulation of the model and bolus considerations." In: *Journal of pharmacokinetics and biopharmaceutics* 14.3 (June 1986), pp. 227–260.

[118] M. S. Roberts and M Rowland. "A dispersion model of hepatic elimination: 2. Steady-state considerations–influence of hepatic blood flow, binding within blood, and hepatocellular enzyme activity." In: *Journal of pharmacokinetics and biopharmaceutics* 14.3 (June 1986), pp. 261–288.

[119] Jason W. Rocks et al. "Limits of multifunctionality in tunable networks". In: *Proceedings of the National Academy of Sciences* 116.7 (2019), pp. 2506–2511. ISSN: 0027-8424.

[120] Henrik Ronellenfitsch and Eleni Katifori. "Global Optimization, Local Adaptation, and the Role of Growth in Distribution Networks". In: *Physical Review Letters* 117.13 (Sept. 2016), H364–5.

[121] Henrik Ronellenfitsch and Eleni Katifori. "Phenotypes of Vascular Flow Networks". In: *Physical Review Letters* 123.24 (Dec. 2019), p. 248101.

[122] Henrik Ronellenfitsch and Eleni Katifori. "Phenotypes of Vascular Flow Networks". In: *Physical Review Letters* 123.24 (Dec. 2019), p. 248101.

[123] A Roth-Nebelsick. "Evolution and Function of Leaf Venation Architecture: A Review". In: *Annals of Botany* 87.5 (May 2001), pp. 553–566.

[124] Timothy W. Secomb et al. "Angiogenesis: An Adaptive Dynamic Biological Patterning Problem". In: *PLOS Computational Biology* 9.3 (Mar. 2013), e1002983–12.

[125] F. C. Serluca, I. A Drummond, and M. C Fishman. "Endothelial signaling in kidney morphogenesis: A role for hemodynamic forces". In: *Current Biology* 12.6 (2002), pp. 492–497.

[126] Mita M. Shah et al. "Branching morphogenesis and kidney disease." In: *Development* 131.7 (Apr. 2004), pp. 1449–1462.

[127] T. F. Sherman. "On connecting large vessels to small. The meaning of Murray's law." In: *The Journal of general physiology* 78.4 (Oct. 1981), pp. 431–453.

[128] Karim Si-Tayeb, Frédéric P Lemaigre, and Stephen A Duncan. "Organogenesis and Development of the Liver". In: *Developmental Cell* 18.2 (Feb. 2010), pp. 175–189.

[129] Kishor K. Sivaraj and Ralf H Adams. "Blood vessel formation and function in bone." In: *Development* 143.15 (Aug. 2016), pp. 2706–2715.

[130] Geoffrey Ingram Taylor. "Dispersion of soluble matter in solvent flowing slowly through a tube". In: *Proceedings of the Royal Society of London. Series A. Mathematical and Physical Sciences* 219.1137 (1953), pp. 186–203.

[131] Elif Tekin et al. "Do Vascular Networks Branch Optimally or Randomly across Spatial Scales?" In: *PLOS Computational Biology* 12.11 (Nov. 2016), e1005223–29.

[132] Atsushi Tero, Ryo Kobayashi, and Toshiyuki Nakagaki. "A mathematical model for adaptive transport network in path finding by true slime mold". In: *Journal of Theoretical Biology* 244.4 (Feb. 2007), pp. 553–564.

[133] Atsushi Tero et al. "Rules for biologically inspired adaptive network design." In: *Science* 327.5964 (Jan. 2010), pp. 439–442.

[134] R. Thoma. *Untersuchung über die Histogenese und Histomechanik des Gefässystems.* Stuttgart, 1893.

[135] Robert J Tomanek. *Assembly of the Vasculature and Its Regulation.* Springer Science & Business Media, Dec. 2012.

[136] Nachiket Vartak et al. "Intravital dynamic and correlative imaging reveals diffusion-dominated canalicular and flow-augmented ductular bile flux". In: *bioRxiv* (2020).

[137] Alethia Villasenor and Ondine Cleaver. "Crosstalk between the developing pancreas and its blood vessels: an evolving dialog." In: *Seminars in Cell and Developmental Biology* 23.6 (Aug. 2012), pp. 685–692.

[138] Pauli Virtanen et al. "SciPy 1.0: Fundamental Algorithms for Scientific Computing in Python". In: *Nature Methods* 17 (2020), pp. 261–272.

[139] Frans N. van de Vosse and Nikos Stergiopulos. "Pulse Wave Propagation in the Arterial Tree". In: *Annual Review of Fluid Mechanics* 43.1 (Jan. 2011), pp. 467–499.

[140] Shin Watanabe et al. "Traffic optimization in railroad networks using an algorithm mimicking an amoeba-like organism, Physarum plasmodium". In: *BioSystems* 105.3 (Sept. 2011), pp. 225–232.

[141] G. B West. "A General Model for the Origin of Allometric Scaling Laws in Biology". In: *Science* 276.5309 (1997), pp. 122–126.

[142] Hans V. Westerhoff and Bernhard O Palsson. "The evolution of molecular biology into systems biology". In: *Nature Biotechnology* 22.10 (Oct. 2004), pp. 1249–1252.

[143] Hassler Whitney. "Non-Separable and Planar Graphs". In: *Transactions of the American Mathematical Society* 34.2 (Apr. 1932), pp. 339–362.

[144] H. R. Williams et al. "Minimum mass vascular networks in multifunctional materials". In: *Journal of The Royal Society Interface* 5.18 (June 2007), pp. 55–65.

[145] Patricia D. Wilson and Beatrice Goilav. "Cystic Disease of the Kidney". In: *Annual Review of Pathology: Mechanisms of Disease* 2.1 (Feb. 2007), pp. 341–368.

[146] Rainer Wüst. *Mathematik für Physiker und Mathematiker 1 Reelle Analysis und Lineare Algebra*. 3. Aufl. Weinheim: Wiley-VCH, 2009. ISBN: 3527408770.

List of Figures

Erklärung des Promovierenden zum Antrag auf Eröffnung des Promotionsverfahrens

1. Die folgende Promotionsordnung in ihrer gültigen Fassung erkenne ich an:

   Bereich Mathematik und Naturwissenschaften - Promotionsordnung vom 23.02.2011

2. Die Promotion wurde an folgendem Institut/an folgender Professur durchgeführt:

   _____

3. Folgende Personen haben die Promotion wissenschaftlich betreut und/oder mich bei der Auswahl und Auswertung des Materials sowie bei der Herstellung des Manuskripts unterstützt:

   _____

   _____

   _____

   _____

4. Ich bestätige, dass für meine Person bisher keine früheren, erfolglosen Promotionsverfahren stattgefunden haben. Andernfalls habe ich diesem Antrag eine Erklärung bzw. Nachweise beigelegt, in dem ersichtlich ist, wo, wann, mit welchem Thema und mit welchem Bescheid diese Promotionsversuche stattgefunden haben

5. Ich versichere weiterhin, dass

(a) ich die vorliegende Arbeit mit dem Titel „Characterization, Analysis and Modeling of Complex Flow Networks in Mammalian Organs." ohne unzulässige Hilfe Dritter und ohne Benutzung anderer als der angegebenen Hilfsmittel selbst angefertigt habe. Hilfe Dritter wurde nur in wissenschaftlich vertretbarem und prüfungsrechtlich zulässigem Ausmaß in Anspruch genommen. Es sind keine unzulässigen geldwerten Leistungen, weder unmittelbar noch mittelbar, im Zusammenhang mit dem Inhalt der vorliegenden Dissertation an Dritte erfolgt.

(b) die aus fremden Quellen direkt oder indirekt übernommenen Gedanken als solche kenntlich gemacht sind.

(c) ich die vorliegende Arbeit bisher weder im Inland noch im Ausland in gleicher oder ähnlicher Form einer anderen Prüfungsbehörde zum Zwecke einer Promotion oder eines anderen Prüfungsverfahrens vorgelegt habe.

6. Mir ist bekannt, dass die Nichteinhaltung dieser Erklärung oder unrichtige Angaben zum Verfahrensabbruch oder zum nachträglichen Entzug des Doktortitels führen können.

Ort, Datum

Unterschrift Antragsteller/in